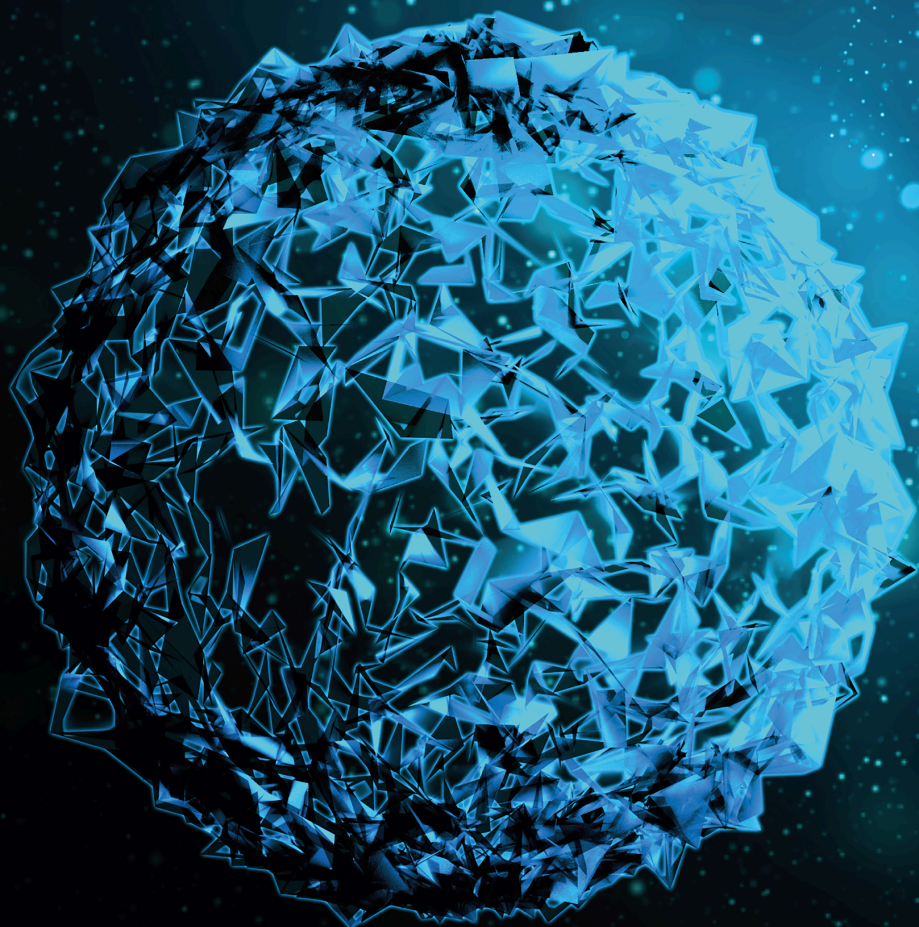


# Control of Infectious Diseases with Bio-Inorganic Nanodrugs

Lead Guest Editor: S Kumaran

Guest Editors: Wilson Aruni and Senthil Rethinam





---

# **Control of Infectious Diseases with Bio-Inorganic Nanodrugs**

BioMed Research International

---

## **Control of Infectious Diseases with Bio-Inorganic Nanodrugs**

Lead Guest Editor: S Kumaran

Guest Editors: Wilson Aruni and Senthil Rethinam



Copyright © 2024 Hindawi Limited. All rights reserved.

This is a special issue published in "BioMed Research International." All articles are open access articles distributed under the Creative Commons Attribution License, which permits unrestricted use, distribution, and reproduction in any medium, provided the original work is properly cited.

## Section Editors

Penny A. Asbell, USA  
David Bernardo , Spain  
Gerald Brandacher, USA  
Kim Bridle , Australia  
Laura Chronopoulou , Italy  
Gerald A. Colvin , USA  
Aaron S. Dumont, USA  
Pierfrancesco Franco , Italy  
Raj P. Kandpal , USA  
Fabrizio Montecucco , Italy  
Mangesh S. Pednekar , India  
Letterio S. Politi , USA  
Jinsong Ren , China  
William B. Rodgers, USA  
Harry W. Schroeder , USA  
Andrea Scribante , Italy  
Germán Vicente-Rodríguez , Spain  
Momiao Xiong , USA  
Hui Zhang , China

## Academic Editors

### Pharmacology

Abdel A. Abdel-Rahman , USA  
Camelia Albu, Romania  
Mohammad Hassan Baig , Republic of Korea  
Dan-Qian Chen , China  
Renata Ferreira , Brazil  
Joohun Ha, Republic of Korea  
Mansour Haddad, Jordan  
Ihsan-ul Haq , Pakistan  
Luis Ricardo Hernández , Mexico  
Kazim Husain , USA  
Ali Imran , Pakistan  
Muhammad Ayub Kakar, Pakistan  
Hye Joung Kim, Republic of Korea  
Zwe- Ling Kong , Taiwan  
Robert J. Lee , USA  
Min-Hui Li , China

Rui Liu , China  
A. M Abd El-Aty , Egypt  
Andrea Mencarelli, Singapore  
Juliana Mozer Sciani , Brazil  
Riccardo Nucera , Italy  
Giacomo Oteri , Italy  
Chi-Un Pae , Republic of Korea  
Ravi Radhakrishnan , USA  
Vickram Ramkumar , USA  
Thaís Ribeiro , Brazil  
Emilio Rojas, Mexico  
Simona Saponara, Italy  
Samuel Silvestre, Portugal  
Janet Sultana, Italy  
Shusen Sun , USA  
Emmanuel Talla, Cameroon  
Paul Vernyuy Tan , Cameroon  
Paul M. Tulkens , Belgium  
Narsingh Verma, India  
Taklo Simeneh Yazie , Ethiopia  
John H. Zhang , USA  
Yao Zheng , China  
Liang-Liang Zhu, China

# Contents

---

**Retracted: Comparative Analysis of Antioxidants Activity of Indigenously Produced *Moringa Oleifera* Seeds Extracts**

BioMed Research International

Retraction (1 page), Article ID 9879751, Volume 2024 (2024)

**Retracted: Development of Deep Learning Technique of Features for the Analysis of Clinical Images Integrated with CANN**

BioMed Research International

Retraction (1 page), Article ID 9847283, Volume 2024 (2024)

**Retracted: Phyto-Extract-Mediated Synthesis of Silver Nanoparticles (AgNPs) and Their Biological Activities**

BioMed Research International

Retraction (1 page), Article ID 9803813, Volume 2024 (2024)

**Retracted: Central Composite Designed Fast Dissolving Tablets for Improved Solubility of the Loaded Drug Ondansetron Hydrochloride**

BioMed Research International

Retraction (1 page), Article ID 9802835, Volume 2024 (2024)

**Retracted: AZ63/Ti/Zr Nanocomposite for Bone-Related Biomedical Applications**

BioMed Research International

Retraction (1 page), Article ID 9796702, Volume 2024 (2024)

**Retracted: Utilization of Bioinorganic Nanodrugs and Nanomaterials for the Control of Infectious Diseases Using Deep Learning**

BioMed Research International

Retraction (1 page), Article ID 9794818, Volume 2024 (2024)

**Retracted: Vancomycin as an Antibacterial Agent Capped with Silver Nanoparticles: An Experimental Potential Analysis**

BioMed Research International

Retraction (1 page), Article ID 9784637, Volume 2024 (2024)

**Retracted: Investigating the Lung Adenocarcinoma Stem Cell Biomarker Expressions Using Machine Learning Approaches**

BioMed Research International



Retraction (1 page), Article ID 9783729, Volume 2024 (2024)

**Retracted: Resveratrol Suppresses Bupivacaine-Induced Spinal Neurotoxicity in Rats by Inhibiting Endoplasmic Reticulum Stress via SIRT1 Modulation**

BioMed Research International


Retraction (1 page), Article ID 9861929, Volume 2023 (2023)

**[Retracted] AZ63/Ti/Zr Nanocomposite for Bone-Related Biomedical Applications**

T. Sathish, R. Saravanan, Sarange Shreepad , T. Amuthan, J. Immanuel Durai Raj, Piyush Gaur, V. Vijayan, and S. Rajkumar 








Research Article (11 pages), Article ID 6297372, Volume 2023 (2023)

**[Retracted] Utilization of Bioinorganic Nanodrugs and Nanomaterials for the Control of Infectious Diseases Using Deep Learning**

R. Priyadarshini, A. Sheik Abdullah, K. V. Karthikeyan, M. Vinoth, Betty Martin, S. Geerthik, Florin Wilfred , Nour M. Alyami, and R. S. Sundaram

Research Article (13 pages), Article ID 7464159, Volume 2023 (2023)

**[Retracted] Resveratrol Suppresses Bupivacaine-Induced Spinal Neurotoxicity in Rats by Inhibiting Endoplasmic Reticulum Stress via SIRT1 Modulation**

Yunpeng Luo , Yang Zhao , Jian Lai , Liling Wei , Gang Zhou , Yue Yu , and Jingchen Liu 

Research Article (13 pages), Article ID 1176232, Volume 2023 (2023)

**[Retracted] Phyto-Extract-Mediated Synthesis of Silver Nanoparticles (AgNPs) and Their Biological Activities**

Muhammad Adnan , Asma Akbar, Sakina Mussarat , Waheed Murad, Ishfaq Hameed, Shaheen Begum, Ruqia Nazir, Nawab Ali, Essam A. Ali, Ahmed Bari, Muhammad Abdul Aziz, and Shahid Niaz Khan







Research Article (10 pages), Article ID 9845022, Volume 2022 (2022)

**[Retracted] Comparative Analysis of Antioxidants Activity of Indigenously Produced *Moringa Oleifera* Seeds Extracts**

Sadaf Tariq, Huma Umbreen, Razia Noreen , Cyril Petitbois, Kiran Aftab, Fatmah Ali Alasmay, Amani Salem Almalki, and Mohammad Abdul Mazid 


Research Article (11 pages), Article ID 4987929, Volume 2022 (2022)

**[Retracted] Development of Deep Learning Technique of Features for the Analysis of Clinical Images Integrated with CANN**

Prabakaran Kasinathan , R. Prabha , R. S. Sabeenian , K. Baskar , A. Ramkumar , and Samson Alemayehu 





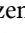




Research Article (7 pages), Article ID 2742274, Volume 2022 (2022)

**[Retracted] Investigating the Lung Adenocarcinoma Stem Cell Biomarker Expressions Using Machine Learning Approaches**

M. S. Bhuvaneswari, S. Priyadharsini, N. Balaganesh, R. Theenathayalan, and Tegegne Ayalew Hailu 

Research Article (11 pages), Article ID 3518190, Volume 2022 (2022)

**[Retracted] Vancomycin as an Antibacterial Agent Capped with Silver Nanoparticles: An Experimental Potential Analysis**






Mohsina Patwekar , Faheem Patwekar, Saad Alghamdi , Mehnaz Kamal , Mamdouh Allahyani , Mazen Almehmadi , Ahmed Kabrah , Anas S. Dablood , Ahad Amer Alsaiari, Talha Jawaid, Anuradha Medikeri , Krupa Samuel, and Fahadul Islam 

Research Article (8 pages), Article ID 3682757, Volume 2022 (2022)

## Contents

---

**[Retracted] Central Composite Designed Fast Dissolving Tablets for Improved Solubility of the Loaded Drug Ondansetron Hydrochloride**

Chandrashekar Thalluri, Ruhul Amin , Jithendar Reddy Mandhadi, Amel Gacem, Talha Bin Emran , Biplab Kumar Dey, Arpita Roy , Mohammed S. Alqahtani , Moamen S. Refat, Sher Zaman Safi, and Amnah Mohammed Alsuhaibani 

Research Article (13 pages), Article ID 2467574, Volume 2022 (2022)



## Retraction

# Retracted: Comparative Analysis of Antioxidants Activity of Indigenously Produced *Moringa Oleifera* Seeds Extracts

### BioMed Research International

Received 8 January 2024; Accepted 8 January 2024; Published 9 January 2024

Copyright © 2024 BioMed Research International. This is an open access article distributed under the Creative Commons Attribution License, which permits unrestricted use, distribution, and reproduction in any medium, provided the original work is properly cited.

This article has been retracted by Hindawi following an investigation undertaken by the publisher [1]. This investigation has uncovered evidence of one or more of the following indicators of systematic manipulation of the publication process:

- (1) Discrepancies in scope
- (2) Discrepancies in the description of the research reported
- (3) Discrepancies between the availability of data and the research described
- (4) Inappropriate citations
- (5) Incoherent, meaningless and/or irrelevant content included in the article
- (6) Manipulated or compromised peer review

The presence of these indicators undermines our confidence in the integrity of the article's content and we cannot, therefore, vouch for its reliability. Please note that this notice is intended solely to alert readers that the content of this article is unreliable. We have not investigated whether authors were aware of or involved in the systematic manipulation of the publication process.

Wiley and Hindawi regrets that the usual quality checks did not identify these issues before publication and have since put additional measures in place to safeguard research integrity.

We wish to credit our own Research Integrity and Research Publishing teams and anonymous and named external researchers and research integrity experts for contributing to this investigation.

The corresponding author, as the representative of all authors, has been given the opportunity to register their agreement or disagreement to this retraction. We have kept a record of any response received.

### References

- [1] S. Tariq, H. Umbreen, R. Noreen et al., "Comparative Analysis of Antioxidants Activity of Indigenously Produced *Moringa Oleifera* Seeds Extracts," *BioMed Research International*, vol. 2022, Article ID 4987929, 11 pages, 2022.

## *Retraction*

# **Retracted: Development of Deep Learning Technique of Features for the Analysis of Clinical Images Integrated with CANN**

### **BioMed Research International**

Received 8 January 2024; Accepted 8 January 2024; Published 9 January 2024

Copyright © 2024 BioMed Research International. This is an open access article distributed under the Creative Commons Attribution License, which permits unrestricted use, distribution, and reproduction in any medium, provided the original work is properly cited.

This article has been retracted by Hindawi following an investigation undertaken by the publisher [1]. This investigation has uncovered evidence of one or more of the following indicators of systematic manipulation of the publication process:

- (1) Discrepancies in scope
- (2) Discrepancies in the description of the research reported
- (3) Discrepancies between the availability of data and the research described
- (4) Inappropriate citations
- (5) Incoherent, meaningless and/or irrelevant content included in the article
- (6) Manipulated or compromised peer review

The presence of these indicators undermines our confidence in the integrity of the article's content and we cannot, therefore, vouch for its reliability. Please note that this notice is intended solely to alert readers that the content of this article is unreliable. We have not investigated whether authors were aware of or involved in the systematic manipulation of the publication process.

Wiley and Hindawi regrets that the usual quality checks did not identify these issues before publication and have since put additional measures in place to safeguard research integrity.

We wish to credit our own Research Integrity and Research Publishing teams and anonymous and named external researchers and research integrity experts for contributing to this investigation.

The corresponding author, as the representative of all authors, has been given the opportunity to register their agreement or disagreement to this retraction. We have kept a record of any response received.

### **References**

- [1] P. Kasinathan, R. Prabha, R. S. Sabeenian, K. Baskar, A. Ramkumar, and S. Alemayehu, "Development of Deep Learning Technique of Features for the Analysis of Clinical Images Integrated with CANN," *BioMed Research International*, vol. 2022, Article ID 2742274, 7 pages, 2022.

## Retraction

# Retracted: Phyto-Extract-Mediated Synthesis of Silver Nanoparticles (AgNPs) and Their Biological Activities

### BioMed Research International

Received 8 January 2024; Accepted 8 January 2024; Published 9 January 2024

Copyright © 2024 BioMed Research International. This is an open access article distributed under the Creative Commons Attribution License, which permits unrestricted use, distribution, and reproduction in any medium, provided the original work is properly cited.

This article has been retracted by Hindawi following an investigation undertaken by the publisher [1]. This investigation has uncovered evidence of one or more of the following indicators of systematic manipulation of the publication process:

- (1) Discrepancies in scope
- (2) Discrepancies in the description of the research reported
- (3) Discrepancies between the availability of data and the research described
- (4) Inappropriate citations
- (5) Incoherent, meaningless and/or irrelevant content included in the article
- (6) Manipulated or compromised peer review

The presence of these indicators undermines our confidence in the integrity of the article's content and we cannot, therefore, vouch for its reliability. Please note that this notice is intended solely to alert readers that the content of this article is unreliable. We have not investigated whether authors were aware of or involved in the systematic manipulation of the publication process.

Wiley and Hindawi regrets that the usual quality checks did not identify these issues before publication and have since put additional measures in place to safeguard research integrity.

We wish to credit our own Research Integrity and Research Publishing teams and anonymous and named external researchers and research integrity experts for contributing to this investigation.

The corresponding author, as the representative of all authors, has been given the opportunity to register their agreement or disagreement to this retraction. We have kept a record of any response received.

### References

- [1] M. Adnan, A. Akbar, S. Mussarat et al., "Phyto-Extract-Mediated Synthesis of Silver Nanoparticles (AgNPs) and Their Biological Activities," *BioMed Research International*, vol. 2022, Article ID 9845022, 10 pages, 2022.

## *Retraction*

# **Retracted: Central Composite Designed Fast Dissolving Tablets for Improved Solubility of the Loaded Drug Ondansetron Hydrochloride**

### **BioMed Research International**

Received 8 January 2024; Accepted 8 January 2024; Published 9 January 2024

Copyright © 2024 BioMed Research International. This is an open access article distributed under the Creative Commons Attribution License, which permits unrestricted use, distribution, and reproduction in any medium, provided the original work is properly cited.

This article has been retracted by Hindawi following an investigation undertaken by the publisher [1]. This investigation has uncovered evidence of one or more of the following indicators of systematic manipulation of the publication process:

- (1) Discrepancies in scope
- (2) Discrepancies in the description of the research reported
- (3) Discrepancies between the availability of data and the research described
- (4) Inappropriate citations
- (5) Incoherent, meaningless and/or irrelevant content included in the article
- (6) Manipulated or compromised peer review

The presence of these indicators undermines our confidence in the integrity of the article's content and we cannot, therefore, vouch for its reliability. Please note that this notice is intended solely to alert readers that the content of this article is unreliable. We have not investigated whether authors were aware of or involved in the systematic manipulation of the publication process.

Wiley and Hindawi regrets that the usual quality checks did not identify these issues before publication and have since put additional measures in place to safeguard research integrity.

We wish to credit our own Research Integrity and Research Publishing teams and anonymous and named external researchers and research integrity experts for contributing to this investigation.

The corresponding author, as the representative of all authors, has been given the opportunity to register their agreement or disagreement to this retraction. We have kept a record of any response received.

### **References**

- [1] C. Thalluri, R. Amin, J. R. Mandhadi et al., "Central Composite Designed Fast Dissolving Tablets for Improved Solubility of the Loaded Drug Ondansetron Hydrochloride," *BioMed Research International*, vol. 2022, Article ID 2467574, 13 pages, 2022.

## Retraction

# Retracted: AZ63/Ti/Zr Nanocomposite for Bone-Related Biomedical Applications

### BioMed Research International

Received 8 January 2024; Accepted 8 January 2024; Published 9 January 2024

Copyright © 2024 BioMed Research International. This is an open access article distributed under the Creative Commons Attribution License, which permits unrestricted use, distribution, and reproduction in any medium, provided the original work is properly cited.

This article has been retracted by Hindawi following an investigation undertaken by the publisher [1]. This investigation has uncovered evidence of one or more of the following indicators of systematic manipulation of the publication process:

- (1) Discrepancies in scope
- (2) Discrepancies in the description of the research reported
- (3) Discrepancies between the availability of data and the research described
- (4) Inappropriate citations
- (5) Incoherent, meaningless and/or irrelevant content included in the article
- (6) Manipulated or compromised peer review

The presence of these indicators undermines our confidence in the integrity of the article's content and we cannot, therefore, vouch for its reliability. Please note that this notice is intended solely to alert readers that the content of this article is unreliable. We have not investigated whether authors were aware of or involved in the systematic manipulation of the publication process.

Wiley and Hindawi regrets that the usual quality checks did not identify these issues before publication and have since put additional measures in place to safeguard research integrity.

We wish to credit our own Research Integrity and Research Publishing teams and anonymous and named external researchers and research integrity experts for contributing to this investigation.

The corresponding author, as the representative of all authors, has been given the opportunity to register their agreement or disagreement to this retraction. We have kept a record of any response received.

### References

- [1] T. Sathish, R. Saravanan, S. Shreepad et al., "AZ63/Ti/Zr Nanocomposite for Bone-Related Biomedical Applications," *BioMed Research International*, vol. 2023, Article ID 6297372, 11 pages, 2023.

## *Retraction*

# **Retracted: Utilization of Bioinorganic Nanodrugs and Nanomaterials for the Control of Infectious Diseases Using Deep Learning**

### **BioMed Research International**

Received 8 January 2024; Accepted 8 January 2024; Published 9 January 2024

Copyright © 2024 BioMed Research International. This is an open access article distributed under the Creative Commons Attribution License, which permits unrestricted use, distribution, and reproduction in any medium, provided the original work is properly cited.

This article has been retracted by Hindawi, as publisher, following an investigation undertaken by the publisher [1]. This investigation has uncovered evidence of systematic manipulation of the publication and peer-review process. We cannot, therefore, vouch for the reliability or integrity of this article.

Please note that this notice is intended solely to alert readers that the peer-review process of this article has been compromised.

Wiley and Hindawi regret that the usual quality checks did not identify these issues before publication and have since put additional measures in place to safeguard research integrity.

We wish to credit our Research Integrity and Research Publishing teams and anonymous and named external researchers and research integrity experts for contributing to this investigation.

The corresponding author, as the representative of all authors, has been given the opportunity to register their agreement or disagreement to this retraction. We have kept a record of any response received.

## **References**

- [1] R. Priyadarshini, A. S. Abdullah, K. V. Karthikeyan et al., "Utilization of Bioinorganic Nanodrugs and Nanomaterials for the Control of Infectious Diseases Using Deep Learning," *BioMed Research International*, vol. 2023, Article ID 7464159, 13 pages, 2023.

## Retraction

# Retracted: Vancomycin as an Antibacterial Agent Capped with Silver Nanoparticles: An Experimental Potential Analysis

### BioMed Research International

Received 8 January 2024; Accepted 8 January 2024; Published 9 January 2024

Copyright © 2024 BioMed Research International. This is an open access article distributed under the Creative Commons Attribution License, which permits unrestricted use, distribution, and reproduction in any medium, provided the original work is properly cited.

This article has been retracted by Hindawi following an investigation undertaken by the publisher [1]. This investigation has uncovered evidence of one or more of the following indicators of systematic manipulation of the publication process:

- (1) Discrepancies in scope
- (2) Discrepancies in the description of the research reported
- (3) Discrepancies between the availability of data and the research described
- (4) Inappropriate citations
- (5) Incoherent, meaningless and/or irrelevant content included in the article
- (6) Manipulated or compromised peer review

The presence of these indicators undermines our confidence in the integrity of the article's content and we cannot, therefore, vouch for its reliability. Please note that this notice is intended solely to alert readers that the content of this article is unreliable. We have not investigated whether authors were aware of or involved in the systematic manipulation of the publication process.

Wiley and Hindawi regrets that the usual quality checks did not identify these issues before publication and have since put additional measures in place to safeguard research integrity.

We wish to credit our own Research Integrity and Research Publishing teams and anonymous and named external researchers and research integrity experts for contributing to this investigation.

The corresponding author, as the representative of all authors, has been given the opportunity to register their agreement or disagreement to this retraction. We have kept a record of any response received.

### References

- [1] M. Patwekar, F. Patwekar, S. Alghamdi et al., "Vancomycin as an Antibacterial Agent Capped with Silver Nanoparticles: An Experimental Potential Analysis," *BioMed Research International*, vol. 2022, Article ID 3682757, 8 pages, 2022.

## Retraction

# Retracted: Investigating the Lung Adenocarcinoma Stem Cell Biomarker Expressions Using Machine Learning Approaches

### BioMed Research International

Received 8 January 2024; Accepted 8 January 2024; Published 9 January 2024

Copyright © 2024 BioMed Research International. This is an open access article distributed under the Creative Commons Attribution License, which permits unrestricted use, distribution, and reproduction in any medium, provided the original work is properly cited.

This article has been retracted by Hindawi following an investigation undertaken by the publisher [1]. This investigation has uncovered evidence of one or more of the following indicators of systematic manipulation of the publication process:

- (1) Discrepancies in scope
- (2) Discrepancies in the description of the research reported
- (3) Discrepancies between the availability of data and the research described
- (4) Inappropriate citations
- (5) Incoherent, meaningless and/or irrelevant content included in the article
- (6) Manipulated or compromised peer review

The presence of these indicators undermines our confidence in the integrity of the article's content and we cannot, therefore, vouch for its reliability. Please note that this notice is intended solely to alert readers that the content of this article is unreliable. We have not investigated whether authors were aware of or involved in the systematic manipulation of the publication process.

Wiley and Hindawi regrets that the usual quality checks did not identify these issues before publication and have since put additional measures in place to safeguard research integrity.

We wish to credit our own Research Integrity and Research Publishing teams and anonymous and named external researchers and research integrity experts for contributing to this investigation.

The corresponding author, as the representative of all authors, has been given the opportunity to register their agreement or disagreement to this retraction. We have kept a record of any response received.

### References

- [1] M. S. Bhuvaneshwari, S. Priyadharsini, N. Balaganesh, R. Theenathayalan, and T. A. Hailu, "Investigating the Lung Adenocarcinoma Stem Cell Biomarker Expressions Using Machine Learning Approaches," *BioMed Research International*, vol. 2022, Article ID 3518190, 11 pages, 2022.



## Retraction

# Retracted: Resveratrol Suppresses Bupivacaine-Induced Spinal Neurotoxicity in Rats by Inhibiting Endoplasmic Reticulum Stress via SIRT1 Modulation

### BioMed Research International

Received 20 June 2023; Accepted 20 June 2023; Published 21 June 2023

Copyright © 2023 BioMed Research International. This is an open access article distributed under the Creative Commons Attribution License, which permits unrestricted use, distribution, and reproduction in any medium, provided the original work is properly cited.

This article has been retracted by Hindawi following an investigation undertaken by the publisher [1]. This investigation has uncovered evidence of one or more of the following indicators of systematic manipulation of the publication process:

- (1) Discrepancies in scope
- (2) Discrepancies in the description of the research reported
- (3) Discrepancies between the availability of data and the research described
- (4) Inappropriate citations
- (5) Incoherent, meaningless and/or irrelevant content included in the article
- (6) Peer-review manipulation

The presence of these indicators undermines our confidence in the integrity of the article's content and we cannot, therefore, vouch for its reliability. Please note that this notice is intended solely to alert readers that the content of this article is unreliable. We have not investigated whether authors were aware of or involved in the systematic manipulation of the publication process.

Wiley and Hindawi regrets that the usual quality checks did not identify these issues before publication and have since put additional measures in place to safeguard research integrity.

We wish to credit our own Research Integrity and Research Publishing teams and anonymous and named external researchers and research integrity experts for contributing to this investigation.

The corresponding author, as the representative of all authors, has been given the opportunity to register their agreement or disagreement to this retraction. We have kept a record of any response received.

### References

- [1] Y. Luo, Y. Zhao, J. Lai et al., "Resveratrol Suppresses Bupivacaine-Induced Spinal Neurotoxicity in Rats by Inhibiting Endoplasmic Reticulum Stress via SIRT1 Modulation," *BioMed Research International*, vol. 2023, Article ID 1176232, 13 pages, 2023.

## Retraction

# Retracted: AZ63/Ti/Zr Nanocomposite for Bone-Related Biomedical Applications

### BioMed Research International

Received 8 January 2024; Accepted 8 January 2024; Published 9 January 2024

Copyright © 2024 BioMed Research International. This is an open access article distributed under the Creative Commons Attribution License, which permits unrestricted use, distribution, and reproduction in any medium, provided the original work is properly cited.

This article has been retracted by Hindawi following an investigation undertaken by the publisher [1]. This investigation has uncovered evidence of one or more of the following indicators of systematic manipulation of the publication process:

- (1) Discrepancies in scope
- (2) Discrepancies in the description of the research reported
- (3) Discrepancies between the availability of data and the research described
- (4) Inappropriate citations
- (5) Incoherent, meaningless and/or irrelevant content included in the article
- (6) Manipulated or compromised peer review

The presence of these indicators undermines our confidence in the integrity of the article's content and we cannot, therefore, vouch for its reliability. Please note that this notice is intended solely to alert readers that the content of this article is unreliable. We have not investigated whether authors were aware of or involved in the systematic manipulation of the publication process.

Wiley and Hindawi regrets that the usual quality checks did not identify these issues before publication and have since put additional measures in place to safeguard research integrity.

We wish to credit our own Research Integrity and Research Publishing teams and anonymous and named external researchers and research integrity experts for contributing to this investigation.

The corresponding author, as the representative of all authors, has been given the opportunity to register their agreement or disagreement to this retraction. We have kept a record of any response received.

### References

- [1] T. Sathish, R. Saravanan, S. Shreepad et al., "AZ63/Ti/Zr Nanocomposite for Bone-Related Biomedical Applications," *BioMed Research International*, vol. 2023, Article ID 6297372, 11 pages, 2023.

## Research Article

# AZ63/Ti/Zr Nanocomposite for Bone-Related Biomedical Applications

**T. Sathish,<sup>1</sup> R. Saravanan,<sup>1</sup> Sarange Shreepad<sup>1</sup>,<sup>2</sup> T. Amuthan,<sup>3</sup> J. Immanuel Durai Raj,<sup>4</sup> Piyush Gaur,<sup>5</sup> V. Vijayan,<sup>6</sup> and S. Rajkumar<sup>7</sup>**

<sup>1</sup>Department of Mechanical Engineering, SIMATS School of Engineering, Chennai, 602 105 Tamil Nadu, India

<sup>2</sup>Department of Mechanical Engineering, Ajeenkya DY Patil School of Engineering Lohegaon Pune, India

<sup>3</sup>Department of Mechanical Engineering, Velammal College of Engineering and Technology, Velammal Nagar, Viraganoor, Madurai, India

<sup>4</sup>Department of Mechanical Engineering, St. Joseph's Institute of Technology, Chennai 600119, India

<sup>5</sup>Department of Mechanical Engineering, Mechanical Engineering Cluster, University of Petroleum and Energy Studies, Bidholi Campus, Via-Premnagar, Dehradun, Uttarakhand 248007, India

<sup>6</sup>Department of Mechanical Engineering, K. Ramakrishnan College of Technology, Samayapuram, Trichy, 621112 Tamilnadu, India

<sup>7</sup>Department of Mechanical Engineering, Faculty of Manufacturing, Institute of Technology, Hawassa University, Ethiopia

Correspondence should be addressed to S. Rajkumar; rajkumar@hu.edu.et

Received 13 August 2022; Revised 2 November 2022; Accepted 21 April 2023; Published 5 May 2023

Academic Editor: Senthil Rethinam

Copyright © 2023 T. Sathish et al. This is an open access article distributed under the Creative Commons Attribution License, which permits unrestricted use, distribution, and reproduction in any medium, provided the original work is properly cited.

Considering the unique properties of magnesium and its alloy, it has a vast demand in biomedical applications, particularly the implant material in tissue engineering due to its biodegradability. But the fixing spares must hold such implants till the end of the biodegradation of implant material. The composite technology will offer the added benefits of altering the material properties to match the requirements of the desired applications. Hence, this experimental investigation is aimed at developing a composite material for manufacturing fixing spares like a screw for implants in biomedical applications. The matrix of AZ63 magnesium alloy is reinforced with nanoparticles of zirconium (Zr) and titanium (Ti) through the stir casting-type synthesis method. The samples were prepared with equal contributions of zirconium (Zr) and titanium (Ti) nanoparticles in the total reinforcement percentage (3%, 6%, 9%, and 12%). The corrosive and tribological studies were done. In the corrosive study, the process parameters like NaCl concentration, pH value, and exposure time were varied at three levels. In the wear study, the applied Load, speed of sliding, and the distance of the slide were considered at four levels. Taguchi analysis was employed in this investigation to optimize the reinforcement and independent factors to minimize the wear and corrosive losses. The minimum wear rate was achieved in the 12% reinforced sample with the input factor levels of 60 N of load on the pin, 1 m/s of disc speed at a sliding distance was 1500 m, and the 12% reinforce samples also recorded a minimum corrosive rate of 0.0076 mm/year at the operating environment of 5% NaCl-concentrated solution with the pH value of 9 for 24 hrs of exposure. The prediction model was developed based on the experimental results.

## 1. Introduction

Currently replacing a fractured bone with an artificial implant in alloy material is one of the innovative research studies [1]. Most of the studies considered the magnesium material in the implant process due to its excellent mechanical properties and lifetime [2]. Currently, in orthopaedic applications, the materials are needed to be highly

corrosion-resistant but degradable. Now, the research work focused on iron-based biodegradable materials used in the orthopaedic function [3–5]. Researchers are taking vast studies to improve the implant material properties through the reinforcement of alloying materials, surface coating, and innovative process methods [6]. There is no divergence of human normal physiological functions even in injured bone by replacing artificial bone implant techniques. The

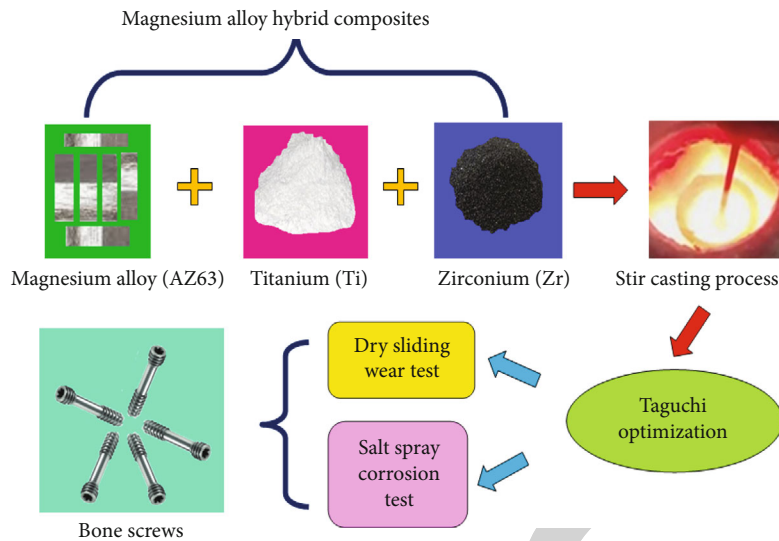
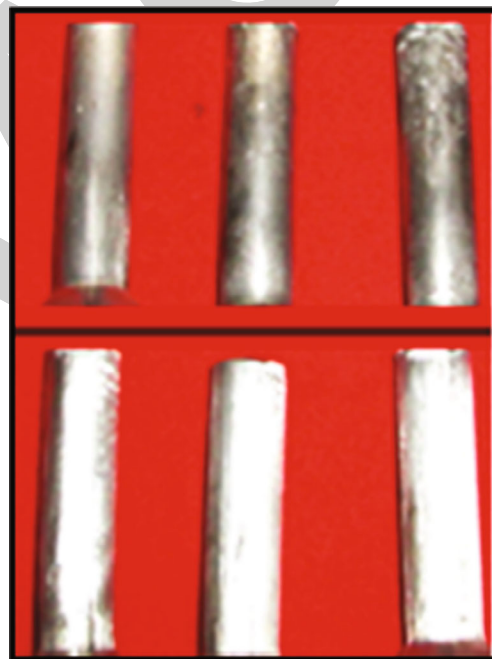


FIGURE 1: Experiment flow diagram.



(a)



(b)

FIGURE 2: Dry sliding wear test: (a) DUCOM wear test apparatus and (b) wear test specimens.

bone implant is reflecting the need for treatment for the normal functioning of joints and also ensures the treatment superiority [7–9]. Now, numerous biomaterials are developed for bone renovation applications such as bioceramics, biometals, and biopolymers [10]. Of all these materials, magnesium and its alloys are the innovative materials for bone implants. Compared with that of the human bone, Young's modulus of the magnesium alloys has similar value; hence, it is an apt material for bone replacement [11–13]. Similarly, the density of the magnesium alloy is  $1.79 \text{ g/cm}^3$ , while it was denoted that the closer density value of the human bone is

$1.75 \text{ g/cm}^3$ . Titanium and its alloys played a vital role in biomedical applications due to their higher Young's modulus and strength in contrast to those of the human bone [14–16]. Magnesium alloy is one of the encouraging materials for the control of processing and making good biomedical parts. Magnesium alloys possess excellent degradation uniqueness. Of all minerals present in the human body, magnesium has taken the fourth place [17]. It is an indispensable element for building bone and soft tissue. Generally, the magnesium alloy bone replacement is classified into two categories such as bone fixation device and bone

tissue engineering scaffold [5, 18, 19]. Normally, the bone screw, bone pin, and bone plates are named bone fixation devices; these are essential parts in repairing an affected bone. Recently, the Mg and Ti alloys have a higher level of usage in the bone fixation device due to their higher modulus compared to natural bone [20]. Zirconium is also the major element used in bone repair; now, hybrid composites are to be developed in the bone implant material [21]. The research gap is AZ63 magnesium alloy property modification through titanium and zirconium nanoparticles at different reinforcement contributions in the nanocomposite matrix. The investigation is aimed at modifying the wear as well as corrosive resistance positively in the application requirement ranges. “Can wear resistance and corrosive resistance of AZ63 Magnesium alloy modify positively by reinforcing titanium and zirconium nanoparticles?” is an unanswered question, and this manuscript tried answering the same question.

This experimental work is considering the AZ63 magnesium alloy reinforced with nanoparticles of titanium and zirconium for the fabrication of magnesium alloy hybrid composites. These composites are prepared by using the stir casting process. Taguchi analysis was used to analyse the wear and corrosion performance of the composites through optimization of the process parameters [22].

## 2. Experimental Procedure

In this composite preparation, the base material is taken as the AZ63 magnesium alloy and the reinforcement nanoparticles are titanium and zirconium. All these base and reinforcement materials are purchased from Exclusive Magnesium Private Limited, Hyderabad. The average particle size of the titanium and zirconium was 30–70 nm [23]. Composite preparation is carried out through a bottom pouring-type stir casting apparatus [24]. Figure 1 illustrates the experimental work as a flow diagram.

In the stir casting process, the magnesium alloy is heated up to 650°C in the furnace for 3 hours [25]. Similarly, the reinforced nanoparticles of titanium and zirconium equally contributed at different wt% of reinforcement (3%, 6%, 9%, and 12%). They were preheated in the preheat chamber with a temperature level of 900°C. The preheating process is maintained for 2 hours for excellent blending of reinforced nanoparticles [26–28]. After that, the preheated reinforced molten material is added to the magnesium melt, and the homogeneous mixture is achieved through stirring action by using stirring mechanism with an electrical controller [29]. The mixture of base material melts and reinforced nanoparticle melt in the furnace is heated at 500°C. Finally, the molten material is poured into the prepared die and allowed to cool [30]. The raw sample was separated from the die and sliced for the required dimensions for preparing samples to investigate the wear and corrosive properties.

A dry sliding wear test is conducted through Pin-on-disc apparatus (DUCOM 20 LE model) as shown in Figure 2(a). The wear test is conducted as per the ASTM G-99 standard; the dimensions of the specimens are 13 mm in diameter and 35 mm in length as shown in Figure 2(b). Different process

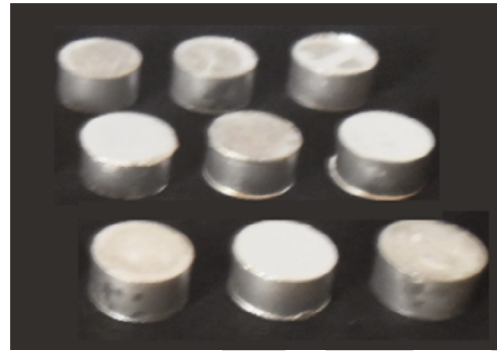


FIGURE 3: Salt spray test specimens.

TABLE 1: Factors and levels for wear rate-based Taguchi analysis.

Sl. no.	Factor	Level of variations			
		1	2	3	4
1	Reinforcement (%)	3	6	9	12
2	Load (N)	15	30	45	60
3	Disc speed (m/s)	1	2	3	4
4	Sliding distance (m)	1000	1200	1500	1700

TABLE 2: Factors and levels for corrosion rate-based Taguchi analysis.

Sl. no.	Factor	Level of variations			
		1	2	3	4
1	Reinforcement (%)	3	6	9	12
2	NaCl (%)	3	4	5	6
3	pH value	6	7	8	9
4	Exposure time (hrs)	24	36	48	60

parameters and levels to be considered to conduct the wear test are the percentage of reinforcement, load disc speed, and sliding distance [31, 32].

A salt spray test is conducted to estimate the corrosion rate of the magnesium alloy hybrid composites; Figure 3 illustrates the salt spray corrosion test specimens. As per the ASTM standard B117, the different parameters considered for conducting corrosion tests are reinforcement (%), NaCl (%), pH value, and exposure time [33]. Before conducting of corrosion test, the specimen surfaces are abraded by using 600 grit size emery sheets.

The factors and their levels were furnished for wear and corrosion analysis and are presented in Tables 1 and 2, respectively.

## 3. Results and Discussion

**3.1. Wear Test.** The minimum wear rate was recorded as 0.0078mm<sup>3</sup>/m by the influence of 12% reinforcement, 60 N of load, 1 m/s of disc speed, and 1500 m of sliding distance (m). Similarly, higher wear was registered as 0.0255 mm<sup>3</sup>/m as presented in Table 3.

TABLE 3: Experimental summary of wear test.

Exp. runs	Reinforcement (%)	Load (N)	Disc speed (m/s)	Sliding distance (m)	Wear rate (mm <sup>3</sup> /m)	S/N ratio (wear rate)	Predicted wear rate
1	3	15	1	1000	0.0112	39.0156	0.0110
2	3	30	2	1200	0.0205	33.7649	0.0229
3	3	45	3	1500	0.0237	32.5050	0.0218
4	3	60	4	1700	0.0203	33.8501	0.0198
5	6	15	2	1500	0.0123	38.2019	0.0118
6	6	30	1	1700	0.0095	40.4455	0.0076
7	6	45	4	1000	0.0164	35.7031	0.0188
8	6	60	3	1200	0.0255	31.8692	0.0253
9	9	15	3	1700	0.0082	41.7237	0.0106
10	9	30	4	1500	0.0157	36.0820	0.0155
11	9	45	1	1200	0.0126	37.9926	0.0121
12	9	60	2	1000	0.0218	33.2309	0.0199
13	12	15	4	1200	0.0149	36.5363	0.0130
14	12	30	3	1000	0.0191	34.3793	0.0186
15	12	45	2	1700	0.0108	39.3315	0.0106
16	12	60	1	1500	0.0078	42.1581	0.0102

TABLE 4: Signal to noise ratios for wear rate responses.

Level	Reinforcement (%)	Smaller is better		
		Load (N)	Disc speed (m/s)	Sliding distance (m)
1	34.78	38.87	39.90	35.58
2	36.55	36.17	36.13	35.04
3	37.26	36.38	35.12	37.24
4	38.10	35.28	35.54	38.84
Delta	3.32	3.59	4.78	3.80
Rank	4	3	1	2

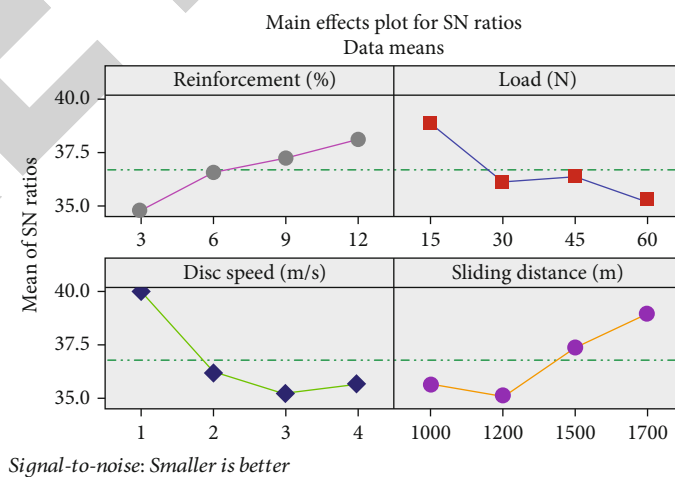


FIGURE 4: Main effects plot for S/N ratios (wear test).

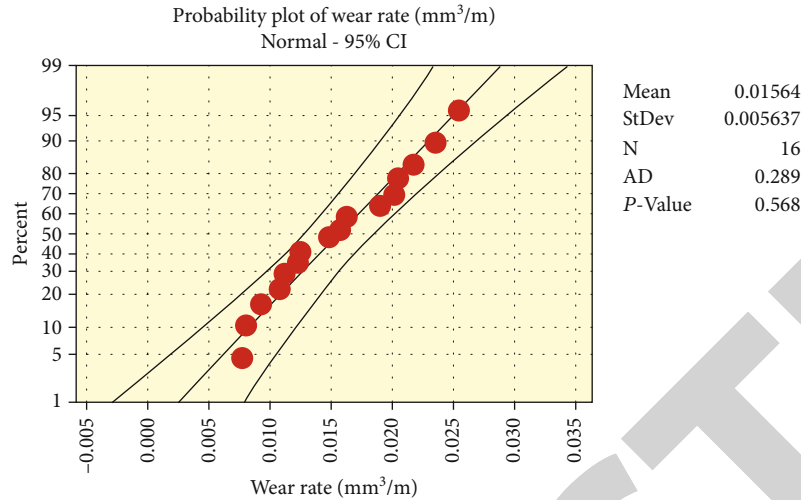


FIGURE 5: Normal probability plot for the wear test.

TABLE 5: Analysis of variance for the wear test.

Source	DF	Seq SS	Contribution	Adj SS	Adj MS	F value	P value
Regression	4	0.000331	69.36%	0.000331	0.000083	6.23	0.007
Reinforcement (%)	1	0.000070	14.63%	0.000070	0.000070	5.25	0.043
Load (N)	1	0.000091	18.99%	0.000091	0.000091	6.82	0.024
Disc speed (m/s)	1	0.000101	21.10%	0.000101	0.000101	7.58	0.019
Sliding distance (m)	1	0.000070	14.63%	0.000070	0.000070	5.25	0.043
Error	11	0.000146	30.64%	0.000146	0.000013		
Total	15	0.000477	100.00%				

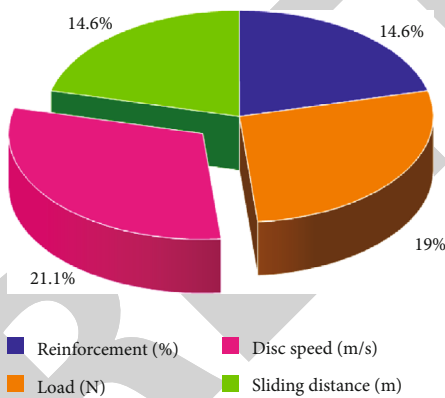


FIGURE 6: Pie chart for parameter contribution in the wear test.

Table 4 presents the higher influencing parameter of the wear test based on the rank and delta value. In the wear test analysis, a higher influence factor was found as disc speed followed by sliding distance, load, and percentage of reinforcement. The optimal parameters of the wear test are 12% of reinforcement, 15 N of load, 1 m/s of disc speed, and 1700 m of sliding distance.

The increase of reinforcement percentage reduces the wear rate of the 12% of reinforced offered minimum wear rate of the hybrid magnesium alloy composites as shown in Figure 4. A minimum applied load such as 15 N provided

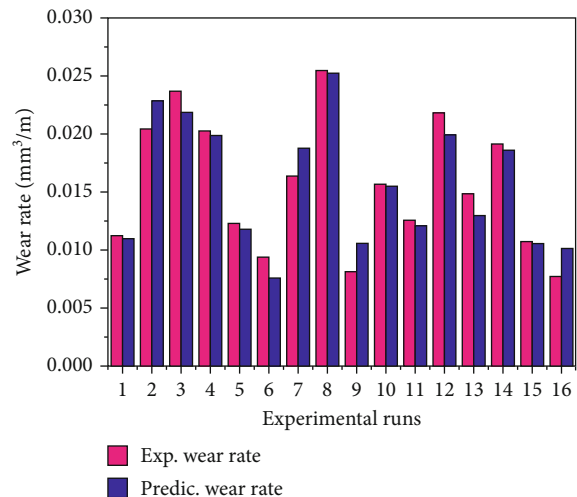


FIGURE 7: Bar chart for comparing the experimental and predicted wear rate.

a minimum wear rate; continually increasing load, the wear rate can be increased simultaneously. Lower disc speed offered a lower wear rate; increasing the disc speed from 1 m/s to 3 m/s, the wear rate also increased. Minimum sliding distance increases the wear rate; the increase of sliding distance from 1000 m to 1700 m the wear rate was reduced.

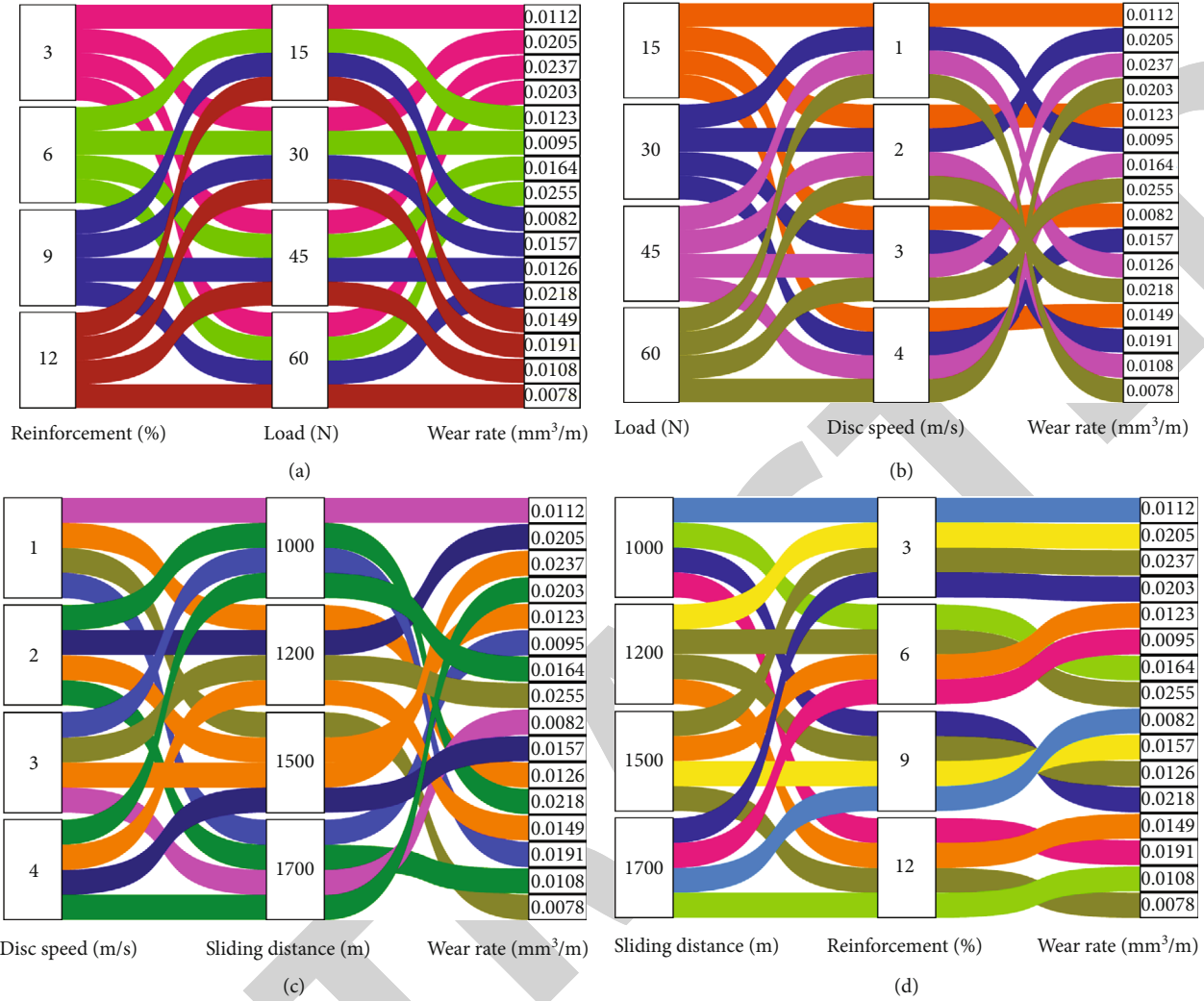


FIGURE 8: Parallel set plot: (a) reinforcement % vs. load; (b) load vs. disc speed; (c) disc speed vs. sliding distance; (d) sliding distance vs. reinforcement %.

Figure 5 presents the normal probability plot for the wear test, which demonstrates the accuracy of data points in a clear manner. All the selected data points are very nearby the mean line, and only very few of them just deviated from it; hence, the chosen model and the parameters were accurate.

Higher contributions of parameters in the wear rate analysis are presented in Table 5. ANOVA results concluded that a higher *F* value indicates a higher contribution of that parameter. In this analysis, as the *P* values were found to be below 0.05, the selected parameters and their influence were significant.

The prediction model for wear rate prediction is presented in equation (1). As  $R^2 > 95\%$ , the model will give good agreement with the experimental results.

$$\begin{aligned}
 \text{Wear rate (mm}^3/\text{m)} &= 0.01986 - 0.000622 \text{ reinforcement (\%)} \\
 &+ 0.000142 \text{ load (N)} \\
 &+ 0.002243 \text{ disc speed (m/s)} \\
 &- 0.000008 \text{ sliding distance (m)}.
 \end{aligned}
 \tag{1}$$

Figure 6 presents the contribution of each parameter in the wear test. Disc speed highly contributed (21.1%), and the load contributed 19%. An equal contribution of 14.6% was recorded for sliding distance and reinforcement factors.

The experimental responses of wear rates were found to be closer to the predicted wear rate as shown in Figure 7. From both the wear rate analyses, experimental wear rate values were closer to predicted ones; hence, the output of the wear analysis was found to have better accuracy.

Two parameters of correlation are presented in Figure 8 through a parallel set plot. Figure 8(a) represents the 12% of reinforcement and 60 N of load offered minimum wear rate. Figure 8(b) correlates that the 60 N of applied load and 1 m/s of disc speed recorded minimum wear rate. Figure 8(c) illustrates that 1 m/s of disc speed and 1500 m of sliding distance offered a lower wear rate. Figure 8(d) presents the 1500 m of sliding distance and 12% reinforcement provided minimum wear rate.

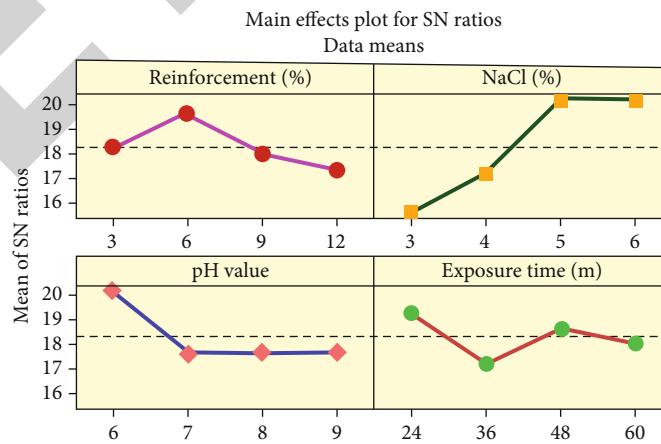


TABLE 6: Experimental summary of corrosion test analysis.

Exp. runs	Reinforcement (%)	NaCl (%)	pH value	Exposure time (hrs)	Corrosion rate $\times 10^{-3}$ (mm/year)	S/N ratio (corrosion rate)	Predicted corrosion rate
1	3	3	6	24	0.126	17.9926	0.124
2	3	4	7	36	0.164	15.7031	0.164
3	3	5	8	48	0.095	20.4455	0.099
4	3	6	9	60	0.114	18.8619	0.111
5	6	3	7	48	0.153	16.3062	0.150
6	6	4	6	60	0.092	20.7242	0.096
7	6	5	9	24	0.076	22.1581	0.078
8	6	6	8	36	0.108	19.3315	0.106
9	9	3	8	60	0.184	14.7036	0.184
10	9	4	9	48	0.155	16.1934	0.153
11	9	5	6	36	0.096	20.3546	0.093
12	9	6	7	24	0.093	20.6303	0.097
13	12	3	9	36	0.211	13.5144	0.215
14	12	4	8	24	0.154	16.2496	0.1517
15	12	5	7	60	0.127	17.9239	0.125
16	12	6	6	48	0.082	21.7237	0.082

TABLE 7: Response table for signal-to-noise ratios (corrosion rate).

Level	Reinforcement (%)	Smaller is better NaCl (%)	pH value	Exposure time (hrs)
1	18.25	15.63	20.20	19.26
2	19.63	17.22	17.64	17.23
3	17.97	20.22	17.68	18.67
4	17.35	20.14	17.68	18.05
Delta	2.28	4.59	2.56	2.03
Rank	3	1	2	4



Signal-to-noise: Smaller is better

FIGURE 9: Main effects plot for S/N ratios (corrosion rate).

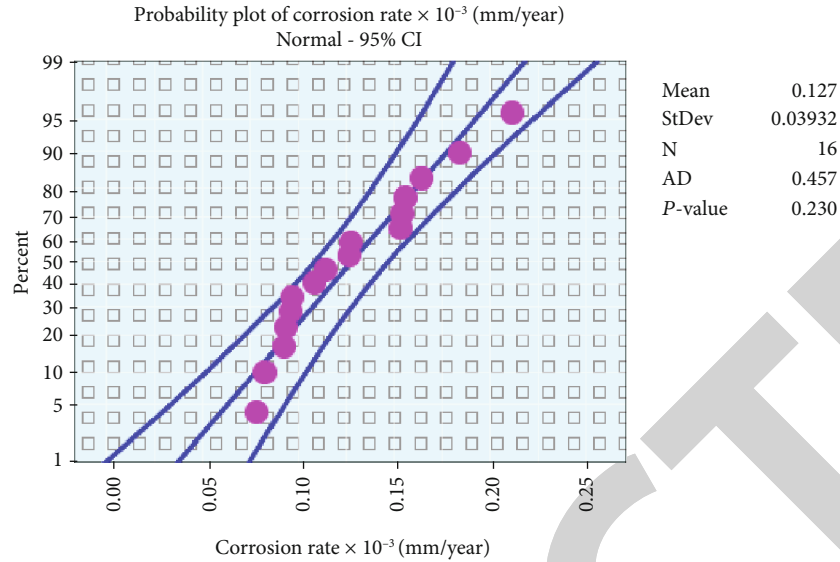


FIGURE 10: Normal probability plot for corrosion rate.

TABLE 8: Results of analysis of variance for corrosion rate.

Source	DF	Seq SS	Contribution	Adj SS	Adj MS	F value	P value
Regression	4	0.016933	73.03%	0.016933	0.004233	7.45	0.004
Reinforcement (%)	1	0.001296	5.59%	0.001296	0.001296	2.28	0.015
NaCl (%)	1	0.012500	53.91%	0.012500	0.012500	21.99	0.001
pH value	1	0.003001	12.94%	0.003001	0.003001	5.28	0.042
Exposure time (hrs)	1	0.000135	0.58%	0.000135	0.000135	0.24	0.035
Error	11	0.006253	26.97%	0.006253	0.000568		
Total	15	0.023186	100.00%				

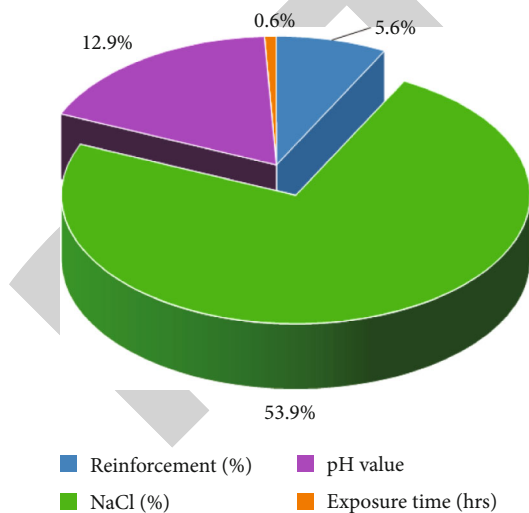


FIGURE 11: Pie chart for parameter contribution in corrosion rate.

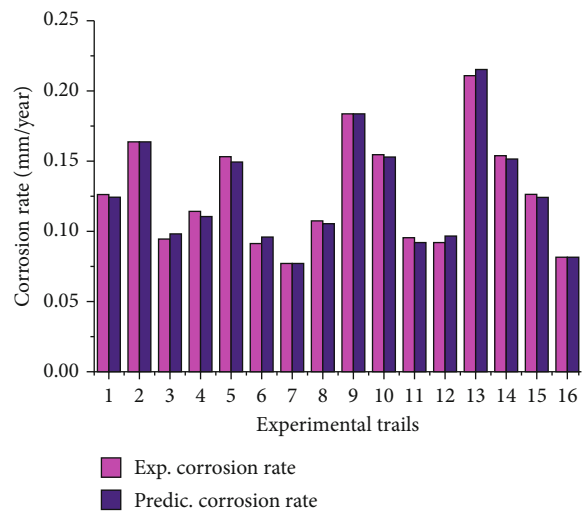


FIGURE 12: Bar chart for analysing experimental and predicted corrosion rate.

3.2. Salt Spray Corrosion Test. The salt spray corrosion test demonstrates the minimum and maximum corrosion rates were obtained through different parameters' influence. The minimum corrosion rate was recorded as 0.0076 mm/year by the influence of 6% reinforcement, 5% of NaCl, a pH value of 9, and 24 hrs of exposure time. On the contrary,

the maximum corrosion rate was found as 0.211 mm/year; it is presented in Table 6. All the experimental values are very close to the predicted values.

Table 7 presents the higher level and lower level influencing parameters of the corrosion rate analysis; it can

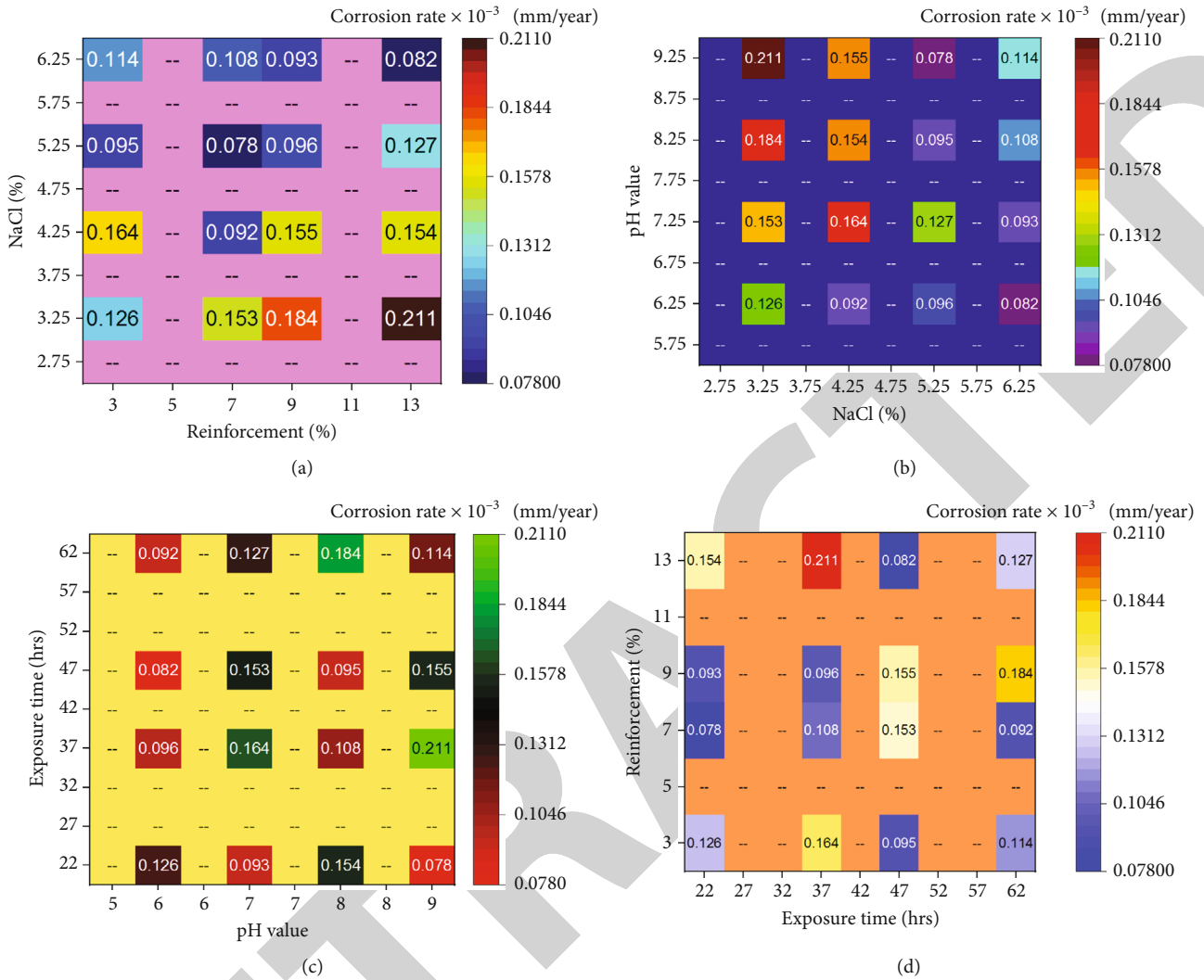


FIGURE 13: Heatmap plot: (a) reinforcement % vs. NaCl (%); (b) NaCl (%) vs. pH value; (c) pH value vs. exposure time; (d) exposure time vs. reinforcement %.

be achieved by rank order and delta value. In corrosion rate analysis, a higher priority parameter was found as % of NaCl, followed by pH value, reinforcement (%), and exposure time. The optimal parameters for the minimum corrosion rate analysis are 6% of reinforcement, 5% of NaCl, and maintaining the pH value of 6 for 24 hrs of exposure time.

In the corrosion rate analysis, until 6% of reinforcement corrosion rate decreases (due to increasing of Signal to noise ratio), then increases (refer to Figure 9). Until NaCl concentration improved to 5%, the corrosion rate decreased and then declines. The lower pH value (6) registered a minimum corrosion rate than higher pH values. Similarly, the shorter exposure time offered a minimum corrosion rate.

Figure 10 illustrates the normal probability plot for the corrosion test, for this plot exhibits the involvement of data points in the corrosion rate analysis. Few of the data points only deviated from the mean line; the remaining values fall closer to the mean line. So it can be proved that the selected parameters were good. Table 8 presents the contributions of various factors. *F* values correlate with the contribution per-

centage of each parameter considered, in the corrosion rate inspection. In this analysis, the NaCl % was extremely contributed.

The prediction model for corrosion rate prediction is presented in equation (2). As  $R^2 > 95\%$ , the model will give good agreement with experimented results.

$$\begin{aligned} \text{Corrosion rate} \times 10^{-3} \text{ (mm/year)} &= 0.1184 + 0.00268 \text{ reinforcement (\%)} \\ &\quad - 0.02500 \text{ NaCl (\%)} + 0.01225 \text{ pH value} \\ &\quad + 0.000217 \text{ exposure time (hrs)}. \end{aligned} \tag{2}$$

Figure 11 presents the higher contribution and lower contribution of the parameters in the corrosion rate analysis. Sodium chloride percentage (NaCl %) was extremely contributed (53.9%), followed by 12.9% of pH value, 5.6% of reinforcement, and lower percentage (0.6%) of exposure time.

The observed corrosion rates were nearer to the predicted corrosion rates (refer to Figure 12); therefore, the output result of the corrosion rate analysis is accurate.

Figure 13 illustrates the correlation between the parameters, with heatmap analysis. Figure 13(a) exemplifies the 6% reinforced sample in the 5% NaCl-concentrated solution offered a minimum corrosion rate. Figure 13(b) demonstrates that the 5% of NaCl concentration at the pH value of 9 registered a minimum corrosion rate. Figure 13(c) illustrates that maintaining the pH value of 9 for 24 hrs of exposure time recorded a lower corrosion rate. Figure 13(d) demonstrates the 24 hrs of exposure time and 6% of reinforcement registered minimum corrosion rate.

#### 4. Conclusion

Magnesium alloy hybrid nanocomposites for biomedical applications were prepared through the stir casting process. The wear and corrosive properties were analysed in the prepared nanocomposite samples successfully. The results of this investigation were drawn as follows:

- (i) In the wear test, the minimum wear rate was recorded as  $0.0078 \text{ mm}^3/\text{m}$  for the 12% reinforced nanocomposite sample at 60 N of load on the pin and 1 m/s of disc speed for the 1500 m of sliding distance (m). On the contrary, higher wear was found at  $0.0255 \text{ mm}^3/\text{m}$ . Optimal parameters of the wear test attained 12% of reinforced nanocomposite sample with 15 N load on the pin at 1 m/s of disc speed for 1700 m of sliding distance
- (ii) Higher contribution of the parameter in the wear test was recorded as disc speed was highly contributed (21.1%), followed by 19% of load and equal contribution (14.6%) which was observed for the factor percentage of reinforcement and sliding distance
- (iii) In the corrosion rate analysis, a minimum corrosion rate was found to be  $0.0076 \text{ mm}/\text{year}$  for the 6% reinforced nanocomposite sample in 5% NaCl concentrated solution with a pH value of 9 for 24 hrs of exposure time. On the contrary, the maximum corrosion rate was registered as  $0.211 \text{ mm}/\text{year}$ . Optimal parameters of the corrosion rate analysis were observed as 6% of reinforced nanocomposite sample in the 5% NaCl concentrated solution with the pH value of 6 for 24 hrs of exposure time
- (iv) Sodium chloride percentage (NaCl %) was exceptionally contributed (53.9%), followed by 12.9% of pH value, 5.6% of reinforcement %, and lower percentage (0.6%) of exposure time

From the above experimental results, it can be understood that the maximum reinforcement outperformed in promoting the wear-resistance properties of the proposed nanocomposite. Similarly, in the salt spray corrosion test, the same kind of trend was observed. Hence, the increase

in reinforcement improved wear resistance and corrosive resistance. As it has reached a maximum value as optimal, there is a chance to improve such resistance by increasing the reinforcement percentage and a maximum possible reinforcement may be found in future research.

#### Data Availability

The data used to support the findings of this study are included in the article. Should further data or information be required, these are available from the corresponding author upon request.

#### Conflicts of Interest

The authors declare that there are no conflicts of interest regarding the publication of this paper. This study was performed as a part of the authors' employment at Hawassa University, Ethiopia.

#### Acknowledgments

The authors thank the Management of SIMATS School of Engineering, Saveetha University, for their appreciation and encouragement to complete this research work with in-house research facilities.

#### References

- [1] M.-H. Kang, H. Lee, T.-S. Jang et al., "Biomimetic porous Mg with tunable mechanical properties and biodegradation rates for bone regeneration," *Acta Biomaterialia*, vol. 84, pp. 453–467, 2019.
- [2] R. Gorejová, L. Haverová, R. Oriňaková, A. Oriňak, and M. Oriňak, "Recent advancements in Fe-based biodegradable materials for bone repair," *Journal of Materials Science*, vol. 54, no. 3, pp. 1913–1947, 2019.
- [3] D. Carluccio, X. Chun, J. Venezuela et al., "Additively manufactured iron-manganese for biodegradable porous load-bearing bone scaffold applications," *Acta Biomaterialia*, vol. 103, pp. 346–360, 2020.
- [4] R. C. Cuozzo, S. C. Sartoretto, R. F. Resende et al., "Biological evaluation of zinc containing calcium alginate hydroxyapatite composite microspheres for bone regeneration," *Journal of Biomedical Materials Research Part B: Applied Biomaterials*, vol. 108, no. 6, pp. 2610–2620, 2020.
- [5] F. Luzi, D. Puglia, and L. Torre, "Natural fiber biodegradable composites and nanocomposites: a biomedical application," in *Biomass, Biopolymer-Based Materials, and Bioenergy*, pp. 179–201, Woodhead Publishing, 2019.
- [6] C. Wen, X. Zhan, X. Huang, X. Feng, L. Luo, and C. Xia, "Characterization and corrosion properties of hydroxyapatite/graphene oxide bio-composite coating on magnesium alloy by one-step micro-arc oxidation method," *Surface and Coatings Technology*, vol. 317, pp. 125–133, 2017.
- [7] S. K. Chourasiya, G. Gautam, and D. Singh, "Mechanical and tribological behavior of warm rolled Al-6Si-3Graphite self lubricating composite synthesized by spray forming process," *Silicon*, vol. 12, no. 4, pp. 831–842, 2020.
- [8] C. Moseke, Y. A. Alramadan, E. Vorndran, and P. Elter, "Electrochemical deposition of zinc-doped hydroxyapatite coatings

## *Retraction*

# **Retracted: Utilization of Bioinorganic Nanodrugs and Nanomaterials for the Control of Infectious Diseases Using Deep Learning**

### **BioMed Research International**

Received 8 January 2024; Accepted 8 January 2024; Published 9 January 2024

Copyright © 2024 BioMed Research International. This is an open access article distributed under the Creative Commons Attribution License, which permits unrestricted use, distribution, and reproduction in any medium, provided the original work is properly cited.

This article has been retracted by Hindawi, as publisher, following an investigation undertaken by the publisher [1]. This investigation has uncovered evidence of systematic manipulation of the publication and peer-review process. We cannot, therefore, vouch for the reliability or integrity of this article.

Please note that this notice is intended solely to alert readers that the peer-review process of this article has been compromised.

Wiley and Hindawi regret that the usual quality checks did not identify these issues before publication and have since put additional measures in place to safeguard research integrity.

We wish to credit our Research Integrity and Research Publishing teams and anonymous and named external researchers and research integrity experts for contributing to this investigation.

The corresponding author, as the representative of all authors, has been given the opportunity to register their agreement or disagreement to this retraction. We have kept a record of any response received.

## **References**

- [1] R. Priyadarshini, A. S. Abdullah, K. V. Karthikeyan et al., "Utilization of Bioinorganic Nanodrugs and Nanomaterials for the Control of Infectious Diseases Using Deep Learning," *BioMed Research International*, vol. 2023, Article ID 7464159, 13 pages, 2023.

## Research Article

# Utilization of Bioinorganic Nanodrugs and Nanomaterials for the Control of Infectious Diseases Using Deep Learning

**R. Priyadarshini,<sup>1</sup> A. Sheik Abdullah,<sup>1</sup> K. V. Karthikeyan,<sup>2</sup> M. Vinoth,<sup>3</sup> Betty Martin,<sup>4</sup> S. Geerthik,<sup>5</sup> Florin Wilfred ,<sup>6</sup> Nour M. Alyami,<sup>7</sup> and R. S. Sundaram<sup>8</sup>**

<sup>1</sup>School of Computer Science and Engineering, Vellore Institute of Technology, Chennai, Tamil Nadu, India

<sup>2</sup>Department of Electronics and Communication Engineering, Sathyabama Institute of Science and Technology, Chennai, 600119 Tamil Nadu, India

<sup>3</sup>Department of Electronics and Communication Engineering, K. Ramakrishnan College of Engineering, Trichy, 621112 Tamil Nadu, India

<sup>4</sup>Department of Electronics and Communication Engineering, SASTRA Deemed to be University, Thirumalaisamuthiram, Thanjavur, 613401 Tamil Nadu, India

<sup>5</sup>Department of Information Technology, Agni College of Technology, Chennai, 600130 Tamil Nadu, India

<sup>6</sup>Department of Electrical, Electronics and Communication Engineering, St. Joseph College of Engineering and Technology, St. Joseph University in Tanzania, Dar es Salaam, Tanzania

<sup>7</sup>Department of Zoology, C. Abdul Hakeem College of Engineering, Vellore, 632509 Tamil Nadu, India

<sup>8</sup>Department of Health Sciences, University of Texas, Austin, TX, USA

Correspondence should be addressed to Florin Wilfred; [florin.wilfred@sjuit.ac.tz](mailto:florin.wilfred@sjuit.ac.tz)

Received 14 September 2022; Revised 27 October 2022; Accepted 18 January 2023; Published 21 April 2023

Academic Editor: Senthil Rethinam

Copyright © 2023 R. Priyadarshini et al. This is an open access article distributed under the Creative Commons Attribution License, which permits unrestricted use, distribution, and reproduction in any medium, provided the original work is properly cited.

As one of the main causes of morbidity and mortality, viral infections have a major impact on the well-being and economics of every nation in the globe. The ability to predictably diagnose viral infections improves the provision of good healthcare as well as the control and prevention of these conditions. Nanomaterials have gained widespread usage in the medical industry recently due to the rapid advancement of nanotechnology and their exceptional chemical and physical qualities, such as their small size and synthesized surface properties. The utilization of nanoparticles for illness detection, surveillance, control, preventive, and therapy, such as the treatment of bacterial infections, is referred to as nanomedicine. Nanomedicine is a comprehensive discipline that is founded on the usage of nanotechnology for clinical objectives. Nanoparticles, which have a nanoscale dimension and exhibit highly controllable optical and physical characteristics as well as the ability to bind to a large variety of chemicals, are among the most popular nanomaterials in nanomedicine. A deep learning framework of autoencoder for categorization study on viral infections is built based on actual hospital patient history of viral infections from August 2015 to August 2020. The information comprises of 10,950 cases, comprising outpatients and inpatients, encompassing the infectious diseases. Of such 10,950 instances, training set made up 70% or 7665 instances, and testing data made up 30% or 3285 instances. The data processing was done using the presented recurrent neural network-artificial bee colony (RNN-ABC) method. Sparse data densifying processes are done through the autoencoder to enhance the system learning outcome. The suggested autoencoder system was also evaluated to other widely used models, including support vector machine, logistic regression, random forest, and Naïve Bayes. In comparison to other approaches, the study's findings demonstrate how well the suggested autoencoder model can predict viral diseases. The methods used for this research can aid in removing reported lags in current monitoring systems, hence reducing society's expenses.

## 1. Introduction

Whenever a person becomes affected with a pathogen from a human or animal source, an infectious illness develops. It is viewed as a societal issue since it not only negatively affects people but also negatively affects society as a whole. All stage of human progress has been associated by infectious illnesses, which continue to pose a severe hazard to public health. Infectious illnesses continue to be the leading global cause of mortality, illness, incapacity, and economic unrest despite medical advancements [1]. In reality, they accounted for even more than 6.7 million fatalities in 2016, ranking third among the world's top ten mortality causes. Among these, 3 million fatalities have been attributed to low respiratory problems, 1.3 million to TB, 1.4 million to diarrheal illnesses, and one million to the human immunodeficiency virus (HIV) and its side effects. These illnesses are associated with significant economic and social risks for the healthcare system, with consequences ranging from the well-being of common people to the sustainability of the international order [2]. Infectious disorders can be brought on by a variety of microorganisms, such as viruses, bacteria, fungus, and parasites which are shown in Figure 1. Internationally, illnesses brought on by infections are the main cause of mortality. Bacteria continue to be the most common cause of mortality amongst microbial infections among infants, the elderly, and individuals with weakened immune systems [3]. Figure 2 depicts the different way to the transmission of infectious disease. Given the extremely high morbidity and death rates associated with bacterial infections and the rising costs associated with patient care, harmful bacteria are a major public health concern [4]. A significant advancement in nanomedicine during the last ten years offers hope for the cure of bacterial infections. To increase the availability and efficacy of an antibiotic, the nanomaterials can function as antimicrobial agents or as the transporters for carrying antimicrobial medicines [5]. Nanoparticles are a new area that has been created as a result of the substantial changes brought about by the advancement of nanotechnology and other pertinent techniques and substances. Because of the rapid advancement of numerous nanomaterials and their distinct benefits, nanomedicine is becoming ever more important in the detection, therapy, and prevention of illness [6].

As a potential diagnostics and theranostic method in nanomedicine, nanoparticles can be synthesized by attaching to certain proteins, accessing particular local locations, or dispersing medicines in particular conditions. In order to help nanomaterials access molecules, regulate molecular interactions, and track variations in the microenvironment, therapeutic or diagnostic compounds have been developed [7]. On either side, nanoparticles' tunable optical, electrical, magnetic, and biological qualities allow them to be manufactured into a variety of forms, dimensions, composition, chemical surface characteristics, and hollowed or solid forms [8]. These characteristics will make nanomaterials suitable for significant clinical illness purposes.

Other tactic to improve the absorption and elimination of germs is the encapsulating of antibiotic medications into

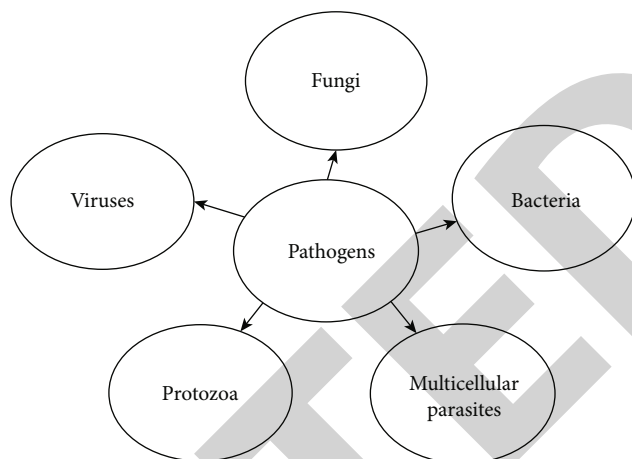


FIGURE 1: Various types of pathogens.

nanocarriers. In comparison to traditional treatment, medication distribution using nanosystems increases effectiveness while potentially lowering toxicity. Nanomaterials' strong bacterial affinities, large surface ratio, potential for surface modification, and ability to carry drug molecules all help them exert effective antibacterial action [9]. With the growing understanding of this fascinating topic, the definition as well as categorization of nanomaterials was constantly changing. Editors believe it is essential to clarify that the upper size limit of nanoparticles is not limited to 100 nm. This information was adapted from technical as well as clinical information on nanomaterials and nanotechnology from the US National Nanotechnology Initiative and European Commission. In fact, certain commercially available nanomedicine compounds, such as Myocet and abraxane (130 nm), are larger than 100 nm (180 nm). To illustrate their inherent benefits in relation to diagnostics and therapies, nanomaterials were generally divided into three categories: organic, inorganic, or hybrid nanotechnology. The vast majority, if not all, of organic nanomaterial-based drug delivery systems make use of biocompatible polymers and liposomes, which have been similar to the proteins, lipids, and carbohydrates found in people and other animals. A field of investigation that is constantly developing is the creation of new biomaterials and techniques for creating nanomedicine "designed principally for treatments" in the framework of controllable size, consistency, percent drug entrapment, and prolonged drug release. The unique optical, electrical, and magnetic characteristics of metallic elements that belong to the inorganic nanoparticles make each other an excellent idea for multifunctional biological devices in optical and electrical detecting, diagnostic testing, photothermal therapy, optogenetics, and a few other fields. These metals include but are not limited to gold, silver, platinum, iron, cobalt, titanium, and lanthanide. Additionally, stem cell biology combined with nanomaterials and nanotechnology has significant implications for regenerative medicine [10]. The next phase of nanomedicines is expected to deliver a tailored, effective treatment with fewer adverse effects. Nanomaterial-based scaffolding in tissue engineering provides a biodegradable support allowing cell growth as well as infiltration that will eventually be spontaneously displaced by

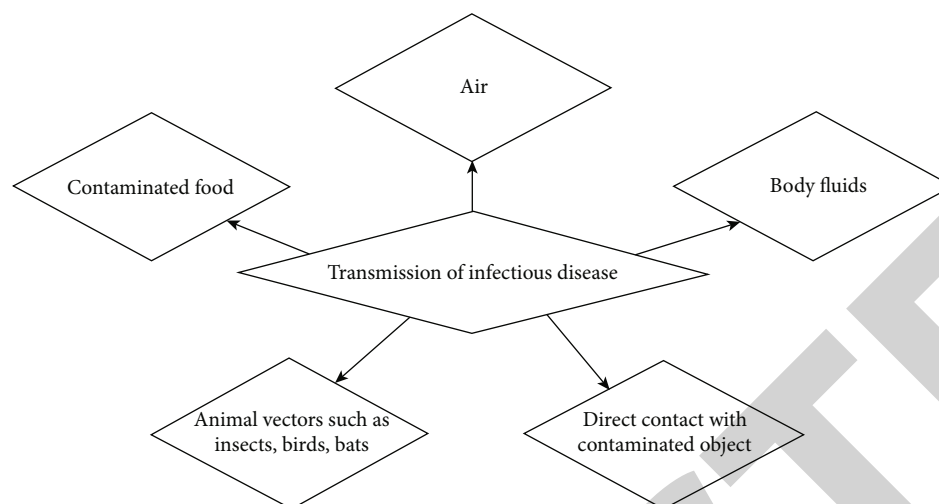


FIGURE 2: Various ways to the transmission of infectious disease.

new biological tissue. Targeting the illness site with smart nanodevices for medication delivery will allow numerous agents for sensing, high-resolution imaging, and therapy to be released under regulated conditions in response to an external trigger [11].

The usage of nanoparticles for illness detection, tracking, management, preventative, and therapy is known as nanomedicine, and it is a multidisciplinary field centred on the usage of nanotechnology for medicinal purposes [12]. By integrating powerful particles that would otherwise be ineffective owing to their inherent toxic effect; utilizing multiple systems of action; maximising effectiveness while reducing dosages and toxic effects; and providing drug targeting, managed, and site-specific discharge, nanomedicine is aimed at revolutionising medical care and exposing novel medications for both treatment and diagnosis. Nanomaterials, nanoscale particles with extremely modifiable optical and physical characteristics and the ability to assemble a huge library of molecules, are among the most popular nanomaterials in nanomedicine [13]. As a result, bioinspired nanomaterials with improved surface biophysicochemical properties have been produced using nanotechnology and biomimetic techniques to deliver drugs and vaccines [14]. The functioning, difficulty, and biocompatibility of biomaterials are combined with the diversity, adaptability, and repeatability of synthetic nanomaterials to create these biomimetic nanoparticles, which have a number of benefits [15]. Nature-inspired nanomaterials themselves can be used as efficient nanotherapies or nanovaccines against infectious illnesses because of their inherent activities. As an option, they might be used as sophisticated nanocarriers to distribute treatments or vaccinations to precise locations.

Nanomaterials and nanotechnology are used often in antibacterial, biosensors, nanomedicine, reinforcement, nanoelectronics, water treatment, and other fields. However, using and creating nanomaterials also comes with a lot of issues and difficulties. It is vital to find solutions for the problems of increasing nanomaterial manufacturing, releasing nanomaterials into the environment, and impacting environmental quality [16].

Additionally, prior to being given to the antigen-presenting cells, nanoparticles could fully insulate antigen components, speeding up the vaccine growth. In particular, regulatory approval for mRNA vaccines administered via lipid nanoparticles came in a record-breaking amount of time. Moreover, when using deep learning techniques, it is feasible to enhance predictive accuracy by refining the deep learning model's variables. In order to compensate for temporal aspects, the gathered dataset in this research had added to it. To further analyze the impacts of every dataset produced by the designing process' input variable combinations on outbreaks of infectious disease and choose the better method with the greatest predictive variable, additional testing of every input parameter combinations is carried out. The effectiveness of the model's predictions is confirmed by contrasting it with viral disease forecasting models that made use of deep learning. In the end, it should be able to develop a system that can forecast patterns about the prevalence of infectious diseases in a timely manner using the findings from this study.

## 2. Related Works

Reverse transcriptase-polymerase chain reactions (RT-PCR) have undergone extensive modification, which has aided in the fight against the COVID-19 pandemic which has now affected millions of people worldwide. In addition to RT-PCR, radiographic imaging tests provide important information for identifying as well as identifying this viral infection. In order to effectively diagnose as well as manage COVID-19 disease, the paper developed a hybrid strategy utilizing computer vision with machine learning. The study made use of a variety of combinational frameworks of image filtering and feature-extraction approaches, including machine-learning techniques to separate COVID-19 positive patients from healthy persons from the rest of the population using chest X-ray pictures. It examined how many machine learning as well as deep learning-based classifications performed while using three noise removal filtering and two feature-extraction strategies. The suggested techniques employ a



conservative normalizing filter: Crimmins speckle reduction and Gaussian filter to first eliminate extraneous noise. Then, to retrieve significantly distinctive feature sets, it uses linear discriminant analysis (LDA) as a linear method combined with principal component analysis (PCA) as a nonlinear feature-extraction methodology. Finally, it trains separate category methods, such as logistic regression, convolutional neural network (CNN), and support vector machine (SVM), using these feature sets (LG). Evidently, when combined with LDA and SVM, the suggested conservative smoothing filter with such a single peak to ensure symmetry in both the vertical and horizontal planes for picture improvement achieved a total accuracy rate of 99.93%. According to experimental findings, the suggested model's computational time is greatly decreased by incorporating feature-extraction techniques in addition to obtaining excellent accuracy levels. The publication does, however, contain a limited amount of dataset, which is a significant drawback [17].

Due to the development of technology for information and communication as well as the current measurement approach, the information captured from public health monitoring has substantially expanded since the start of the twenty-first century. AdaBoost, support vector machine, random forest, decision tree, artificial neural network, Naïve Bayes, and Bootstrap aggregating are supervised learning techniques that may effectively control the classification and regression problems in health data. By grouping patients into subgroups and identifying anomalous patients, other unsupervised learning techniques, such as K-means, may help researchers narrow their emphasis on these medical instances. In order to facilitate trustworthy disease-oriented observation with projections in the technology age, this study intends to emphasise the advantages acquired through the application of Artificial Intelligence (AI) approaches. It is expected that platforms for information management including machine learning would make it possible to analyze numerous outbreaks of transmissible diseases. Government organizations and healthcare organizations, including healthcare experts, would be interested in risk analysis as well as resource allocation based on the advances in syndromic monitoring that result. It is intended that efforts to use well-established theories and methodology from computer science, information technology, clinical diagnostics, and disease epidemiological would be made across disciplines in order to construct a big data analytic methodology for various disease conditions. A special calibration to disease-specific circumstances may be needed for AI algorithms, nevertheless. In other words, not every disease situations could be amenable to a one-size-fits-all method [18].

Lipid droplet (LD) development, a crucial characteristic of foam cells, makes atherosclerotic an alluring target for therapeutic treatment. Nevertheless, despite improvements in cellular scanning approaches, active foam cells can only be studied with a restricted number of current noninvasive as well as quantitative analysis. Here, researchers carried out a label-free quantitative morphology and physiological characterization of active foam cells utilizing optical diffraction tomography (ODT). By confirming the exact optical

properties with correlated scanning that combined three-dimensional imaging techniques with ODT, researchers were able to identify LDs in foam cells. Researchers accurately and quantitatively assessed the therapeutic value of a nanodrug (mannose-polyethylene glycol-glycol chitosan-fluorescein isothiocyanate-lobeglitazone; MMR-Lobe) intended to affect the therapeutic efficacy of lobeglitazone to foam cells derived from high mannose receptor specificity. This was done by time-lapse tracking of tridynamics of label-free living foam cells. Moreover, researchers performed treatment assessment at the single-cell level using a machine attempting to learn picture analysis. Such findings imply that refractive index assessment is a useful method for researching new medications for metabolic illnesses associated with LD. In conclusion, by observing the biological and morphological features in active cells without the use of exogenous labeling reagents, researchers were able to identify atherogenic foam cells and differentiate them from macrophages. The research also shows that the ODT approach, which enables 3D tracking of specific LDs in living cells, may be used to evaluate therapeutic medicines in real time, including targeted nanoparticles, in lipid-containing cells. Inflammatory reactions via lipid as well as cholesterol accumulation are intimately linked to metabolic diseases such as cancer, obesity, and diabetes mellitus in addition to atherosclerosis. As a result, they think that the label-free and quick 3D ODT technique in combination with cutting-edge machine-learning techniques could offer easily comprehensible and significant assessment of drug efficacy to find new treatments for treating various metabolic illnesses. The proposed technique has not been able to validate the existence of some viruses linked to particular disorders [19].

For disorders like diabetes and heart disease, nanomedicine techniques were first modified and then effectively translated to medical applications. Unmet medical demands associated with diseases like leishmaniasis could undoubtedly be helped by these measures. In its visceral form, the latter damages internal organs and results in skin blisters. The goal of treating cutaneous leishmaniasis (CL) is to hasten the healing of wounds, lessen scarring and cosmetic morbidity, stop the spread of the parasite, and avoid relapse. However, the efficiency of existing medications is subpar, and none of them will be created expressly to address this illness condition. Diabetic wounds were getting treated in clinics employing cell growth utilizing nanobased devices along with drug administration. In order to achieve nonsurgical healing of wounds, targeting subsequent bacterial infection, as well as minimise drug toxicity, researchers therefore critically evaluate the application of nanomedicine-based techniques to cure CL injuries in this study. Secondary microbiological infections are a significant side effect of CL. Leishmaniasis-ulcerated lesions were extremely vulnerable to infectious diseases, which lead to purulent discharges, further skin tissue destruction, necrosis, and inflammation, so extending the illness and delaying healing. An effective treatment must be capable of treating certain concurrent secondary infections as well as the parasite load, lessening the financial and medication burden on caregivers and patients. The difficulty is compounded by the fact that the origin of the Leishmania parasite determines how the sores

develop. The well-being of CL individuals could benefit from an innovative strategic approach that combines machine learning, clinical experience, nanomaterials, and scaffold technology. Sandflies must be readily available, and rates of infection must be maintained over time, for this strategy to work [20].

A health care-associated disease called *Clostridium (Clostridioides) difficile* infection (CDI) can have significant consequences. Admission to the intensive care unit (ICU), toxic megacolon growth is in need for a colectomy or mortality, which is all possible consequences. It can be difficult to pinpoint the patients who are most prone to experience complex CDI, though. In order to do this, researchers investigated the usefulness of a machine-learning (ML) strategy for complications risk categorization utilizing electronic health record (EHR) data. They took into account adult subjects who require a CDI diagnosis at the University of Michigan hospitals during October 2010 and January 2013. If the infection led to an ICU admission, a colectomy, or 30-day death, the case was classified as complex. Researchers developed a model for predicting subsequent problems on every one of the three days following diagnosis using EHR data. Researchers contrasted the EHR-based model with one that relied only on a select number of hand-selected features. Utilizing a held-out data set, they assessed predictive accuracy in terms of the area under the receiver operating characteristic curve. Eight percent of the 1118 CDI individuals experienced complications. The approach achieves an AUROC of 0.69 on the day of diagnosis. Performance improved and outperformed a model built on a carefully selected set of features when using information taken two days following CDI diagnosis. We can precisely categorize CDI cases based on their propensity to experience problems using EHR data. Future clinical research looking into interventions which might stop or lessen complex CDI might follow such a methodology. The investigation does not, however, examine whether elaborate CDI definitions drawn only from the EHR are acceptable. Additionally, we cannot rule out the chance that patients may encounter the outcome in a different hospital, and as a result, we may have overestimated the severity of CDI consequences [21].

A public health problem is the introduction and quick transmission of multidrug-resistant bacterial pathogens. The abuse as well as excessive use of antibiotics, which hastened the development of antibiotic-resistant strains, is to blame for this emergence. The nanoscale, which ranges from 1 to 100 nm, is made up of things called nanoparticles (NPs), which have all three exterior dimensions. Because of the increase in nosocomial as well as community-obtained diseases brought on by pathogens, study on NPs with improved antibacterial activities as antibiotic substitutes has accelerated. Nanoinformatics has made use of machine-learning (ML) technologies with encouraging outcomes. Due to their clear successes on a number of predictive tasks, ML approaches are piquing the interest of many different stakeholders. Throughout the study, researchers provide a machine-learning (ML) technique that accurately predicts the antibacterial capability of NPs, with positive findings from the model's validation ( $R^2 = 0.78$ ). Key physicochemical (p-chem) characteristics and experimental set-

tings (exposure factors and bacterial clustering) from in vitro investigations were collected following an examination of the literature comprising 60 papers. Researchers trained a variety of logistic regression after homogenising and processing the data, followed by an evaluation process using a range of performance indicators. Finally, a ranking of the traits that are most crucial for predicting the result—known as an important attribute evaluation—was done. According to attribute significance, the major factors in determining the antibacterial impact of NPs are the NP core size, the exposed dose, and the bacterial species. Depending on their p-chem characteristics and different exposure settings, the tool aids a variety of stakeholders including scientists in forecasting the antimicrobial properties of NPs. Through combining functionality tools, this idea also supports the safe-by-design approach. The research emphasises the want for further data, alerting the research establishment to the dearth of comprehensive information about the antibacterial capability of NPs [22].

With the development of nanotechnology, researchers are witnessing a shift in the global economy and deep infiltration of nanoproducts ranging from essentials to cutting-edge electronics, healthcare, and pharmaceuticals. Nanoproducts should be closely controlled to prevent undesirable consequences because they can have unfavourable side effects. The limitations of conventional safety evaluation methods are highlighted by the toxicity as well as safety concerns that would arise with relation to the rapid integration of nanomaterials with different functionalities and properties into consumer products. The simulation and modelling of nanobiointeractions are presently expected to benefit from artificial intelligence and machine-learning techniques, and this extends to the postmarketing monitoring of nanomaterials in the actual world. In order to gain unique insights on the disruption of complex biological activities following integration with nanoparticles, machine learning might be combined with biology including nanomaterials. The possibility of integrating integrative omics with machine learning in assessing nanomaterial security and risk evaluation is discussed in the paper, along with advice for regulatory bodies. In order to investigate the security as well as risk evaluation of pre- and postmarketing monitoring of nanomaterials, the paper focuses on the synergistic integration of AI methodologies with biological information. Researchers have also seen a rise in the integration of a wide range of information, from molecular to clinical, while using DL to investigate the end points of nanotoxicity caused by the intricate interplay of multiple biological systems. Each omics research is a big data enterprise, necessitating a lot of digital backups, powerful computers, and the statistical know-how required to work with large data sets. However, since researchers do not know how neural networks arrived at a specific result, they cannot establish their reliability for ongoing drug discovery [23].

### 3. Materials and Methods

**3.1. Study Layout.** Patients admitted between 2015 and 2020 at a sizable general hospital have been chosen as the study objective in this investigation. Initially, a quality control

procedure was used in this study to examine the EHRs' eligibility. 305,762 medical records have been left after removing those with missing information, conflicting data, or follow-up data. The dataset has been subsequently filtered using the inclusion criteria listed in Figure 3: (1) the department dealing with infections must be the admittance department. (2) Information about noncommunicable illnesses is excluded. (3) Additional infectious illnesses and infectious subillness that are not infectious have been excluded. 10,950 medical records were found to be eligible after processing, with 42.65 years of average age. Men made up 47.95%, and women made up 52.05 percent.

**3.2. Data.** It is necessary to have patient medical data with a variety of specific details for the identification of infectious illnesses. The Medical Data Center was primarily used in this investigation to gather the medical data. Information from the outpatient as well as inpatient departments is pooled to increase the dataset due to the dearth of individuals with infectious disorders. Data has been taken out of electronic medical records (EMRs) that are not organized. Prior to actually training the prognosis model, this information needs to be handled in a number of phases due to its lack of homogeneity. For instance, the knowledge base takes the role of the alias and subcategory identities of the traits and illnesses employed in the database.

Natural language processing (NLP) techniques and regular expressions have been used in this study to produce features. The training databases have been then vectorized and organized. Consideration is given to a vast array of data that significantly affects infectious diseases. The information used to construct the training system are shown in Table 1. The sample has been labeled with a medical prognosis, and the rest obtained information is employed as the system's input feature. The data consists of five different types of files: laboratory test reports, outpatient records, admission records, patient personal data, and evaluation reports.

**3.3. Unorganized Data Processing.** The patient's complete, precise, and thorough personal health data are contained in the EMRs. In order to extract a significant amount of potentially useful information, our research carefully analyses and mines the data in the EMRs. Nevertheless, unorganized free text information makes up a significant amount of the information in the EMRs in complement to organized information like medical laboratory test outcomes. The free text has numerous ambiguities and possible polysemy in every section. Unstructured data is typically challenging for prototype training to comprehend and utilize. This information may be successfully transformed by NLP into organized information that the system can identify, which forms the basis for building the model of supplemental diagnostics for infectious diseases [24]. Among the essential NLP operations for information retrieval as well as processing deep semantics, encompassing named entity identification, word meaning, word tagging, and keyword extraction, is sequence labeling. EMR sequence tagging can be used to identify items such as illnesses, symptoms, medications, laboratory tests, and the connections between them. The present open-

source approach recurrent neural network- (RNN-) artificial bee colony (ABC) optimization, which successfully executes sequence annotation, provides the foundation for this research. RNN-ABC is used in this study together with the rule framework and other techniques to achieve the actual EMR information extraction. After executing word segmentation, the study first inputs the serialized word into the RNN layer, where the hidden state findings are then integrated to produce the RNN output.

Then, the RNN-ABC network architecture is created by sending the RNN outcome to ABC as to even the input. Depending on the RNN element, this architecture successfully keeps the data preceding and following the entire sentence and extracts the feature data within the phrase. It incorporates the benefits of RNN with ABC. It can efficiently learn the limited data in the training corpus and increase the precision of information retrieval with the aid of the ABC layer. The layers of RNN-ABC are shown in Figure 4. The RNN and ABC extraction outcomes are then saved in the system. At this point, the free text information from the sufferer's medical data is converted into organized field feature information. In order to enter the field information into the deep learning (DL) framework, it is also necessary to operate the organized data using feature engineering. The information has been processed to include both continuous and discrete statistical elements. Continuous statistical features like systolic blood pressure, body temperature, and diastolic blood pressure should be evaluated first for aberrant values before filtering out those that substantially deviate from the usual value range. Then, continuous characteristics will be normalized to the threshold [0,1] in an attempt to remove the negative effects of differing dimensions between distinct characteristics on prototype training. For item aliases like symptoms, illnesses, and indications, conventional names have been then used in place of the item aliases for distinct aspects like gender, manifestations, and past illnesses. The feature description and its chapter description must also be combined. The same item information may appear in various chapters of the medical file, but they could have distinct medical interpretations.

One depicts the current primary manifestations, whereas the other indicates the complaints that have occurred in the prior, i.e., the previous history. For instance, the symptoms name in the primary complaint will be similar at the time point in the latest medical history. As a result, research must combine feature names predicated on chapters, like "primary complaint" and "prior history" when referring to a femoral neck fracture. In order to encode the fundamental category characteristics with 0/1 in high-dimensional form, one-hot coding has been then used. Table 2 displays the information following word segmentation and transforms it into a characteristic; a number of 1 denotes the presence of this characteristic, whereas a number of 0 denotes its absence.

258,590 dimensional features have been collected as system input data following interpreting discrete and continuous features, containing patient personal data with 2-dimensional features like age and gender. There are 217,229 dimensional features in the inpatient and outpatient data.

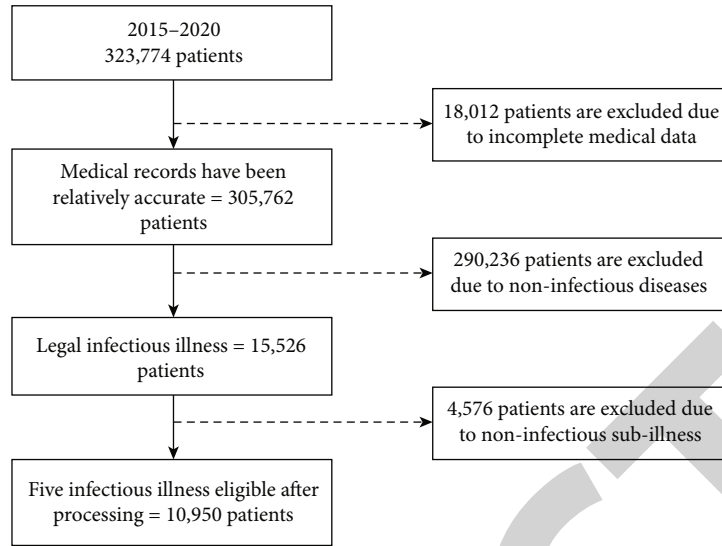


FIGURE 3: Enrollment flowchart.

TABLE 1: Important details obtained from medical data.

Target data category	Particular extraction
Patient personal data	Gender
	Age
	Visiting time
Medical history	Current disease history
	Medication
	Main complaint
	Anamnesis
Physical examination	Blood pressure
	Respiratory rate
	Temperature
	Pulse
	Results
Examination data	Evaluation item name
	Value range
Laboratory test data	Item name
	Results

There are 1,892 dimensional features in the lab testing outcomes. 28,519 dimensional characteristics can be found in examination data. Additionally, one-hot coding has been used to diagnose the sample’s learning label. Following the aforementioned procedures, 10,950 samples in overall have been acquired. Table 3 lists the number of cases for each group of infectious diseases.

**3.4. Model.** The detection of infectious illnesses has been typically accomplished using the classification machine-learning (ML) technique. This research also took into consideration other factors in the present multiclassification challenge of simultaneous detection of several infectious illnesses using ML-based classification technique. This

research uses a multiclassification technique to convert a two-class ML framework into a multiclass framework. The ML model includes logistic regression (LR), random forest (RF), Naïve Bayes (NB), and support vector machine (SVM). The workflow of the research is shown in Figure 5.

**3.4.1. Proposed DL Autoencoder for Infectious Disease Identification.** The input, hidden, and output layers make up the multiclass neural network (NN) fundamental structure. When implemented to multiclassification, the NN assignments, the ultimate output layer’s activating function ought to be the softmax function to ensure that the network may compute the classification chances of many categories concurrently, with the group with the highest classification probability which was the final identification result. A DL autoencoder has been created in this work for a number of prevalent infectious disorders. High-dimensional data or sparse data with higher 0 values makes training computationally complex and makes it challenging to improve the model. Consequently, the technique for compressing data and extracting features must be used. Autoencoder DL has been employed to efficiently conduct extraction of features and representation of features on higher dimensional data due to the significant number of sparse datasets in medical information. Sparse data may be densified using the autoencoder to make the system simpler to learn and to produce better outcomes. The autoencoder trains the properties of the samples as the NN input and the model label, simultaneously; therefore, it does not have to use the infectious disease classification to which the samples correspond as the label throughout the optimization procedure.

It utilizes the sample’s conceptual properties to describe the Z vector through reducing the reconstructive error (middle hidden layer’s output vector). Figure 6 depicts the basic components of the autoencoder system used in this research, including the decoder, hidden layer, and encoder. Two-layer NN is present in both the decoder and encoder. The

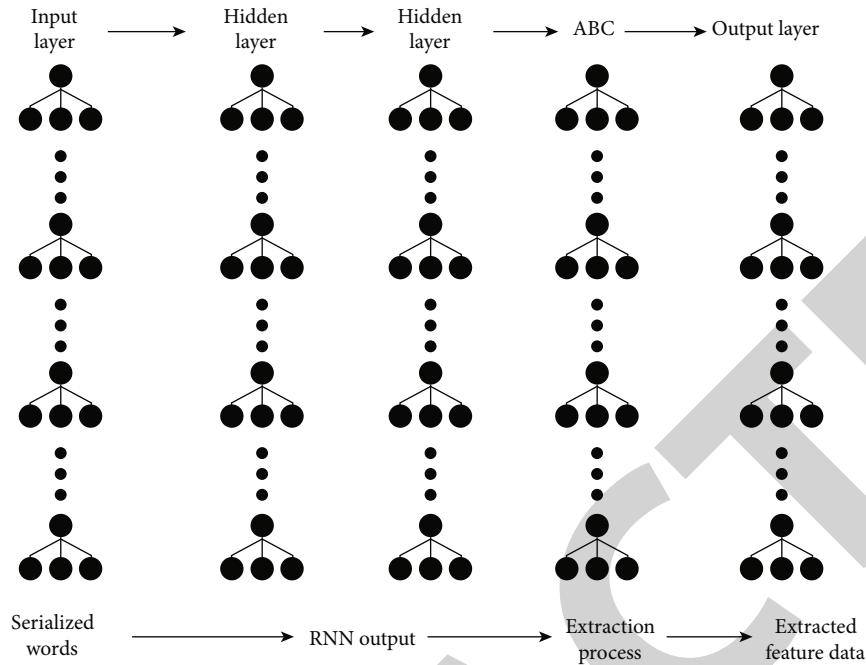


FIGURE 4: RNN-ABC layers.

TABLE 2: Transformation of data into features following word segmentation.

Data		Case number	
		1	2
Fractured femoral neck	Major complaint (pain)	1	0
	Past history	0	1
Main complaint symptoms	Fever	1	0
	Chest pain	1	1
Temperature		0.92	0.88

TABLE 3: Infectious disease samples.

Category of infectious illness	Samples
Syphilis	942
Measles	160
Influenza	3458
Tuberculosis	2620
Viral hepatitis	3770

encoder's two-layer network has anywhere from being more to fewer neurons. However, the middle hidden layer has just one NN. In order to reinstate the hidden layer's output to the initial characteristic dimension, the autoencoder first compressed the initial higher dimensional sparse vector towards the lower dimensional hidden layer via the encoder NN. The difference between the ultimate model outcome as well as the calculated original features is less, indicating that the less information that was lost throughout the compressing procedure to the hidden layer that may resemble the

original feature after compression, the better. The framework's decoder component is removed once the autoencoder has been pretrained, and the Z vector outcome from the hidden layer has been then directly utilized as the actual characteristic dense representation and given to the next categorization model. Considering that distinct medical data contains varied kinds and amounts of characteristics, this research creates separate autoencoder systems for varying records in the densification operation so as to acquire their own more efficient abstract characteristic representations.

In more detail, there are 4096 and 1024 neurons in each of the encoder's two layers, 256 neurons are inside the hidden layer, and 1024 and 4096 neurons are in each of the decoder's two layers. The decoder outcome's 4096 dimension is then plotted corresponding to the input functionality dimension as well as the input information in order to compute the losses. Two autoencoders have been trained in accordance with the model's architecture, one for information for outpatient care, an admissions record, as well as an inspection data. Lastly, each autoencoder enters the actual high-dimensional sparse data's dense vector representation obtained from the 1024 hidden layers output into the ensuing self-attention component. After learning, the autodecoder encoder's component is removed, and the residual structure has been then merged with the self-attention component. In particular, the coding vector holding the patient's personal details is joined with the dense information provided by the hidden units in the two autoencoders, resulting in an overall of 1045 dimensional characteristics. The merged vectors undergo the layer normalization method's normalization step before being input into the following classification framework. The self-attention component then receives the results. After being acquired from

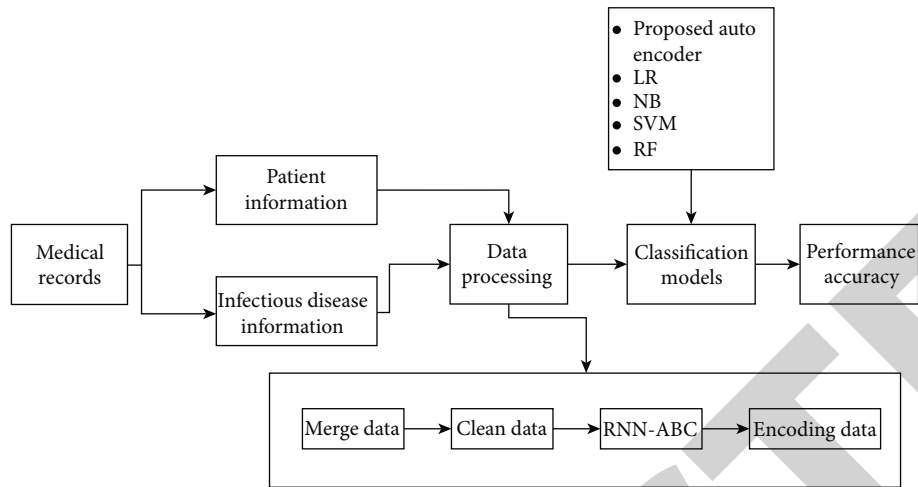


FIGURE 5: Workflow of research.

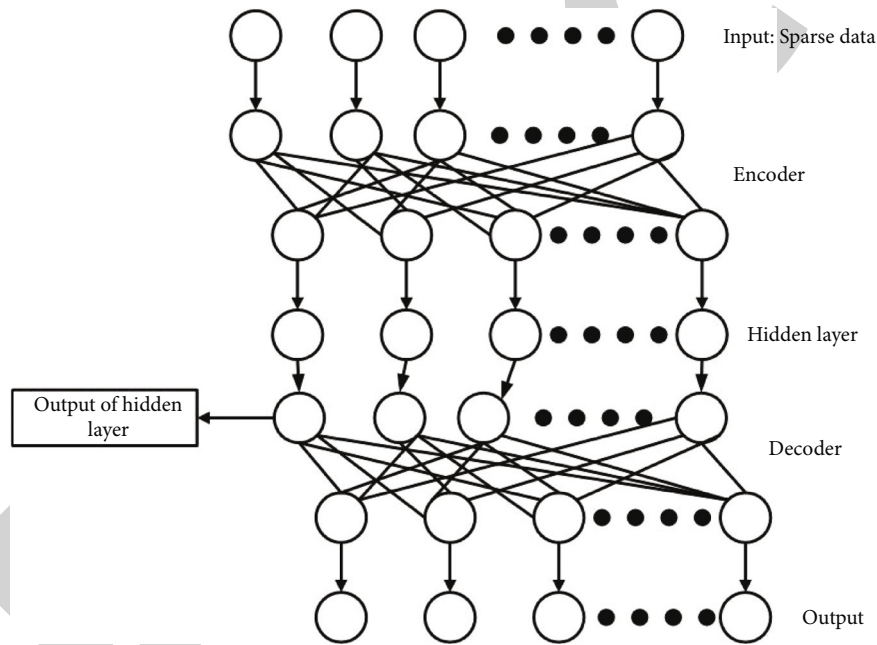


FIGURE 6: Proposed autoencoder architecture.

several papers, the dense vector one feature value space does not contain all autoencoders. The whole vector is normalized using layer normalization to lessen the influence of the aforementioned problems on the training outcomes. The dense vector is appended to the outcome of the self-attention computation, and the addition outcome is then explicitly added to the NN computation outcome. In order to produce the relevant probability of infectious illnesses, the model ultimately utilizes softmax as an activation function to classify infectious diseases simultaneously.

3.4.2. *Naïve Bayes (NB)*. The Naïve Bayes (NB) ML method is employed to identify infectious diseases. NB classifiers are probabilistic classifiers that were developed using the NB theorem. The NB approach of classification seems to be a

quick and efficient approach. One of NB’s primary benefits is that it is an extremely scalable method. The NB classifier basically asserts that the existence of one feature does not preclude the existence of any other qualities in the category. This theory has been adopted in classifying the infectious illness:

$$Q^* = \operatorname{argmax}_Q P\left(\frac{Q}{D}\right), \tag{1}$$

$$Q^* = \operatorname{argmax}_Q P\left(\frac{Q}{D}\right) \times \left(\frac{p(Q)}{p(D)}\right), \tag{2}$$

where  $Q$  is the infectious disease and  $D$  is the processed data. This classification technique assumes that all feature values

are completely independent and examines the relationship between each feature and each class in a processed data. Each feature is assessed separately, and a conditional probability has been calculated for the associations between attribute values and classification. The classification with the highest probability score has been selected as the predicted class.

**3.4.3. Support Vector Machine (SVM).** Support vector machines (SVMs) are one of the most employed disease classifiers. Among the tactics employed in supervised ML are SVMs. SVMs use a training method to develop a classifier that will be used to assign new, unclassified diseases to one of the numerous established categories. SVMs can be used in both linear and nonlinear illness classification. Additionally, SVMs could be applied to supervised and unsupervised learning. A hyperplane or a set of hyperplanes is created by SVM and used for classification. Moreover, in SVMs, the classes are in the form of hyperplane, which is shown in

$$S \cdot G + b = 0, \quad (3)$$

where  $S$  is the vector's weight,  $G$  is the input vector, and  $b$  denotes bias.

**3.4.4. Logistic Regression (LR).** A binary classification approach predicated on the integration of a linear regression framework with a sigmoid activation function was called a logistic regression strategy. The prototype has a straightforward layout. The logistic regression framework simply has a single level of weight, as opposed to the deep neural network, making its weight easier to comprehend. The prototype output's value range falls between  $[0, 1]$ , which could be interpreted as the likelihood of falling into a particular class. In logistic regression, the result variable was binary. As a classification model, it is employed to categorize observations into a finite set of categories and heavily relies on probability.

**3.4.5. Random Forest (RF).** A vast number of decision trees have been constructed in this method as they work together. The cornerstones of this method are decision trees. Another notion that is created utilizing the decision tree method is to create a decision tree. These trees make up the random forest that has been employed to categorize new objects from such an input vector. For categorization, each decision tree that is generated has been used. The ensemble method known as the random forest has been used to create predictive algorithms for both categorization and regression issues. It is made up of a random assortment of trees that produce the desired results. It adheres to the group learning approach. These decision trees decide towards the most well-liked category in classification issues, although in regression issues, the answer of the tree seems to be an approximation of the contingent parameters given the determinants.

**3.5. Evaluation Metrics.** According to the autoencoder approach, the initial diagnosis is accurate if it agrees with the patient's clinical diagnostic; if not, it is mistaken. Disease outbreaks are provided mainly from other noncommunicable diseases in accordance with healthcare safety manage-

TABLE 4: Performance metrics evaluated using multiclass approach.

Labels	Identification outcome		
	1st class	2nd class	3rd class
1st class	$T_1$	$S_{1,2}$	$S_{1,3}$
2nd class	$S_{2,1}$	$T_2$	$S_{2,3}$
3rd class	$S_{3,1}$	$S_{3,2}$	$T_3$

TABLE 5: Outcome following autoencoder training through different amount neurons.

Amount of neurons	Accuracy of testing set
256	79.2%
1024	87.7%
4096	90.3%

ment guidelines. As a result, the order of diagnosis has no bearing on the reliability of infectious disease diagnosis. Table 4 displays the confusion matrix that the multiclassification method assumes (three categories were given as illustrations).  $S_{j,l}$  specifies the number of entries whose real labeling is  $l$  in which the analysis prior  $j$ .  $F$  signifies the total amount of categories of multiple classifications, and  $TP_k$  denotes the number of observations whose real label is  $k$  for which the model predicts  $l$ . The multiclassification confusion matrix specification is used to analyze the model's overall prediction accuracy and performance. The particular formula is in

$$A = \frac{\sum_l^F T_l}{\sum_l^F T_l + \sum_l^F \sum_{j \neq l}^F S_{l,j}} \times 100. \quad (4)$$

Precision and recall are employed in Equations (5) and (6) to evaluate the multiclassification model's prediction effectiveness in order to more thoroughly enhance it.

$$P_l = \frac{T_l}{T_l + \sum_{j \neq l}^F S_{j,l}}, \quad (5)$$

$$R_l = \frac{T_l}{T_l + \sum_{j \neq l}^F S_{l,j}}. \quad (6)$$

## 4. Result and Discussion

The outcomes of the classification research employing the autoencoder for the identification of several infectious diseases are presented in this section. The experiment's whole data set was derived from genuine hospital medical records. The infectious disease data is first employed to filter the normalized infectious disease names, after which it is utilized to weed out the tuberculosis-related subdiseases that are not pathogenic. For instance, tuberculosis of the thyroid and the kidney is listed under the kind of TB that is not contagious. Secondly, bacterial infections with less than 10 cases each quarter were excluded to guarantee the balancing of

TABLE 6: Testing and training outcome for autoencoder.

Pathogenic infections	Amount of training data	Accuracy of training set	Amount of testing data	Recall of testing set	Precision of testing set	F measure
Measles	180	38.1%	70	43.1%	49.1%	1.2223
Tuberculosis	3240	84.2%	2045	74.3%	89.2%	0.7448
Hepatitis	3845	98.1%	615	98.2%	88.1%	0.9578
Influenza	2915	96.3%	910	94.8%	89.1%	0.9125
Syphilis	1302	79.9%	305	81.2%	90.3	0.9001

TABLE 7: Detection of F1 measure, recall, and accuracy of entities.

Methods	Symptoms			Lab tests			Screening examination			Diagnosis		
	Rec	Acc	F1-m	Rec	Acc	F1-m	Rec	Acc	F1-m	Rec	Acc	F1-m
CRF++	72.3	71.4	78.0	77.9	84.5	69.8	72.6	88.7	80.6	88.2	88.6	82.1
LSTM-CRF	76.9	69.7	79.2	78.1	80.5	77.2	84.6	89.6	90.8	80.2	78.8	74.2
HMM	54.3	85.3	87.5	81.8	87.8	82.5	91.2	90.2	91.5	89.6	88.5	80.2
BiLSTM-CRF	87.5	88.4	90.1	87.5	87.8	91.8	90.6	91.2	82.6	85.3	84.1	82.1
RNN-ABC	98.9	96.9	95.3	94.0	93.4	92.4	97.2	92.4	93.2	90.3	92.4	90.2

the data utilized in the learning algorithm as well as the testability of the model's predictive capability. Lastly, seven contagious diseases have been foreseen and confirmed. Word segmentation as well as entity recognition techniques implemented using RNN-ABC methodology is used to create the input data for the autoencoder for the training of records relating to infectious diseases and change the format using one-hot encoding. Finally, 20,620 research-ready samples of top-notch clinical records are obtained. 16,496 samples from the training set make up 80% of the data, whereas 4124 samples from the test set make up 20%. The study utilizes a total of 1024 neurons in the intermediate layer and an autoencoder that transforms the 395,936-dimensional sparse data into a 1024-dimensional dense vector. 256 feed-forward neurons make up the categorization structure. 32 epochs were used to train the model in this investigation, with a training rate of 0.001. Only the model from the test set with the lowest loss is kept after the operation is terminated, and learning is halted when the loss reaches 10 epochs.

There are 32 training epochs that are useful. Additionally, autoencoders are constructed that had various numbers of hidden layer neurons, ranging of 256, 1024, and 4096. Table 5's findings demonstrate an increase in hidden units from 256 to 1024, as the succeeding multiclassification findings are enhanced. The precision of the model does not, nevertheless, significantly increase when the amount of neurons increases beyond 1024. 1024 is ultimately chosen as the perfect amount of hidden layer neurons after taking the prediction error, calculation effectiveness, and subsequent practical deployments as well as application into account.

Through the study, it was discovered that the model, whose objective is to overcome the multiclassification task of concurrently estimating every classifications, is comparable to training all classifications with the same amount of epochs that makes it more susceptible to a poorly balanced number of categorization specimens. The metrics of cate-

gory mass as well as numerous tasting for categories with a limited number of samples are incorporated in this study to address the issue of unbalanced tests. Lastly, the test set's overall accuracy of the model for all infectious diseases is 89.52%. Table 6 lists the specific outcomes for every infectious disease.

Table 6 shows that in the trial for diagnosing several pathogens, autoencoder produced better prediction outcomes. Related traits are utilized to diagnose similar disorders, and the category weight is changed accordingly. In comparison to disease categorization with less sample data, categorization of diseases with more sample data has much higher prediction accuracy. For instance, the training data included 3845 and 2915 cases of viral hepatitis and flu correspondingly, and the associated test recall levels were 98.2% and 94.8%. Syphilis and measles, in comparison, have much less training sets that are the equivalent test recall rates for 1,302 and 180 which are 81.2% and 43.1%, respectively. The prediction rate is significantly impacted by the growth of the elements that interfere with the illness diagnosis feature. In the case of tuberculosis, the sample size is 3240, and the prediction overall accuracy is 74.3%. Additionally, there are both positive and negative etiologies for tuberculosis, as well as the clinical diagnosis of the condition is more difficult than that of viral hepatitis, influenza, and other illnesses. The features of contagious diseases, however, cannot be learned properly throughout training for infectious diseases that have little data, including measles, and the reliability of the training set is low. As a result, the accuracy of the testing dataset is also low, as well as the model could not be widely validated using a small test set. To further demonstrate the model's efficacy for illnesses with less data samples, the data volume must be raised.

It is evaluated to the classic ML algorithms CRF, HMM, and deep learning models LSTM-CRF BiLSTM-CRF with the suggested RNN-ABC for information extraction. Twenty



TABLE 8: Comparison of disease diagnosis among proposed autoencoder and existing methods.

Pathogenic infections	Proposed autoencoder	SVM	NB	RF	LR
Measles	60.65	56.38	56.38	54.26	56.38
Tuberculosis	86.88	83.08	80.21	76.29	82.31
Hepatitis	95.17	90.03	88.29	84.44	85.49
Influenza	99.44	96.19	90.13	85.19	91.26
Syphilis	95.38	91.51	89.47	82.27	90.49

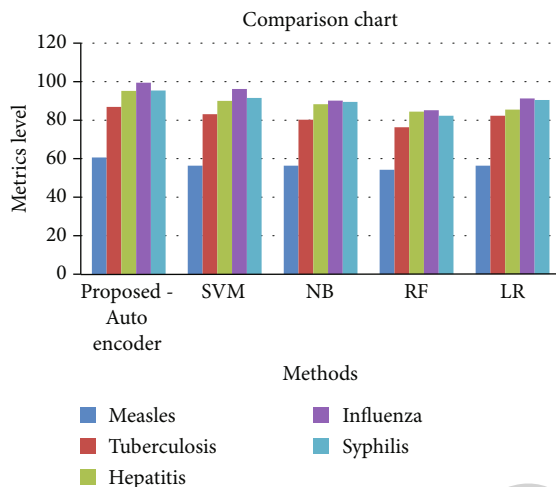


FIGURE 7: Comparison cohort of proposed RNN-ABC with existing methods.

six thousand two hundred twenty two electronic medical record data containing five kinds of entity labels—disease diagnosis, symptom, medication, laboratory test, and imaging examination—are identified using the model. 15,678 samples from the training set make up 80% of the data, whereas 3481 samples from the test set make up 20%. Following training, Table Table 7 presents the comparison's findings. The DL model outperforms the conventional machine-learning approach overall. In comparison to the 87.5% of the BiLSTM-CRF model, the F1-score of the RNN-ABC model is 98.9% on average across five different types of entities, particularly in the imaging examination entity. However, it is clear that the two-way LSTM structure more accurately pinpoints the entity border.

A comparison is made between the autoencoder model and other models from existing studies. The comparable conclusion is given in Table 8 using the similar data source. When it comes to the classification of bacterial infections into many categories, the autoencoder method is superior to other methods. The autoencoder model is also noticeably superior than the other approaches, also for tuberculosis that is challenging to partition. This demonstrates the model's superiority within the multiclassification of unstructured infectious illness clinical data.

Figure 7 shows the comparison cohort of the existing and proposed method. This study suggests autoencoder experimentation along with existing approaches applied in different research. Using viral hepatitis as an illustration,

the precision of 95.17% of autoencoder is much greater than random forest, SVM, logistic regression, and the Bayesian approach. The same is true for other illnesses. These results attest to the value of AI-based assisted making choices for infectious illness diagnosis with more effective diagnosis.

## 5. Conclusion

Viral infections rank among the leading causes of illness and mortality, having a significant influence on the health and economy of every country on the planet. The provision of high-quality healthcare as well as the management and prevention of these illnesses is all improved by the capacity to predictably diagnose viral infections. Since the recent growth of nanotechnology as well as their excellent chemical and physical capabilities, such as their small size and synthetic surface properties, nanomaterials are now widely used in the medical business. Nanomedicine refers to the use of nanoparticles for disease detection, surveillance, control, prevention, and therapy, such as the dealing of pathogenic diseases. The foundation of the broad field of nanomedicine is the application of nanotechnology to medical goals. Among the most used nanomaterials in nanomedicine are nanoparticles, which have a nanoscale dimension, highly controlled optical and physical properties, and the capacity to bind to a wide range of substances. The recurrent neural network-artificial bee colony (RNN-ABC) approach was used to process the data. To improve the effectiveness of system learning, methods for sparse data densification are carried out by the autoencoder. Other popular models, such as support vector machine, logistic regression, random forest, and Naïve Bayes, were compared to the recommended autoencoder system. The outcome shows that the suggested autoencoder method could predict viral illnesses better than existing approaches. The techniques utilized in this study may help to eliminate reported lags in present monitoring systems, cutting costs for society.

## Data Availability

The data used to support the findings of this study are included within the article.

## Conflicts of Interest

The authors declare that there is no conflict of interest regarding the publication of this article.

## Retraction

# Retracted: Resveratrol Suppresses Bupivacaine-Induced Spinal Neurotoxicity in Rats by Inhibiting Endoplasmic Reticulum Stress via SIRT1 Modulation

### BioMed Research International

Received 20 June 2023; Accepted 20 June 2023; Published 21 June 2023

Copyright © 2023 BioMed Research International. This is an open access article distributed under the Creative Commons Attribution License, which permits unrestricted use, distribution, and reproduction in any medium, provided the original work is properly cited.

This article has been retracted by Hindawi following an investigation undertaken by the publisher [1]. This investigation has uncovered evidence of one or more of the following indicators of systematic manipulation of the publication process:

- (1) Discrepancies in scope
- (2) Discrepancies in the description of the research reported
- (3) Discrepancies between the availability of data and the research described
- (4) Inappropriate citations
- (5) Incoherent, meaningless and/or irrelevant content included in the article
- (6) Peer-review manipulation

The presence of these indicators undermines our confidence in the integrity of the article's content and we cannot, therefore, vouch for its reliability. Please note that this notice is intended solely to alert readers that the content of this article is unreliable. We have not investigated whether authors were aware of or involved in the systematic manipulation of the publication process.

Wiley and Hindawi regrets that the usual quality checks did not identify these issues before publication and have since put additional measures in place to safeguard research integrity.

We wish to credit our own Research Integrity and Research Publishing teams and anonymous and named external researchers and research integrity experts for contributing to this investigation.

The corresponding author, as the representative of all authors, has been given the opportunity to register their agreement or disagreement to this retraction. We have kept a record of any response received.

### References

- [1] Y. Luo, Y. Zhao, J. Lai et al., "Resveratrol Suppresses Bupivacaine-Induced Spinal Neurotoxicity in Rats by Inhibiting Endoplasmic Reticulum Stress via SIRT1 Modulation," *BioMed Research International*, vol. 2023, Article ID 1176232, 13 pages, 2023.

## Research Article

# Resveratrol Suppresses Bupivacaine-Induced Spinal Neurotoxicity in Rats by Inhibiting Endoplasmic Reticulum Stress via SIRT1 Modulation

Yunpeng Luo <sup>1</sup>, Yang Zhao <sup>1</sup>, Jian Lai <sup>1</sup>, Liling Wei <sup>1</sup>, Gang Zhou <sup>1</sup>, Yue Yu <sup>2</sup>, and Jingchen Liu <sup>1</sup>

<sup>1</sup>Department of Anesthesiology, The First Affiliated Hospital of Guangxi Medical University, 22 Shuangyong Road, Nanning, 530021 Guangxi, China

<sup>2</sup>Department of Anesthesiology, The Second Affiliated Hospital of Guangxi Medical University, 166 Daxuedong Road, Nanning, 530007 Guangxi, China

Correspondence should be addressed to Jingchen Liu; [jingchenliunn@163.com](mailto:jingchenliunn@163.com)

Yunpeng Luo and Yang Zhao contributed equally to this work.

Received 15 September 2022; Revised 9 October 2022; Accepted 12 October 2022; Published 21 February 2023

Academic Editor: S Kumaran

Copyright © 2023 Yunpeng Luo et al. This is an open access article distributed under the Creative Commons Attribution License, which permits unrestricted use, distribution, and reproduction in any medium, provided the original work is properly cited.

Bupivacaine (BUP) may cause neurotoxic effects after spinal anesthesia. Resveratrol (RSV), a natural agonist of Silent information regulator 1 (SIRT1), protects various tissues and organs from damage by regulating endoplasmic reticulum (ER) stress. The aim of this study is to explore whether RSV could alleviate the neurotoxicity induced by bupivacaine via regulating ER stress. We established a model of bupivacaine-induced spinal neurotoxicity in rats using intrathecal injection of 5% bupivacaine. The protective effect of RSV was evaluated by injecting intrathecally with 30  $\mu\text{g}/\mu\text{L}$  RSV in total of 10  $\mu\text{L}$  per day for 4 consecutive days. On day 3 after bupivacaine administration, tail-flick latency (TFL) tests and the Basso, Beattie, and Bresnahan (BBB) locomotor scores were assessed to neurological function, and the lumbar enlargement of the spinal cord was obtained. H&E and Nissl staining were used to evaluate the histomorphological changes and the number of survival neurons. TUNEL staining was conducted to determine apoptotic cells. The expression of proteins was detected by IHC, immunofluorescence, and western blot. The mRNA level of SIRT1 was determined by RT-PCR. Bupivacaine caused spinal cord neurotoxicity by inducing cell apoptosis and triggering ER stress. RSV treatment promoted the recovery of neurological dysfunction after bupivacaine administration by suppressing neuronal apoptosis and ER stress. Furthermore, RSV upregulated SIRT1 expression and inhibited PERK signaling pathway activation. In summary, resveratrol suppresses bupivacaine-induced spinal neurotoxicity in rats by inhibiting endoplasmic reticulum stress via SIRT1 modulation.

## 1. Introduction

Bupivacaine, an amide-type local anesthetic, is one of the most widely used local anesthetics for surgical anesthesia and pain management. Previous studies have reported that bupivacaine might be neurotoxic and even clinically recommended dose of bupivacaine also can cause severe neurological complications, which brings extra medical and economic burden to the patients and their families [1–3]. However, the exact mechanism underlying the neurotoxicity of bupivacaine is unclear.

Endoplasmic reticulum (ER) stress, which results from the accumulation of misfolded proteins triggered by nutrient deprivation, hypoxia, and calcium overloading, is a highly evolutionarily conserved stress response pathway [4]. As it may facilitate cell death, ER stress is crucial for the pathological process of neuronal damage [5]. Our previous study has revealed that ER stress can cause mitochondrial dysfunction and apoptosis and aggravate the neuronal injury, which is vital for bupivacaine-induced spinal neurotoxicity [6, 7]. Therefore, alleviate ER stress maybe the treatment target of bupivacaine-mediated neurotoxicity.

Resveratrol (RSV), a natural agonist of SIRT1, protects various tissues and organs from damage by regulating ER stress [8–10]. However, the effect of RSV on spinal neurotoxicity induced by bupivacaine is unclear. The aim of this study is to explore whether RSV could alleviate the neurotoxicity induced by bupivacaine via regulating ER stress. Findings from this study may highlight RSV as a potential agent for alleviating bupivacaine-induced spinal neurotoxicity.

## 2. Materials and Methods

**2.1. Animals.** All experimental protocols adhered to National Institutes of Health guidelines for the Care and Use of Laboratory Animals (No. 8023, revised in 1978) and were approved by the Animal Care and Use Committee of Guangxi Medical University (No. SYXK GUI 2020-0004). In total, 48 male Sprague-Dawley rats (8–10 weeks, weighting 250–300 g) were obtained from Animal Experimental Center of Guangxi Medical University and housed in separate cages of standard living conditions (temperature:  $23 \pm 2^\circ\text{C}$ , relative humidity  $50 \pm 10\%$ , and 12:12 light/dark cycles). All rats had free access to standard rodent chow and water.

**2.2. Intrathecal Catheterization and Groups.** Intrathecal catheterization was done as previously described [11]. Before surgery, animals were anesthetized using 1% pentobarbital sodium (50 mg/kg, i.p.). Next, a 2 cm longitudinal dorsal midline incision was made in the L4–L5 gap. The subarachnoid space was then cannulated using a polyethylene catheter (PE10, Smiths Medical, Lower Pemberton Kent, UK) through the puncture point of ligamentum flavum and advanced by 1.5 cm in the cephalad direction. The distal end of the catheter was then closed and fixed subcutaneously. The rats were then housed in separate cages for 1 day for recovery before being randomly split by SPSS software ( $n = 12$  per group) into the saline group (group saline), bupivacaine group (group BUP), bupivacaine+resveratrol group (group BUP+RSV), and bupivacaine+DMSO group (group BUP+DMSO). RSV and BUP were purchased from Sigma-Aldrich (St. Louis, Missouri, USA). RSV was dissolved in 20% DMSO. The saline group was intrathecally administered with saline ( $0.12 \mu\text{L/g}$ ). The groups BUP, BUP+RSV, and BUP+DMSO were administered 5% bupivacaine ( $0.12 \mu\text{L/g}$ ) in three injections at 90 min intervals. The group BUP+RSV intrathecally received  $30 \mu\text{g}/\mu\text{L}$  RSV in total of  $10 \mu\text{L}$  per day for 4 consecutive days which beginning 1 day before bupivacaine administration and stopping 2 days after bupivacaine administration. Meanwhile, the group BUP+DMSO intrathecally received  $10 \mu\text{L}$  20% DMSO solution only [12]. All rats were sacrificed by cervical dislocation under inhalation of isoflurane after behavioral tests, and the lumbar enlargement of the spinal cord was obtained for further experiments.

**2.3. Behavioral Tests.** Behavioral tests were conducted on day 3 after bupivacaine administration by the same observer who is unaware of the allocation details. The TF machine (model YLS-12A; Huaibei Zhenghua Biological Instrument Equip-

ment Co., Anhui, China) was employed to perform the tail-flick latency (TFL) test to assess tail sensory function. Results were converted to percentage maximal possible effect (%MPE). The hindlimb locomotor function was determined using the Basso, Beattie, and Bresnahan (BBB) locomotor scale as previously described [13].

**2.4. Hematoxylin and Eosin (H&E) and Nissl Staining.** Lumbar enlargement spinal cord samples were fixed in 4% paraformaldehyde for 24 h at room temperature, embedded in paraffin, and sectioned at a thickness of  $5 \mu\text{m}$ . The sections used to H&E staining were then subjected to hematoxylin and eosin for 10 min, while sections used to Nissl staining underwent staining in preheated 0.05% ( $w/v$ ) cresyl violet solution for the 20 s at  $37^\circ\text{C}$ , followed by examination under a light microscope (BX53, Olympus Corporation, Tokyo, Japan). The number of survival neurons in the spinal dorsal horn was calculated.

**2.5. Apoptosis Analysis.** The rates of apoptosis were examined using the TUNEL assay. Briefly, endogenous peroxidase was quenched by incubating the sections with 3% hydrogen peroxide for 15 min. The TUNEL assay was then carried out according to manufacturer instructions (Roche Diagnostics, Mannheim, Germany). The number of TUNEL-positive cells was counted under a fluorescent microscope, and the percentage of the apoptotic cells was calculated.

**2.6. Immunohistochemistry (IHC).** The paraffin-embedded sections were incubated with 3% hydrogen peroxide for 15 minutes to block endogenous peroxidase activity and then blocked using 5% goat serum albumin for 1 h. They were then incubated overnight at  $4^\circ\text{C}$  with primary antibodies against Bax (1:300, Proteintech), Bcl2 (1:200, Wanleibio), and cleaved Caspase3 (1:300, Wanleibio). They were then incubated with HRP-conjugated secondary antibodies at room temperature for 15 min, washed thrice with PBS, signal developed using diaminobenzidine (DAB) solution, counterstained using hematoxylin solution, and examined under a microscope. The ratio of DAB-positive area to total area in each field was analyzed.

**2.7. Immunofluorescence.** The paraffin-embedded sections were dewaxed, rehydrated, and blocked using 5% goat serum albumin for 1 h. They were then incubated overnight at  $4^\circ\text{C}$  with anti-SIRT1 (1:1000, Abcam) and anti-GRP78 (1:300, Proteintech) primary antibodies, followed by incubation with Alexa Fluor-488 secondary antibody (1:500, Invitrogen) and DAPI. The images were visualized on a fluorescent microscope, and the mean fluorescence intensity was analyzed in each field.

**2.8. RT-PCR Analysis.** The TRIzol reagent (TaKaRa, Shiga, Japan) was used for RNA extraction from lumbar enlargement spinal cord tissues following the manufacturer's protocol. The total RNA samples were retrotranscribed into cDNA using PrimeScript™ RT reagent Kit (TaKaRa, Shiga, Japan). Real-time PCR analysis of SIRT1 mRNA levels was done using the following conditions: initial denaturation:  $95^\circ\text{C}$  for 30 s, followed by 40 cycles at  $95^\circ\text{C}$  for 5 s,  $60^\circ\text{C}$  for 30 s, and  $72^\circ\text{C}$  for 10 min using GAPDH as reference gene.

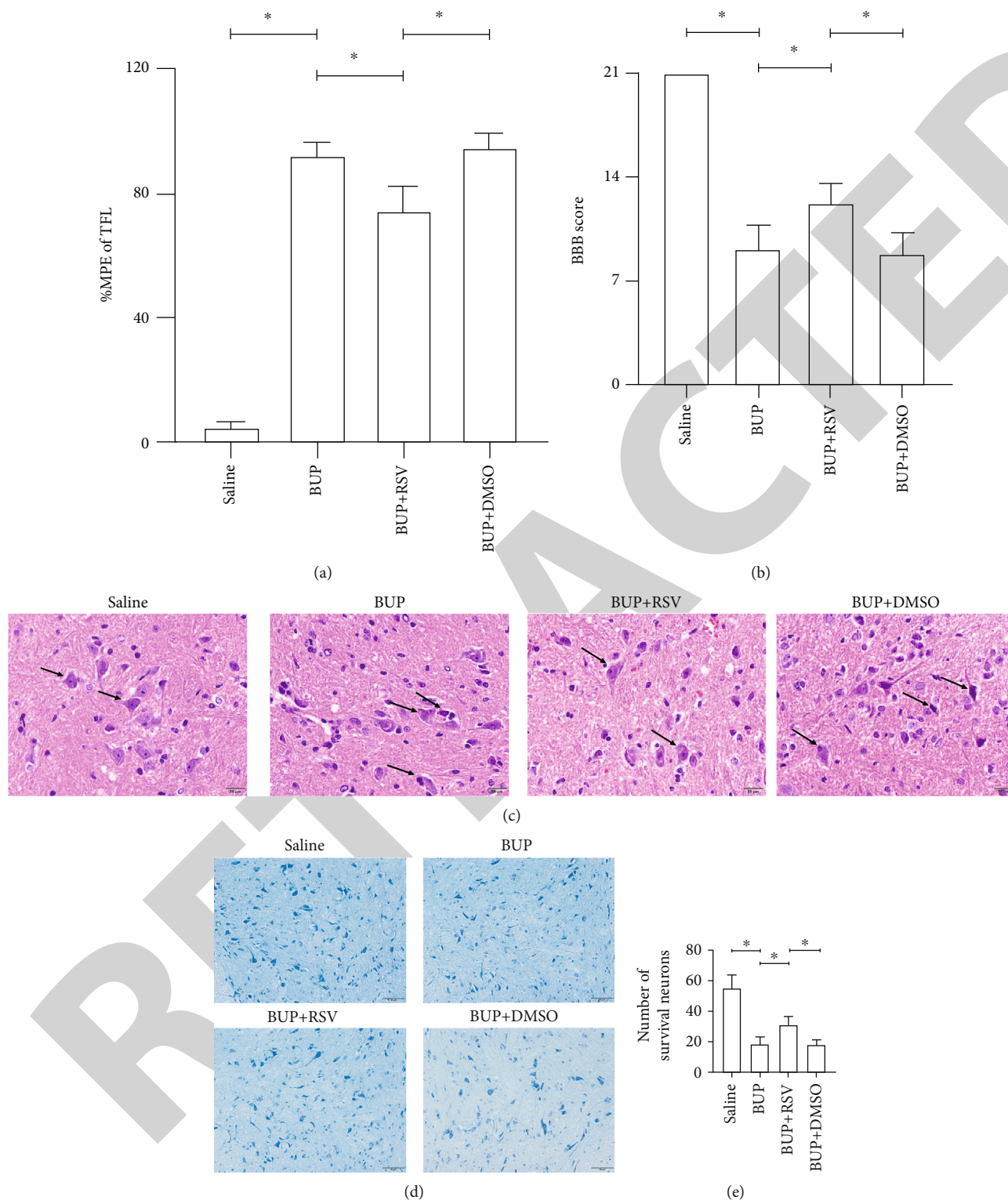


FIGURE 1: RSV attenuated neurological dysfunction induced by bupivacaine. Note: (a) %MPE evaluated tail sensation restoration in each group ( $n = 12$  in each group). (b) BBB scores reflect hindlimb locomotor recovery ( $n = 12$  in each group). (c) H&E staining assessed histological changes (neurons were indicated by the black arrows) (scale bar =  $20 \mu\text{m}$ ). (d) Nissl staining was detected to evaluate survival neurons (scale bar =  $50 \mu\text{m}$ ). (e) Quantitative calculation of the number of survival neurons of each group ( $n = 6$  in each group). Data are presented as mean  $\pm$  SEM. \*  $P < 0.05$ .

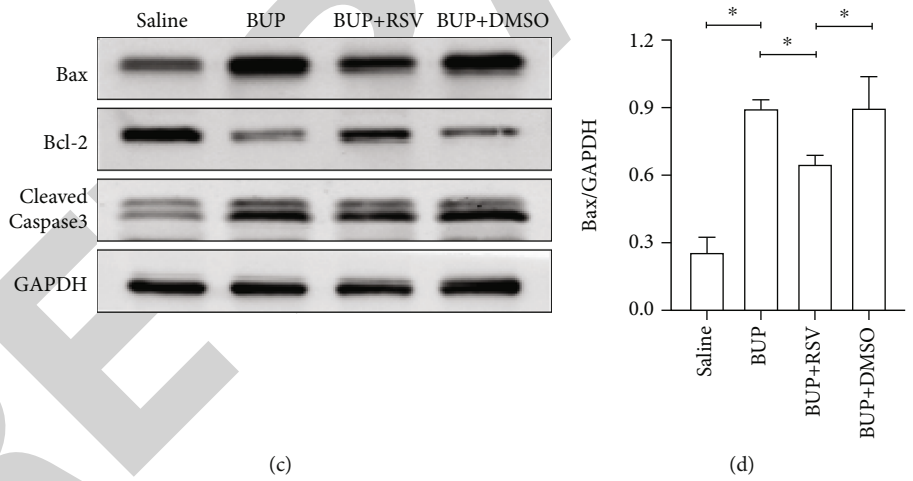
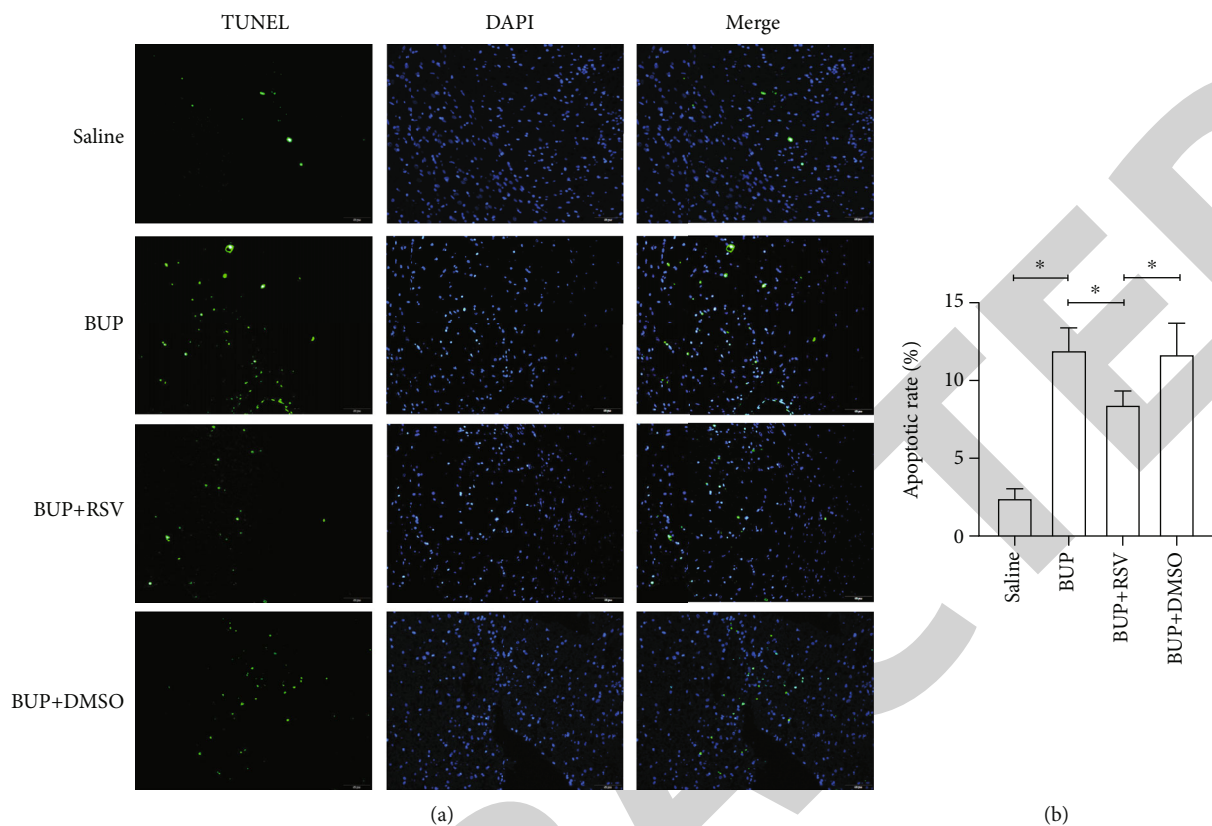


FIGURE 2: Continued.

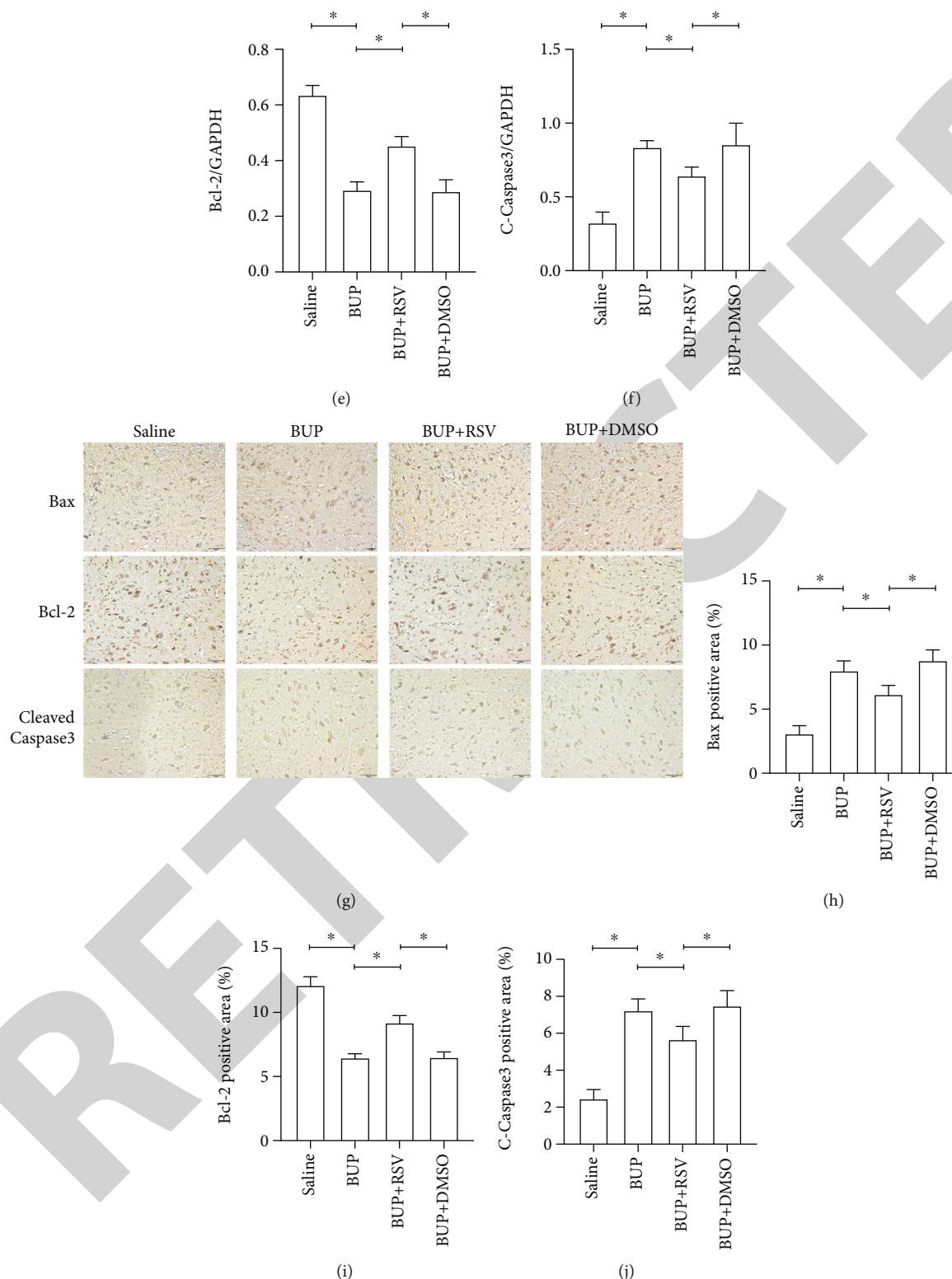
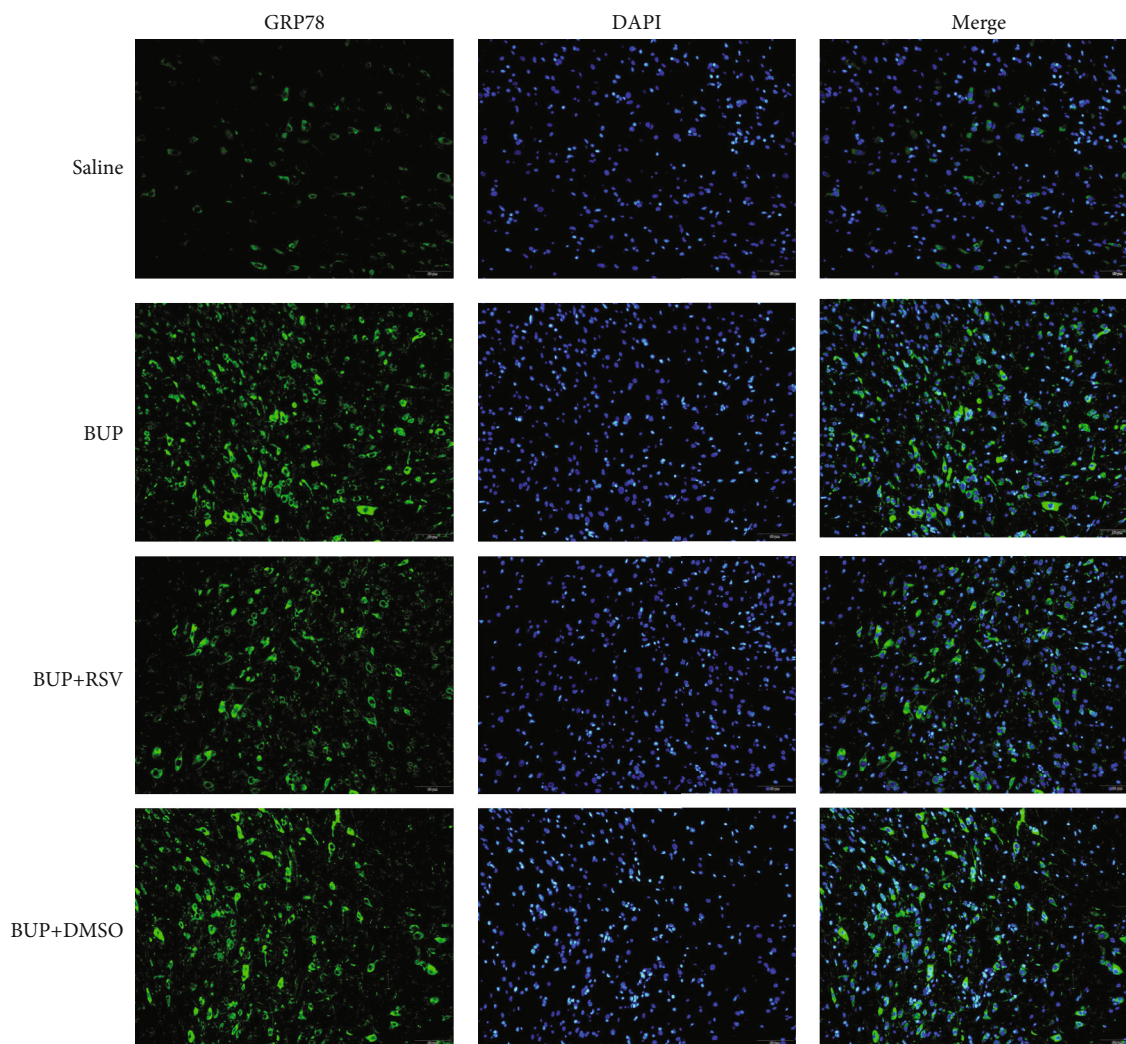
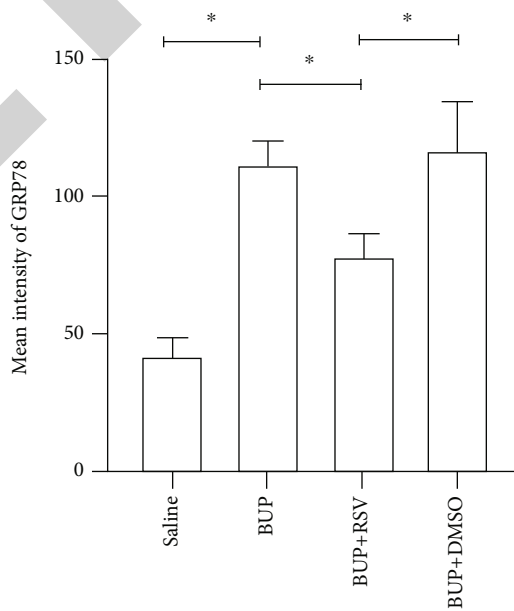


FIGURE 2: RSV suppressed neuronal apoptosis induced by bupivacaine. Note: (a) representative image of TUNEL staining (green) (scale bar = 50  $\mu$ m). (b) Quantitative analysis of TUNEL-positive cells of each group. (c) Western blot images exhibiting apoptosis-related proteins Bax, Bcl2, and Cleaved Caspase3 levels. (d-f) Quantitative analysis of apoptosis-related protein levels of each group. (g) Immunohistochemical staining images exhibiting Bax, Bcl2, and Cleaved Caspase3 protein levels (scale bar = 50  $\mu$ m). (h-j) Quantitative analysis of percentage of Bax, Bcl2, and Cleaved Caspase3 positive area in total area of each group. Data are presented as mean  $\pm$  SEM ( $n = 4$  in each group). \*  $P < 0.05$ .



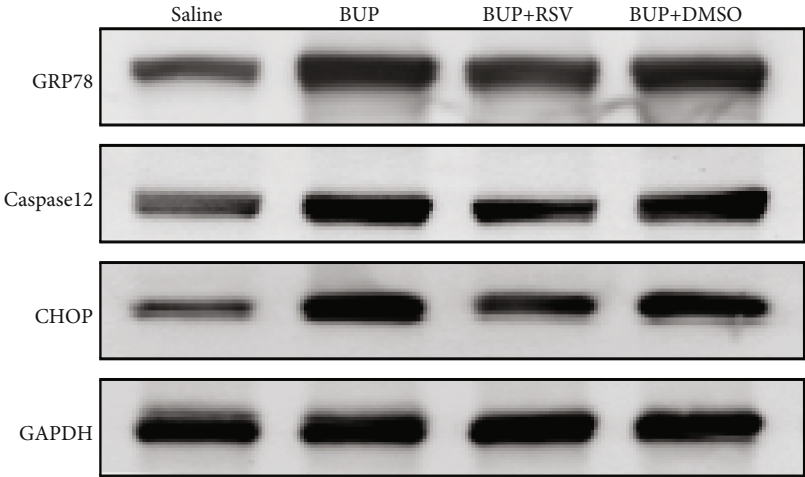
(a)



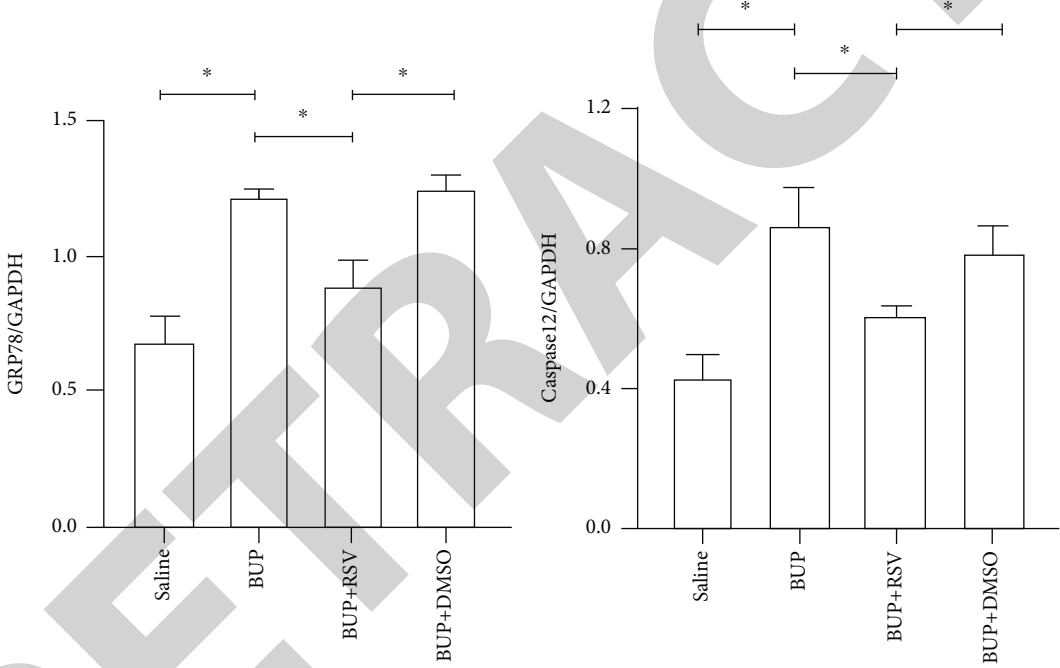
(b)

FIGURE 3: Continued.





(c)



(d)

(e)

FIGURE 3: Continued.

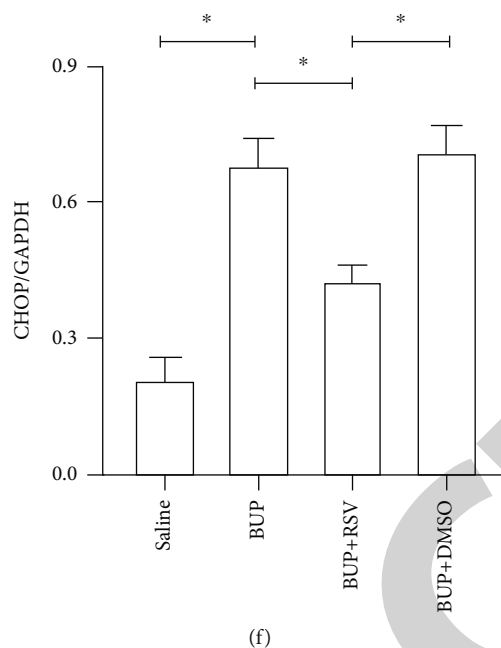


FIGURE 3: RSV alleviated ER stress induced by bupivacaine. Note: (a) representative images of GRP78 immunofluorescence staining (green) (scale bar = 50  $\mu$ m). (b) Quantitative intensity of GRP78 of each group. (c) Western blot images exhibiting ER stress marker protein levels of GRP78, caspase12, and CHOP. (d-f) Quantitative analysis of ER stress marker protein levels of GRP78, caspase12, and CHOP of each group. Data are presented as mean  $\pm$  SEM ( $n = 4$  in each group). \* $P < 0.05$ .

The  $2^{-\Delta\Delta CT}$  method was employed to calculate relative mRNA levels of target genes. The primers used for PCR included: SIRT1: forward 5'-ccgagacaacctctgttg-3' and reverse 5'-attgttcgaggatcggtgcc-3' and GAPDH: forward 5'-gccttcggttctctacc-3' and reverse 5'-cctgcttcaccaccttctt-3'.

**2.9. Western Blot.** Lumbar enlargement spinal cord tissues were collected for western blot analysis as previously described [11]. After protein transfer, membranes were incubated overnight (4°C) with primary antibodies against PERK (1:1000, CST), ATF4 (1:1000, CST), CHOP (1:1000, CST), p-eIF2 $\alpha$  (1:1000, Abcam), eIF2 $\alpha$  (1:1000, Abcam), Caspase12 (1:1000, Abcam), p-PERK (1:1000, Wanleibio), Bcl2 (1:1000, Wanleibio), cleaved Caspase3 (1:1000, Proteintech), GRP78 (1:1000; Proteintech), Bax (1:1000, Proteintech), and GAPDH (1:10000, Proteintech). After washing thrice with TBST, the membranes were incubated with infrared-labeled goat anti-rabbit or goat anti-mouse secondary antibodies (1:10000, Invitrogen) for 1 hour at 4°C. The array image was acquired on a LI-COR Biosciences Odyssey Infrared imaging system (Li-Cor Biosciences, Lincoln, IL, USA), and band pixel intensity was quantified on ImageJ (NIH, Bethesda, MD, USA).

**2.10. Statistical Analysis.** Statistical analyses were performed by SPSS version 25.0 (IBM, Armonk, New York, USA). Data are presented as mean  $\pm$  SEM. One-way ANOVA followed by Tukey's post hoc test was used to analyze differences among groups.  $P < 0.05$  indicates statistically significant.

### 3. Results

**3.1. RSV Improves Hindlimb Locomotor and Tail Sensory Functions in Rats.** Analysis of the effect of RSV against bupivacaine-induced spinal cord neurotoxicity was done using tail-flick latency tests (Figure 1(a)) and the Basso, Beattie, and Bresnahan (BBB) locomotor scale (Figure 1(b)). H&E and Nissl staining were used for histological analysis in lumbar enlargement spinal cord of each group after bupivacaine administration. Compared with the saline group, BBB scores were markedly lower in the BUP and BUP+DMSO groups, while the %MPE was markedly elevated. However, rats in the BUP+RSV group exhibited significantly better hindlimb locomotor and tail sensory function with higher BBB scores and lower %MPE values compared to BUP and BUP+DMSO groups. H&E analysis revealed that neurons were normal in the saline group, with intact axons and deep-dyed nucleoli. However, swelling and atrophy of neurons, axons, and nucleoli disappear, and high levels of glial cell hyperplasia and satellitosis were observed in the dorsal horn of the spinal cord in the BUP and BUP+DMSO groups. Notably, the BUP+RSV group exhibited milder swelling of neurons with visible nucleoli, and axons appeared relatively intact part of neurons, and glial cell hyperplasia was decreased significantly (Figure 1(c)). Nissl staining showed that neuron density decreased by varying degrees in rats after bupivacaine administration (Figure 1(d)). Consistent with the H&E staining results, Nissl staining revealed more surviving neurons in the BUP+RSV group when compared with BUP and BUP+DMSO groups (Figure 1(e)).

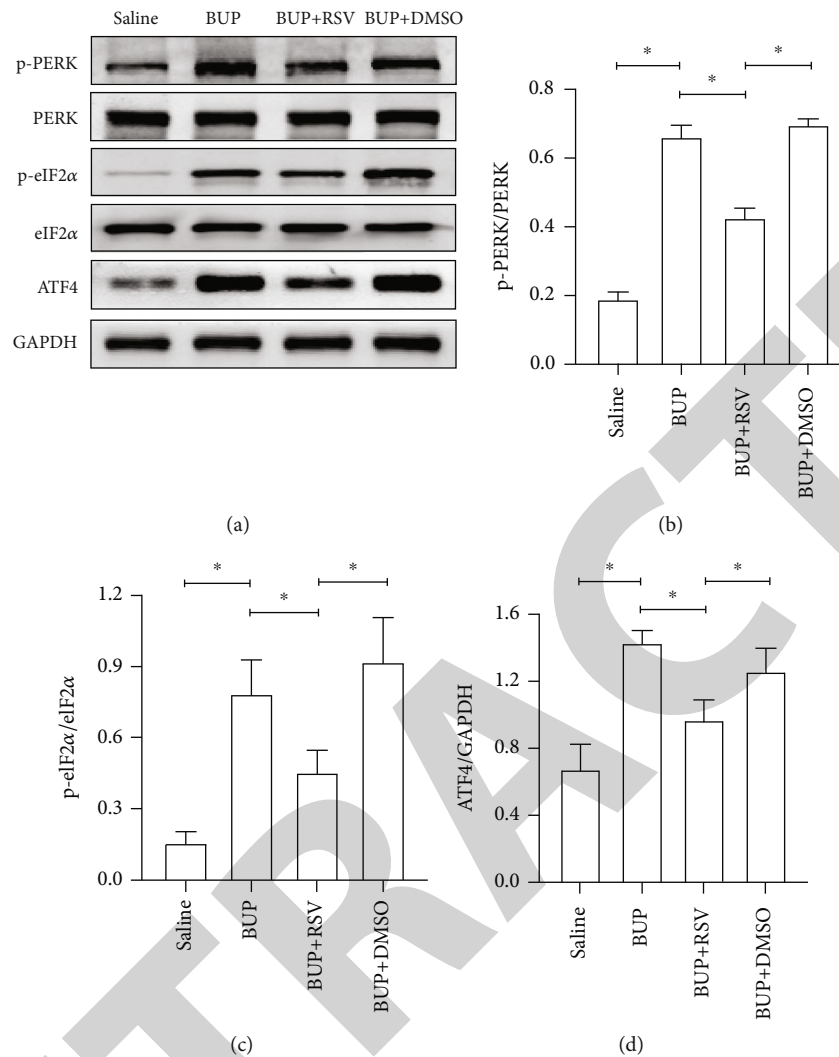


FIGURE 4: RSV inhibited the activation of PERK signaling pathway induced by bupivacaine. Note: (a) western blot images exhibiting PERK signaling protein levels of p-PERK, PERK, p-eIF2α, eIF2α, and ATF4. (b–d) Quantitative analysis of the ratio of p-PERK/PERK and p-eIF2α/eIF2α protein levels and the ATF4 protein levels of each group. Data are presented as mean ± SEM ( $n = 4$  in each group). \* $P < 0.05$ .

### 3.2. RSV Suppressed Bupivacaine-Induced Neuronal Apoptosis.

Next, we assessed if RSV could reduce bupivacaine-induced apoptosis using TUNEL staining (Figure 2(a)). This analysis revealed that when compared with the saline group, the group that received bupivacaine had a significantly higher number of TUNEL-positive cells, while RSV significantly decreased the number of TUNEL-positive neurons (Figure 2(b)). Western blot (Figure 2(c)) and IHC (Figure 2(g)) analyses of the levels of apoptotic factors in rat spinal cord tissues from the four groups (Figure 2(c)) revealed that Cleaved Caspase-3 and Bax were upregulated after bupivacaine administration, while Bcl-2 was markedly downregulated ( $P < 0.05$ ). However, RSV significantly reduced Bax and Cleaved caspase-3 expression while increasing Bcl-2 levels (Figures 2(d)–2(j)).

**3.3. RSV Alleviated ER Stress by Inhibiting PERK/eIF2/ATF4 Pathway Activation.** Based on our preliminary findings that ER stress regulates bupivacaine-induced neurotoxicity, we examined the expression of GRP78 in spinal cord tissue from

different groups using immunofluorescence analyses (Figure 3(a)). Immunofluorescence staining showed that the expression of GRP78 protein (green) significantly increased in the cytoplasm of spinal dorsal horn after bupivacaine administration. However, RSV treatment significantly decreased the expression of GRP78 in spinal dorsal horn (Figure 3(b)). Western blotting (Figure 3(c)) was performed to measure ER stress marker protein levels of GRP78, caspase12, and CHOP in the spinal cord, and the results indicated that bupivacaine upregulated the expression of GRP78, Caspase12, and CHOP in the spinal cord, which was markedly reversed by RSV treatment (Figures 3(d)–3(f)). To further investigate the effect of RSV against bupivacaine-induced ER stress, we assessed PERK/eIF2/ATF4 signaling activity using western blot analysis (Figure 4(a)) and observed that the ratio of p-eIF2α/eIF2α and p-PERK/PERK and the levels of ATF4 were markedly elevated in rats after bupivacaine administration. Notably, these effects were markedly suppressed by RSV (Figures 4(b)–4(d)).

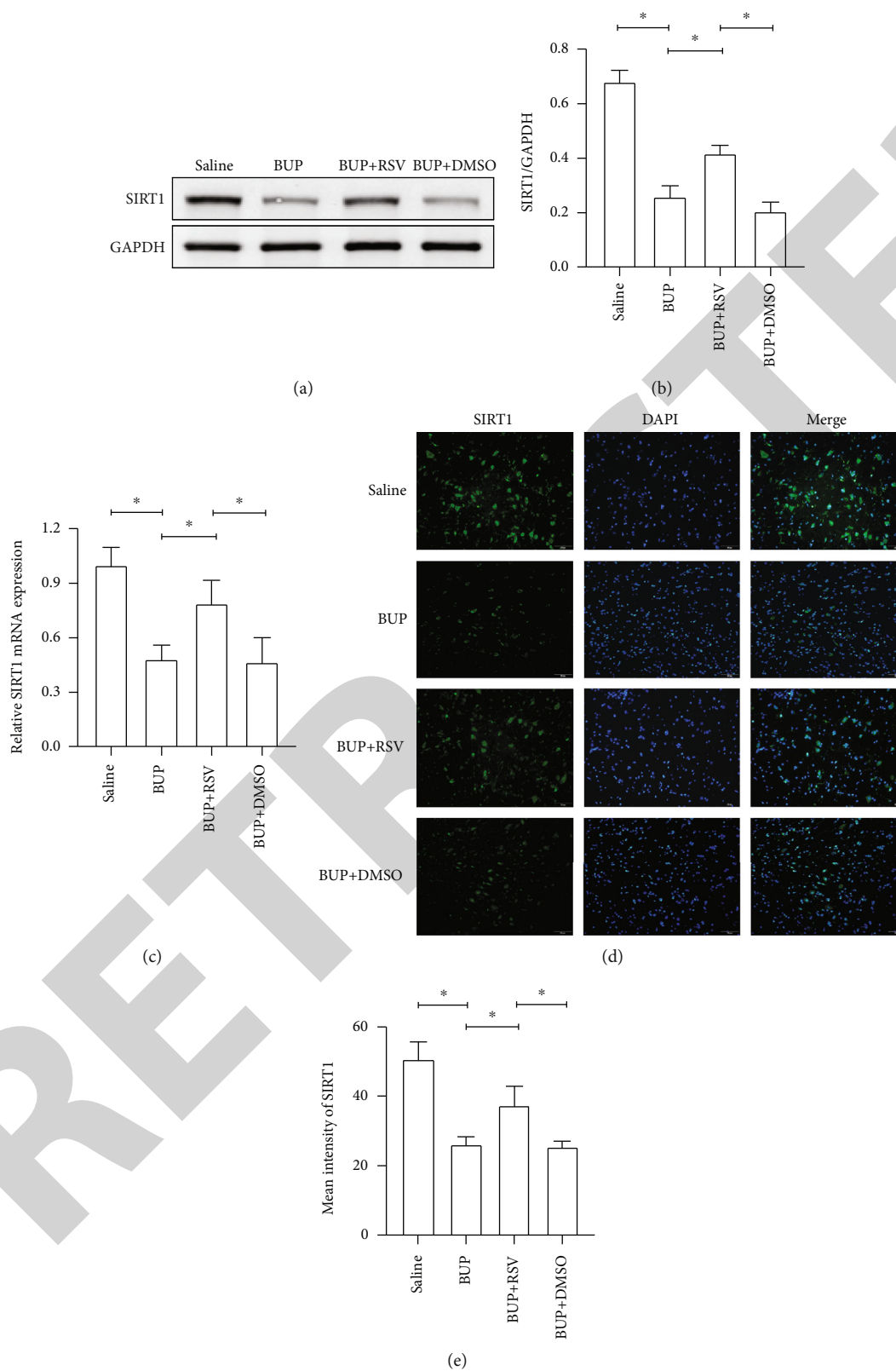


FIGURE 5: RSV rescued the neurotoxicity induced by bupivacaine through upregulating SIRT1. Note: (a) western blot images exhibiting protein levels of SIRT1. (b) Quantitative analysis of protein levels of SIRT1 of each group. (c) Quantitative analysis of the expression of SIRT1 mRNA levels determined by RT-PCR of each group. (d) Representative images of SIRT1 immunofluorescence staining (green) (scale bar = 50  $\mu$ m). (e) Quantitative intensity of SIRT1 of each group. Data are presented as mean  $\pm$  SEM ( $n = 4$  in each group). \* $P < 0.05$ .

**3.4. RSV Rescued the Neurotoxicity Induced by Bupivacaine through Upregulating SIRT1.** We used RT-PCR, western blot, and immunofluorescence to assess SIRT1 expression in the spinal cord. Western blot (Figure 5(a)) and RT-PCR analyses reported that SIRT1 expression was downregulated after bupivacaine administration in the spinal cord while rescued by RSV treatment (Figures 5(b) and 5(c)). Similar results were obtained using immunofluorescence analysis (Figures 5(d) and 5(e)).

## 4. Discussion

We induced spinal cord neurotoxicity in rats using intrathecal injection of 5% bupivacaine, as we previously described [14]. As our preliminary findings revealed that neuronal apoptosis peaked on day 3 after bupivacaine administration, we evaluated the neuroprotective effect, neurological function restoration, and antiapoptotic roles of RSV on day 3 after bupivacaine injection intrathecally [6]. RSV can improve neurological function restoration by alleviating neuronal degeneration, reducing neuronal loss, and mitigating neurological dysfunction. Furthermore, our results indicated that RSV ameliorated bupivacaine-induced ER stress and apoptosis by inhibiting PERK/eIF2 $\alpha$ /ATF4 signaling activation via SIRT1 modulation, indicating that RSV might have a neuroprotective effect against bupivacaine-induced spinal neurotoxicity.

Apoptosis has been associated with bupivacaine-induced neurotoxicity [15]. We have previously reported that bupivacaine induces neurotoxicity by activating apoptosis via the mitochondrial pathway in mouse neuroblastoma cells [16]. Previous studies have reported that regulating pro- and antiapoptotic protein levels suppresses bupivacaine-induced neuronal apoptosis [17]. Here, we found that RSV alleviated histological damages of spinal cord neurons in rats after bupivacaine administration. Additionally, we also observed that RSV decreased the number of TUNEL-positive neurons and altered levels of pro- and antiapoptotic proteins. Our results show that RSV decreases the protein levels of Bax and cleaved Caspase-3 while increasing Bcl-2 expression. These findings indicate that RSV attenuated bupivacaine-induced neurotoxicity by inhibiting apoptosis.

Previous studies have implicated ER stress involved in neuronal apoptosis after spinal cord injury (SCI) [18]. We show that the protein levels of the ERS markers, GRP78, Caspase12, and CHOP were significantly increased after bupivacaine administration and downregulated by RSV, which is consistent with previous findings that RSV suppressed tunicamycin-induced ER stress in a mouse model of steatohepatitis [19]. Ample evidence suggests that the PERK/eIF2 $\alpha$ /ATF4 signaling pathway modulates ER stress-triggered apoptosis [20, 21]. Meng et al. reported that PERK pathway activation aggravated secondary brain injury during intracerebral hemorrhage by triggering neuronal apoptosis, while inhibition of the PERK signaling pathway promoted neuronal survival and improved neurological function [22]. In the present study, we find that bupivacaine activated the PERK/eIF2 $\alpha$ /ATF4 signaling pathway, as revealed by increased protein levels of p-PERK, p-eIF2 $\alpha$ ,

and ATF4 in the spinal cord after bupivacaine administration, while RSV downregulated the expression of these factors. These data indicate that RSV treatment mitigated bupivacaine-triggered ERS via a mechanism involving PERK/eIF2 $\alpha$ /ATF4 pathway inhibition.

Mounting evidence shows that SIRT1 deficiency is associated with apoptosis, oxidative stress, inflammation, and autophagy in chronic morphine tolerance, SCI, spinal cord ischemia-reperfusion injury, and neuropathic pain [23–26]. RSV, a SIRT1 agonist, is reported to exert neuroprotection by upregulating and activating SIRT1 [27]. He et al. reported that RSV attenuates morphine antinociceptive tolerance by regulating spinal cord SIRT1 activity in rats [25]. Furthermore, Zheng et al. found that lidocaine downregulates SIRT1 expression and that increasing SIRT1 protein levels significantly reversed lidocaine-induced neuronal apoptosis [28]. Here, we examined the effect of bupivacaine on spinal cord SIRT1 levels in rats and confirmed that it downregulates SIRT1 levels. Recent studies have shown that SIRT1 alleviates ER stress by inhibiting PERK signaling pathway activation [29]. To further study the upstream regulatory mechanism of the PERK/eIF2 $\alpha$ /ATF4 signaling pathway in neurotoxicity induced by bupivacaine, we hypothesized that there is a link between SIRT1 downregulation and PERK signaling pathway activation during bupivacaine-induced neurotoxicity. Our findings show that RSV rescued SIRT1 downregulation, which was accompanied by suppressed PERK/eIF2 $\alpha$ /ATF4 pathway activation. These findings are consistent with those of another study that showed that terpinen-4-ol ameliorates ER stress-triggered vascular calcification by inhibiting the PERK-eIF2 $\alpha$ -ATF4 axis via increasing SIRT1 protein levels [30]. Prola et al. found that SIRT1 alleviated ER stress-triggered apoptosis via inhibiting the PERK/eIF2 $\alpha$  axis [31]. Together, these findings indicate that RSV ameliorates bupivacaine-induced spinal neurotoxicity via SIRT1-mediated PERK/eIF2 $\alpha$ /ATF4 pathway activation.

## 5. Conclusion

In summary, our findings suggest that RSV inhibits ER stress, reduces neuronal apoptosis, and alleviates bupivacaine-induced spinal neurotoxicity by upregulating SIRT1 expression and suppressing PERK/eIF2 $\alpha$ /ATF4 pathway activation. These observations highlight a potential novel therapeutic strategy for the treatment of bupivacaine-induced spinal neurotoxicity.

## Abbreviations

BUP:	Bupivacaine
BBB:	Basso, Beattie, and Bresnahan
ER stress:	Endoplasmic reticulum stress
MPE:	Maximal possible effect
RSV:	Resveratrol
SCI:	Spinal cord injury
TFL:	Tail-flick latency
PERK:	PKR-like ER kinase
eIF2 $\alpha$ :	Eukaryotic translation initiation factor 2 alpha

ATF4: Activating transcription factor 4  
 GRP78: Glucose-regulated protein 78  
 CHOP: C/EBP-homologous protein.

## Data Availability

All data generated or analyzed during this study are included in this published article, and supporting data can be obtained from the corresponding author upon reasonable request.

## Ethical Approval

This study was approved by the Animal Care and Use Committee of Guangxi Medical University (No. SYXK GUI 2020-0004), and all experimental protocols adhered to National Institutes of Health guidelines for the Care and Use of Laboratory Animals (No. 8023, revised in 1978). The study was carried out in compliance with the ARRIVE guidelines. All methods are reported in accordance with ARRIVE guidelines (<https://arriveguidelines.org>) for the reporting of animal experiments.

## Conflicts of Interest

The authors declare that they have no competing interests.

## Authors' Contributions

Yunpeng Luo was assigned in investigation, conceptualization, and writing—original draft. Yang Zhao worked on data curation, software, and visualization. Jian Lai worked on investigation, data curation, and validation. Liling Wei was assigned in investigation, data curation, and validation. Gang Zhou worked on data curation, validation, and software. Yue Yu was assigned in investigation and data curation. Jingchen Liu was assigned in project administration, conceptualization, writing-review and editing, visualization, and validation. All authors have read and agreed to the published version of the manuscript. Yunpeng Luo and Yang Zhao contributed equally to this work and share co-first authorship.

## Acknowledgments

This research was funded by the Innovation Project of Guangxi Graduate Education (YCBZ2022091 and YCSW2022208).

## References

- [1] X. Chen, Z. Xu, R. Lin, and Z. Liu, "Persistent cauda equina syndrome after cesarean section under combined spinal-epidural anesthesia: a case report," *Journal of Clinical Anesthesia*, vol. 27, no. 6, pp. 520–523, 2015.
- [2] N. M. Dunne and W. J. Kox, "Neurological complications following the use of continuous extradural analgesia with bupivacaine," *British Journal of Anaesthesia*, vol. 66, no. 5, pp. 617–619, 1991.
- [3] L. Markova, N. Umek, S. Horvat et al., "Neurotoxicity of bupivacaine and liposome bupivacaine after sciatic nerve block in healthy and streptozotocin-induced diabetic mice," *BMC Veterinary Research*, vol. 16, no. 1, p. 247, 2020.
- [4] R. Ghemrawi and M. Khair, "Endoplasmic reticulum stress and unfolded protein response in neurodegenerative diseases," *International Journal of Molecular Sciences*, vol. 21, no. 17, p. 6127, 2020.
- [5] N. T. Sprenkle, S. G. Sims, C. L. Sanchez, and G. P. Meares, "Endoplasmic reticulum stress and inflammation in the central nervous system," *Molecular Neurodegeneration*, vol. 12, no. 1, p. 42, 2017.
- [6] B. Liu, J. Ji, Q. Feng et al., "Monosialoganglioside protects against bupivacaine-induced neurotoxicity caused by endoplasmic reticulum stress in rats," *Drug Design, Development and Therapy*, vol. 13, pp. 707–718, 2019.
- [7] K. Vannuvel, P. Renard, M. Raes, and T. Arnould, "Functional and morphological impact of ER stress on mitochondria," *Journal of Cellular Physiology*, vol. 228, no. 9, pp. 1802–1818, 2013.
- [8] Y. Lou, Z. Wang, Y. Xu et al., "Resveratrol prevents doxorubicin-induced cardiotoxicity in H9c2 cells through the inhibition of endoplasmic reticulum stress and the activation of the Sirt1 pathway," *International Journal of Molecular Medicine*, vol. 36, no. 3, pp. 873–880, 2015.
- [9] A. Singh, A. K. Yadawa, S. Chaturvedi, M. Wahajuddin, A. Mishra, and S. Singh, "Mechanism for anti-Parkinsonian effect of resveratrol: involvement of transporters, synaptic proteins, dendrite arborization, biochemical alterations, ER stress and apoptosis," *Food and Chemical Toxicology*, vol. 155, article 112433, 2021.
- [10] K. T. Howitz, K. J. Bitterman, H. Y. Cohen et al., "Small molecule activators of sirtuins extend *Saccharomyces cerevisiae* lifespan," *Nature*, vol. 425, no. 6954, pp. 191–196, 2003.
- [11] J. Lai, J. M. Ji, M. Y. Chen et al., "Melatonin ameliorates bupivacaine-induced spinal neurotoxicity in rats by suppressing neuronal NLRP3 inflammasome activation," *Neuroscience Letters*, vol. 772, article 136472, 2022.
- [12] Q. Yin, F. F. Lu, Y. Zhao et al., "Resveratrol facilitates pain attenuation in a rat model of neuropathic pain through the activation of spinal Sirt1," *Regional Anesthesia and Pain Medicine*, vol. 38, no. 2, pp. 93–99, 2013.
- [13] D. M. Basso, M. S. Beattie, and J. C. Bresnahan, "A sensitive and reliable locomotor rating scale for open field testing in rats," *Journal of Neurotrauma*, vol. 12, no. 1, pp. 1–21, 1995.
- [14] J. Ji, X. Yan, Z. Li, Z. Lai, and J. Liu, "Therapeutic effects of intrathecal versus intravenous monosialoganglioside against bupivacaine-induced spinal neurotoxicity in rats," *Biomedicine & Pharmacotherapy*, vol. 69, pp. 311–316, 2015.
- [15] L. Zhang, L. Zhang, and F. Guo, "MiRNA-494-3p regulates bupivacaine-induced neurotoxicity by the CDK6-PI3K/AKT signaling," *Neurotoxicity Research*, vol. 39, no. 6, pp. 2007–2017, 2021.
- [16] Y. Liang, J. Ji, Y. Lin, Y. He, and J. Liu, "The ganglioside GM-1 inhibits bupivacaine-induced neurotoxicity in mouse neuroblastoma Neuro2a cells," *Cell Biochemistry and Function*, vol. 34, no. 6, pp. 455–462, 2016.
- [17] T. Wang, L. Zheng, and W. Zhang, "Hesperidin alleviates bupivacaine anesthesia-induced neurotoxicity in SH-SY5Y cells by regulating apoptosis and oxidative damage," *Journal of Biochemical and Molecular Toxicology*, vol. 35, no. 7, article e22787, 2021.

## Retraction

# Retracted: Phyto-Extract-Mediated Synthesis of Silver Nanoparticles (AgNPs) and Their Biological Activities

### BioMed Research International

Received 8 January 2024; Accepted 8 January 2024; Published 9 January 2024

Copyright © 2024 BioMed Research International. This is an open access article distributed under the Creative Commons Attribution License, which permits unrestricted use, distribution, and reproduction in any medium, provided the original work is properly cited.

This article has been retracted by Hindawi following an investigation undertaken by the publisher [1]. This investigation has uncovered evidence of one or more of the following indicators of systematic manipulation of the publication process:

- (1) Discrepancies in scope
- (2) Discrepancies in the description of the research reported
- (3) Discrepancies between the availability of data and the research described
- (4) Inappropriate citations
- (5) Incoherent, meaningless and/or irrelevant content included in the article
- (6) Manipulated or compromised peer review

The presence of these indicators undermines our confidence in the integrity of the article's content and we cannot, therefore, vouch for its reliability. Please note that this notice is intended solely to alert readers that the content of this article is unreliable. We have not investigated whether authors were aware of or involved in the systematic manipulation of the publication process.

Wiley and Hindawi regrets that the usual quality checks did not identify these issues before publication and have since put additional measures in place to safeguard research integrity.

We wish to credit our own Research Integrity and Research Publishing teams and anonymous and named external researchers and research integrity experts for contributing to this investigation.



The corresponding author, as the representative of all authors, has been given the opportunity to register their agreement or disagreement to this retraction. We have kept a record of any response received.

### References

- [1] M. Adnan, A. Akbar, S. Mussarat et al., "Phyto-Extract-Mediated Synthesis of Silver Nanoparticles (AgNPs) and Their Biological Activities," *BioMed Research International*, vol. 2022, Article ID 9845022, 10 pages, 2022.

## Research Article

# Phyto-Extract-Mediated Synthesis of Silver Nanoparticles (AgNPs) and Their Biological Activities

Muhammad Adnan <sup>1</sup>, Asma Akbar,<sup>1</sup> Sakina Mussarat <sup>1</sup>, Waheed Murad,<sup>2</sup> Ishaq Hameed,<sup>3</sup> Shaheen Begum,<sup>4</sup> Ruqia Nazir,<sup>5</sup> Nawab Ali,<sup>6</sup> Essam A. Ali,<sup>7</sup> Ahmed Bari,<sup>7</sup> Muhammad Abdul Aziz,<sup>8</sup> and Shahid Niaz Khan<sup>9</sup>

<sup>1</sup>Department of Botany, Kohat University of Science and Technology, Kohat 26000, Pakistan

<sup>2</sup>Department of Botany, Abdul Wali Khan University Mardan, Pakistan

<sup>3</sup>Department of Botany, University of Chitral, Chitral 17200, Pakistan

<sup>4</sup>Department of Environmental Sciences, Fatima Jinnah Women University, Rawalpindi, Pakistan

<sup>5</sup>Department of Chemistry, Kohat University of Science and Technology, Kohat 26000, Pakistan

<sup>6</sup>Department of Biotechnology and Genetic Engineering, Kohat University of Science and Technology, Kohat 26000, Pakistan

<sup>7</sup>Department of Pharmaceutical Chemistry, College of Pharmacy, King Saud University, Riyadh 11451, Saudi Arabia

<sup>8</sup>Department of Environmental Sciences, Information and Statistics, Ca Foscari University of Venice, Vio Tornio 155, 30172 Venezia, Italy

<sup>9</sup>Department of Zoology, Kohat University of Science and Technology, Kohat 26000, Pakistan

Correspondence should be addressed to Sakina Mussarat; [sakinamussarat78@yahoo.com](mailto:sakinamussarat78@yahoo.com)

Received 2 August 2022; Accepted 7 October 2022; Published 16 November 2022

Academic Editor: Wilson Aruni

Copyright © 2022 Muhammad Adnan et al. This is an open access article distributed under the Creative Commons Attribution License, which permits unrestricted use, distribution, and reproduction in any medium, provided the original work is properly cited.

**Background.** Nanotechnology finds broad applications in the field of nanomedicine, an emerging new field used for diagnosis, treatment, prevention of diseases, and improvement of health. **Objectives.** To synthesize silver nanoparticles (AgNPs) from *Withania somnifera* and *Fagonia indica* and to carry out their antimicrobial, insecticidal, and phytotoxic activities, a step toward the new range of nanomedicines. **Methods.** Silver nanoparticles were synthesized from *Withania somnifera* and *Fagonia indica* by chemical reduction method, and further biological activities of these nanoparticles were compared with crude methanolic extract, prepared through cold maceration process, at the concentration of 50 mg/ml. **Results.** Among all tested bacterial pathogens, crude extract of *W. somnifera* showed a statistically high significant inhibition zone in millimeter against *Pseudomonas aeruginosa* (21;  $p < 0.01$ ). AgNPs showed highly significant result against *Streptococcus pneumonia* (14;  $p < 0.01$ ). In comparison with crude extracts, AgNPs showed statistically significant ( $p < 0.01$ ) results against *S. pneumonia* (AgNPs, 14; crude, 8.33 mm). Crude extract showed significant inhibition zone against two bacterial strains, *P. aeruginosa* (crude, 21; AgNPs, 11.67 mm) and *Klebsiella pneumoniae* (crude, 11.33; AgNPs, 8 mm). Crude extracts of *F. indica* showed the significant activity against *Vibrio cholera* ( $p < 0.01$ ; 11.33 mm). Silver nanoparticles of *F. indica* exhibited the highest significant activity against *Aspergillus flavus* and *Fusarium oxysporum* while AgNPs of *W. somnifera* were active only against *A. flavus*. Extracts of *W. somnifera* and *F. indica* showed increasing phytotoxic activity with increasing concentrations. The highest significant inhibition was obtained for crude extract (46.7) and AgNPs (45.7) of *F. indica* at 1000 µg/ml. Insecticidal activity of crude and AgNPs of both plants showed significant inhibition against all tested insects with increasing time intervals, and the highest significant result was obtained at 72 hours with a value of  $p < 0.01$  except *T. castaneum*. **Conclusions.** Both crude and AgNPs showed potent activity; however, in comparison, silver nanoparticles showed slightly enhanced activity. Crude and AgNPs of both plants showed good phytotoxic and insecticidal inhibition. Antimicrobial studies of AgNPs on diseases causing pathogens open a door for new antimicrobial agents and could be the answer to antibiotic resistance after further analysis.



## 1. Introduction

Plants used as medicines to treat different diseases are a rich source of various bioactive components like volatile tannins, oils, alkaloids, flavonoids, and phenols which have a prominent role in the discovery of new drugs to treat infectious diseases. Many scientists have isolated and characterized different pharmacologically dynamic compounds from traditionally used medicinal plants. With the progress of drug development, there is a need to utilize advanced technology such as nanotechnology which has tremendous application in the pharmaceutical industries [1]. Nanotechnology finds broad applications in the field of nanomedicine, an emerging new field used for diagnosis, treatment, prevention of diseases, and improvement of health. Due to specific characteristics of nanoparticles such as small size, distribution, and morphology, these have new applications and properties. Nanoparticles can be synthesized by different methods like chemical and photochemical reactions [2], thermal decomposition [3], and microwave assisted process [4] and also by biological methods [5, 6]. Both in the medical and industrial processes, silver has a good inhibitory effect on microbes, and silver nanoparticles have applications in the medical industry such as in topical ointments to prevent infection of burn and wounds as well as prevent bacterial contamination in humans [7]. Nowadays, silver nanoparticles (AgNPs) have interesting antibacterial activities and have played a crucial role in inhibiting bacterial growth in aqueous and solid media [8, 9] and may be an answer to bacterial resistance, caused by the overuse of antibiotics. *Withania somnifera* (L.) Dunal (Solanaceae), a commonly used plant in traditional and Ayurvedic medicine, has withanolide-type active compounds and is widely used in crude form throughout the world due to its nontoxic and high medicinal value. Nowadays, this plant is cultivated as a crop to support the high demand for biomass and fulfill the needs of pharmaceutical industry. Similarly, *Fagonia indica* Burm.f. (*Zygophyllum indicum* (Burm.f.) Christenh. & Byng) is a small spiny herb widely used in Ayurvedic medicine belonging to Zygophyllaceae having analgesic, antimicrobial, febrifuge, and anti-inflammatory properties with active phytoconstituents [10]. The present study has been designed to synthesize AgNPs by using *W. somnifera* and *F. indica* extract and to carry out the antimicrobial, insecticidal, and phytotoxic activities and their comparison with the crude extract, a step toward the new range of antimicrobial agents in the field of nanomedicine.

## 2. Materials and Methods

**2.1. Collection and Formulation of Plant Extracts.** *F. indica* and *W. somnifera* were collected from Karak and Kohat, identified by the taxonomist at the Department of Botany, Kohat University of Science and Technology, Kohat. Collected plant parts were washed, dried in shade, powdered, and stored in airtight bottles. The crude methanolic extract was prepared through cold maceration extraction technique and further used for biological activities.

**2.2. Synthesis of Silver Nanoparticles (AgNPs).** Chemical reduction method was used to synthesize the silver nanoparticles (AgNPs) of *F. indica* and *W. somnifera* [11]. 1 ml of silver nitrate solution was diluted; then, 100 g of both plant extracts was dissolved in 100 ml of deionized water. Both the plant extracts and silver nitrate solution were mixed in 1:1 in a beaker. A homogeneous solution was obtained when this mixture was stirred and placed on a hot plate. After that, a reducing agent Sodium Borohydrate ( $\text{NaBH}_4$ ) was added dropwise through a burette with a constant stirring. The formation of silver nanoparticles was finished when the solution color was changed from light brown to dark.

**2.3. Antibacterial Assay.** Eight bacterial strains *Escherichia coli*, *Salmonella typhimurium*, *Shigella flexneri*, *Proteus mirabilis*, *Streptococcus pneumoniae*, *Pseudomonas aeruginosa*, *Vibrio cholera*, and *Klebsiella pneumoniae* and all the ATCC cultures except *S. flexneri* and *V. cholera* that were hospital-acquired clinical isolates were obtained from the laboratory of Department of Microbiology, and antibacterial activities were determined by Agar Well diffusion method [12] at 50 mg/ml concentration. Dimethyl sulfoxide (DMSO) was used as negative control while ampicillin as a positive control. Experiments were repeated three times, and average zones of inhibition were recorded.

**2.4. Antifungal Assay.** Two fungal strains *Aspergillus flavus* and *Fusarium oxysporum* were obtained from the laboratory of Department of Microbiology. Test tube dilution method, with slight modification, was followed to check the antifungal activities [13], and 6.5 g of Sabouraud Dextrose Agar (SDA) was mixed in 100 ml of distilled water and autoclaved, and 9 ml of this mixture was taken in a test tube. Every test tube was loaded with 1 ml of extract solutions before solidifying. The tubes were inoculated with a 4 mm diameter piece of the fungal pathogen, allowed to solidify, and placed in a slanting position in an incubator at 28°C for 7 days. Miconazole was used as a positive control to compare the antifungal activity. The inhibition zone was measured in millimeter.

**2.5. Phytotoxic Activity.** Phytotoxic activity was carried out against *Lemna minor* [14]. E-medium was prepared and autoclaved at 15 psi, 121°C for 15 minutes. Each plant extract of 30 mg (crude and silver nanoparticles) was then dissolved in methanol (1.0 ml) which served as a stock solution. Seven petri dishes were autoclaved, and 20 ml medium on each plate and 60 ml of plant extract having one frond of *Lemna minor* were added. Paraquat was used as a negative control, and plates were placed in a growth cabinet; the number of fronds per plate was counted and recorded, and the experiment was repeated three times.

**2.6. Insecticidal Activity.** *Rhyzopertha dominica*, *Sitophilus oryzae*, *Callosobruchus analis*, and *Tribolium castaneum* were selected for the present study. Filter papers of 9 cm or 90 mm were cut out and put out on the plate. Plant extract (50 mg/ml) was poured over the filter papers, and then, these plates were left for almost one day. 10 healthy insects of equal size/age were put out on the second day of each species

in each plate and were incubated at 27°C. Permethrin was used as a positive control. The results were noted after 24 hours, 48 hours, and 72 hours, respectively. Experiments were repeated three times.

**2.7. Statistical Analysis.** Data were organized and analyzed using Microsoft Word and Microsoft Excel software. All the experiments were repeated, and the average zone of inhibition and standard deviations were calculated by using Microsoft Excel software 2007. Significant values of all activities were found by using one-way ANOVA and *t*-test.

### 3. Results

**3.1. Antibacterial Effect of Crude Extracts and Silver Nanoparticles.** Among all tested bacterial pathogens, crude extract of *W. somnifera* showed highly significant inhibition against *P. aeruginosa* (21;  $p < 0.01$ ), followed by *S. flexneri* (12.33 mm) and *K. pneumoniae* (11.33 mm). The lowest inhibitory activity was measured for the *S. typhimurium* (5 mm). The tested antibiotic is sensitive to this bacterium (25 mm). AgNPs also showed highly significant results against *S. pneumonia* (14;  $p < 0.01$ ), followed by *P. mirabilis* (11.67 mm) and *P. aeruginosa* (11.67 mm) (Table 1). The lowest inhibition zone was measured for *S. typhimurium* (6.33 mm) as compared to the antibiotic inhibitory zone (25 mm). In the comparison of both extracts, AgNPs showed statistically highly significant ( $p < 0.01$ ) results against *S. pneumonia* (AgNPs, 14; crude, 8.33 mm). Crude extract showed significant inhibition against two bacterial strains, *P. aeruginosa* (crude, 21; AgNPs, 11.67 mm) and *K. pneumonia* (crude, 11.33; AgNPs, 8 mm) (Table 1).

Crude extracts of *F. indica* showed the highest significant inhibition zone at  $p < 0.01$  for *Vibrio cholera* (11.33 mm) followed by *S. pneumonia* (10.33 mm). The lowest inhibition zone was measured for the *E. coli* (7.00 mm). Similarly, AgNPs showed an inhibition zone ranging from 8.00 to 11.67 mm. The highest significant inhibition zone at  $p < 0.01$  was measured for *S. flexneri* (11.67 mm) and *V. cholera* (11.67 mm) followed by *P. aeruginosa* (10.33 mm) and *E. coli* (10 mm) as compared to the antibiotic activity of 26 mm, 21 mm, 20 mm, and 22 mm, respectively.

**3.2. Antifungal Activity of Crude Extracts and Silver Nanoparticles.** AgNPs of *W. somnifera* exhibited the highest significant antifungal activity as compared to crude extract against *A. flavus* (12;  $p < 0.01$ ). AgNPs of *F. indica* also showed statistically significant inhibition as compared to crude extract against both tested fungal strains (Table 2).

**3.3. Phytotoxic Activity of Crude Extracts and Silver Nanoparticles.** Phytotoxic activity of both plants showed increasing inhibition with the increasing concentration against the growth of the *Lemna minor*. Both extracts of *W. somnifera* crude and silver nanoparticles displayed the most important spectrum of activity, at the highest concentration 1000 µg/ml, and silver nanoparticles, which is a non-significant value.

Statistically, all the treatments of *F. indica* are highly significant at the highest concentration of 1000 µg/ml among

crude and silver nanoparticles, individually (Table 3). The highest significant inhibition value (46.7) has been obtained on 1000 µg/ml for the crude extract of *F. indica*. The highest significant value (45.7) has been obtained on treatment supplemented by silver nanoparticles at 1000 µg/ml concentration. Overall, crude extract showed slightly enhanced activity but the comparison was nonsignificant.

**3.4. Insecticidal Activity of Crude Extracts and Silver Nanoparticles.** Crude extracts and AgNPs of *W. somnifera* were evaluated against the insects including *R. dominica*, *S. oryzae*, *C. analis*, and *T. castaneum* with different time intervals (24, 48, and 72 hours); significant differences were observed for both crude and AgNP treatment. Crude extract of *W. somnifera* showed significant inhibition against all tested insects with increasing time intervals while AgNPs showed significant inhibition against *S. oryzae* and *C. analis* (Figure 1). Crude extract and AgNPs of *F. indica* showed the highest significant value at 72 hrs (4.33 inhibition of insects) ( $p < 0.01$ ) for all tested insects except *T. castaneum* (Figure 2).

### 4. Discussion

In the present study, both the crude and AgNP extracts of both selected plants, *W. somnifera* and *F. indica*, showed good inhibition against the bacterial, fungal, insecticidal, and phytotoxic activity. However, AgNPs showed slightly more inhibition against bacterial and fungal strains than crude extract. AgNPs synthesized from *W. somnifera* has a good antimicrobial effect against gram-positive, gram-negative, and fungal pathogens by breaking out the cell membrane of bacteria, as confirmed by SEM analysis [15]. These AgNPs are small, easily penetrate the cell, and target the disease site as well as damage the cellular structure of pathogenic microbes. AgNPs from the same family, Solanaceae, also showed effective antimicrobial activity against gram-negative bacteria [16]. A group of monomeric glycoproteins, namely, WSG (*Withania somnifera* glycoprotein), isolated from *W. somnifera* roots tuber exposed the antimicrobial activities against bacterial and fungal isolates, and it is reported that nanoparticles encased with phytoconstituents can be more effective [17]. A study conducted by Mallesh and Satish [18] investigated that *W. somnifera* extracts of methanol depicted significant antimicrobial activities against a group of bacteria. DNA replication weakening and inactivation proteins are the mechanisms behind the antimicrobial activity of metallic nanoparticles [19].

Antimicrobial approach for the AgNPs is due to the discharge of silver ions (Ag<sup>-</sup>) in the cells and attached bioactive constituents [20]. Govindaraju et al. [21] reported antimicrobial activity of synthesized silver nanoparticles against *P. aeruginosa*, *S. aureus*, *A. flavus*, and *A. niger*. Mechanisms involved are changing in cell membrane permeability [22], generation of a group of free radicals that are responsible for the cell membrane damage [23], and indulgence of the single proton (H<sup>+</sup>) attractive force responsible for the damage of the cell membrane [24], but the exact procedure has not been fully explained. Moreover, the effect of silver

TABLE 1: Antibacterial zone of inhibition (mm) of crude and silver nanoparticles' extracts of *W. somnifera* and *F. indica* at 50 mg/ml concentration.

Bacteria	Crude (mean ± SD)	<i>W. somnifera</i> Silver nanoparticles (mean ± SD)	T-test	Crude (mean ± SD)	<i>F. indica</i> Silver nanoparticles (mean ± SD)	T-test	Control Antibiotic (AMP)
<i>E. coli</i>	10.67 ± 1.53	9.33 ± 1.15	Ns	7 ± 1	10 ± 1	Ns	22
<i>S. pneumoniae</i>	8.33 ± 1.15	14 ± 1	$p < 0.01$	11 ± 1	9.67 ± 0.58	Ns	15
<i>S. flexneri</i>	12.33 ± 0.58	8 ± 1	$p < 0.05$	10 ± 1	11.67 ± 1.15	Ns	26
<i>P. mirabilis</i>	8.33 ± 0.58	11.67 ± 1.53	Ns	9.33 ± 0.58	8.67 ± 0.58	Ns	30
<i>P. aeruginosa</i>	21 ± 1	11.67 ± 1.15	$p < 0.05$	7.67 ± 0.58	10.33 ± 0.58	Ns	20
<i>V. cholera</i>	8 ± 1	9.33 ± 0.58	Ns	11.33 ± 1.53	11.67 ± 2.08	Ns	21
<i>K. pneumoniae</i>	11.33 ± 0.58	8 ± 1	$p < 0.05$	10 ± 1	8 ± 1	Ns	26
<i>S. typhimurium</i>	5 ± 1	6.33 ± 0.58	Ns	10.33 ± 1.53	9 ± 1	Ns	25
ANOVA	$p < 0.01$	$p < 0.01$		$p < 0.01$	$p < 0.01$		

Key: SD: standard deviation; AMP: ampicillin; Ns: nonsignificant.

TABLE 2: Antifungal zone of inhibition (mm) of crude and silver nanoparticles' extracts of *W. somnifera* and *F. indica* at 50 mg/ml concentration.

Fungus	Crude (mean ± SD)	<i>W. somnifera</i> Silver nanoparticles (mean ± SD)	T-test	Crude (mean ± SD)	<i>F. indica</i> Silver nanoparticles (mean ± SD)	T-test	Control Miconazole
<i>A. flavus</i>	7.67 ± 1.15	12 ± 1	$p < 0.01$	7.67 ± 0.58	13 ± 1	$p < 0.05$	22
<i>F. oxysporum</i>	11 ± 1	12.67 ± 0.58	Ns	8.33 ± 0.58	13 ± 1	$p < 0.01$	25

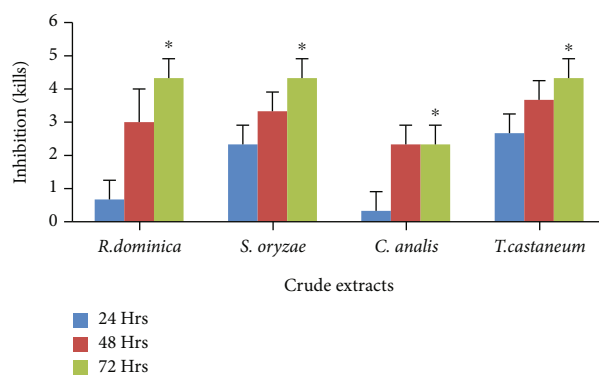
nanoballs on different bacteria, i.e., *E. coli*, *S. typhimurium*, *P. aeruginosa*, and *B. subtilis*, by the formation of colony forming unit (cfu) and growth rate at a different concentration of 40 lg/ml showed significant retardation of bacterial growth [25]. Numerous fungal strains showing drug resistance like *F. solani*, *Candida albicans*, *A. flavus*, and *Candida glabrata* have been reported for resistance [26]. A study conducted by Malesh and Satish [18] investigated that *W. somnifera* crude extracts depicted significant antifungal activities against *Aspergillus flavus*, *Drechslera turcica*, and *Fusarium verticillioides*. Vivek et al. [27] have also reported the antifungal activities of AgNPs and mechanisms to suggest that depending on composition, the cell wall can act as a barrier preventing drugs from reaching the site of action. Interaction between AgNPs and the membrane structure of *A. flavus* and *F. oxysporum* cells was confirmed and found out significant changes to their cell membrane integrity, due to the "pits" on their surface site and also the formation of pores, and causes death of a cell [28]. The positive charge on Ag<sup>+</sup> may have potent toxicity or antimicrobial activities as it forms complexes with DNA/RNA and specifically interacts with the nucleosides [29]. Moreover, the electrostatic attraction among the negatively charged microbial cells and positively charged NP has been reported [30]. The Ag<sup>+</sup> ions bind to the cytoplasm and cell wall due to electrostatic attractions and affinity for sulphur proteins, signifi-

cantly increase the permeability, and cause disintegration of bacterial casing.

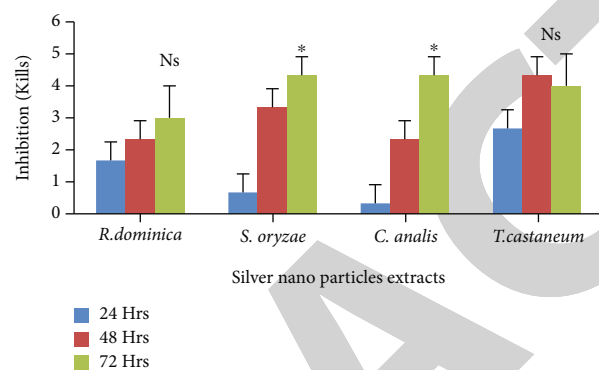
The field of allelopathy is a significant ecological factor in the kingdom Plantae together with such types of phytotoxic medicinal plants in which flavonoids and alkaloids are studied as allelochemicals [31]. *Lemna minor* inhibition variations by plants might be due to different types of plant extract, their different components, and mode of extraction [32]. Phytotoxic effects of nanoparticles on shrimp's larvae can be linked with anticancer activity, and nanoparticles could be an alternative source of anticancer drugs [33]. Toxicological study of the crude extract regarding intracutaneous toxicity and acute systematic toxicity in experimental animal models shows toxic nature of plants. The toxicity of this plant and the mechanism of action cannot be explained until unequivocal identification of its constituents [34].

Insects are cosmopolitan and occupy more than two-thirds of the known species of the animal kingdom. Flora including medicinal plants is part of insect's food and also destroys them and other stored products causing a huge amount of loss to the food and food quality [35]. Nanotechnology is the modern approach for the better management of insects and pest control in agriculture. The larvicidal activity of *Azima* crude extract and AgNPs is 100% at 24- and 48-hour exposure periods which may be due to the interactions of the compounds [36]. Larvicidal activities of

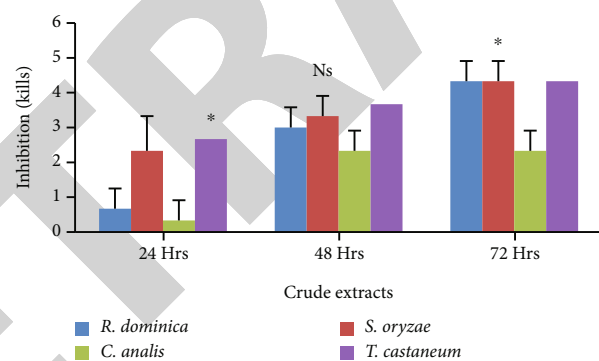




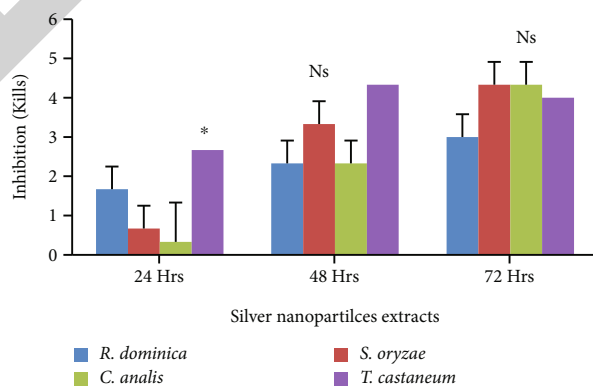
(a)



(b)



(c)



(d)

FIGURE 1: Insecticidal activity of crude and silver nanoparticles of *W. somnifera*. \* represents statistical significance (ANOVA); Ns: nonsignificant.

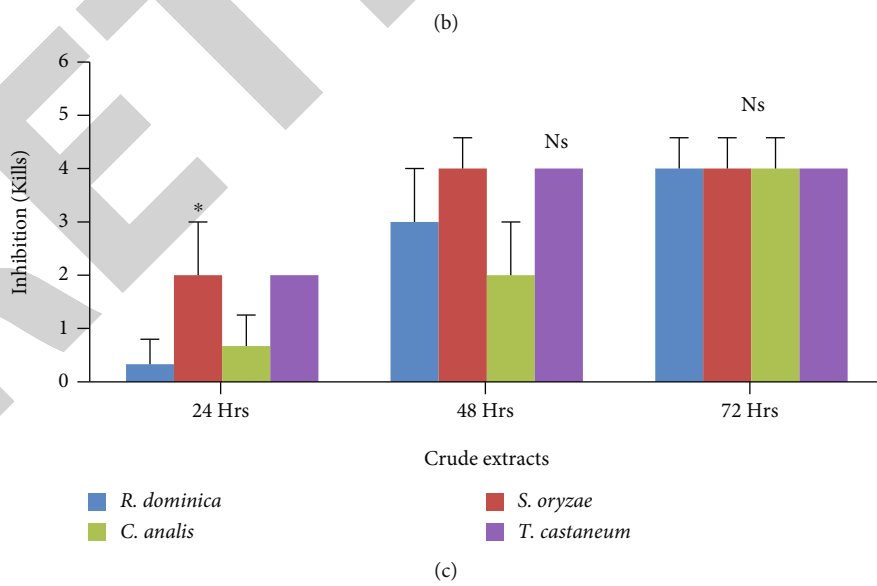
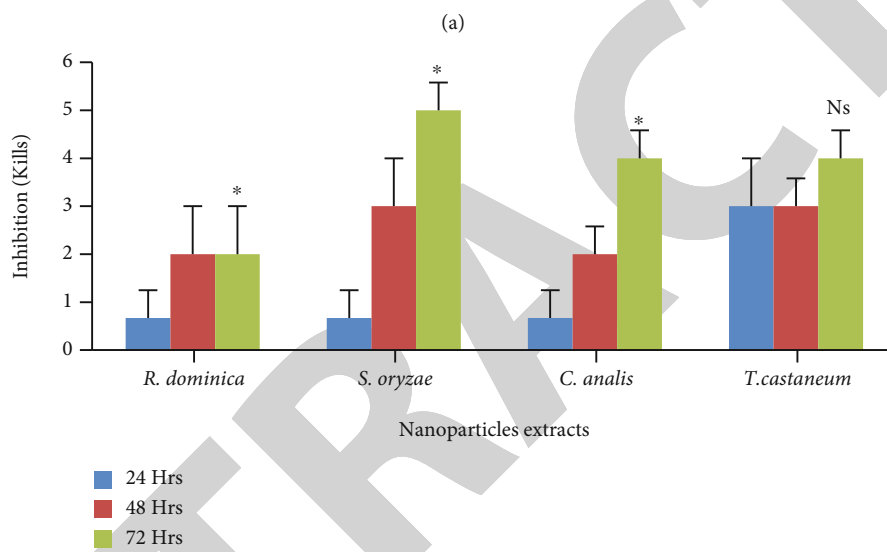
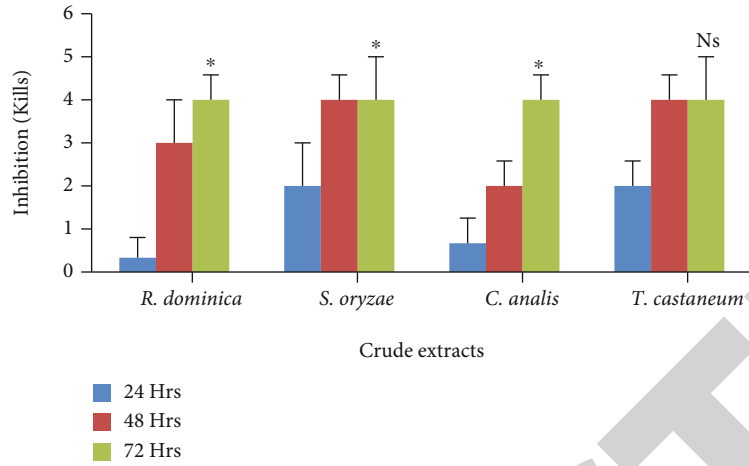


FIGURE 2: Continued.

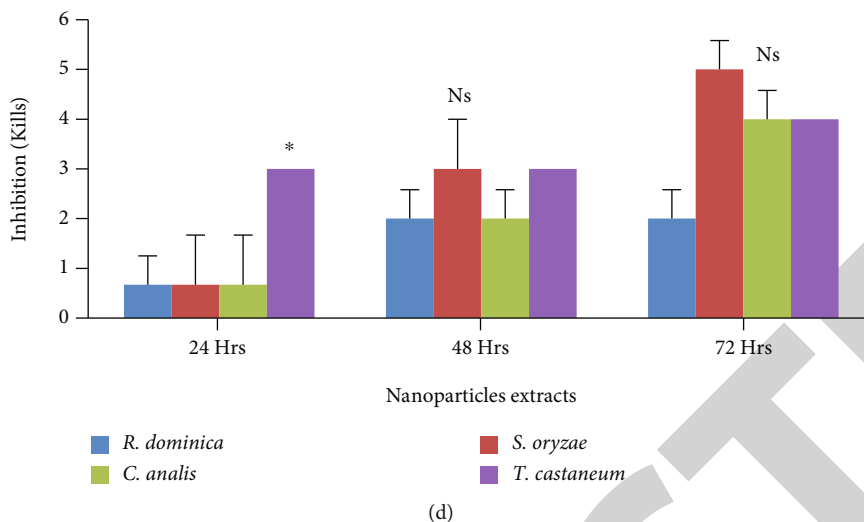


FIGURE 2: Insecticidal activities of crude and silver nanoparticles of *F. indica*. \* represents statistical significance (ANOVA); Ns: nonsignificant.

AgNPs using aqueous extract of *Eclipta prostrata* were studied against *Culex tritaeniorhynchus*, *Anopheles subpictus*, and *Diptera culicidae* and showed different inhibitions for a period of one day [37]. The extracts of *P. harmala* have an insect's mortality rate of 21.0%, followed by the medicinal plant of *F. cretica* 9.0% while *Tribulus terrestris* has 2.6%. All treatments from 5 to 20% showed validity in killing *T. castaneum*. Goswami et al. [38] reported the activity of different surface functionalized hydrophilic nanoparticles, against *S. oryzae*. Yang et al. [39] checked the activity of polyethylene glycol-coated nanoparticles loaded with garlic essential oil against adult *T. castaneum* and observed the control efficacy of about 80%, presumably due to the slow and persistent release of the active components from the nanoparticles. Khan et al. [40] reported the importance of nanoparticles and their mechanistic approach in the field of medicine to treat chronic diseases like cancer. Similarly, anticancer and antimicrobial activity of silver nanoparticles synthesized from *Conocarpus lancifolius* showed marked inhibition [41]. Gold nanoparticles from *Rauwolfia serpentina* showed antibacterial and antioxidant potential that have relevant results with the present study [42]. So, different types of nanoparticles can be used for efficient management in agriculture and formulation of new insecticides. Although the standard drug used in comparison showed higher inhibition, the crude extracts of plants and AgNPs synthesized by chemical and biological methods are cost-effective and eco-friendly to use.

## 5. Conclusions

In conclusion, crude and AgNPs exhibit good effects; however, in comparison, AgNPs synthesized from both plants, i.e., *W. somnifera* and *F. indica*, showed enhanced inhibition against bacterial and fungal pathogens. In phytotoxic results, crude extracts of both tested plants are more effective as compared to AgNPs. Biological activities of AgNPs on tested pathogens open a door for new antimicrobial agents and

could be the answer to antibiotic resistance as well nanomaterials in different forms can be used as an effective management in agriculture and formulation of new insecticides. The present study has provided a base for the researcher in the field of nanomedicine to synthesize and check the biological activities of nanoparticles and isolated compounds from other medicinal plants against other microorganisms. New antibiotics and therapeutics in nanoform should be made from these natural products and replaced with those showing resistance to microorganisms. Toxicology studies of these AgNPs should be recommended to ensure the safety. Studies on the comparison and characterization of silver nanoparticles to other phytochemicals need to be carried out.

## Data Availability

All the available data are incorporated in the manuscript.

## Conflicts of Interest

The authors declare that they have no conflicts of interest.

## Authors' Contributions

Muhammad Adnan and Asma Akbar contributed equally to this work.

## Acknowledgments

The authors wish to thank Researchers Supporting Project No. RSP-2021/45 at King Saud University, Riyadh, Saudi Arabia, for the financial support. This article is a part of Asma Akbar M. Phil thesis, who passed away during the COVID-19 pandemic, before submission of this article. The authors dedicate this work to the deceased sole author "Asma Akbar" for her restless efforts to make this teamwork successfully.

## References

- [1] R. W. Lee, D. B. Shenoy, and R. Sheel, "Micellar nanoparticles: applications for topical and passive transdermal drug delivery," in *Handbook of non-invasive drug delivery systems*, pp. 37–58, Elsevier, 2010.
- [2] A. Taleb, C. Petit, and M. Pileni, "Synthesis of highly monodisperse silver nanoparticles from AOT reverse micelles: a way to 2D and 3D self-organization," *Chemistry of Materials*, vol. 9, no. 4, pp. 950–959, 1997.
- [3] K. Esumi, T. Tano, K. Torigoe, and K. Meguro, "Preparation and characterization of bimetallic palladium-copper colloids by thermal decomposition of their acetate compounds in organic solvents," *Chemistry of Materials*, vol. 2, no. 5, pp. 564–567, 1990.
- [4] I. Pastoriza-Santos and L. M. Liz-Marzán, "Synthesis of silver nanoprisms in DMF," *Nano Letters*, vol. 2, no. 8, pp. 903–905, 2002.
- [5] N. A. Begum, S. Mondal, S. Basu, R. A. Laskar, and D. Mandal, "Biogenic synthesis of Au and Ag nanoparticles using aqueous solutions of Black Tea leaf extracts," *Colloids and Surfaces B: Biointerfaces*, vol. 71, no. 1, pp. 113–118, 2009.
- [6] H. Bar, D. K. Bhui, G. P. Sahoo, P. Sarkar, S. P. De, and A. Misra, "Green synthesis of silver nanoparticles using latex of *Jatropha curcas*," *Colloids and Surfaces A: Physicochemical and Engineering Aspects*, vol. 339, no. 1-3, pp. 134–139, 2009.
- [7] N. Krithiga, A. Rajalakshmi, and A. Jayachitra, "Green synthesis of silver nanoparticles using leaf extracts of *Clitoria ternatea* and *Solanum nigrum* and study of its antibacterial effect against common nosocomial pathogens," *Journal of Nanoscience*, vol. 2015, Article ID 928204, 2015.
- [8] D. Cruz, P. L. Falé, A. Mourato, P. D. Vaz, M. L. Serralheiro, and A. R. L. Lino, "Preparation and physicochemical characterization of Ag nanoparticles biosynthesized by *Lippia citriodora* (Lemon Verbena)," *Colloids and Surfaces B: Biointerfaces*, vol. 81, no. 1, pp. 67–73, 2010.
- [9] A. I. Lukman, B. Gong, C. E. Marjo, U. Roessner, and A. T. Harris, "Facile synthesis, stabilization, and anti-bacterial performance of discrete Ag nanoparticles using *Medicago sativa* seed exudates," *Journal of Colloid and Interface Science*, vol. 353, no. 2, pp. 433–444, 2011.
- [10] P. Anil, B. Nikhil, G. Manoj, and N. Prakash, "Phytochemicals and biological activities of *Fagonia indica*," *Int Res J Pharm*, vol. 3, pp. 56–59, 2012.
- [11] J. A. Creighton, C. G. Blatchford, and M. G. Albrecht, "Plasma resonance enhancement of Raman scattering by pyridine adsorbed on silver or gold sol particles of size comparable to the excitation wavelength," *Journal of the Chemical Society, Faraday Transactions 2: Molecular and Chemical Physics*, vol. 75, pp. 790–798, 1979.
- [12] W. Kirby, G. Yoshihara, K. Sundsted, and J. Warren, "Clinical usefulness of a single disc method for antibiotic sensitivity testing," *Antibiotics Annual*, vol. no. p. 892, 1956.
- [13] L. Scorzoni, T. Benaducci, A. M. F. Almeida, D. H. S. Silva, V. d. S. Bolzani, and M. J. S. M. Gianinni, "The use of standard methodology for determination of antifungal activity of natural products against medical yeasts *Candida* sp and *Cryptococcus* sp," *Brazilian Journal of Microbiology*, vol. 38, pp. 391–397, 2007.
- [14] J. L. McLaughlin, C.-j. Chang, and D. L. Smith, "Simple bench-top bioassays (brine shrimp and potato discs) for the discovery of plant antitumor compounds: review of recent progress," *Human Medicinal Agents from Plants*, pp. 112–137, 1993.
- [15] G. Marslin, R. K. Selvakesan, G. Franklin, B. Sarmiento, and A. C. Dias, "Antimicrobial activity of cream incorporated with silver nanoparticles biosynthesized from *Withania somnifera*," *International Journal of Nanomedicine*, vol. 10, p. 5955, 2015.
- [16] I. Fatimah, H. Hidayat, B. Nugroho, and S. Husein, "Green synthesis of silver nanoparticles using *Datura metel* flower extract assisted by ultrasound method and its antibacterial activity," *Recent Patents on Nanotechnology*, 2021.
- [17] K. Girish, K. Machiah, S. Ushanandini et al., "Antimicrobial properties of a non-toxic glycoprotein (WSG) from *Withania somnifera* (Ashwagandha)," *Journal of Basic Microbiology*, vol. 46, no. 5, pp. 365–374, 2006.
- [18] B. Mahesh and S. Satish, "Antimicrobial activity of some important medicinal plant against plant and human pathogens," *World Journal of Agriculture Sciences*, vol. 4, no. 5, pp. 839–843, 2008.
- [19] A. L. Silva, R. S. Santos, D. G. Xisto, S. D. V. Alonso, M. M. Morales, and P. R. Rocco, "Nanoparticle-based therapy for respiratory diseases," *Anais da Academia Brasileira de Ciências*, vol. 85, pp. 137–146, 2013.
- [20] J. R. Morones, J. L. Elechiguerra, A. Camacho et al., "The bactericidal effect of silver nanoparticles," *Nanotechnology*, vol. 16, no. 10, pp. 2346–2353, 2005.
- [21] K. Govindaraju, S. Tamilselvan, V. Kiruthiga, and G. Singaravelu, "Biogenic silver nanoparticles by *Solanum torvum* and their promising antimicrobial activity," *Journal of Biopesticide*, vol. 3, pp. 394–399, 2010.
- [22] I. Sondi and B. Salopek-Sondi, "Silver nanoparticles as antimicrobial agent: a case study on *E. coli* as a model for Gram-negative bacteria," *Journal of Colloid and Interface Science*, vol. 275, no. 1, pp. 177–182, 2004.
- [23] J. S. Kim, E. Kuk, K. N. Yu et al., "Antimicrobial effects of silver nanoparticles," *Nanomedicine: Nanotechnology, Biology and Medicine*, vol. 3, no. 1, pp. 95–101, 2007.
- [24] C.-N. Lok, C.-M. Ho, R. Chen et al., "Proteomic analysis of the mode of antibacterial action of silver nanoparticles," *Journal of Proteome Research*, vol. 5, no. 4, pp. 916–924, 2006.
- [25] R. Tripathi, A. Saxena, N. Gupta, H. Kapoor, and R. Singh, "High antibacterial activity of silver nanoballs against *E. coli* MTCC 1302, *S. typhimurium* MTCC 1254, *B. subtilis* MTCC 1133 and *P. aeruginosa* MTCC 2295," *Dig J Nanomater Bios*, vol. 5, no. 2, pp. 323–330, 2010.
- [26] S. Saha, D. Dhanasekaran, S. Chandreleka, and A. Panneerselvam, "Synthesis, characterization and antimicrobial activity of cobalt metal complex against multi drug resistant bacterial and fungal pathogens," *Facta universitatis-series: Physics, Chemistry and Technology*, vol. 7, no. 1, pp. 73–80, 2009.
- [27] M. Vivek, P. S. Kumar, S. Steffi, and S. Sudha, "Biogenic silver nanoparticles by *Gelidiella acerosa* extract and their antifungal effects," *Avicenna Journal of Medical Biotechnology*, vol. 3, no. 3, p. 143, 2011.
- [28] G. Zhao and S. E. Stevens, "Multiple parameters for the comprehensive evaluation of the susceptibility of *Escherichia coli* to the silver ion," *Biometals*, vol. 11, no. 1, pp. 27–32, 1998.
- [29] S. A. Ahmad, S. S. Das, A. Khatoun et al., "Bactericidal activity of silver nanoparticles: a mechanistic review," *Materials Science for Energy Technologies*, vol. 3, pp. 756–769, 2020.



## Retraction

# Retracted: Comparative Analysis of Antioxidants Activity of Indigenously Produced *Moringa Oleifera* Seeds Extracts

### BioMed Research International

Received 8 January 2024; Accepted 8 January 2024; Published 9 January 2024

Copyright © 2024 BioMed Research International. This is an open access article distributed under the Creative Commons Attribution License, which permits unrestricted use, distribution, and reproduction in any medium, provided the original work is properly cited.

This article has been retracted by Hindawi following an investigation undertaken by the publisher [1]. This investigation has uncovered evidence of one or more of the following indicators of systematic manipulation of the publication process:

- (1) Discrepancies in scope
- (2) Discrepancies in the description of the research reported
- (3) Discrepancies between the availability of data and the research described
- (4) Inappropriate citations
- (5) Incoherent, meaningless and/or irrelevant content included in the article
- (6) Manipulated or compromised peer review

The presence of these indicators undermines our confidence in the integrity of the article's content and we cannot, therefore, vouch for its reliability. Please note that this notice is intended solely to alert readers that the content of this article is unreliable. We have not investigated whether authors were aware of or involved in the systematic manipulation of the publication process.

Wiley and Hindawi regrets that the usual quality checks did not identify these issues before publication and have since put additional measures in place to safeguard research integrity.

We wish to credit our own Research Integrity and Research Publishing teams and anonymous and named external researchers and research integrity experts for contributing to this investigation.

The corresponding author, as the representative of all authors, has been given the opportunity to register their agreement or disagreement to this retraction. We have kept a record of any response received.

### References

- [1] S. Tariq, H. Umbreen, R. Noreen et al., "Comparative Analysis of Antioxidants Activity of Indigenously Produced *Moringa Oleifera* Seeds Extracts," *BioMed Research International*, vol. 2022, Article ID 4987929, 11 pages, 2022.

## Research Article

# Comparative Analysis of Antioxidants Activity of Indigenously Produced *Moringa Oleifera* Seeds Extracts

Sadaf Tariq,<sup>1</sup> Huma Umbreen,<sup>2</sup> Razia Noreen ,<sup>1</sup> Cyril Petitbois,<sup>3</sup> Kiran Aftab,<sup>4</sup> Fatmah Ali Alasmay,<sup>5</sup> Amani Salem Almalki,<sup>5</sup> and Mohammad Abdul Mazid <sup>6</sup>

<sup>1</sup>Department of Biochemistry, Government College University Faisalabad, Pakistan

<sup>2</sup>Department of Nutritional Sciences, Biochemistry, Government College University, Faisalabad, Pakistan

<sup>3</sup>Inserm U1029 LAMC Group « 3D' Spectro-Imaging », University of Bordeaux, 33600 Pessac, France

<sup>4</sup>Department of Chemistry, Government College University Faisalabad, Pakistan

<sup>5</sup>Chemistry Department, College of Science, King Saud University, Riyadh 11451, Saudi Arabia

<sup>6</sup>Department of Pharmaceutical Chemistry, Faculty of Pharmacy, University of Dhaka, Dhaka 1000, Bangladesh

Correspondence should be addressed to Razia Noreen; [itsrazia@yahoo.com](mailto:itsrazia@yahoo.com) and Mohammad Abdul Mazid; [ma.mazid@du.ac.bd](mailto:ma.mazid@du.ac.bd)

Received 11 August 2022; Revised 13 September 2022; Accepted 23 September 2022; Published 15 October 2022

Academic Editor: Wilson Aruni

Copyright © 2022 Sadaf Tariq et al. This is an open access article distributed under the Creative Commons Attribution License, which permits unrestricted use, distribution, and reproduction in any medium, provided the original work is properly cited.

Medicinal plants are used to control and remediate oxidative stress related diseases caused by free radicals. Thus, these plants find their use as remedy. *Moringa oleifera* is an extremely valued plant for its medicinal properties. Herein, two indigenously produced accessions of *Moringa oleifera* seeds [originated from Multan (M-Mln) and India (PKM1)] were investigated for their antioxidant properties by 2,2-Diphenyl-1-picrylhydrazyl (DPPH) assay, total phenolics content and total flavonoids content. The presence of various phenolics as well as flavonoids was further confirmed by high performance liquid chromatography. Moreover, fourier transform infrared spectroscopy detected the presence of various functional groups. In conclusion, these findings revealed that the methanol extract of M-Mln variety seeds showed high antioxidant potential, having IC<sub>50</sub> value of 84 µg/ml. While, hexane extract of PKM1 showed least activity. The methanol extract of M-Mln was found to show highest total phenolics content as 33.83 ± 1.19 mg GAE/g. The methanol extract of M-Mln was found to show highest total flavonoids content as 76.07 ± 1.10 mg CAE/g. The hexane extract of PKM1 was found to show least total flavonoids content as 22.47 ± 1.70 mg CAE/g. The detection of phenolics (ferulic acid, caffeic acid, chlorogenic acid, coumaric acid, and gallic acid) as well as flavonoids (catechin and quercetin) revealed the potential of methanol extracts of both varieties as a good source of antioxidants. The results indicated the importance of seed extracts in the treatment of oxidative stress related diseases. In future, the use of natural antioxidants will prevent the progression of diseases.

## 1. Introduction

In living systems, oxidation reactions occur commonly. The cellular metabolism and respiration are reactions which frequently occur in human body. These oxidation reactions produce free radicals, such as reactive oxygen species as well as reactive nitrogen species [1]. These free radicals not only initiate different chain reactions, often toxic to cells, but also cause several destructive effects such as lipid peroxidation, DNA damage, protein degradation, and tissue injury which contribute to different diseases such as arthritis, liver diseases, atherosclerosis, diabetes, cancer, neurodegenerative

disorders, and ageing [2, 3]. The detrimental effects of free radicals cause potential biological damage in living cells, also known as oxidative stress, when production of free radicals is overwhelmed by the body's ability to defend against free radicals [4, 5].

The human body is naturally blessed with different antioxidants (i.e., enzymatic and nonenzymatic) as defensive mechanism like thioredoxin, superoxide dismutases, catalases, uric acid, glutathione, and ascorbic acid which help the body to terminate the chain reactions initiated by free radicals [6, 7]. Nowadays, there is an increased interest in natural antioxidants that may be used to oppose free radicals

with a view to lower the risk of associated diseases. Such reservoirs of natural antioxidants are different products of plant origin [4, 8].

*Moringa oleifera* (*M. oleifera*) is a small sized shrub like deciduous tree with soft and fragile stem found in different regions of the world, which belongs to family Moringaceae, native to Pakistan, India, Pacific Island, South America, Africa, Arabian Peninsula, Southeast Asia, and Caribbean Islands [1, 2]. It is grown in tropics and subtropics regions of the world. Because it is being cultivated in different regions of the world, *M. oleifera* is also known by many other local names i.e., horseradish tree, miracle tree, drumstick tree, and ben oil tree [9]. Due to its excessive use at household, it is commonly called as “The Mother’s Best Friend”. A number of therapeutics and various medicinal characteristics have been attributed to different parts of tree due to presence of minerals and vitamins. Moringa species contain numerous unique compounds and it contains compounds rich in rhamnose, a simple carbohydrate. Glucosinolates and isothiocyanates, a group of compound is characteristically found in moringa family.

Specific parts of Moringa are reported to have 4-(4'-O acetyl rhamnopyranosyloxy) benzyl isothiocyanate, an effective antibacterial agent (Bhattacharya et al.), pterygospermin, benzyl isothiocyanate [10], 4 (L-rhamnopyranosyloxy) benzyl glucosinolate [11], 4 (L-rhamnopyranosyloxy) benzyl isothiocyanate [12], and niazimicin as effective hypotensive and anticancer agents [13]. *M. oleifera* plant have potent antimicrobial, aphrodisiac, antihyperglycemic, antiulcer, antioxidant, antiepileptic, anticancer, antihypertensive, and anti-inflammatory activities (Asmari et al.) as listed in Table 1. The hypotensive, antibacterial, and anticancer activity is reported in seeds extracts due to some specific components as 4-(4'-acetyl rhamnopyranosyloxy)benzyl isothiocyanate, benzyl isothiocyanate, niazimicin, and pterygospermin [14, 15]. It is a source of polyphenols which are reported for antioxidant, antimicrobial, anticancer, anti-inflammatory, antihypertensive, antitumor, and antifungal activity. Some of the most reported phytochemical compounds are flavonoids, luteolin, quercetin, tannins, triterpenes, and glycosides. The antioxidant activity varies with environmental conditions, plant tissues, and harvest season [16, 17].

The seeds of the plant exhibit various biological activities like, antidiabetic [31], anti-inflammatory [32], hepatoprotective [33], anticancer [34], cardiovascular, CNS, analgesic [35], wound healing [36], antiallergic, antifertility, antiasthmatic [37], antiulcer, and antipyretic activity [38]. Therefore, this study was designed to evaluate the antioxidant potential of *M. oleifera* seeds of two different accessions from different regions. This study quantified the polyphenolic contents (i.e., total phenolics and total flavonoids) and estimated phytochemicals to investigate free radical scavenging activity *viz a viz* the antioxidant activity of various extracts of *M. oleifera* Multan (M-Mln) and Indian (PKM1) variety seeds.

## 2. Materials and Methods

**2.1. Plant Material and Extraction.** The seeds of *M. oleifera* of two different accessions, originated from Multan (M-

Mln) and India (PKM1) were collected from *M. oleifera* plants grown at Department of Crop Physiology, University of Agriculture, Faisalabad, Pakistan. The seeds were authenticated by the Faculty of Department of Botany, Government College University, Faisalabad, Pakistan. Prior to extraction, the seed wings and coats were removed manually and the obtained kernels were ground in blender to obtain fine powder. The powder of both varieties were extracted with 100% methanol and n-Hexane. It was filtered by Whatman No. 1 filter paper. The excess solvent was evaporated at 40°C in a rotary evaporator and it was concentrated to crude extract and it was kept at 4°C in air tight dark bottles. The sample and solvent mass ratio was kept at 1 : 10 during extraction.

**2.2. Fourier Transform Infrared Spectroscopy.** FTIR spectroscopy (Perkin Elmer, USA) was done to evaluate the presence of various compounds and functional groups through ATR sampling technique in % transmittance mode (in the range of 4000-500 cm<sup>-1</sup>) with 45 scan recorder [39]. Dry powder of *M. oleifera* seeds was used for FTIR analysis. 10 mg of dry powder was encapsulated in 100 mg of potassium bromide pellets. The samples were loaded in FTIR spectrophotometer, and recorded spectra was obtained.

**2.3. High Performance Liquid Chromatography.** HPLC was performed in accordance with chromera HPLC system (Perkin Elmer, USA). HPLC was done to estimate different phenolics and flavonoids in methanol seed extracts of both varieties [40]. The sample was prepared by dissolving 50 mg of extract in 40 ml methanol, acidified by dissolving in HCl, and filtered by syringe filter. The filtered sample was injected in HPLC stream. Phenolics and flavonoids were identified by recording their retention time and peaks.

### 2.4. Antioxidant Activity Assay

**2.4.1. DPPH Free Radical Scavenging Assay.** The antioxidant potential of methanol and n-Hexane extracts of M-Mln and PKM1 seeds was checked by determining the scavenging activity of DPPH free radicals based on method of Hossain et al. [41] with slight modification. 1 mL of DPPH (Sigma-Aldrich) solution was prepared. 55 µL of extracts was mixed in Dimethyl Sulphoxide (DMSO), and it was further dissolved in 150 µL of DPPH. The solution was then reconstituted in methanol (0.1 mM), and the final volume was made up to 250 µL. The mixture was then placed in dark for 30 minutes to observe color change, and absorbance was taken at 540 nm with a spectrophotometer. The blank was run concurrently containing DMSO. The experiment was carried out in triplicate. Free radicals scavenging activity was calculated using the following formula:

$$\text{inhibition rate(\%)} = \left( \text{Abs}_{\text{control}} - \text{Abs}_{\text{sample}} \right) \times \frac{100}{\text{Abs}_{\text{control}}} \quad (1)$$

The 50% inhibitory concentration (IC50) was calculated to evaluate the minimum active quantity of the extracts required to react with a half quantity of DPPH free radicals.

TABLE 1: Comparative analysis of various phytochemicals and their uses isolated from different parts of *Moringa oleifera*.

Part of <i>Moringa oleifera</i>	Identified compounds	Benefits	References
Seeds	Proteins, fats, carbohydrates, amino acids (methionine, cysteine), cationic proteins, Rhamnose (4-( $\alpha$ -L-rhamnopyranosyloxy)-benzylglucosinolate), benzylglucosinolate, moringyne, monopalmitic acid, dioleic triglyceride, vitamin A, beta carotene, pterygospermin	Decrease lipid peroxides, water treatment, and antirheumatism	[11, 18–20]
Flowers	D-mannose, polysaccharide, proteins, D-glucose, and ascorbic acid	Cholagogue, aphrodisiac anti-inflammatory; cures muscle diseases, antitumor, antihysteria; stops enlargement of spleen; lower serum cholesterol level; controls lipid level of liver, and heart	[21, 22]
Roots	4-( $\alpha$ -L-rhamnopyranosyloxy)-benzylglucosinolate and benzylglucosinolate	Laxative, rubefacient, circulatory tonic; treat kidney and back pain; antifertility, antirheumatism, and antiarthritis	[14, 23, 24]
Leaves	Glycosides, kaempferol-3-O-glucoside, quercetin, 4-[4-O-acetyl-( $\alpha$ -L-rhamnopyranosyloxy) benzyl] isothiocyanate, niazirin, niazirin, three mustard oil glycosides, niaziminin A and B, and 3-caffeoylquinic	Full of nutrition; headache reliever; treat fever; helps in curing piles; cures throat, eyes, and ears infections; cure scurvy; control blood glucose levels	[10, 11, 18]
Gum	L-arabinose, D-mannose, D-galactose, L-rhamnose, leucoanthocyanin, D-glucuronic acid, and D-xylose	Treats dental problems; relieves headache; abortifacient; treats syphilis, and cures rheumatism; prevents dysentery; relieves intestinal pain	[25–27]
Bark	4-( $\alpha$ -L-rhamnopyranosyloxy)-benzylglucosinolate	Aids in treatment of delirium; cures eye infections; soothes earaches; work as a painkiller.	[28–30]

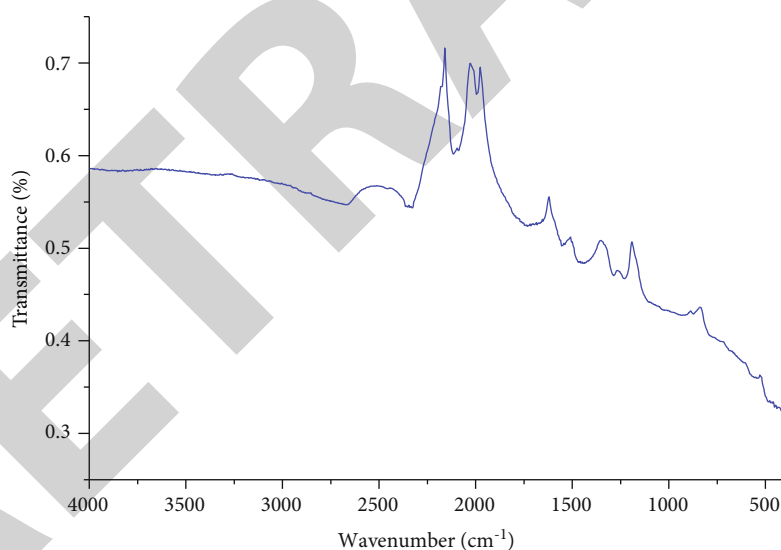


FIGURE 1: FTIR spectrum of M-Mln variety seeds.

**2.4.2. Total Flavonoids Content.** The TFC of M-Mln and PKM1 varieties of *M. oleifera* seeds methanol and n-Hexane extracts were evaluated by protocol of Sharma et al. [42] with slight modification. The extract was mixed with 2 mL of water and 0.15 mL of sodium nitrate solution, and it was incubated in an incubator for 6 minutes. Then, 4% NaOH solution was added to the mixture. The final volume was made up to 5 mL by adding methanol. Catechin was taken as a reference and standard compound. The absorbance was measured at 415 nm after the incubation in a double beam UV-Vis spectrophotometer. The total flavo-

noids content of the extract was expressed as catechin equivalents from standard curve of the catechin.

**2.4.3. Total Phenolic Content.** The TPC of methanol and n-Hexane extracts of M-Mln and PKM1 varieties of *M. oleifera* seeds were assessed with Folin-Ciocalteu assay [43] with slight modification. To make a standardization curve at 0.5, 1.0, 1.5, 2.0, 2.5, 3.0, and 3.5, and 4.0 mL of gallic acid equivalent, stock solution was poured in 100 mL flask. It was further mixed with distilled water to make gallic acid and sodium carbonate solution. The concentrations of

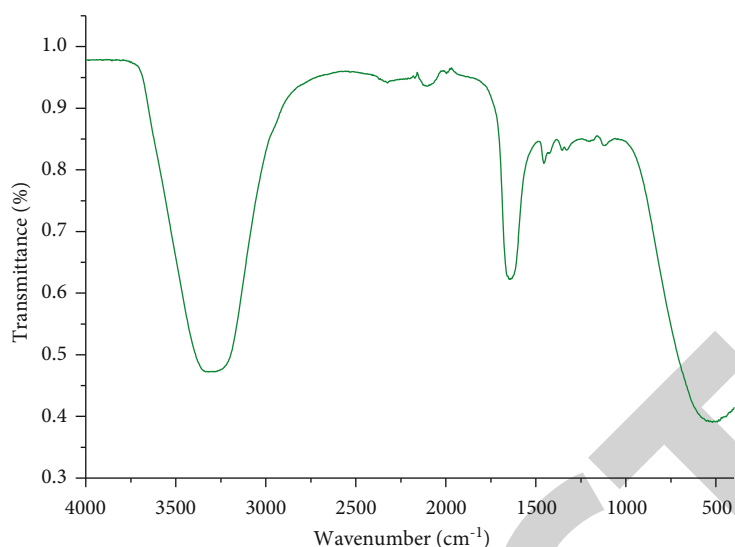


FIGURE 2: FTIR spectrum of PKM1 variety seeds.

TABLE 2: FTIR peak values and functional groups of both varieties of seeds [48–51].

S. no	Accessions	Wavenumber (cm <sup>-1</sup> )	Assignment	Possible nutrient type
1	M-Mln	608	CH out-of-plane bending vibrations	Organic compounds
		935	Carbon-related component	Organic compounds
		1047	C-O stretching coupled with C-O bending of the C-OH	Carbohydrates
		1160	CO stretching, stretching vibrations of hydrogen-bonding C-OH groups	Proteins
		1235	Asymmetric PO <sub>2</sub> <sup>-</sup> stretching	Amide III
		1456	Asymmetric CH <sub>3</sub> bending modes of the methyl group	Proteins
		1633	C-C stretch	Proteins
		1648	C = O, C = N, and N-H stretching vibrations	Proteins
		1749	Ester group (C = O) vibration of triglycerides	Lipids
		2348, 2859	NH component	Lipids
		2932, 2956	Asymmetric stretching vibration of CH <sub>3</sub> of acyl chains	Lipids
2	PKM1	738	C-cl stretching vibration	Aliphatic chloro compounds
		1160	C-O bending vibration	Proteins and carbohydrates
		1270	Aryl-O stretching vibration	Aromatic ethers
		1402	Symmetric stretching vibration of COO <sup>-</sup> group of amino acids	Proteins
		1524	Stretching vibrations of C = N, C = C, and C = N	Proteins
		3093, 3275	C-H ring	Aromatic compounds

phenols were checked by using reagent at 650 nm. The gallic acid was used as a standard, and thus total phenolic concentrations were expressed in the form of gallic acid equivalents.

### 3. Results and Discussion

**3.1. FTIR Spectroscopy.** The FTIR analysis, a reliable and sensitive technique, was done to detect various bonds and stretches and functional groups based on peak values in IR region [44]. FTIR spectra was obtained by using a Bruker, vector using KBr pellets at room temperature with wave-

number measured in frequency range of 4000-500 cm<sup>-1</sup>. The obtained peak ratio was used to separate and identify the functional groups. The FTIR spectra of M-Mln variety was recorded and the characteristic peaks (Figure 1). Most of the peaks represent major functional groups present in M-Mln variety and presents a comprehensive outlook on the presence of proteins, carbohydrates, and lipid components in the sample. A sharp peak at the 2920 cm<sup>-1</sup> and 2850 cm<sup>-1</sup> can be attributed and related symmetrical and asymmetrical C-H stretch [45]. Another sharp peak at 1640 cm<sup>-1</sup> can be attributed to the presence of C = O bond. An amide vibration also appeared at 1420 cm<sup>-1</sup>.

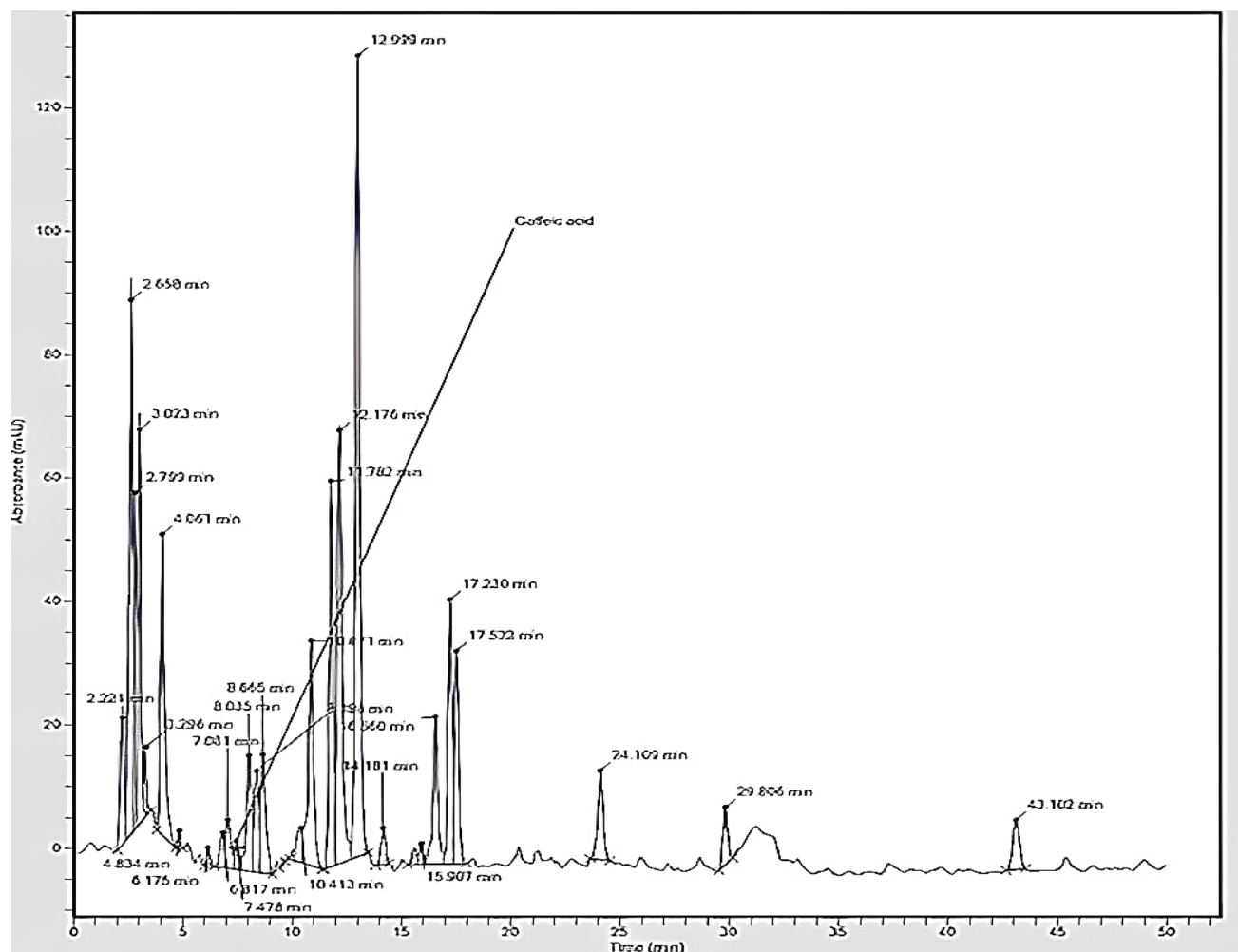


FIGURE 3: HPLC spectrum of compounds from methanol extract of M-Mln variety *M. oleifera* seeds.

The broad-band centered at  $3420\text{ cm}^{-1}$  can be assigned to the presence of protein and fatty acids [45] (Figure 2). Additionally, the peak in the region of  $1370\text{ cm}^{-1}$  is due to the combination of deformation of methyl and methylene groups [46]. Another peak at  $1030\text{ cm}^{-1}$  can be related to the presence of carbohydrates due to  $C=O$  stretch. Furthermore, the peaks at  $1300\text{ cm}^{-1}$  can be attributed to the low-molecular-weight carbohydrates as this region is commonly characterized as fingerprint region [47]. Moreover, the appearance of specific peaks at  $3350\text{ cm}^{-1}$  confirmed the presence of phenolic compounds [48], signifying the antioxidant potential of seeds.

The characteristic peak values, bonds, stretches, and functional groups of both varieties are illustrated in Table 2. 13 peaks can be observed through the spectrum of M-Mln seeds sample. The corresponding peaks revealed the presence of high content of proteins and lipids in M-Mln seeds. Whereas, the spectrum of PKM1 sample showed 7 peaks of functional groups which can be related to the proteins and lipids as possible nutrients. The presence of characteristic peaks in the spectra of both varieties exhibited the presence of phenolics as well as flavonoids. These readings show that M-Mln seeds can be used as rich source of proteins and lipids due to the presence of comparatively

more functional groups than that of PKM1, indicating that the indigenously produced M-Mln seeds may be an ideal source of pharmaceutical uses.

**3.2. HPLC.** HPLC is one of the most promising analytical methods used to identify and quantify different antioxidants present in plants. During this study, HPLC was used to identify the antioxidants in the methanol extracts of both varieties of *M. oleifera* seeds due to its high resolution, faster evaluation, better compound separation, and high sensitivity. The HPLC chromatograms of both varieties were successfully developed by using reverse phase column. The mobile phase at high resolution was used to obtain different peaks to quantify these compounds. Various phenolics, such as gallic acid, catechin, chlorogenic acid, coumaric acid, and sinapic acid were detected in M-Mln variety chromatogram, while quercetin was detected as flavonoid (Figure 3). Additionally, PKM1 variety chromatogram exhibited the presence of sinapic acid and salicylic acid along with coumaric acid and caffeic acid (Figure 4). The presence of phenolics and flavonoids revealed that the methanol extracts of both varieties are good source of antioxidants. The peaks of HPLC chromatogram of M-Mln variety seed methanol

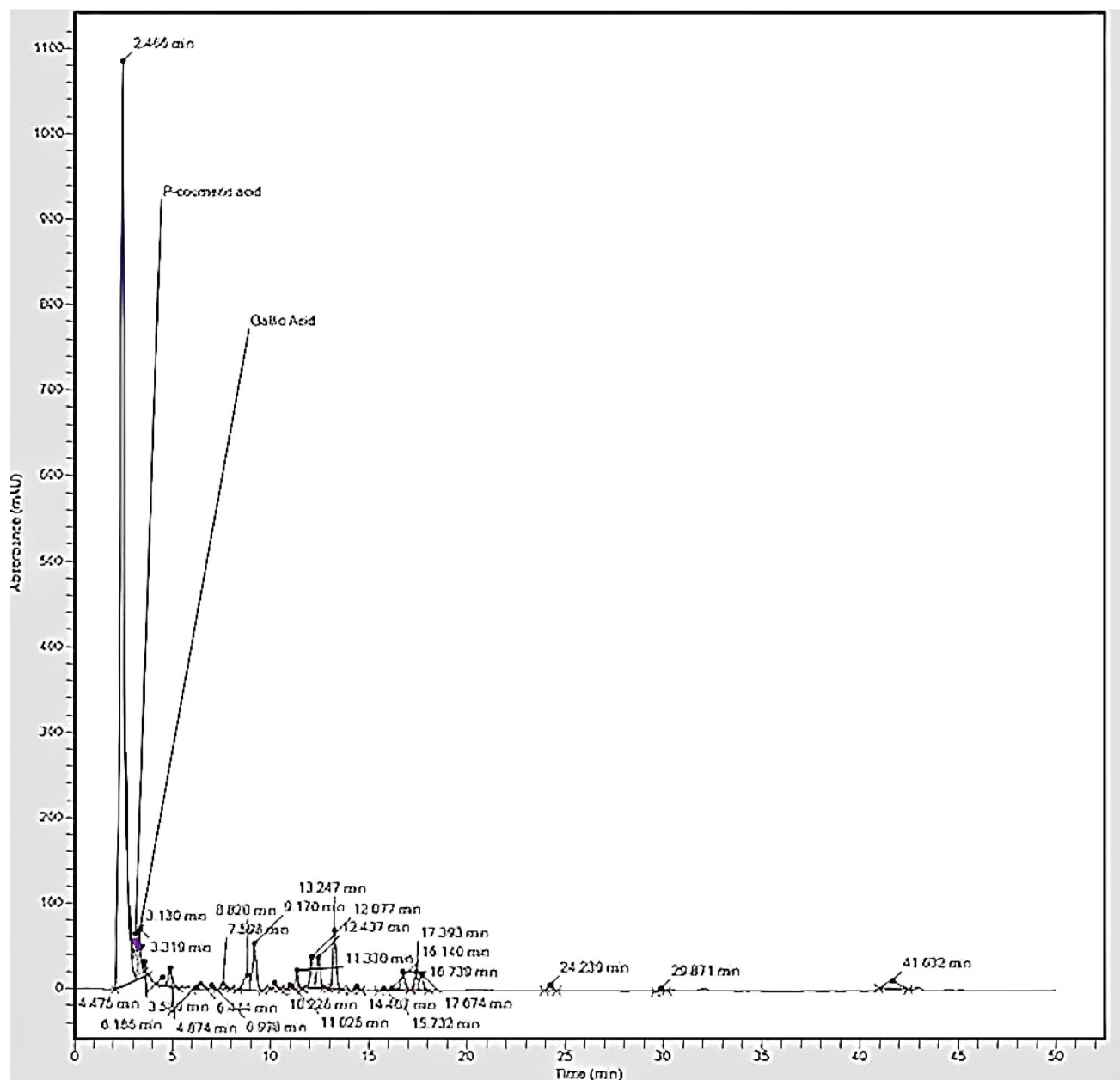


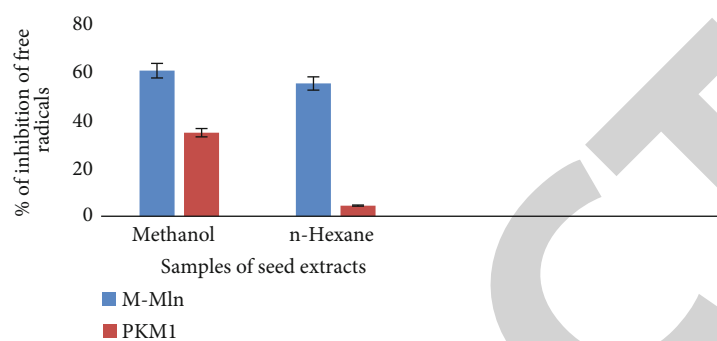
FIGURE 4: HPLC spectrum of compounds from methanol extract of PKM1 variety *M. oleifera* seeds.

TABLE 3: Characteristic absorption peaks with their amount of M-Mln variety.

Peaks	Retention time (min)	Component	Nature	Area	Height	K-factor	Total amount (ppm)
1	2.806	Gallic acid	Phenolic	544,037.4	71,328.6	0.0007	380.82618
2	3.386	Catechin	Phenolic	338,226.6	49,771.5	0.000254	85.909
3	5.227	Chlorogenic acid	Phenolic	104,856.7	11,091.5	0.000556	58.3003
4	5.596	P-coumeric acid	Phenolic	116,404.2	12,438.0	0.000871	101.388
5	7.041	BHT	Phenolic	762,383.8	80,103.7	0.00025	190.595
6	7.842	Caffeic acid	Phenolic	1,318,761.3	70,615.5	0.00040	527.50
7	12.679	Sinapic acid	Phenolic	344,898.5	33,079.7	0.000435	150.030
8	12.967	Ferulic acid	Phenolic	542,153.2	51,932.4	0.000877	475.46
9	24.893	Querctin	Flavonoid	270,762.4	20,610.2	0.000665	180.05

TABLE 4: Characteristic absorption peaks with their amount of PKM1 variety.

Peak	RT (min)	Component	Nature	Area	Height	K- factor	Final amount (ppm)
1	2.799	Chlorogenic acid	Phenolic	484,088.1	53,554.5	0.0008	387.27
2	3.023	Coumaric acid	Phenolic	537,838.6	62,551.3	0.0001	53.7838
3	7.478	Caffeic acid	Phenolic	73,891.8	4,703.5	0.0004	29.556
4	12.176	Sinapic acid	Flavonoid	1,039,867.8	70,823.3	0.0003	311.96
5	15.608	Salicylic acid	Flavonoid	34,881.7	2,630.1	0.00023	80.2227

FIGURE 5: Percentage of inhibition of free radicals by seed extracts of *M. oleifera*.

extract showed that it consists of high content of phenolics and flavonoids.

Caffeic acid was detected in highest amount among all the phenolics. Caffeic acid is known for its most potent antioxidant activity. The amount of phenolics can be ordered as caffeic acid > ferulic acid > gallic acid > BHT > sinapic acid > P – coumaric acid > catechin > chlorogenic acid (Table 3). Quercetin was the only flavonoid detected through HPLC chromatogram. Quercetin is one of the most potent antioxidant and also used commercially in pharmaceutical purposes. Moreover, it is a potent and versatile antioxidant, medically used to protect the cells from injury induced by inner or outer stimuli. The anti-inflammatory and antioxidant properties of phenolics and flavonoids help to remove free radicals and provide protection against free radical damage.

The maximum amount of chlorogenic acid as phenolic was detected in PKM1 seeds (Table 4). The amount of phenolic can be ordered as: chlorogenic acid > coumaric acid > caffeic acid. The amount of flavonoid in PKM1 seeds can be ordered as: sinapic acid > salicylic acid. The salicylic acid is one of the most explored and commercially used flavonoid for its antioxidative properties. Both varieties possess good amount of phenolic and flavonoid. M-Mln contains more phenolics than PKM1. HPLC analysis of methanol extract of both varieties can allow the researchers to adjust the nutritional proportions for clinical uses as antioxidants as M-Mln seeds are rich source of antioxidants specifically phenolics. Therefore, the use of moringa seeds as natural antioxidants could prove more beneficial than the synthetic and commercially available antioxidants.

### 3.3. Antioxidant Activity Assay

**3.3.1. DPPH Assay.** DPPH radical scavenging assay is commonly used to determine the antioxidant potential, and only

the potent antioxidant candidate can promisingly scavenge the DPPH free radicals, thus it may also inhibit major mechanisms associated with oxidative stress, mainly caused by lipid peroxidation. In order to evaluate the DPPH radical-scavenging activity of the two extracts of *M. oleifera* seeds, we examined a significant ( $p < 0.05$ ) decrease in the concentration of DPPH free radicals through our specific experimental setup, due to the scavenging potential of these extracts (Figure 5).

Free radicals scavenging activity of methanol and n-Hexane extracts of M-Mln and PKM1 seeds were compared. The results were expressed as percentage of inhibition (%). The highest percentage of inhibition and least IC<sub>50</sub> of all samples were recorded (Table 5). The highest mean percentage of inhibition of DPPH free radicals was observed in methanol extracts as compared to the n-Hexane extract of M-Mln seeds as reported by [52]. The results of DPPH free radical scavenging activity indicated that *M. oleifera* seed extracts have significant and concentration-dependent scavenging activity with the methanol fraction being the most active one as shown in Figure 5.

The results showed that the methanol M-Mln seed extract possess the highest percentage of inhibition with  $60.22 \pm 1.32\%$  and followed by the methanol PKM1 seed extract which possess the percentage of inhibition of  $54.92 \pm 1.13\%$  (Table 5). Though, the lowest inhibitory concentration (IC<sub>50</sub>) was  $84 \mu\text{g/ml}$  detected in methanol M-Mln seed extract. Many researches have revealed the effectiveness of *M. oleifera* as a source of antioxidants as evidenced by identification of Ascorbic acid, flavonoid, tocopherols, and phenolic [43, 53–55]. These findings concluded the M-Mln seeds as an excellent source of natural antioxidants.

As illustrated in Table 5, methanol extract of M-Mln seeds showed the lowest IC<sub>50</sub> values ( $84 \mu\text{g/ml}$ ), which correspond to the greatest DPPH radical scavenging potential,



TABLE 5: Mean (%) inhibition of DPPH radicals of M-Mln and PKM1 seeds of *M. oleifera*.

Extract	Samples	Mean (%) inhibition of DPPH radicals $\pm$ SD	IC50 ( $\mu$ g/ml)
Methanol	M-Mln	60.22 $\pm$ 1.32	84
	PKM1	54.92 $\pm$ 1.13	540
Hexane	M-Mln	34.53 $\pm$ 1.51	
	PKM1	29.13 $\pm$ 1.24	

$n = 3$  means values represent mean percentage inhibition of DPPH radicals of M-Mln and PKM1 seeds of *M. oleifera*.

followed by IC50 value of PKM1 (540  $\mu$ g/ml). Consistent with the reported studies, the DPPH free radicals can be effectively inhibited by methanol extract of *M. oleifera* seeds with an excellent inhibition of 60.22%, whereas the hexane extracts showed comparatively less DPPH scavenging potential, and respective percentage inhibitions were 34.53% and 29.13% at the same concentration. The radical scavenging ability of *M. oleifera* seeds is remarkable to inhibit the oxidative stress.

**3.3.2. Total Flavonoids Content.** The antioxidant activity of extracts is mainly associated with the active phytochemicals, ubiquitous in plants. Flavonoids, a special class of phenolic compounds, can scavenge/delay the oxidation via transfer of electrons to radicals. Flavonoids are secondary metabolites, enhance the activity of Vitamin C, biologically active and important antioxidants. In this study, TFC was done to quantify the antioxidants in *M. oleifera* seeds extracts (Figure 6). It could be seen that the methanol extract of M-Mln seeds showed the highest TFC, followed by methanol extract of PKM1. These findings were consistent with reported higher radical scavenging efficiency.

The total flavonoids content was higher in both methanol seed extracts than n-Hexane extracts (Figure 6). The methanol extract of M-Mln was found to comprise thrice flavonoids of hexane extract. Whereas, the least was observed from the n-Hexane extract of PKM1 (Table 6) as reported by [56]. The methanol extract of M-Mln was found to show highest TFC as 76.07  $\pm$  1.10 mg/g. The hexane extract of PKM1 was found to show least TFC as 22.47  $\pm$  1.70 mg/g.

These findings indicated that the TFC in methanol extracts were significantly higher than that of other extracts. Methanol extracts exhibited most potent radical-scavenging activity, consistent with other studies, in which the role of flavonoids as antioxidants had previously suggested. Furthermore, the antioxidant activity in plants is mainly contributed by their phenolic compounds, such as flavonoids, therefore, such findings could play a pivotal role in corresponding medicinal plants.

**3.3.3. Total Phenolics Content.** The antioxidant efficacy of phenol-based antioxidants is mainly linked to the redox properties of the compounds and their structural characteristics such as hydrogen-donating hydroxyl groups, which ultimately afford the quenching of free radicals generated

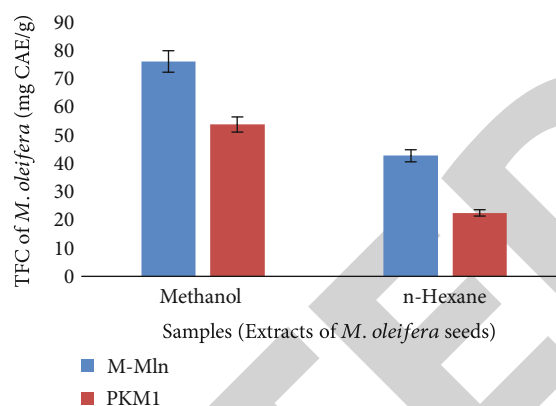


FIGURE 6: Total flavonoid content of extracts of *M. oleifera* seeds (mg CAE/g).

TABLE 6: Total flavonoid content of extracts of *M. oleifera* seeds.

Extracts	Samples	TFC of <i>M. oleifera</i> (mg CAE/g)
Methanol	M-Mln	76.07 $\pm$ 1.10
	PKM1	53.75 $\pm$ 0.90
Hexane	M-Mln	42.68 $\pm$ 2.12
	PKM1	22.47 $\pm$ 1.70

$n = 3$  represents mean values of TFC of *M. oleifera* seeds.

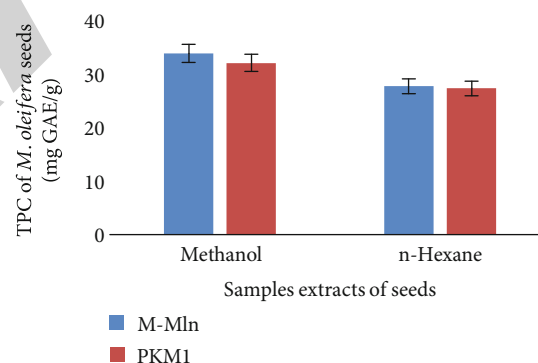


FIGURE 7: Total phenolic content of extracts of *M. oleifera* seeds (mg GAE/g).

in response to oxidative damage. TPC of methanol extracts of M-Mln was found to be higher than hexane extracts (Figure 7) as the findings of [57].

The methanol extract of M-Mln was found to show highest TPC as 33.83  $\pm$  1.19 mg/g. The hexane extract of PKM1 was found to show least TPC as 27.28  $\pm$  0.95 mg/g (Table 7). It is due to the difference in polarity of two solvents used during study. The phenolics can be extracted in polar solvents. The results indicated the presence of fine phenolics in M-Mln variety than PKM1 variety.

Solvent based extraction of seeds has shown substantial role in varied antioxidant activity depending on their phenolic content extracted. Hydroxyl (OH) group in phenolics may be directly involved in enhanced antioxidant activity and a key determinant of their free radical scavenging

TABLE 7: Total phenolic content of *M. oleifera* seeds.

Extracts	Samples	TPC of <i>M. oleifera</i> seeds (mg GAE/g) mean SD
Methanol	M-Mln	33.83 ± 1.19
	PKM1	32.07 ± 1.13
n-hexane	M-Mln	27.69 ± 1.50
	PKM1	27.28 ± 0.95

$n = 3$  represents mean value of *M. oleifera* seeds.

ability. Nevertheless, phenolics have been reported as a significant class of secondary metabolites which are found in medicinal plants. Thus, *M. oleifera* can be used as a source of phenolics. However, its use can help to reduce the risk of diseases by its antioxidant power.

#### 4. Conclusion

This study has showed that the seeds of *M. oleifera* is a potent source of antioxidants. Two indigenously produced varieties were analyzed. The antioxidant activity was greatly affected by the solvent used for extraction. The methanol extracts of both varieties showed better free radical scavenging activity than those of hexane extracts. These findings verified and validated the traditional use of seeds in order to treat oxidative stress related diseases as well as other diseases. The methanol extract of M-Mln variety with lowest IC50 value proved its more antioxidant potential than hexane extract. Besides, the total phenolics as well as flavonoids content also proved better potential of methanol extracts over hexane extracts, which contributed to antioxidant activity. Phenols and flavonoids are naturally found secondary metabolites in medicinal plant, which are extracted to cure various diseases related to oxidative stress caused by free radicals. These findings showed that the *M. oleifera* seeds possess the potency to cure oxidative stress, which can be ascribed to the presence of important phytochemicals. Thus, the present work along with previous researches reveal that the *M. oleifera* is a tremendous plant for its biomedical applications, which can be used to improve the health concerns along with overall nutrition rate in developing countries due to its nutritional benefits and biologically active products. Further work is needed to carry out more pharmacological support behind its use for its antioxidant purposes.

#### Data Availability

There is no data availability for this manuscript.

#### Conflicts of Interest

The authors declare that they have no conflicts of interest.

#### Acknowledgments

This work was funded by the Researchers' Supporting Project Number (RSP-2021/259), King Saud University, Riyadh, Saudi Arabia.

#### References

- [1] I. A. Jahan, M. H. Hossain, K. S. Ahmed, Z. Sultana, P. K. Biswas, and K. Nada, "Antioxidant activity of Moringa oleifera seed extracts," *Oriental Pharmacy and Experimental Medicine*, vol. 18, no. 4, pp. 299–307, 2018.
- [2] L. Liang, C. Wang, S. Li, X. Chu, and K. Sun, "Nutritional compositions of Indian Moringa oleifera seed and antioxidant activity of its polypeptides," *Food Science & Nutrition*, vol. 7, no. 5, pp. 1754–1760, 2019.
- [3] H. A. Ogbunugafor, F. U. Eneh, A. N. Ozumba et al., "Physicochemical and antioxidant properties of Moringa oleifera seed oil," *Pakistan Journal of Nutrition*, vol. 10, no. 5, pp. 409–414, 2011.
- [4] T. A. Aderinola, T. N. Fagbemi, V. N. Enujiugha, A. M. Alashi, and R. E. Aluko, "Amino acid composition and antioxidant properties of Moringa oleifera seed protein isolate and enzymatic hydrolysates," *Heliyon*, vol. 4, no. 10, p. e00877, 2018.
- [5] A. F. Santos, A. C. C. Argolo, P. M. G. Paiva, and L. C. B. B. Coelho, "Antioxidant activity of Moringa oleifera tissue extracts," *Phytotherapy Research*, vol. 26, no. 9, pp. 1366–1370, 2012.
- [6] W. D. Fitriana, T. Ersam, K. Shimizu, and S. Fatmawati, "Antioxidant activity of Moringa oleifera extracts," *Indonesian Journal of Chemistry*, vol. 16, no. 3, pp. 297–301, 2016.
- [7] S. Sreelatha and P. Padma, "Antioxidant activity and total phenolic content of Moringa oleifera leaves in two stages of maturity," *Plant Foods for Human Nutrition*, vol. 64, no. 4, pp. 303–311, 2009.
- [8] A. Khalid Rai, A. Hameed, and R. Noreen, "Antioxidant potential and biochemical analysis of Moringa oleifera leaves," *International Journal of Agriculture & Biology*, vol. 19, no. 4, pp. 941–950, 2017.
- [9] X. Gu, Y. Yang, and Z. Wang, "Nutritional, phytochemical, antioxidant,  $\alpha$ -glucosidase and  $\alpha$ -amylase inhibitory properties of Moringa oleifera seeds," *South African Journal of Botany*, vol. 133, pp. 151–160, 2020.
- [10] A. Bhattacharya, P. Tiwari, P. K. Sahu, and S. Kumar, "A review of the phytochemical and pharmacological characteristics of Moringa oleifera," *Journal of Pharmacy & Bioallied Sciences*, vol. 10, no. 4, pp. 181–191, 2018.
- [11] K. Chandrashekar, T. Ajay, and K. Prasanna, "Anti-inflammatory activity of Moringa oleifera stem bark extracts against carrageenin induced rat paw edema," *Journal of Chemical and Pharmaceutical Research*, vol. 2, no. 3, pp. 179–181, 2010.
- [12] A. P. Chauhan, D. M. Patel, J. D. Pate, and N. K. Singh, "Extraction, screening, and characterization of bioactive compounds from Moringa oleifera: extends life-span of *Caenorhabditis elegans*," *Current Trends in Biotechnology and Pharmacy*, vol. 15, no. 3, pp. 282–298, 2021.
- [13] A. N. Nasution, "Enhance effectiveness of Moringa leaves with staphylococcus epidermidis bacteria," *Budapest International Research and Critics Institute-Journal (BIRCI-Journal)*, vol. 4, no. 2, pp. 1705–1712, 2021.
- [14] Z. Ma, J. Ahmad, H. Zhang, I. Khan, and S. Muhammad, "Evaluation of phytochemical and medicinal properties of Moringa (*Moringa oleifera*) as a potential functional food," *South African Journal of Botany*, vol. 129, pp. 40–46, 2020.
- [15] B. S. Mushtaq, I. Pasha, R. Omer et al., "Characterization of Moringa oleifera leaves and its utilization as value added ingredient in unleavened flat bread (chapatti)," *Journal of Microbiology, Biotechnology and Food Sciences*, vol. 2021, pp. 750–755, 2021.

- [16] I. Vicente, S. Gomez-Martinez, L. E. Diaz-Prieto et al., "Effect of Moringa oleifera as a dietary supplement on the control of prediabetic subjects' glycaemia in annals of nutrition and metabolism," *Annals of Nutrition and Metabolism*, vol. 76, supplement 4, 2020.
- [17] H. Nhut, N. T. Q. Hung, B. Q. Lap et al., "Use of Moringa oleifera seeds powder as bio-coagulants for the surface water treatment," *International journal of Environmental Science and Technology*, vol. 18, no. 8, pp. 2173–2180, 2021.
- [18] A. Bakar, A. Uba, and T. Oyeyi, "Antimicrobial profile of moringa oleifera lam. Extracts against some food – borne microorganisms," *Journal of Pure and Applied Sciences*, vol. 3, no. 1, 2010.
- [19] P. H. Chuang, C. W. Lee, J. Y. Chou, M. Murugan, B. J. Shieh, and H. M. Chen, "Anti-fungal activity of crude extracts and essential oil of Moringa oleifera lam," *Bioresource Technology*, vol. 98, no. 1, pp. 232–236, 2007.
- [20] G. Dewangan, K. M. Koley, V. P. Vadlamudi, A. Mishra, A. Poddar, and S. D. Hirpurkar, "Antibacterial activity of Moringa oleifera (drumstick) root bark," *Journal of Chemical and Pharmaceutical Research*, vol. 2, no. 6, pp. 424–428, 2010.
- [21] U. Eilert, B. Wolters, and A. Nahrstedt, "The antibiotic principle of seeds of Moringa oleifera and Moringa stenopetala," *Planta Medica*, vol. 42, no. 5, pp. 55–61, 1981.
- [22] J. W. Fahey, "Moringa oleifera: a review of the medical evidence for its nutritional, therapeutic, and prophylactic properties," *Part 1. Trees for life Journal*, vol. 1, no. 5, pp. 1–15, 2005.
- [23] J. Lietava, "Medicinal plants in a middle Paleolithic grave Shanidar IV?," *Journal of Ethnopharmacology*, vol. 35, no. 3, pp. 263–266, 1992.
- [24] P. Nepolean, J. Anitha, and R. Emilin, "Isolation, analysis and identification of phytochemicals of antimicrobial activity of Moringa oleifera lam," *Current Biotica*, vol. 3, no. 1, pp. 33–37, 2009.
- [25] A. Jaja-Chimedza, B. L. Graf, C. Simmler et al., "Biochemical characterization and anti-inflammatory properties of an isothiocyanate-enriched moringa (Moringa oleifera) seed extract," *PLoS One*, vol. 12, no. 8, p. e0182658, 2017.
- [26] I. L. Jung, "Soluble extract from Moringa oleifera leaves with a new anticancer activity," *PLoS One*, vol. 9, no. 4, p. e95492, 2014.
- [27] J. N. Kasolo, G. S. Bimenya, L. Ojok, J. Ochieng, and J. W. Ogwal-Okeng, "Phytochemicals and uses of Moringa oleifera leaves in Ugandan rural communities," *Journal of Medicinal Plants Research*, vol. 4, no. 9, pp. 753–757, 2010.
- [28] Z. Hübsch, R. L. van Zyl, I. E. Cock, and S. F. van Vuuren, "Interactive antimicrobial and toxicity profiles of conventional antimicrobials with southern African medicinal plants," *South African Journal of Botany*, vol. 93, pp. 185–197, 2014.
- [29] O. Igado and J. Olopade, "A review on the possible neuroprotective effects of Moringa oleifera leaf extract," *Nigerian Journal of Physiological Sciences*, vol. 31, no. 2, pp. 183–187, 2016.
- [30] O. S. Ijarotimi, O. A. Adeoti, and O. Ariyo, "Comparative study on nutrient composition, phytochemical, and functional characteristics of raw, germinated, and fermented Moringa oleifera seed flour," *Food Science & Nutrition*, vol. 1, no. 6, pp. 452–463, 2013.
- [31] X.-F. Wang, Y. Fan, F. Xu et al., "Characterization of the structure, stability, and activity of hypoglycemic peptides from Moringa oleifera seed protein hydrolysates," *Food & Function*, vol. 13, no. 6, pp. 3481–3494, 2022.
- [32] A. M. E. Sayed, F. A. Omar, M. M. A. A. Emam, and M. A. Farag, "UPLC-MS/MS and GC-MS based metabolites profiling of Moringa oleifera seed extract with its anti-helicobacter pylori and anti-inflammatory activities," *Natural Product Research*, vol. 6, pp. 1–6, 2022.
- [33] I. Ezebuio, A. Ododo, and U. I. Apugo, "Hepato-renal activities of hydro-methanol leaf extract of Cnidioscolus aconitifolius in adult male Wistar rats," *Journal of Drug Delivery and Therapeutics*, vol. 11, no. 4, pp. 5–9, 2021.
- [34] E. R. Zunica, S. Yang, A. Coulter, C. White, J. P. Kirwan, and L. A. Gilmore, "Moringa oleifera seed extract concomitantly supplemented with chemotherapy worsens tumor progression in mice with triple negative breast cancer and obesity," *Nutrients*, vol. 13, no. 9, p. 2923, 2021.
- [35] M. Abdul Haseeb, M. Z. Sarkhil, M. Fayazuddin, and F. Ahmad, "Peripheral analgesic activity of Moringa oleifera seeds - An experimental study," *Asian Journal of Pharmacy and Pharmacology*, vol. 7, no. 5, pp. 200–203, 2021.
- [36] A. Ali, P. Garg, R. Goyal et al., "An efficient wound healing hydrogel based on a hydroalcoholic extract of Moringa oleifera seeds," *South African Journal of Botany*, vol. 145, pp. 192–198, 2022.
- [37] D. A. Palupi, T. W. Prasetyowati, D. Murtiningsih, and D. Mahdiyah, "Antiasthma activities of Moringa oleifera lam. Leaves extract on the eosinophil count and mast cells in BALB/c mice," *Borneo Journal of Pharmacy*, vol. 4, no. 3, pp. 171–177, 2021.
- [38] S. R. Farhan, A. H. AL-Azawi, W. Y. Salih, and A. A. Abdullhassan, "The antibacterial and antioxidant activity of Moringa oleifera seed oil extract against some foodborne pathogens," *Indian Journal of Forensic Medicine & Toxicology*, vol. 15, no. 4, p. 2529, 2021.
- [39] T. G. Kebede, S. Dube, and M. M. Nindi, "Fabrication and characterization of electrospun nanofibers from Moringa stenopetala seed protein," *Materials Research Express*, vol. 5, no. 12, article 125015, 2018.
- [40] A. A. Gaafar, E. A. Ibrahim, M. S. Asker, A. F. Moustafa, and Z. A. Salama, "Characterization of polyphenols, polysaccharides by HPLC and their antioxidant, antimicrobial and anti-inflammatory activities of defatted Moringa (Moringa oleifera L.) meal extract," *International Journal of Pharmaceutical and Clinical Research*, vol. 8, no. 6, pp. 565–573, 2016.
- [41] M. A. Hossain, N. K. Disha, J. H. Shourove, and P. Dey, "Determination of antioxidant activity and total tannin from drumstick (Moringa oleifera lam.) leaves using different solvent extraction Methods," *Science and Technology*, vol. 8, no. 12, pp. 2749–2755, 2020.
- [42] S. Sharma, D. C. Saxena, and C. S. Riar, "Antioxidant activity, total phenolics, flavonoids and antinutritional characteristics of germinated foxtail millet (Setaria italica)," *Cogent Food & Agriculture*, vol. 1, no. 1, p. 1081728, 2015.
- [43] T. Katsube, H. Tabata, Y. Ohta et al., "Screening for antioxidant activity in edible plant products: comparison of low-density lipoprotein oxidation assay, DPPH radical scavenging assay, and Folin-Ciocalteu assay," *Journal of Agricultural and Food Chemistry*, vol. 52, no. 8, pp. 2391–2396, 2004.
- [44] R. Noreen, M. Moenner, Y. Hwu, and C. Petibois, "FTIR spectro-imaging of collagens for characterization and grading of gliomas," *Biotechnology Advances*, vol. 30, no. 6, pp. 1432–1446, 2012.
- [45] C. S. Araújo, V. N. Alves, H. C. Rezende et al., "Characterization and use of Moringa oleifera seeds as biosorbent for removing

## *Retraction*

# **Retracted: Development of Deep Learning Technique of Features for the Analysis of Clinical Images Integrated with CANN**

### **BioMed Research International**

Received 8 January 2024; Accepted 8 January 2024; Published 9 January 2024

Copyright © 2024 BioMed Research International. This is an open access article distributed under the Creative Commons Attribution License, which permits unrestricted use, distribution, and reproduction in any medium, provided the original work is properly cited.

This article has been retracted by Hindawi following an investigation undertaken by the publisher [1]. This investigation has uncovered evidence of one or more of the following indicators of systematic manipulation of the publication process:

- (1) Discrepancies in scope
- (2) Discrepancies in the description of the research reported
- (3) Discrepancies between the availability of data and the research described
- (4) Inappropriate citations
- (5) Incoherent, meaningless and/or irrelevant content included in the article
- (6) Manipulated or compromised peer review

The presence of these indicators undermines our confidence in the integrity of the article's content and we cannot, therefore, vouch for its reliability. Please note that this notice is intended solely to alert readers that the content of this article is unreliable. We have not investigated whether authors were aware of or involved in the systematic manipulation of the publication process.

Wiley and Hindawi regrets that the usual quality checks did not identify these issues before publication and have since put additional measures in place to safeguard research integrity.

We wish to credit our own Research Integrity and Research Publishing teams and anonymous and named external researchers and research integrity experts for contributing to this investigation.

The corresponding author, as the representative of all authors, has been given the opportunity to register their agreement or disagreement to this retraction. We have kept a record of any response received.

### **References**

- [1] P. Kasinathan, R. Prabha, R. S. Sabeenian, K. Baskar, A. Ramkumar, and S. Alemayehu, "Development of Deep Learning Technique of Features for the Analysis of Clinical Images Integrated with CANN," *BioMed Research International*, vol. 2022, Article ID 2742274, 7 pages, 2022.

## Research Article

# Development of Deep Learning Technique of Features for the Analysis of Clinical Images Integrated with CANN

**Prabakaran Kasinathan** <sup>1</sup>, **R. Prabha** <sup>2</sup>, **R. S. Sabeenian** <sup>3</sup>, **K. Baskar** <sup>4</sup>,  
**A. Ramkumar** <sup>5</sup> and **Samson Alemayehu** <sup>6</sup>

<sup>1</sup>Department of Computer Science and Engineering, School of Computing, Vel Tech Rangarajan Dr. Sagunthala R&D Institute of Science and Technology, Chennai, 600062 Tamil Nadu, India

<sup>2</sup>Department of Electronics and Communication Engineering, Sri Sai Ram Institute of Technology, Chennai, 600044 Tamil Nadu, India

<sup>3</sup>Department of Electronics and Communication Engineering, Sona College of Technology, Salem, 636005 Tamil Nadu, India

<sup>4</sup>Department of Artificial Intelligence and Data Science, Kongunadu College of Engineering and Technology, Trichy, 621215 Tamil Nadu, India

<sup>5</sup>Department of Electrical and Electronics Engineering, Kalasalingam Academy of Research and Education, Krishnankoil, Tamil Nadu, India

<sup>6</sup>Department of Electrical and Computer Engineering, Faculty of Electrical and Biomedical Engineering, Institute of Technology, Hawassa University, Ethiopia

Correspondence should be addressed to Samson Alemayehu; samson@hu.edu.et

Received 12 August 2022; Accepted 30 September 2022; Published 14 October 2022

Academic Editor: Senthil Rethinam

Copyright © 2022 Prabakaran Kasinathan et al. This is an open access article distributed under the Creative Commons Attribution License, which permits unrestricted use, distribution, and reproduction in any medium, provided the original work is properly cited.

Computer tomography is an extensively used method for the detection of the disease in the subjects. Basically, computer-aided tomography depending on the artificial intelligence reveals its significance in smart health care monitoring system. Owing to its security and the private issue, analyzing the computed tomography dataset has become a tedious process. This study puts forward the convolutional autoencrypted deep learning neural network to assist unsupervised learning technique. By carrying out various experiments, our proposed method produces better results comparative to other traditional methods, which efficaciously solves the issues related to the artificial image description. Hence, the convolutional autoencoder is widely used in measuring the lumps in the bronchi. With the unsupervised machine learning, the extracted features are used for various applications.

## 1. Introduction

Computed tomography is a widely used method in recent years, in which clinician early examines the nature of the disease in a very systematic manner and the cause of the disease is also detected priorly. For each and every subject, there may be several images taken for examination due to this complexity and proper validation is not possible; thus, to solve this, smart medical management plays a vital role [1]. Primarily, detection of the lumps in the bronchi is of main task; hence, this helps in detecting the early stage of

the tumor in the bronchi through the enormous quantity of the pneumatic computed tomography images. Thus, the examination of the images is done in several ways: (i) to define the ROI (region of interest), (ii) image segmentation, and (iii) manual feature extraction and finally classification [2]. In order to analyze the lump, the extraction of the features is performed. Considering the size, shape, and edges of the lump, the disease is classified. The systematic approach does not provide better results [3]. Medical expertise may produce a defective result in examining the disease. Thus, the feature extraction process helps in the analyses of

the lump in the bronchi. Thus, convolution neural network plays a significant role in the determining the lump in the bronchi better than that of the manual feature extraction process. Hence, the numerous datasets are needed for this feature extraction process [4].

To overcome these challenges, an effective deep learning framework depending on convolutional autoencrypted neural network (CANN) was used for categorizing the lump in the bronchi [5]. The initial stage required for examining the lump in the bronchi uses the normal image, and then from the input image, the features are represented. In order to classify the lump in the bronchi, the computed tomography images are required and the spotted images are extracted. Each respective spot contains the particular set of results. The result proves that the suggested method is much effective in the feature extraction process [6]. The main essential of using convolutional autoencoder neural network rather than using CNN is to acquire the low-dimensional noiseless image representation and acquisition for the purpose of extracting its features and classification and hence would yield higher accuracy results. It also aids the added advantage of a unique case of an unsupervised learning model for reproducing the best noiseless input image with its adequate feature attribute values.

The illustration of the system defining the lack of unlabeled feature samples has been depicted in Figure 1. In addition to that, the illustration over the schematic block functional representation of CANN for medical image analysis has been depicted in Figure 2. From the actual computed tomography images, the spotted parts are thoughtlessly selected for the examination of the lumps in the bronchi. Thus, the labelling of the image and the region of the interest are calculated efficiently by the clinician [7]. Hence, there exists a lump in the respiratory track; thus, to solve this issue, the learning approach is implemented. In order to eliminate the huge amount of data obtained from manual feature extraction process, our proposed method uses CANN to avoid such issues; they are capable of effectively detecting the inadequacy in the training data. Through the original image, the feature extraction process is performed. This kind of extinguished method does not require segmentation process to detect the spot; these unsupervised data are used in other various applications [8]. Performance realizations over the various classifications as shown in Table 1.

## 2. Related Literature Survey

So as to obtain the extracted feature, the selection of features has to be done. Deep learning is an emerging work performed in the recent years. Comparative to the traditional method, the data-driven feature learning approach produces better results [9, 10]. With the help of the deep learning technique, the feature extraction process is carried from the original image datasets, and the intricate features are extracted by the reoccurring layers. Essentially, the representation learning is categorized into two types; one is unsupervised learning and supervised learning [11]. For the prediction purpose, the data are transmitted from the initial

stage to the top most layer. The back propagation is the technique used for evaluating the cost function linking the predicted and the target value [12, 13]. CNN is basically used in speech identification, image examination, and text exploration. In the image examination, the CNN plays a vital role in face identifying, segmentation of the cell, identifying the breast images, and identifying the injury in the brain. Whereas in unsupervised learning to predict the features of the images, the unlabeled features are used and the fewer amount of supervised data are used for attenuating the parameters [14]. In this study, a convolutional autoencrypted learning algorithm is proposed to determine the features of the computed tomography bronchi images and to categorize the spot in the respiratory track. In our proposed study, the unsupervised autoencrypted feature and CNN were combined to extricate the feature of the image. Owing to the lack of medical labeling images for the training purpose, the unsupervised learning methods are incorporated [15].

## 3. Proposed CANN Model

The spot segregated from the original computed tomography image is given as the input to the CANN for the feature learning and representation process. The labelled data are used for attenuating the parameters of the CANN. The spot separated from the normal image is denoted by  $x \in X$ ,  $X \subset \mathbb{R}^{m \times d \times d}$  where  $m$  is the total number of the input channel and  $d \times d$  is the size of the input image. The labeled data are denoted by  $y \in Y$ ,  $Y \subset \mathbb{R}^n$  where  $n$  represents the number of output classification. The hypothesis function is denoted as  $f : X \rightarrow Y$ . Thus, in the proposed model, the hypothesis function  $f$  comprises of the multiple layers, and they are not connected to  $X$  to  $Y$  directly [16]. The center layer constitutes the three-pooling layer, three-convolution layer, and fully connected layer. The structure of the CANN is depicted in Figure 3.

The training data comprises of the labelled data and the unlabeled data,  $UD = \{x, x \in X\}$  and  $D = \{x, y; x \in X, y \in Y\}$  where  $UD$  denotes the unsupervised learning and the  $D$  represents supervised learning.

**3.1. Standard Autoencoder.** Thus, to perform data-driven representation learning, the supervised approach is initiated. The weights are applied to both the forward and the backward algorithms. The unlabeled input data are obtained from the unsupervised approach compared to that of the supervised approach. Autoencrypted method is applied in this study [18]. Later on, in performing several iterations, the cost function is validated. The input data is denoted by  $I$ ; it corresponds to  $m$  dimension vector  $I \in \mathbb{R}^m$ .

**3.2. Convolution Autoencoder.** Convolution autoencoder integrates convolution relation with the autoencrypted process. The values obtained from the output are patched via reverse convolution encrypted process. With the help of unsupervised training, the decoding and encoding performances are evaluated. The convolution encoder is represented by  $f(\cdot)$ , and the convolution decoder is denoted by

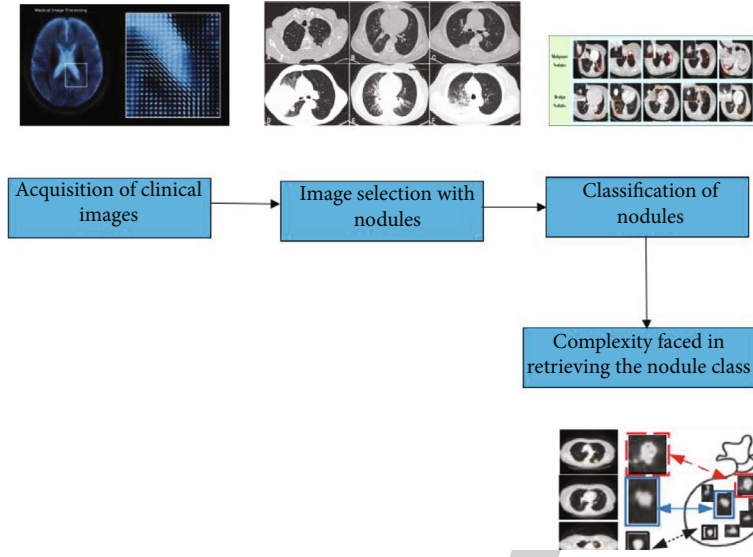


FIGURE 1: Illustration of the system defining the lack of unlabeled feature samples.

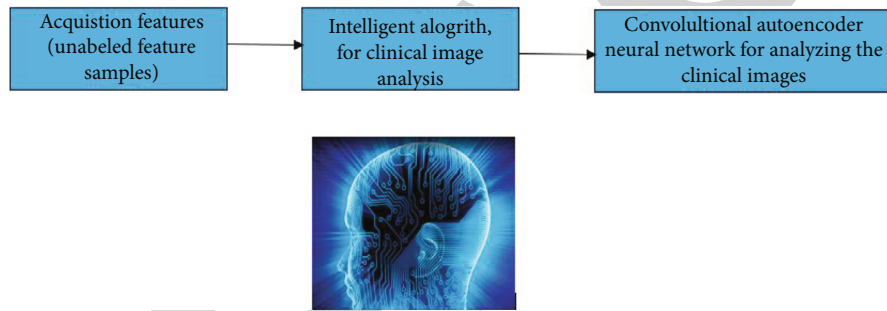


FIGURE 2: Illustration of CANN for medical image analysis.

TABLE 1: Performance realizations over the various classifications.

Methodology	Precision (%)	Recall (%)	Accuracy (%)	AUC	F1 (%)
AE	78.45	77.24	77.43	0.82	77.35
CANN	93.45	92.42	92.16	0.98	92.19
CNN	90.46	91.28	91.99	0.93	91.56
MCCNN	91.22	90.65	89.14	0.96	91.23

$f(\cdot)$ . Thus, the convolution autoencoder process includes  $m$  convolution kernels.  $n$  is considered as the number of input channel. The convolution kernel size is  $d \times d$ .

The indiscriminate activation function is denoted by  $\sigma$ . This comprises of the various functions such as the elliptical function, inflated tangent function, and the rectified linear function (Relu).

$$\text{Relu}(x) = \begin{cases} x & x \geq 0, \\ 0 & x < 0. \end{cases} \quad (1)$$

3.3. *Pooling*. The proposed CANN method is analogous to that of CNN. The pooling layer is connected to that of the convolutional layer. In the proposed CANN method, there

exists the max pooling layer succeeding the convolutional layer [18].

$$o_j^i = \max(x_j^i). \quad (2)$$

As per the size of the pooling layer, the input feature map is subdivided into  $n$  overlapping regions. Thus,  $x_j^i$  denotes the region in the  $i$ th place and the feature map of the  $j$ th position, and the  $o_j^i$  denotes the region in the  $i$ th place and the feature map of the  $j$ th position. In the pooling layer, the number of inputs is equal to that of the number of the output. After the pooling operation, the neurons in the

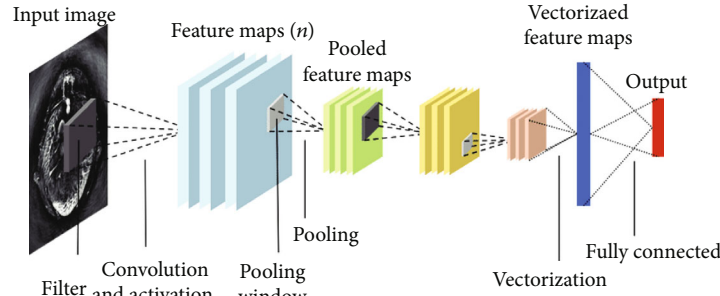


FIGURE 3: Illustration over the structure of CANN for clinical image analysis [17].

feature map gets reduced. Thus, there is reduction in the computational complexity.

**3.4. Cost Function.** SoftMax layer is useful for categorizing according to the feature such as the max pooling layer, fully connected layer, and multiple convolution autoencrypted process. The bronchi computed tomography image is distinguished into several categories [19]. Basically,  $\hat{y}_i$  denotes the random probability of the lumps and the absence of the lumps.

$$\hat{y}_i = \frac{e^{(o_i)}}{\sum_{k=1}^2 e^{o_k}}, i = 0, 1. \quad (3)$$

The cost function is represented by  $L$ . In order to reduce  $L$ , the SGD is initialized. Thus,  $y$  is denoted as the sample data. The absence of lumps is represented by 1.

$$L = -(y \log \hat{y}_0 + (1 - y) \log \hat{y}_1). \quad (4)$$

### 3.5. Training Parameters

**3.5.1. Convolution Autoencoder.** The unsampled images are used for training the autoencrypted process. With the use of cost function, the gradient is calculated. Each sample is incorporated in the particular set of process; for each iteration, 50 samples are utilized; thus, the total number of samples per layer is denoted by  $50 \times (N/100)$ . Hence, numerous channels are accompanied in the convolution encoder and decoder.

**3.5.2. Fully Connected Layer.** The fully connected layer attains its input from the last layer called the pooling layer. They are represented by 500 neurons. They are interconnected by the SoftMax classifier. At the fully connected layer, the parameter obtained via supervised learning is classified by the SoftMax classifier. For the categorizing process, 1800 labelled data are utilized [20].

**3.5.3. Algorithm of Training CANN.** The training in CANN depends on both the supervised and unsupervised learning.

## 4. Results and Discussions

**4.1. Dataset.** The data used for classification are gathered in the health center present in China [18]. It comprises of the 5000 subjects' bronchi images from 2012 to 2015. Hence,

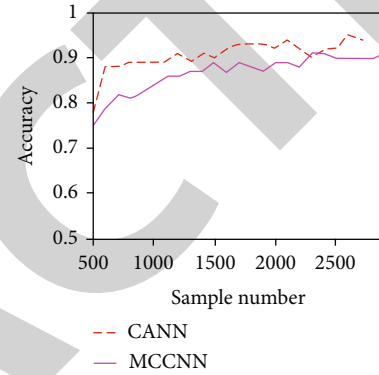


FIGURE 4: The resultant characteristics of training sample count read over the accuracy of classification over MCNN and CANN.

for each lump, the clinician examines the region of interest portion. The data are segregated into several datasets, namely, D1, D2, and D3, respectively [21, 22].

D1: it constitutes 50000 samples from the unlabeled data of the unsupervised learning with the spot traced about of  $64 \times 64$ . These minute spots are examined in each subject [23]

D2: D2 comprises of the labelled data with the spot of  $64 \times 64$ , approximately of 3700 traces. These are determined by the clinician out of which 1890 constitutes diseased image and the 1810 comprises of normal images [24]

D3: the D3 comprises of the 500 pair of the labelled spot. These images are notified by the clinician. The resemblance predicted is from 1 to 4 where 4 is the greatest resemblance obtained and 1 is the lowest resemblance occurred. Thus, the 60 samples are vomited with the same resemblance of the value 2. It is determined that the midway resemblance value is vomited

**4.2. Architecture Built with Convolution.** In our study, two kinds of CANN are suggested; one is C-CANN and the other is S-CANN. The C-CANN is used for classification purpose, and the S-CANN is used for computing the similarity in the process [25]. The C-CANN comprises of three groups connecting the pooling and the convolution layer accompanied by the fully connected layer and a classifier. The specification is represented below. The experimentation is being carried out using MATLAB version 2018.

The input constitutes  $64 \times 64$  spots.



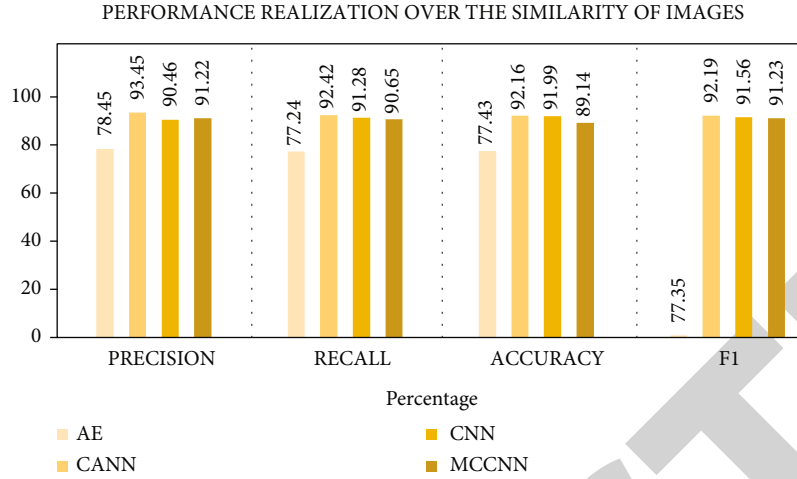


FIGURE 5: Performance realization over the similarity of images.

There are three convolution layer and three max pooling layers.

C1: in the initial phase, the convolution layer comprises of  $5 \times 5$  spots, and the total number of the convolutional part is 50

P1: the pooling area constitutes the size of about  $2 \times 2$

C2: in the next phase, the convolution layer comprises of  $3 \times 3$  spots, and the total number of the convolutional part is 50

P2: the pooling area constitutes the size of about  $2 \times 2$

C3: the convolution layer comprises of  $3 \times 3$  spots, and the total number of the convolutional part is 50

P3: the pooling area constitutes the size of about  $2 \times 2$

S-CANN comprises of 8 layers similar to that of the C-CANN. The feature extraction is done for the set of images and the evaluation is carried out.

### 4.3. Classification

4.3.1. *Impact of Sample Images.* Depending on the accuracy of the CANN and MCNN, the performance of them is computed. Thus, with the value of 2950 for both, the method execution is well performed. When it reaches 700 or 800, CANN produces better results [17].

4.3.2. *Performance Comparison and Classification.* Both the CNN and the conventional learning method produce identi-

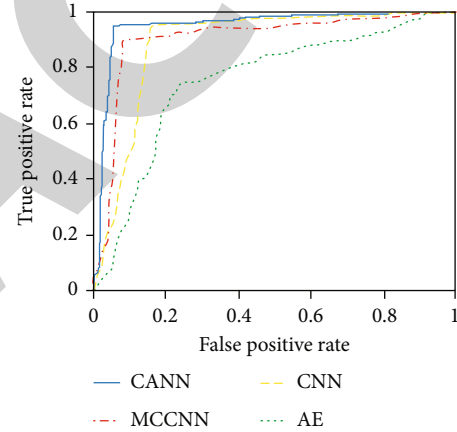


FIGURE 6: Receiver operating characteristics over classification.

cal result in determining the spot in the bronchi; they both use the labelled dataset for classification. Utilizing the forward and backward propagation, the network parameters are learnt. MCNN is an alternative of the CNN. The performances of the CNN, CANN, and MCCNN are compared and the ROC is plotted. The performance metrics such as precision, recall, accuracy, and F1 score have been calculated as follows:

$$\text{Precision} = \frac{TP}{TP + FP} = \frac{\text{Total number of perfectly predicted true instances}}{\text{Total number of positive predictions as result of experimentation}}, \quad (5)$$

$$\text{Accuracy} = \frac{TP + TN}{TP + TN + FP + FN} = \frac{\text{Total correct predictions}}{\text{Total predictions}}, \quad (6)$$

$$\text{Recall} = \frac{TP}{TP + FN}, \quad (7)$$

$$F1 \text{ score} = 2 * \frac{\text{Recall} * \text{Precision}}{\text{Recall} + \text{Precision}}. \quad (8)$$

The architecture of the CANN is utilized by the CNN and MCCNN. Thus, the precision, recall, accuracy, and *F1* are obtained as 93.45%, 92.42%, 92.16%, and 92.19%, respectively. Despite the above method, the AE produces the precision, recall, accuracy, and *F1* of about 78.45%, 77.24%, 77.43%, and 77.35%, respectively. The evaluation index of the CNN is 90.46%, 91.28%, 91.99%, and 91.56%. In addition to that, the evaluation index of MCNN is 91.22%, 90.65%, 89.14%, and 91.23%. Thus, the performance of the CANN is better compared to that of the CNN and MCCNN. Consequently, the AUC of AE, CANN, CNN, and MCCNN are 0.82, 0.98, 0.93, and 0.96, respectively, as shown in Figure 4.

**4.4. Similarity Check.** This technique enables clinician to predict the occurrence of the similar image. The similarity determination includes several parameters to be encountered; they are patterning, size, depth, boundary, etc.

Figure 5 shows the CANN performance regarding the similarity, classification, recall, accuracy, and *F1*. Thus, better results are obtained with the CANN method. Figure 6 depicts the ROC over classification performance. It is inferred that the attained error rate is being realized with the value of 0.92 which is as close to unity.

## 5. Conclusion

In this study, the image analysis pair of approaches has been initialized. The traditional approach is time-consuming and it requires huge labor; thus, data-driven approach is capable of losing the data about the spot occurred in the bronchi, whereby due to scarcity of the labelled data, these two methods are not implemented. Hence, our study proposed a CANN-based data-driven model with the addition of numerous unlabeled data and the fewer labelled data are used. The main novelty which has been incorporated is the processing of data being made in a pattern of grid with minimal complexity and minimal noises, and it follows the adaptive strategy in acquiring the hierarchical feature subsets from minimal to maximal level patterns. This study evaluates the spot in the bronchi and performs classification task as well as the similarity validation is also performed. Through lot of experiments, the proposed method is estimated as best for classifying the spot in the bronchi. Our future work involves combining the data-driven feature learning with the base knowledge, and further process is performed.

## Data Availability

The data used to support the findings of this study are included in the article. Should further data or information be required, these are available from the corresponding author upon request.

## Disclosure

This study was performed as a part of the employment of Hawassa University, Ethiopia.

## Conflicts of Interest

The authors declare that there are no conflicts of interest regarding the publication of this paper.

## Acknowledgments

The authors appreciate the technical assistance to complete this experimental work from the Department of Computer Science and Engineering, K. Ramakrishnan College of Technology, Samayapuram, Trichy 621112, India.

## References

- [1] M. Chen, Y. Ma, Y. Li, D. Wu, Y. Zhang, and C. H. Youn, "Wearable 2.0: enabling human-cloud integration in next generation healthcare systems," *IEEE Communications Magazine*, vol. 55, no. 1, pp. 54–61, 2017.
- [2] M. Chen, Y. Ma, J. Song, C. F. Lai, and B. Hu, "Smart clothing: connecting human with clouds and big data for sustainable health monitoring," *Mobile Networks and Applications*, vol. 21, no. 5, pp. 825–845, 2016.
- [3] T. Messay, R. C. Hardie, and T. R. Tuinstra, "Segmentation of pulmonary nodules in computed tomography using a regression neural network approach and its application to the lung image database consortium and image database resource initiative dataset," *Medical Image Analysis*, vol. 22, no. 1, pp. 48–62, 2015.
- [4] Y. Balagurunathan, Y. Gu, H. Wang et al., "Reproducibility and prognosis of quantitative features extracted from CT images," *Translational Oncology*, vol. 7, no. 1, pp. 72–87, 2014.
- [5] F. Han, G. Zhang, H. Wang et al., "A texture feature analysis for diagnosis of pulmonary nodules using LIDC-IDRI database," in *2013 IEEE International Conference on Medical Imaging Physics and Engineering*, pp. 14–18, Shenyang, China, 2013.
- [6] T. W. Way, B. Sahiner, H. P. Chan et al., "Computer-aided diagnosis of pulmonary nodules on CT scans: improvement of classification performance with nodule surface features," *Medical Physics*, vol. 36, no. 7, pp. 3086–3098, 2009.
- [7] W. Shen, M. Zhou, F. Yang, C. Yang, and J. Tian, "Multi-scale convolutional neural networks for lung nodule classification," in *International conference on information processing in medical imaging*, pp. 588–599, Springer, Cham, 2015.
- [8] Y. Bengio, A. Courville, and P. Vincent, "Representation learning: a review and new perspectives," *IEEE Transactions on Pattern Analysis and Machine Intelligence*, vol. 35, no. 8, pp. 1798–1828, 2013.
- [9] K. Hwang and M. Chen, *Big-Data Analytics for Cloud, IoT and Cognitive Computing*, John Wiley & Sons, 2017.
- [10] Y. LeCun, L. Bottou, Y. Bengio, and P. Haffner, "Gradient-based learning applied to document recognition," *Proceedings of the IEEE*, vol. 86, no. 11, pp. 2278–2324, 1998.
- [11] H. Su and C. Jung, "Perceptual enhancement of low light images based on two-step noise suppression," *IEEE Access*, vol. 6, pp. 7005–7018, 2018.
- [12] Y. Sun, X. Wang, and X. Tang, "Deep Learning Face Representation from Predicting 10,000 Classes," in *Proceedings of the IEEE conference on computer vision and pattern recognition*, pp. 1891–1898, Columbus, OH, USA, 2014.

## Retraction

# Retracted: Investigating the Lung Adenocarcinoma Stem Cell Biomarker Expressions Using Machine Learning Approaches

### BioMed Research International

Received 8 January 2024; Accepted 8 January 2024; Published 9 January 2024

Copyright © 2024 BioMed Research International. This is an open access article distributed under the Creative Commons Attribution License, which permits unrestricted use, distribution, and reproduction in any medium, provided the original work is properly cited.

This article has been retracted by Hindawi following an investigation undertaken by the publisher [1]. This investigation has uncovered evidence of one or more of the following indicators of systematic manipulation of the publication process:

- (1) Discrepancies in scope
- (2) Discrepancies in the description of the research reported
- (3) Discrepancies between the availability of data and the research described
- (4) Inappropriate citations
- (5) Incoherent, meaningless and/or irrelevant content included in the article
- (6) Manipulated or compromised peer review

The presence of these indicators undermines our confidence in the integrity of the article's content and we cannot, therefore, vouch for its reliability. Please note that this notice is intended solely to alert readers that the content of this article is unreliable. We have not investigated whether authors were aware of or involved in the systematic manipulation of the publication process.

Wiley and Hindawi regrets that the usual quality checks did not identify these issues before publication and have since put additional measures in place to safeguard research integrity.

We wish to credit our own Research Integrity and Research Publishing teams and anonymous and named external researchers and research integrity experts for contributing to this investigation.

The corresponding author, as the representative of all authors, has been given the opportunity to register their agreement or disagreement to this retraction. We have kept a record of any response received.

### References

- [1] M. S. Bhuvaneshwari, S. Priyadharsini, N. Balaganesh, R. Theenathayalan, and T. A. Hailu, "Investigating the Lung Adenocarcinoma Stem Cell Biomarker Expressions Using Machine Learning Approaches," *BioMed Research International*, vol. 2022, Article ID 3518190, 11 pages, 2022.

## Research Article

# Investigating the Lung Adenocarcinoma Stem Cell Biomarker Expressions Using Machine Learning Approaches

**M. S. Bhuvaneshwari,<sup>1</sup> S. Priyadharsini,<sup>1</sup> N. Balaganesh,<sup>1</sup> R. Theenathayalan,<sup>2</sup> and Tegegne Ayalew Hailu<sup>3</sup>**

<sup>1</sup>Department of Computer Science and Engineering, Mepco Schlenk Engineering College, Sivakasi, Tamil Nadu 626005, India

<sup>2</sup>Department of Civil Engineering, Mepco Schlenk Engineering College, Sivakasi, Tamil Nadu 626005, India

<sup>3</sup>Department of Electrical and Computer Engineering, Kombolcha Institute of Technology, Wollo University, Ethiopia

Correspondence should be addressed to Tegegne Ayalew Hailu; tegegneayalew@kiot.edu.et

Received 12 July 2022; Revised 29 August 2022; Accepted 8 September 2022; Published 24 September 2022

Academic Editor: Senthil Rethinam

Copyright © 2022 M. S. Bhuvaneshwari et al. This is an open access article distributed under the Creative Commons Attribution License, which permits unrestricted use, distribution, and reproduction in any medium, provided the original work is properly cited.

The objective of the study is to look at the activation of stem cell-related markers in lung adenocarcinoma. Utilizing an unsupervised machine learning approach centered on the mRNA expression of pluripotent stem cells as well as its subsequent developed progeny, the mRNA stemness index of further around 500 LUAD patients from The Cancer Genome Atlas dataset was generated. In LUADs, mRNAsi had first been investigated using differential variations, survivability analyses, medical phases, and sexuality. A computational approach is used for identifying cell clusters utilizing fuzzy clustering. There at transcriptional as well as protein stages, the interactions between the genetic markers were investigated. The functionality and processes of the important genes were annotated using expression values. The degree of gene expression related to the clinical symptoms and the likelihood of surviving have also been confirmed. In cancer patients, the mRNAsi genes were highly elevated. In particular, the mRNAsi score rises with advanced trials and varies markedly by sexuality. Within several years, reduced mRNAsi categories will have superior overall survivability in large LUADs. Individuals with chronic LUAD had greater mRNAsi and had reduced average survivability. The important genes and the distinguished categories have been chosen based on their mRNAsi connections. Some of the major genes related to cell proliferating Gene Ontology concepts were found enriched out from the cell cycle Kyoto Encyclopedia of Genes and Genomes (KEGG) process. Specific genes were found to be linked to CSC features. Their activation grew in lockstep with the progression of LUAD's pathology, so these markers appeared amplified in pan-cancers. These important markers were discovered to have substantial connections as a group, suggesting that they could be exploited as drug applications in the therapy of LUAD by suppressing stemness traits.

## 1. Introduction

Cancer is defined as a condition in which aberrant cells proliferate uncontrollably, ultimately invading nearby tissues. The kind of cell which originally experienced an oncogenic alteration is used to identify cancer. As the condition advances, unregulated cellular proliferation results in tumors, which are lesions made up of aberrant tissues. Tumors are made up of a diverse collection of cells. Tumor-generating cells, which have really stem cell-like traits and activities, were among such diverse cell groups. Just these tumors start participating organizations to tumorigenesis and can produce new tumors,

which distinguishes them from the rest of the tumor cells. Such tumor cells were dubbed cancer stem cells because their features were similar to some of cancer stem cells (CSC). Cancer stem cells, which are self-renewing and proliferate indefinitely, cause therapeutic resistance in lung disease [1]. The cancer stem cell (CSC) hypotheses of malignancies have gotten a lot of press in current history. Even though the theory that cancers rely on a sparse number of stem-like genes for proliferation has been there for over a century, it was only in the last few generations that technological advancements allowed people to back up these theories with experimental evidence. One of the main reasons for the CSC model's

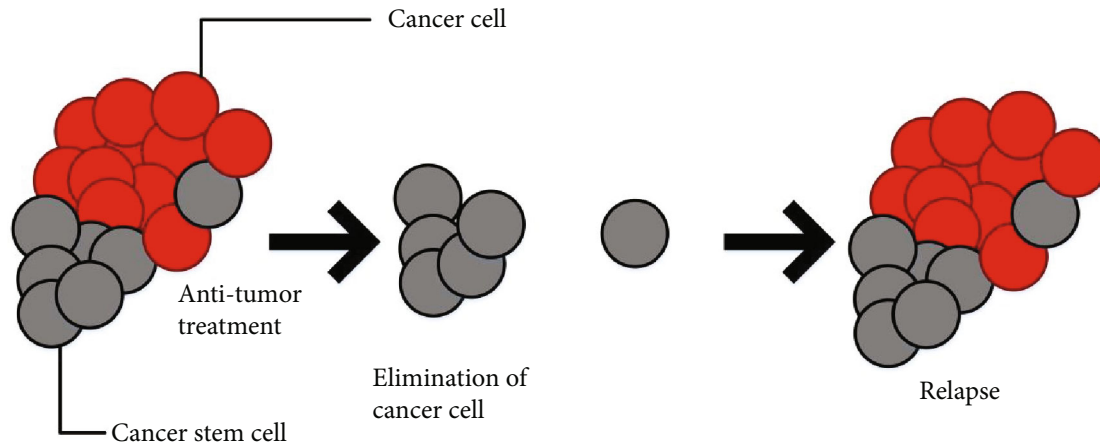


FIGURE 1: Structure of stem cell.

popularity is because it can explain significant but largely unknown clinical phenomena such as drug resistance, minimum residual illness, and tumor recurrence. However, as new data challenges and redefines the CSC notion, the CSC model's original explanatory strength has diminished in many circumstances [2]. The discovery since not every cell in tumors remains equivalent is fundamental to the CSC. In the CSC, cancer growth is powered through a smaller selection of devoted stem cells capable of independence, analogous to the proliferation of healthy proliferative tissues like bone marrow, skin, or gut epithelial. Cancer is made up of both rapidly dividing cells and postmitotic, developed cells. Because neither of those major groups of cells seems to be having the capability to self-renew, their significance to the cancer's long-term survival is minimal. CSCs are thought to even have gained the structural arsenal of typical stem cells, including the ability to replenish them, and also are constructed to endure a generation, be resistant to magnetic and biochemical shocks, sleep for extended periods of time, and invade additional areas of the body. Rare CSCs might well be capable of surviving such therapeutic regimens, indicating why localized resurgence is usually always the result of effective radioactivity or cancer chemotherapy for tumor cells [3]. Figure 1 shows the structure of the stem cell.

Cancer is not just a "sack" of cancerous cells that are all the same. Instead, cancer is a complicated environment that includes tumor cells along with invading endothelium, hematopoietic, stromal, and other cell types that might affect the tumor's overall activity. Certain nontumor cell types could strongly impact tumor tissues and cause metabolic alterations including hypoxia and nutritional imbalances, which contributes to malignant cell heterogeneity in functioning. Self-renewal is often upregulated in CSC. Stem cells are a unique group of cancer cells that could be separated from the rest of the tumor cells and demonstrated to behave clonal long-term recolonization and self-renewal capability, which are the distinguishing characteristics of a CSC [4]. Leukemias, breast cancer, bladder cancer, colon carcinoma, CNS malignancies, ovarian cancer, head and neck cancer, malignant melanoma, pancreatic cancer, Ewing sarcoma,

and liver cancer have all been found to have tumorigenesis phenotypes that fit the description of CSCs. It is presently unknown whether CSC subpopulations exist in all malignancies [5]. CSCs are a special type of tumor cell that can sustain the development of a malignant growth of cells indeterminately.

The population has indeed known through types of names; however, the word cancer stem cell (CSC) has gained widespread acceptance. The CSC is usually regarded to have grown from such a healthy tissue stem cell as well as, as a result, become the cells that gave rise to cancer. The question of whether CSCs are matured tissue stem cells that have experienced tumor transformation or even more distinguishable cells that reinitiate stemness program as part of, or after, diagnose conversion is still being debated [6]. Prior to the introduction of functional assays to evaluate stem cell capability, morphological and proliferative assessments revealed that not every cell inside a tissue was equal: certain cells are presently being more distinguished than some others because not all cells actively multiply at around the same period. However, since most cells exhibit CSC functionality, it really has proved difficult to identify CSCs from non-CSCs in several forms of cancers [7]. These tumors appear to be homogeneous or have a very minimal hierarchical structure. Functional assays like in vitro clonogenic assays, transplanting, and lineage-tracing procedures have been used to study SCs. It has historically been known that not all tumor cells are the same and that certain malignancies, such as teratocarcinoma, have a component of tumor cells that are more distinguished than others, leading to the hypothesis that the undifferentiated tumor cells are tumor stem cells [8]. Following the discovery of a population of cells capable of initiating a full "tumor," the next significant step in CSC biology would have been to identify that population. The introduction of fluorescence antibodies, flow cytometry, and related cell sorting made it possible to isolate phenotypically specified cell types in a repeatable manner. Furthermore, the establishment of mice breeds with severe immune deficiencies improved tumor transplantation [9]. Figure 2 shows the basic structure of CSC.

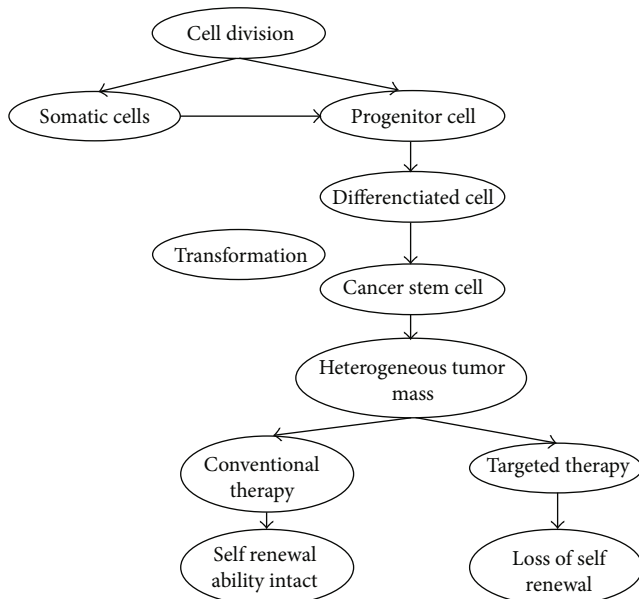


FIGURE 2: Basic structure of CSC.

Stem cells were not developed by a single scientist or a group of researchers; rather, the hypothesis was developed over several generations by several researchers. Stem cells were formerly thought to only exist in a few tissues, including the blood, liver, and intestinal epithelia, but many have already been discovered throughout each part of the body. The capacity to reproduce while maintaining an indeterminate phenotype for extended periods of time, as well as the pluripotency of differentiating through every pathway with the main 3 germ layers, endoderm, mesoderm, and ectoderm, describes embryonic stem cells [10]. During the process by which normal stem cells are converted into CSCs, several changes, including abnormal cellular division as well as epigenetic and genomic modifications, could take place. In light of this information, it can be concluded that the mutation theory of cancer genesis is not always sound. Repairing broken DNA requires the participation of genes that do DNA repair. Cells that have mutations in these genes frequently generate further mutations in other genes as well as changes in their chromosomes, such as the duplication or deletion of portions of their chromosomes. It is possible that the cells will become malignant as a result of all of these changes. The significant numbers of malignancies are thought to have their origins in the process of conversion. The majority of carcinogenesis procedures typically consist of a sequence of phases that lead to cancer. Those are far more vigorous and specialized subtypes of cells that cause tumor development and recurring. Due to self-renewal and the development of distinguished progenies, the subcategory of cancer cells has the capability to establish and sustain malignancies when transferred into completely impervious host species. CSC development leads to cellular heterogeneity in malignancies, as well as innate antibiotic resistance and increased aggressive capability, all of which contribute significantly to cancer progression and metastatic development. As a result, CSCs ought to be a key target for several malignancies' elimination [11].

Despite the gradual pace of peripheral lung epithelial cell replacement and the tendency for human lung tissue to heal instead of regenerate, lung malignancies are common, most likely as a result of both self-inflicted and passive assaults from chemicals and carcinogens in the environment. A lot of research has demonstrated the link between both inflammatory and carcinogenesis. It is well known that cigarette smoking causes an inflammatory reaction in the lungs. The carcinogens present in cigarette smoke have a profound impact on the lung epithelium's inhabitant growth of cells and ecosystem. Tumor in lungs is the leading source of melanoma death globally, accounting for almost 1 million fatalities within a year. In contrast to lung tumors arising within lung tissue, the highly vascularized lungs are indeed a preferred site for the metastasis proliferation of cancerous cells of extrapulmonary origination, such as breast malignancies and melanomas. There seem to be currently a considerable number of cancer subtypes classified inside the main groups of lung cancer [12].

Single lung tumors could be exceedingly diverse, with cells ranging from undeveloped to well-differentiated phenotypes making up the tumor aggregate. Heterogeneous tumors, which have less variance in differentiating status and yet are composed of a range of cell types, could also arise in the lungs. It is a complicated illness with two separate pathology classifications: non-small-cell lung cancer (NSCLC), which is totally for 80% of all cases, and small-cell lung cancer (SCLC), which accounts for 20% of all cases. Adenocarcinoma (ADC; 30-50 percent of NSCLC) and squamous cell carcinoma (SCC; 30 percent of NSCLC) are the most frequent types of NSCLC [13]. Despite the fact that our understanding of lung CSC biology is poor, a variety of CSC biomarkers have been discovered and researched. These CSC indicators have been linked to anticancer drug resistance. CD133, side population (Hoechst-negative), aldehyde dehydrogenase (ALDH1), CD117, CD44, and CD87 are just a few of them. Additionally, tumor cells are capable of displaying expression profiles that are heterogeneous. Epigenetic modifications in the background are frequently to blame for this. Different sections of an individual's tumor samples have been found to have distinct expression signatures, and these differences have been uncovered. It is still challenging to discover specific lung CSC markers due to the intratumoral heterogeneity and significant plasticity that can encourage unpredictability of the CSC phenotype and the deterioration of cell seeming indicators [14]. These factors can be attributed to the development of lung cancer.

The most common pathological classification of NSCLC is adenocarcinoma. Despite the fact that morphological characterization of lung carcinomas could substantially categorize individuals, people at elevated danger for recurring or metastatic illness must be identified [15]. Characteristics in individuals with NSCLC's preoperative mortality have indeed been found. Prognostic factors include tumor size, vascularization, poor segmentation, a higher cancer-proliferative index, and various genomes abnormalities, such as K-ras and p53 abnormalities. Passive smoking has been linked to an increase in the incidence of cytosine to adenine mutations in adenocarcinomas and squamous cell

carcinomas. Due to the fact that adenine is larger than cytosine, it will not be able to form an accurate base pair with the guanine found on the complementary strand. This will result in the DNA being more bloated. The mutagenesis impact of carcinogen treatment explains the high somatic mutation content of lung cancer samples (e.g., cigarette smoke). As a result of exposure to ultraviolet light, melanoma samples also have a significant mutational burden. The occurrence of abnormalities in adenocarcinoma genes likewise shows spatial variability. The degree of expression of genes has been one of the variables that influence the distribution of variants. Since of transcription-coupled compensatory mechanisms, the variation rates in differentially expressed genes are thought to be minimal. The use of many separately analysed genes or regulatory genes to reliably predict individual survival in lung cancer has also been examined. Technologies that evaluate the transcription of hundreds of genes at the very same time can be used to connect gene expression variations with a range of diagnostic indicators, such as treatment outcomes, in order to forecast tumor activity in patient characteristics [16].

Several fields, including wireless technology, and search engines, including voice recognition, have effectively employed machine learning (ML). For several academics with a history in medical or biological, machine learning (ML) might be perplexing because it is frequently associated along big data, artificial intelligence (AI), blockchain technology, cloud technology, and other technologies. It is, nevertheless, a universal notion and procedure that should be used in all domains, particularly medical and biological. In general, unsupervised learning, supervised learning, (deep) neural networks, reinforcement learning, and classification techniques are all examples of machine learning approaches. Nevertheless, hardly any research has ever been done on the mRNA index utilizing fuzzy clustering. As a result, this study presents a computational approach for identifying cell clusters utilizing fuzzy clustering and mRNA stemness index data. In the use of fuzzy clustering, the technique has numerous benefits. Fuzzy clustering is a grouping technique that allows measured values to belong to multiple groups ("clusters"). Clustering divides population into categories based on asset similarity and looks for patterns or likeness between objects in a gathering; clustering objects should be as comparable to each other as desirable yet remaining as independent as possible from those in other groupings. Calculating fuzzy boundaries is significantly easier than deciding on a separate cell for a specific location. Every data point should always be in one grouping in "hard" clustering. In "soft" or "fuzzy" clustering, measured values could potentially belong to a wide variety of different groups. The least squares method is utilised by fuzzy clustering in order to find the most optimal placement for every given dataset [17]. When the model residuals have a normal distribution with zero as the mean, the least squares method is utilised since this method is comparable to the maximum likelihood method. The best position maybe somewhere in the probabilities distance between two (or more) groups. The detection of cell clusters is among the most difficult aspects of single-cell generation sequencing. Because it could be used to identify cell types,

unsupervised learning (clustering) plays an important role in analyzing mRNAsi data. Generally, FCM attempts to preserve the participation matrices with the input database, which have been reorganized on each repetition, by calculating the equal weightage of each sampling site in order to determine its degree of similarity. The average among all data points towards other clusters equals unity. The capacity to build clusters of overlapping data points and the findings satisfying the characteristic of converging are two of the key advantages of this technique for mRNAsi data. The antecedent requirement of an assessment is necessary for excellent clustering results, and outliers may be allocated to the comparable membership functions throughout all the clusters, which are possible constraints of cluster reliability. Because of these restrictions, employing any type of gene expression data is less acceptable. The remaining sections are arranged as follows: in Section 2, the related work was presented. The materials and methods of the stem cell analysis are in Section 3. Section 4 put the result and discussion to the test in terms of performance and efficiency, with figures and charts displaying the findings. The final section summarizes the paper's conclusions.

## 2. Related Works

The considerably lower surviving percentage of lung cancer patient need enhanced investigative techniques in order to provide the best therapeutic approaches and improving health care. Multivariable biological profiles, including such blood-borne microRNA (miRNA) markers, might well have greater incidence of accuracy and precision, but their generalisation requires more research with comparison groups and consistent assessments. Inside an expanded group of symptoms patients and healthy controls individuals, evaluate the utility of blood-borne miRNAs as possible circulation indicators for diagnosing lung cancer. During March 3, 2009, until March 19, 2018, 3102 individuals were enrolled by sampling techniques throughout this multicenter randomized trial, which also included individuals across particular circumstance as well as group investigations (TREND and COSYCONET). Population screening has been used in the TREND group research. 3046 individuals (606 with non-small-cell and malignant cancerous cancer, 593 with nontumor respiratory problems, 883 with illnesses without characterized by inflammation, and 964 undamaged matched controls) were given patient conditions. Due to the obvious experimental problems, no specimens were deleted. During April 2018 until November 2019, the information is evaluated. Accuracy and precision of liquid biopsy for diagnosis of lung cancer employing miRNA profiles are calculated. A combination with 2103 patients were recruited, through a median (SD) age of 52.1 (15.2) years. There have been 2856 individuals, and information on their gender was provided for 1727 (60.5%) of them. Machine learning approaches have been used to analyse the genomic sequence miRNA patterns of clinical specimens from 3046 people. By dividing the information evenly into train and test sets, several categorization situations were studied. The circulation biomarker testing, however, somehow does not replace

neuroimaging, sputum cytology, or biopsy testing, and the survey purposes to be verified systematically [18].

To use a radiogenomics technique which combines gene transcription as well as imaging techniques to uncover predictive neuroimaging biomarker in non-small-cell lung cancer (NSCLC) individuals for whom survivor results are not accessible by using surviving information on public gene regulation large datasets, image characteristics were linked to groupings of coexpressed genomics (metagenes) using a radiogenomics technique. For a bilateral link among feature representation and metagenes, a radiogenomics correlation mapping is first built. Then, utilizing sparse regression analysis, estimation techniques of metagenes were accompanied by the development of picture attributes. In the same way, metagenes have been used to build prediction models of image characteristics. Furthermore, the anticipated picture features' predictive importance is assessed using a public genomic information collection with overall survival. The radiogenomics technique was used on a group of 26 NSCLC patients who have access to the expression of genes and 180 imaging characteristics from computerized tomography (CT) and positron emission tomography (PET)/CT. There have been 243 bilateral associations among picture characteristics and NSCLC metagenes that were statically significant. Metagenes found identified with a 59 percent–83 percentage points using picture characteristics. In regard to metagenes, 141 of 180 CT image characteristics as well as the PET aggregate impact values have been forecasted with a 65 percent–86 percent accuracy. Tumor size, edge form, and sharpness rated top for predictive relevance when the projected picture attributes were linked to a public gene sequences set including prognostic factors. The information obtained as proof-of-concept for this radiogenomics investigation has limitations. Researchers looked at data from a limited group of NSCLC patients that did not adequately represent the disease's diversity in neuroimaging and gene function profiles, nor the variation owing to histological subtype [19].

Early identification of malignancy considerably improves the odds of appropriate treatment; however, diagnosis for certain tumors, such as lung adenocarcinoma (LA), is insufficient. For large-scale medical evaluation, an optimal early-stage diagnosis of LA should include speedy identification, minimal invasiveness, and strong result. To detect potential LA, researchers use machine learning to analyse serum biochemical trends. They use 50 nL of serum and 1 s of customized ferric particle-assisted laser desorption/ionization chromatographic techniques to obtain direct biochemical pathways. With 143 m/z characteristics, they identify a metabolism spectrum of 100–400 Da. Researchers use sparse regression machine learning of features to detect earlier phase LA with accuracy of 70–90% and precision of 90–93%. To discriminate earlier phase of LA from individuals ( $p$  0.05), researchers developed a diagnostic profile of seven biomarkers including geometrically similar. However, metabolite concentration and specimen sophistication influence MS detection, and for extraction and segregation of metabolites through complicated bio-mixtures, extensive pretreatment methods are necessary [20]. The disappearance of a specialized phenotypic and the development of prede-

cessor as well as stem cell-like features are hallmarks of tumor growth. Researchers present new stemness metrics for determining the degree underlying oncogenic transdifferentiation in this paper. They extracted transcriptomic and epigenetic sets of features using nontransformed pluripotent stem cells including their differentiating progeny utilizing an improved one-class logistic regression (OCLR) machine learning technique. They have been willing to disclose completely undiscovered biochemical processes related with the dedifferentiated oncogenic condition through using OCLR. The cancer microenvironment was studied, where researchers discovered an unexpected link between tumor stemness and immunotherapeutic transcription and invading inflammatory responses. The dedifferentiated oncogenic phenotypic would be most prevalent in metastatic cancers, according to our findings. The stemness index sequence is repeated of intratumor genomic polymorphism when applied to single-cell data. However, it is unclear from some of those data whether the therapy's efficacy is confined to specific HNSC genes associated [21].

Cancer stem cells are self-renewing cancer cells that could lead to different results of tumor cells, and they play a critical role in the progression of lung squamous cell carcinoma (LSCC). The goal of this research was to look at the transcriptional activation connected to LSCC stem cells. The RNA-seq information, as well as the clinical and prognosis characteristics of LSCC patients, was retrieved from of the TCGA searchable database. It was determined and discussed how useful a prognostic tool the mRNA expression-based stiffness index (mRNAsi) of LSCC can be. After that, we utilised a weighted gene coexpression network analysis in order to locate significant genes that are connected to LSCC mRNAsi (WGCNA). A bioinformatics tool known as weighted gene coexpression network analysis, or WGCNA, can be used to investigate the connections that exist between various gene sets, sometimes known as modules, or between gene sets and clinical characteristics. In LSCC, mRNAsi is an important prognostic factor. According on WGCNA, we evaluated 5 important genes that contribute to LSCC mRNAsi (BUB1, BIRC5, CCNB2, KIF15, and SPAG5). When compared to conventional specimens, the important pathways remained substantially elevated in the malignant tumors. Furthermore, there is indeed a strong link between the molecules of these important genes, as well as a significant transcriptional coexpression relationship. Thus to summarize, mRNAsi plays a significant role in LSCC. Five important genes associated to mRNAsi were selected as targeted therapy for decreasing the regenerative medicine features of LSCC (BUB1, BIRC5, CCNB2, KIF15, and SPAG5). These findings suggest that such five genes are involved in the maintenance of cancer stem cell features in LSCC. Several genes could be used as targeted therapies to block LSCC's stem cell properties. However, because the calculations are based on retrospective data, more studies are needed to confirm them [22].

### 3. Materials and Methods

*3.1. Application and Packages.* In this study, the R 3.6.1 (Action of the Toes) software is employed on the Windows operating system. The R packages have all been open-



source software, and they were all acquired through bioconductor. Throughout this study, Strawberry Perl version 5.14.2.1 (64 bit) was used to combine large datasets using a merging script. Every one of the materials remained open-source and free.

**3.2. Database.** The TCGA dataset was used to acquire the transcriptome sequencing through RNA sequencing (RNA-seq) of the LUAD collection and also material on sexuality, aging, life status, and phases. As of the 5th of October, 2019, those figures remained accurate. Perl was used to merging the RNA-seq findings of 30 baseline characteristics and 380 cancer specimens into a matrix. The Ensembles IDs were then converted into formal genetic identifiers using the Ensembles databases. The data of the microarray (GSE21656) was acquired using the Gene Expression Omnibus (GEO). The mRNasi index in all kinds of cells in the TCGA was collected from Tathiane M. Malta's article attachments. A Perl merging script is used to combine the miRNasi index of lung adenocarcinoma individuals using TCGA information of lung adenocarcinomas, having mismatched instances removed. The Wilcox test has been used to determine whether the LUAD subgroups have substantial differences in mRNasi.

**3.3. Investigation of Differentially Expressed Genes.** The Wilcox strategy was applied in the analysis of differentially expressed analyses by using program "limma." The cut-offs for screening for DEGs comparing lung cancer and normal groups have been folding change > 1 and adj.p (false discovery rate, FDR) 0.05. R's "pheatmap" package has been used to create the heat map and volcano plot. R's "ggpubr" package was used to graph the box-plots of the genetic markers for verification. GEPIA [23], a web application for normal and cancer cells gene function monitoring and interaction analytics, has been used to create various genetic comparisons. To modify the expression profile before graphing, simply set the log-scale option to log2(TPM+1). The approach for determining differential gene expression is ANOVA, with the disease phase as a parameter. Statistical significance was defined as Pr(> F) 0.05.

**3.4. The Curve of Total Survivability.** Individuals with low and high levels of mRNasi indexes can be compared using the Kaplan-Meier plots to determine the effectiveness of mRNasi scores in predicting life expectancy. The Kaplan-Meier estimator produces a plot that looks like a series of horizontal steps that get smaller from left to right. If the sample size is high enough, this plot will converge on the actual survival function for the population being studied. For this portion, the R packages "survival" and "surviving" have been used, and the connection was evaluated using the log-rank function. The available web Kaplan-Meier plotter was used to create Kaplan-Meier survival curves of either the genetic markers during verification [24].

**3.5. Identifying Cell Clusters by Fuzzy Clustering Analysis.** For such preliminary amount of clustering,  $c = 2, 3, \dots$ , a renowned grouping algorithm is used, fuzzy clustering. Here, udc is a user-defined cluster size, representing udc-1 series of case studies, and produced four model evaluation

indexes from every study research: partition coefficient, partitioning entropy, fuzzy silhouette index, and modified partition coefficient.

Within field of ML, fuzzy clustering is a grouping technique application of fuzzy participation idea. Although each characteristic has a set of qualities, the fuzzy  $c$ -means clustering technique divides  $n$  collected data (data points)  $I = \{i_1, i_2, i_3 \dots i_n\} n * p$  into  $c (1 \leq c \leq n)$  fuzzy clusters. Assume  $Ce = \{ce_1, ce_2, ce_3, \dots, ce_c\} c * q$  is the collection of cluster centers, and  $R = [r]$  is the collection of nodes in the cluster.  $R_{ys}$  indicates the degree of membership of  $s$  features to  $c$ th cluster center, and  $cn$  is a  $cn$  matrix of degrees of membership. The following requirements are met by the above matrix:

$$\begin{aligned} \sum_{y=1}^c R_{ys} &= 1, \\ R_{ys} &\geq 0, \\ R_{ys} &\in [0, 1]. \end{aligned} \quad (1)$$

For solving the optimization problems of the appropriate fuzzy optimal clustering, the fuzzy  $c$ -means technique includes the following optimization problem. Below is the definition of the optimization problem  $Y_{fm}$ :

$$Y_{fm} = \sum_{y=1}^c \sum_{s=1}^n R_{ys}^v \|i_s - ce_y\|^2. \quad (2)$$

Here,  $v (1 \leq v \leq \delta)$  is the fuzzification coefficient, which denotes the amount of clustering that is imprecise.  $v = 1$  is utilised in the research. Every norm evaluating the resemblance between the cluster center as well as any measurable data can be used here. The optimization problem  $Y_{fm}$  must be as small as possible.

The objective equation is solved using the logistic regression methodology with the constraint  $\sum_{y=1}^c R_{ys} = 1 (s = 1, 2, 3 \dots n)$ , while the participation level and cluster centers are modified using the following calculations:

$$\begin{aligned} R_{ys} &= \sum_{y=1}^c \left( \frac{\|i_s - ce_y\|}{\|i_s - ce_y\|} \right)^{2/(v-1)}, \\ ce_y &= \frac{\sum_{s=1}^n (R_{ys}^v i_s)}{\sum_{s=1}^n R_{ys}^v}. \end{aligned} \quad (3)$$

The method ends when the conditions  $\max_{ys} |R_{ys}^{x-1} - R_{ys}^x| \leq \epsilon$  are met, with  $\epsilon$  be a terminating variable among 0 and 1 and  $x$  denoting the iterative step id. The objective function  $Y_{fm}$  coheres to a local optima or a saddle point using this approach.

**3.6. Cluster Validity Parameter Measurements.** There are two cluster weight index values: partition coefficient (PC) and

partition entropy (PE). The following are the definitions for  $e_p$  and  $c_p$ :

$$e_p = -\frac{x}{n} \sum_{y=1}^c \sum_{s=1}^n Rys * \log_e Rys, \quad (4)$$

$$c_p = \frac{x}{n} \sum_{y=1}^c \sum_{s=1}^n Rys^2.$$

The monotonic tendency of the partition coefficient (PC) was addressed by the development of the modified partition coefficient (MPC). A normalised squared Euclidean distance of membership degree vectors to the center of the fuzzy  $c$ -partition is used to calculate the adjusted partition coefficient, which is an average of this distance. MPC has a range of values among 0 and 1. The following is how  $pc_m$  is represented:

$$pc_m = 1 - \frac{c}{c-1} (1 - c_p). \quad (5)$$

The fuzzy silhouette index (FSI) is a statistic that identifies the two clusters with the greatest degree of membership in  $i_s$ . Equations (6) and (7) are a brief description of  $f^s$ :

$$f^s = \frac{\sum_{s=1}^n (R1s - R2s)M(i_s)}{\sum_{s=1}^n (R1s - R2s)}, \quad (6)$$

where

$$M(i_s) = \frac{\mu(i_s, i_{cd}) - \alpha(i_s, i_{cd})}{\max\{\mu(i_s, i_{cd}), \alpha(i_s, i_{cd})\}}. \quad (7)$$

In this case, a dataset component (point)  $i_s$  is component of the cluster  $i_{cd}$  ( $i_{cd} \in \{i_{cd}1, i_{cd}2, i_{cd}3, \dots, i_{cd}c\}$ ), whereas  $\alpha(i_s, i_{cd})$  is the intracluster length, which represents the average distance among  $i_s$  and other such elements in the similar cluster  $i_{cd}$ . On the other hand,  $\mu(i_s, i_{cd})$  is an intercluster distance which represents the distance among  $xq$  and the cluster  $i_{cd}$ 's nearest neighbor.  $c_p$ ,  $pc_m$ , and  $f^s$  must be increased, whereas  $e_p$  must be lowered, in order to produce the best clusters.

**3.7. Investigation of Gene Coexpression.** To study the robustness of such interactions at the level of transcription, the coexpression associations among important genes inside a module are being determined based upon gene expression profiles. The Pearson correlations among genetics were calculated using the R “corrplot” tool. On Linked Omics, the relationship involving MSRB3 and PRKG1 was investigated. The Pearson correlation test was utilised in order to analyse the data that was taken from the LUAD database, which was selected for research purposes by TCGA. The Pearson correlation coefficient is a test statistic that quantifies the statistical link or association between two continuous variables. It is named after its namesake, Karl Pearson. Because it is founded on the theory of covariance, it has earned a reputation as the most accurate way for determining how closely

two variables are associated with one another. The findings have been considered to be statistically significant if indeed the coefficient of correlation was more than 0.3 and the  $p$  value was less than 0.01.

**3.8. Protein-Protein Interaction System Development.** The PPI structure was obtained through STRING version 11.0, and the graph plot depicts the number of nodes with the highest connection. The minimum necessary interaction score is set to 0.4 with moderate probability and disconnected any hidden nodes in the network. It estimated the total of neighboring nodes for every genotype in the PPI network and used a bar plot to order the genomes by the number of adjacent nodes [25].

**3.9. DEG Filtering Assessment.** The R packages “cluster profile,” “enrich plot,” and “ggplot2” have been used to enhance DEGs through using Gene Ontology (GO) functional enrichment and Kyoto Encyclopedia of Genes and Genomes (KEGG) mechanism enriching ( $p$  value 0.05,  $q$  value 0.05). The essential genetic mutations were mapped with both the Ensembles ID using the R package “http://org.Hs.eg.DB,” commonly known as genome-wide characterization for humanity. R created the bar plot and the bubble plot to visualize the top findings.

## 4. Result and Discussion

As from the TCGA database, transcriptome profiling is downloaded for gene expression and diagnostic features for 380 LUAD individuals and 30 healthy individuals. Sexuality, aging, life status, survivability, cancer stage, and tumor node metastasis (TNM) phase categorization are all included in the data, with uncertain information removed during research. Every case's mRNasi value was retrieved using Malta's appendix and then integrated with both the TCGA database. The mRNasi and EREG-mRNasi ratings varied from 0 to 1, stemless and stemness, correspondingly, as per the OCLR methodology. The mRNasi is evaluated in numerous ways in this study, including between tumor and normal groups, higher and lower mRNasi rating groups, and distinct subtypes. Figure 3 depicts that the mRNasi rating in the cancer category is greater than those in the normal group, indicating that mRNasi is important in lung ADC.

The 404 LUAD instances are divided into lower and higher categories depending on the mRNasi rankings as well as plotted the Kaplan-Meier (K-M) survival curvatures to see if there was a link between survival rates and high mRNasi rankings as shown in Figure 4. The K-M survival curves are still not clinically meaningful in the aggregate. The lower and higher curves, on the other hand, displayed a remarkable collision near the very end of the 5th year. Lung cancer has a poor five-year survival rate; therefore, most individuals in the study survived for 5 years. The surviving value of higher mRNasi index instances would be lesser than the lowest of the key case during the first 5 years, and the surviving probability curves are practically flat for the next two years.

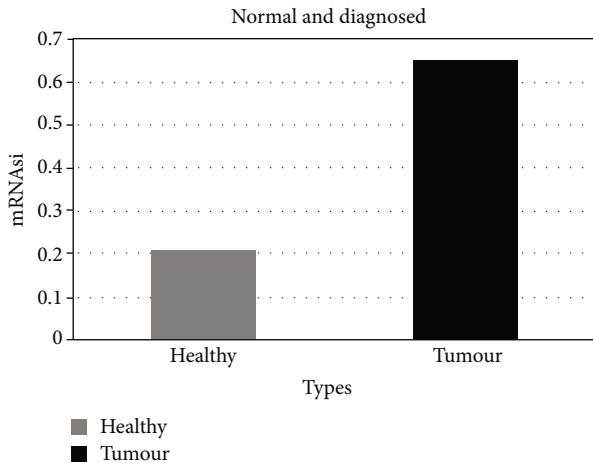


FIGURE 3: Normal and cancer mRNAasi.

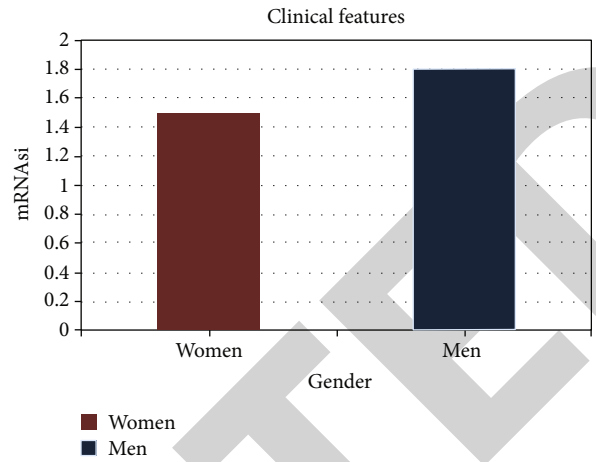


FIGURE 5: Clinical feature and profile chart.

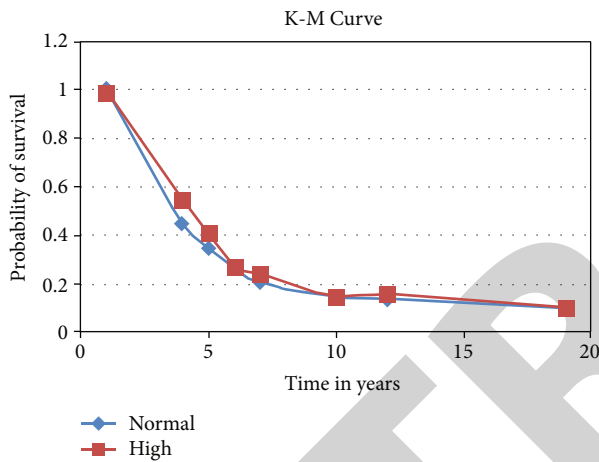


FIGURE 4: K-M curve graph of survival probability.

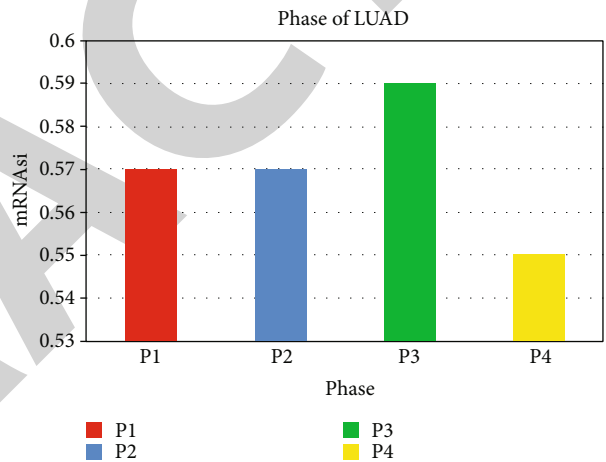


FIGURE 6: Phases of LUAD.

The plots are used to show the relationship between overall mRNAasi profiles and clinical characteristics. In regard to gender presented in Figure 5, males had a larger mRNAasi index over females in the instances that looked at ( $p$  value 0.001). It is discovered also that mRNAasi rating for early-phase lung disease P1 was lesser than the medium and progressed phase (P1-P4) LUAD grouping is shown in Figure 6, while there is a modest drop within P3 lung cancer grouping.

T and M phases were statistically significant when combined by TNM plotting. The tumor's size is represented by the T phase given Figure 7. The mRNAasi ratings of the S2 and S3 groupings have been considerably higher than those of the S1 group. Despite the fact that the S4 group's mRNAasi value reduced, the difference in the number remained greater than the S1 category. The M phase indicates if the cancers have spread to other parts of the body as depicted in Figure 8. The MD1 group's mRNAasi index is greater than the MD2 group's ( $p$  value = 0.016).

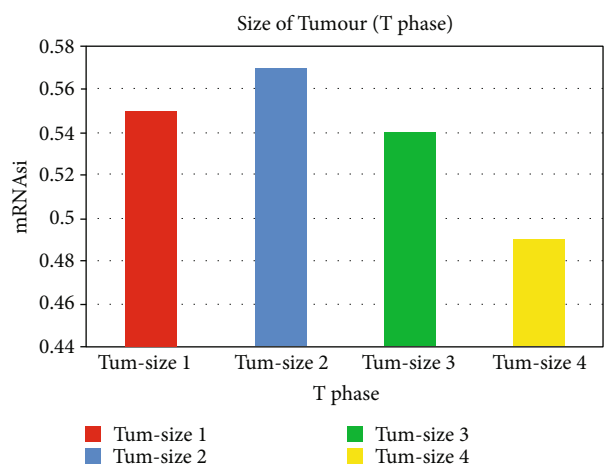


FIGURE 7: Tumor size in T phase.

4.1. Cell Grouping with Fuzzy Clustering. In the fuzzy cell clustering, to group the cells, fuzzy  $c$ -means clustering is used for various starting numbers of clusters,  $c = 2, 3 \dots 10$ ,

and calculated the results of the 4 high similarity indices: PC, FSI, MPC, and PE. Table 1 shows the chronology model evaluation ratings out from mRNAasi expression dataset, and Figure 9 shows its graphical representation.

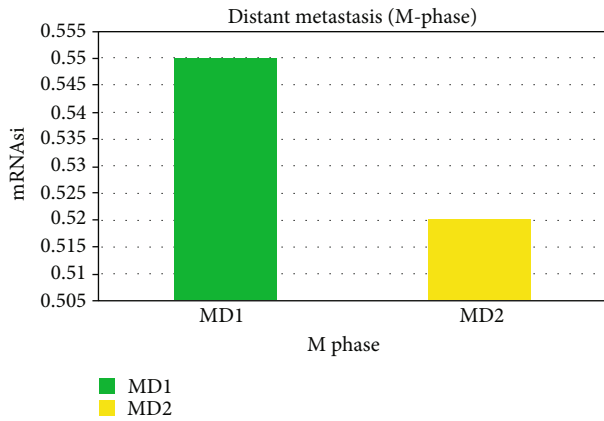


FIGURE 8: Distant metastasis of M phase.

TABLE 1: Chronology model evaluation ratings out from mRNAasi expression dataset.

Chronologies	Fuzzy silhouette index	Partition entropy	Partition coefficient	Modified partition coefficient
1 <sup>st</sup> C	0.591	0.345	0.476	0.265
2 <sup>nd</sup> C	0.435	0.158	0.347	0.165
3 <sup>rd</sup> C	0.674	0.545	0.173	0.093
4 <sup>th</sup> C	0.543	0.153	0.457	0.348
5 <sup>th</sup> C	0.348	0.348	0.143	0.198
6 <sup>th</sup> C	0.458	0.653	0.634	0.59
7 <sup>th</sup> C	0.325	0.168	0.151	0.78
8 <sup>th</sup> C	0.672	0.189	0.178	0.82

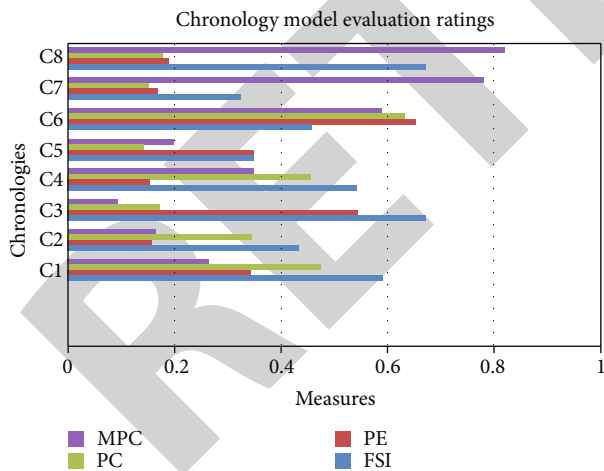


FIGURE 9: Graphical representation of chronology model evaluation ratings.

4.2. Analysis of the Relevant Genomes in LUAD. The important genetic mutations in the modules have been screened using the parameters  $MM > 0.8$  and  $GS > 0.6$ : cell division cycle-associated 7 (CDCA7), heat shock 70 kDa protein 4 (HSPA4), cyclin-dependent kinase 1 (CDK1), cell division cycle 20 (CDC20), cyclin B1 (CCNB1), CAP-GLY domains

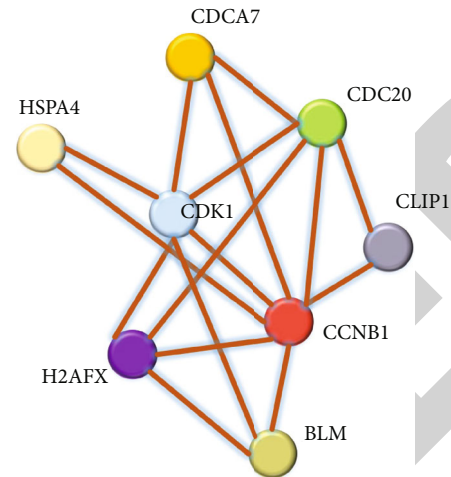


FIGURE 10: PPI among markers.

comprising linkage protein 1 (CLIP1), bloom syndrome, RecQ helicase-like (BLM), and H2A histone family, member X (H2AFX). According to the Oncomine database, the expression levels of the several kinds of cancer and eight markers in cancer and normal specimens differ significantly.

4.3. Investigation of Significant Genetic Expression and Correlations. The “clusterProfiler” R package has been utilised for GO and KEGG pathway improvement investigation to examine the biologically active compounds and relevance of the genetic mechanisms. The important markers appeared concentrated in management of the cell growth checkpoints, negative regulator of the mitotic division phase control point, damaged DNA interaction, and so on, according to GO analyses. The important genes have been shown to be abundant in cell cycle, oocyte meiosis, and other KEGG pathways. The STRING-evaluated protein-protein interaction networks revealed a significant link here between genetic markers as shown in Figure 10.

4.4. Validation and Analysis of Genes. At a clinic, the frequencies of mRNA expression in 30 LUAD as well as 23 equivalent healthy lung tissues from 21 LUAD individuals have been identified and evaluated. Table 2 shows the features of individuals with LUAD. With the exception of CLIP1, mRNA protein expression of genomic sequences appeared greater in cancerous tissue.

Figure 11 shows the individuals with various ADC. The verification cohort’s OS could not have been examined because so many of the individuals were surviving. Nevertheless, CDC20, CDK1, CCNB1, and H2AFX showed a substantial association, demonstrating that perhaps the methodologies used in this work are viable for identifying important genes implicated in CSC features. Microarrays are used to confirm the important genes. GSE21656 information was obtained out from GEO dataset, and the DEGs were retrieved using the web program GEO2R. The microarray has been utilised in order to investigate the differences that exist between cisplatin-resistant lung cancer cells, also known as CDDP-R, and their parental cells. It is possible

TABLE 2: Features of individuals with LUAD.

Features	Total	Percentage (%)
Age		
Average	48 (24-62)	
Sexuality		
Men	7	19.7
Women	14	62.3
Immunology		
ADC	4	12.4
Less ADC	6	24.1
Unwanted ADC	14	68.2
Unwanted mucinous ADC	2	5.9

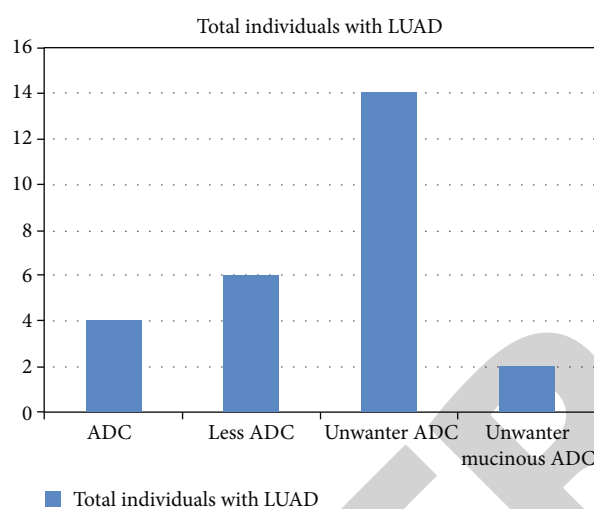


FIGURE 11: Individuals with various ADC.

to determine the expression of thousands of genes all at once by using something called a microarray. DNA microarrays are slides for microscopes that have been printed with thousands of minute spots in predetermined positions. Each spot on the slide contains a gene or DNA sequence that is already known.

The PPI clustering, which has 12 nodes and 64 edges, has much more interconnections than the anticipated nine edges, and the coregulation data suggest that perhaps the clustering collection of 13 genes is operationally connected as well. It is discovered that such genes significantly elevated not only in LUAD, using GEPIA's multiple gene comparison between tumor as well as normal patients. It suggests that such important genes' stem cell capabilities might well be ubiquitous. We used GEPIA to correlate the expression patterns of gene mutations with the pathological cancer type in LUADs so that we could gain additional knowledge regarding the key genes. GEPIA is a recently designed, user-friendly web server for examining the expression data obtained from RNA sequencing. GEPIA gives users the ability to customize their experience by providing features such as tumor/normal differential expression analysis and profiling according to cancer kinds or pathological stages, patient survival analysis, comparable gene finding, correlation anal-

ysis, and dimensionality reduction analysis. In distinct kinds of cancer, eight mRNAsi-related critical markers have been discovered to be differently elevated among cancerous and noncancerous tissues. Those eight essential markers have been found to be significantly linked and mostly involved in the cell cycle. The spinning assembling checkpoint, which is involved in chromosomal partitioning and mitosis release, is CDC20's targeting. Notably, LUAD individuals with elevated CDC20 markers seemed to have a greater overall survival rate than someone with low CDC20 concentrations, which were also equivalent in lung squamous cell carcinoma.

## 5. Conclusion

Therapeutic resistance in lung illness is caused by CSC, which were self-renewing and grow endlessly. The mRNAsi of roughly 404 LUAD patients from The Cancer Genome Atlas dataset was created using an unsupervised machine learning approach centered on the mRNA expression of pluripotent stem cells and their later formed progeny. In LUADs, differential variations, survival analyses, medical stages, and sexuality were used to explore mRNAsi. Fuzzy clustering is used to detect cell groupings using a computer approach. The connections between the genetic markers were studied at both the transcriptional and protein phases. Expression values were used to interpret the functionality and processes of the key genes. The relationship between gene expression and clinical symptoms, as well as the likelihood of survival, has been verified. The mRNAsi genes were found to be substantially increased in cancer patients. The mRNAsi score, in instance, rises with advanced trials and differs significantly by sexuality. Reduced mRNAsi groups will have higher overall survivorship in large LUADs in a few years. Chronic LUAD patients exhibited higher mRNAsi and a lower average survival. The distinct categories and significant genes were picked based on their mRNAsi linkages. The cell cycle Kyoto Encyclopedia of Genes and Genomes (KEGG) process enhanced some of the key genes associated to cell proliferating Gene Ontology categories. CSC characteristics were discovered to be associated to specific genes. These markers appeared to be increased in pan-cancers because their activation developed in lockstep with the advancement of LUAD pathogenesis. These critical indicators were discovered to have significant linkages as a group, implying that they could be used to treat LUAD by lowering stemness features as a medication.

## Data Availability

The data used to support the findings of this study are included within the article. Further data or information is available from the corresponding author upon request.

## Conflicts of Interest

The authors declare that there is no conflict of interest regarding the publication of this article.

## Retraction

# Retracted: Vancomycin as an Antibacterial Agent Capped with Silver Nanoparticles: An Experimental Potential Analysis

### BioMed Research International

Received 8 January 2024; Accepted 8 January 2024; Published 9 January 2024

Copyright © 2024 BioMed Research International. This is an open access article distributed under the Creative Commons Attribution License, which permits unrestricted use, distribution, and reproduction in any medium, provided the original work is properly cited.

This article has been retracted by Hindawi following an investigation undertaken by the publisher [1]. This investigation has uncovered evidence of one or more of the following indicators of systematic manipulation of the publication process:

- (1) Discrepancies in scope
- (2) Discrepancies in the description of the research reported
- (3) Discrepancies between the availability of data and the research described
- (4) Inappropriate citations
- (5) Incoherent, meaningless and/or irrelevant content included in the article
- (6) Manipulated or compromised peer review

The presence of these indicators undermines our confidence in the integrity of the article's content and we cannot, therefore, vouch for its reliability. Please note that this notice is intended solely to alert readers that the content of this article is unreliable. We have not investigated whether authors were aware of or involved in the systematic manipulation of the publication process.

Wiley and Hindawi regrets that the usual quality checks did not identify these issues before publication and have since put additional measures in place to safeguard research integrity.

We wish to credit our own Research Integrity and Research Publishing teams and anonymous and named external researchers and research integrity experts for contributing to this investigation.










The corresponding author, as the representative of all authors, has been given the opportunity to register their agreement or disagreement to this retraction. We have kept a record of any response received.

### References

- [1] M. Patwekar, F. Patwekar, S. Alghamdi et al., "Vancomycin as an Antibacterial Agent Capped with Silver Nanoparticles: An Experimental Potential Analysis," *BioMed Research International*, vol. 2022, Article ID 3682757, 8 pages, 2022.

## Research Article

# Vancomycin as an Antibacterial Agent Capped with Silver Nanoparticles: An Experimental Potential Analysis

**Mohsina Patwekar** <sup>1</sup>, **Faheem Patwekar**,<sup>1</sup> **Saad Alghamdi** <sup>2</sup>, **Mehnaz Kamal** <sup>3</sup>,  
**Mamdouh Allahyani** <sup>4</sup>, **Mazen Almeahmadi** <sup>4</sup>, **Ahmed Kabrah** <sup>2</sup>, **Anas S. Dablood** <sup>5</sup>,  
**Ahad Amer Alsaari**,<sup>4</sup> **Talha Jawaid**,<sup>6</sup> **Anuradha Medikeri** <sup>1</sup>, **Krupa Samuel**,<sup>1</sup>  
**and Fahadul Islam** <sup>7</sup>

<sup>1</sup>Lugman College of Pharmacy, Gulbarga, Karnataka, India

<sup>2</sup>Laboratory Medicine Department, Faculty of Applied Medical Sciences, Umm Al-Qura University, Makkah, Saudi Arabia

<sup>3</sup>Department of Pharmaceutical Chemistry, College of Pharmacy, Prince Sattam Bin Abdulaziz University, Al-Kharj 11942, Saudi Arabia

<sup>4</sup>Department of Clinical Laboratory Sciences, College of Applied Medical Sciences, Taif University, P.O. Box 11099, Taif 21944, Saudi Arabia

<sup>5</sup>Department of Public Health, Health Sciences College at Al-Leith, Umm Al-Qura University, Makkah, Saudi Arabia

<sup>6</sup>Department of Pharmacology, College of Medicine, Al Imam Mohammad Ibn Saud Islamic University (IMSIU), Riyadh 13317, Saudi Arabia

<sup>7</sup>Department of Pharmacy, Faculty of Allied Health Sciences, Daffodil International University, Dhaka 1207, Bangladesh

Correspondence should be addressed to Mohsina Patwekar; [mohsina.patwekar@gmail.com](mailto:mohsina.patwekar@gmail.com) and Fahadul Islam; [fahadul29-774@diu.edu.bd](mailto:fahadul29-774@diu.edu.bd)

Received 16 July 2022; Revised 30 July 2022; Accepted 6 August 2022; Published 21 August 2022

Academic Editor: Wilson Aruni

Copyright © 2022 Mohsina Patwekar et al. This is an open access article distributed under the Creative Commons Attribution License, which permits unrestricted use, distribution, and reproduction in any medium, provided the original work is properly cited.

For the treatment of various infections, a variety of antimicrobial drugs are formulated. Nevertheless, many bacterial infections now exhibit antibiotic resistance due to the widespread utilization antibiotics. Methicillin-resistant among the most dangerous multidrug-resistant bacteria is *Staphylococcus aureus* (MRSA). Vancomycin became a viable therapy option due to MRSA resistance to methicillin medicines. One of the well-informed antibacterial compounds with wideband antibacterial activity is silver nanoparticles (AgNPs). AgNPs are thus suitable candidates for usage in conjunction alongside vancomycin to increase its antibacterial effect. The goal of the present research work is to boost the antibacterial potency of the glycopeptide antibiotic vancomycin towards Gram-positive (*Staphylococcus aureus*) but also Gram-negative (*Escherichia coli*) bacteria. The chemical reduction approach is used to create a colloidal solution of silver nanoparticles utilizing silver nitrate as a precursor in the environment of the ionic surfactant trisodium citrate that serves as covering including reducing reagent. Vancomycin was used to functionalize the synthesized nanoparticles and create the nanodrug complex (Van@AgNPs). The synergistic antibacterial potential of silver nanoparticles coated with vancomycin on both test pathogens was investigated using the agar well diffusion technique. The antibacterial potency for both classes of bacteria has significantly increased, according to the well diffusion test. It has been noted that this improvement is synergistic instead of additive.

## 1. Introduction

As more bacterial infections develop multidrug resistance (MDR), the availability of antibiotics has been a critical issue

for the healthcare professionals [1]. The most difficult issues for leading experts in the field of biomedicine are the rise in multiple-drug resistant confined of *Pseudomonas aeruginosa*, *Staphylococcus aureus*, *Klebsiella pneumoniae*, *Escherichia coli*,

TABLE 1: Compounds employed and their uses.

Compounds	Uses
Silver nitrate ( $\text{AgNO}_3$ )	A precursor
Trisodium citrate ( $\text{Na}_3\text{C}_6\text{H}_5\text{O}_7$ )	In the production of silver nanoparticle, it is employed as reducing agent as well as capping agent
Vancomycin ( $\text{C}_{66}\text{H}_{75}\text{Cl}_2\text{N}_9\text{O}_{24}$ )	A medication utilized for storing on the surface area of formulated silver nanoparticles
Double deionized water	Each of the solutions was prepared using water that had been twice deionized

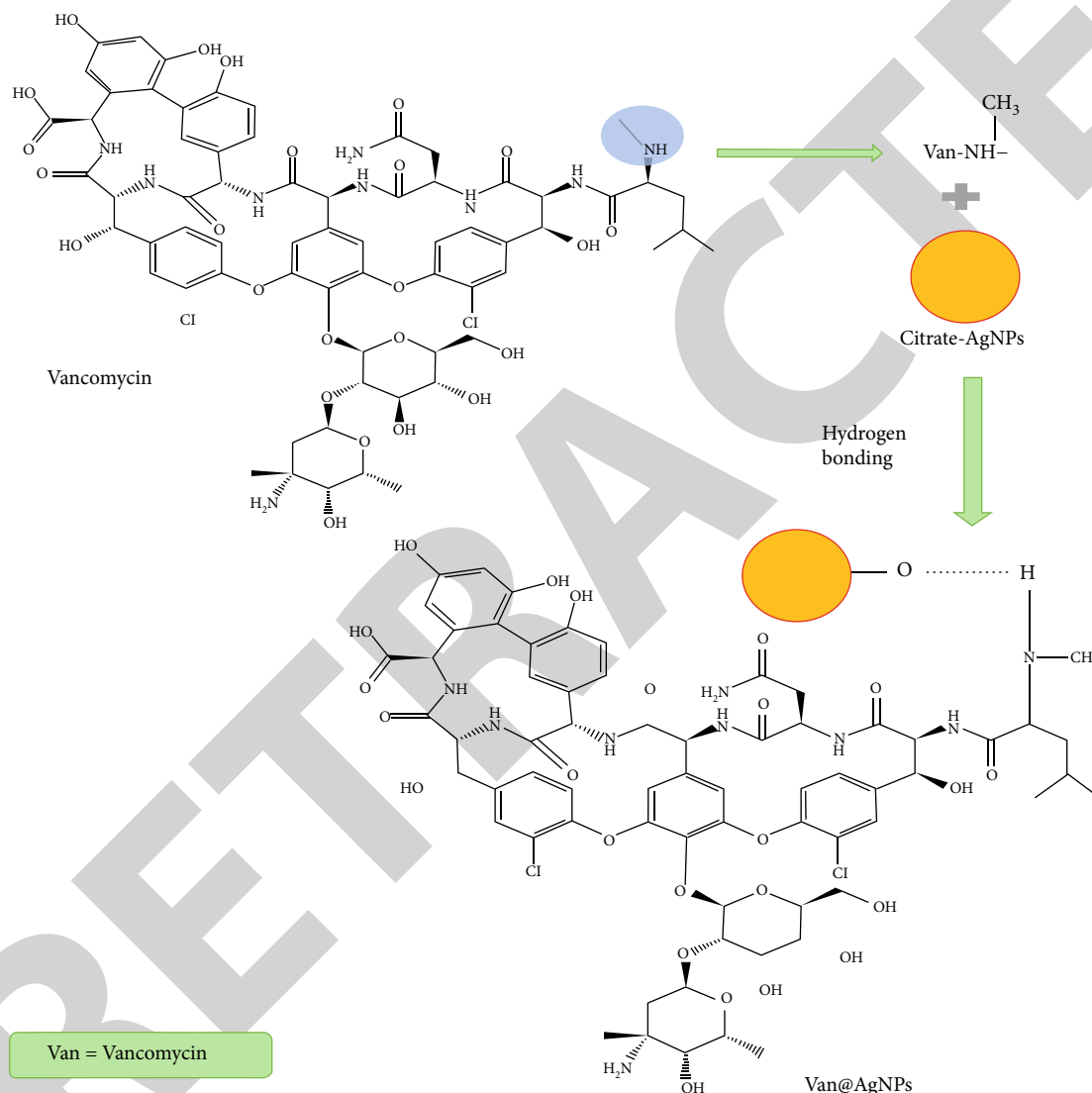


FIGURE 1: Reaction expressing the addition of vancomycin with AgNPs.

*Enterococcus faecium*, and *Enterobacter* species to the numerous traditional antibiotics. Antibiotic usage in any form can put more strain on bacteria due to selection. This causes vulnerable bacteria to perish while allowing resistant bacteria to thrive [2, 3]. Alternative therapies are becoming more and more necessary as antibiotic resistance spreads. Nanoparticles offer enormous opportunity for medicinal delivery systems for tiny molecules including medicines, DNA, and proteins. The antibacterial effectiveness of noble metal nanoparticles, that is, because of their huge surface area permitting large synergistic effect which is derived by several interactions, has recently

emerged as one of the most potential tools in the antibacterial inventory [4]. Some antimicrobial agents can be made more efficient by diminishing the cell membrane or enhancing cellular penetration. So, by reducing the negative effects related to medication molecules, metal nanoparticles combined with antibacterial pharmaceuticals may demonstrate better efficacy in particular therapies [5]. Since the earliest times, silver was already thoroughly studied for its ability to prevent infections, and silver nanoparticles (AgNPs) were established antibacterial properties towards a variety of bacterial species [6].



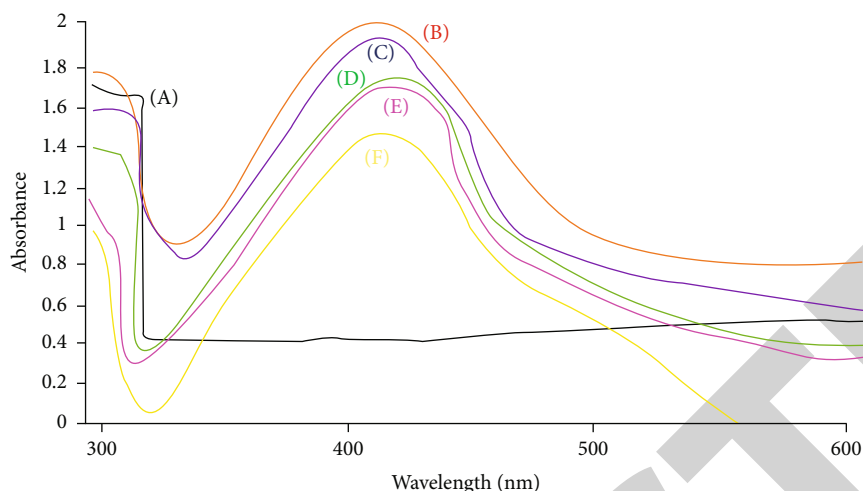


FIGURE 2: UV absorption spectra of (a) vancomycin, (b) citrate-AgNPs, and (c–f) Van@citrate-AgNPs at concentrations 0.05 mM, 0.07 mM, 0.1 mM, and 0.3 mM, respectively.

Vancomycin has been the dominant antibacterial medication employed to cure infections brought on by methicillin-resistant *Staphylococcus aureus* (MRSA) in the early 1950s. The widespread burden of vancomycin resistance among Gram-positive cocci is getting worse nowadays. Vancomycin advancement research showed that staphylococci vancomycin resistance proved challenging to establish *in vitro* [7]. In 1988, the first types of vancomycin-resistant enterococci (VRE) were discovered. Ever after, an increasing number of glycopeptide-resistant strains are also identified, indicating that such bacteria will possess the ability to spread the genes that give them vancomycin resistance to other bacterial species. Nanomedicines have aided in the advancement of new therapies being developed to combat VRE. Due to their acceptable biological deeds, silver nanoparticles (AgNPs) have several uses as antibacterial therapeutics [8]. The utilization of the silver nanoparticle along with vancomycin to increase the potency of the vancomycin specifically in MRSA is the main goal of this research paper.

## 2. Resources and Procedures for Experiments

**2.1. Resources.** Every one of the compounds included in this experiment would be of the analytical grade as well as were not subsequently purified before usage (Table 1).

**2.2. Generation of Silver Nanoparticles with a Citrate Capping (Figure 1).**

- (i) Silver nitrate ( $\text{AgNO}_3$ ) was used like a precursor in a chemical reduction process to create colloidal citrate-capped AgNPs (citrate-AgNPs), with sodium citrate acting like a reducing and shielding factor
- (ii) In this procedure, a 50 mL solution of  $\text{AgNO}_3$  (1 mM) in deionized water was brought near boiling while being continuously stirred on a magnetic hot plate

- (iii) During at that time as quickly as possible, the  $\text{AgNO}_3$  solution started to boil; 350 L sodium citrate solution (20 mM) has been poured dropwise
- (iv) The solution gradually becomes brownish yellow that also shows a sign that the  $\text{Ag}^+$  ions have been reduced
- (v) The solution was heated for a little while longer while being stirred, then thereafter cooled to room temperature for additional experiments

**2.3. Vancomycin-Coated Silver Nanoparticle Formulation.** A separate aqueous solution of vancomycin (5 mg/5 mL) has been produced beneficial to the manufacturing related to vancomycin loaded citrate-AgNPs (Van@ citrate-AgNPs). Vancomycin was utilized at different quantities like 0.05, 0.07, 0.1, 0.3, and 0.5 mM. Concentration of citrate-AgNPs remained unchanged, i.e., 1 mM. Using a magnetic stirrer which is set at room temperature, the solution then permitted to agitate for 20 to 25 minutes. The solution was left overnight, after which it was refrigerated for future testing but also characterisation. UV-Vis spectra of vancomycin, citrate-AgNPs, and Van@citrate-AgNPs at different concentration is presented in Figure 2.

**2.4. Microbiological Evaluation Processes.** Employing of agar well diffusion technique, the antibacterial action of vancomycin-capped silver nanoparticles is evaluated with reference to medication. The media and glassware utilized throughout this test were sterile for twenty minutes at  $120^\circ\text{C}$  in an autoclave. This procedure is utilized for calculation of the zone of inhibition with both Gram-positive bacteria (such as *S. aureus*) and Gram-negative bacteria (such as *E. coli*) in order to study antibacterial action. Both bacteria had been cultivated for 24 hrs at  $37^\circ\text{C}$  in Luria broth (LB) medium. The whole area of the agar plate was covered with a certain amount of microbial inoculation. Thereafter, tiny holes having a diameter of about 5 mm had been made using a sterile

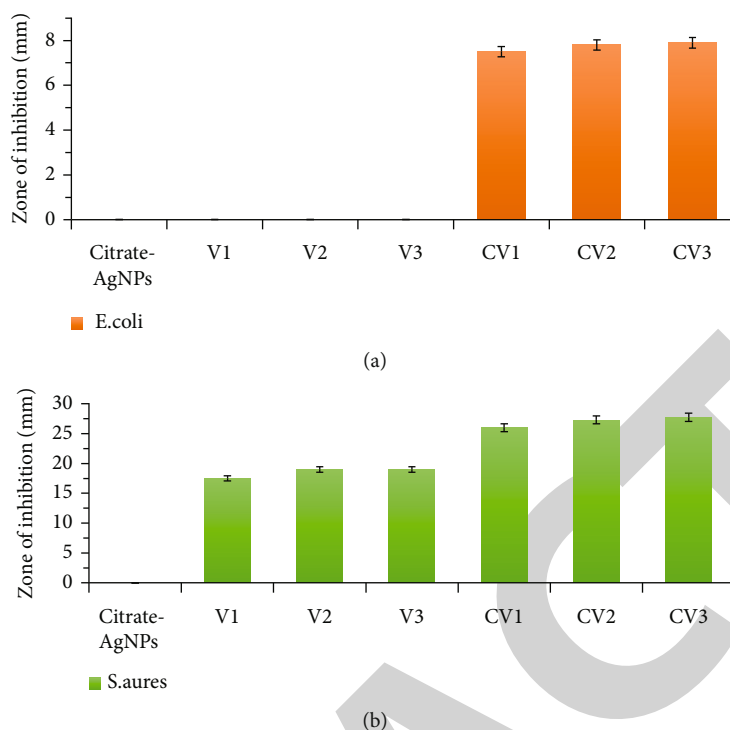


FIGURE 3: Antibacterial action of bacterial strain in the form of zone of inhibition  $\pm$  S.D.

TABLE 2: Zone of inhibition (mm)  $\pm$  S.D. of AgNPs, Van, and Van@AgNPs against *S. aureus* and *E. coli*.

	Gram-positive bacteria ( <i>Staphylococcus aureus</i> )	Gram-negative bacteria <i>Escherichia coli</i>
AgNPs	0 $\pm$ 0	0 $\pm$ 0
Van1: 0.05 mM	17.5 $\pm$ 1.0	0 $\pm$ 0
Van2: 0.1 mM	19 $\pm$ 0.6	0 $\pm$ 0
Van3: 0.3 mM	19 $\pm$ 0.6	0 $\pm$ 0
Van@AgNPs1: 0.05 mM	26 $\pm$ 0.6	7.5 $\pm$ 0.5
Van@AgNPs2: 0.1 mM	27.3 $\pm$ 0.5	7.8 $\pm$ 0.9
Van@AgNPs3: 0.3 mM	27.7 $\pm$ 0.4	7.8 $\pm$ 0.9

cork borer. 50 L of each of the following solutions was added into the holes separately: vancomycin, silver nitrate (AgNPs), vancomycin-AgNPs (Van@citrate-AgNP complex), and also regular saline solution.

**2.5. Study on In Vitro Antibacterial Action.** By employing standard agar well diffusion approach, the synergistic antibacterial impact produced from the citrate-capped AgNPs containing vancomycin is examined under this work. Independent effects of the unbounded vancomycin and uncovered silver nanoparticles, targeting both kinds of Gram-positive (*S. aureus*) as well as Gram-negative (*E. coli*) strains, are examined. Citrate functions as linkage between the vancomycin and the AgNPs. Because citrate is anionic capping agent boosts AgNP stability throughout an electrostatic stabilizing mechanism, its usage is rationalized. At the evaluation concentration 60 g/mL, the bare AgNPs which do not contain drug had no antibacterial impact on either strain.

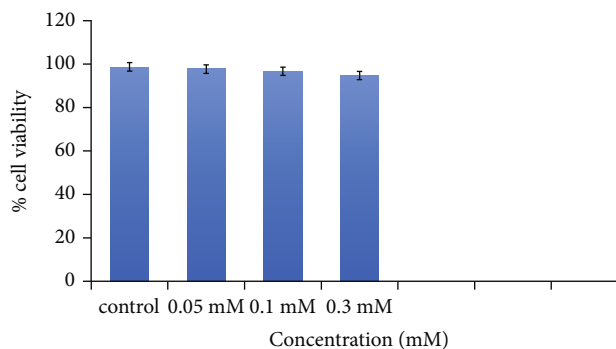


FIGURE 4: Percentage of cell availability in different concentration.

However, mentioned citrate-capped AgNPs containing antibiotic had a noteworthy synergistic impact. AgNP-vancomycin combination was shown to be more efficient towards *S. aureus* than *E. coli*.

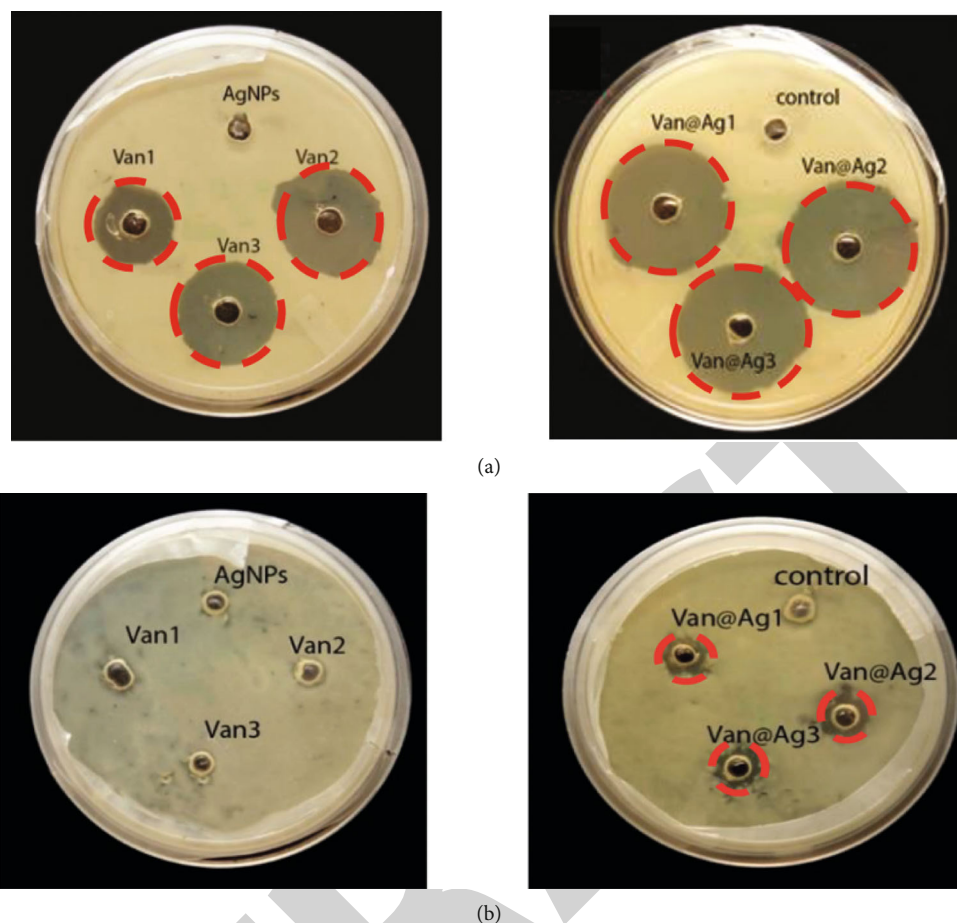


FIGURE 5: Illustration of agar plates demonstrating antifungal effect of vancomycin, AgNPs, and Van@citrate-AgNPs against (a) *S. aureus* and (b) *E. coli* at various concentrations.

Simultaneous testing of AgNPs, free vancomycin, and also vancomycin-coated silver nanoparticles (Van@AgNPs) was conducted versus both trial strains throughout the antibacterial investigation. When used over both Gram-positive and Gram-negative classes of bacteria, vancomycin-coated silver nanoparticles had a broader inhibition zone but also consequently had greater antibacterial activity (Figure 3). Vancomycin-coated silver nanoparticles inhibited *S. aureus* and *E. coli*'s growth more effectively than vancomycin did against these bacteria.

According to the prior studies, it is shown that vancomycin is exclusively efficient against strains of Gram-positive bacteria; it is ineffective towards strains of Gram-negative bacteria [9]. However, it was shown during this investigation that vancomycin showed zero effect supporting to the development of *E. coli*, whereas the AgNP-vancomycin combination somewhat suppresses it. As a result, AgNP-vancomycin combination became effective against vancomycin-resistant *E. coli*. Additionally, the impact was more potent towards Gram-positive than Gram-negative bacteria.

2.5.1. Note. Van1:0.05 mM (V1),  
Van2:0.1 mM (V2),  
Van3:0.3 mM (V3),  
Van@AgNPs1:0.05 mM (CV1),

Van@AgNPs2:0.1 mM (CV2),  
Van@AgNPs3:0.3 mM (CV3).

The ZOI rises from 0 to 7.8 mm for *E. coli* while ZOI rises in between 0 and 27.7 mm for *S. aureus* (Table 2). Both the vancomycin-sensitive *S. aureus* and the vancomycin-sensitive *E. coli* were more delicate to the drug conjugate AgNPs after being cherished with Van@citrate-AgNPs. Vancomycin along with AgNPs has been found to have a synergistic impact against both classes of Gram-positive bacteria. Following treatment with Van@citrate-AgNPs, the morphological alterations in the bacterial cell walls of both *S. aureus* and *E. coli* have been observed (Figures 4 and 5). Similar findings have also been observed in other earlier publications [10, 11].

Based on diversity of the cell membranes of Gram-positive as well as Gram-negative bacteria, it is possible to explain why Van@citrate-AgNPs are more efficient against *S. aureus*. However, compared to Gram-negative bacteria which contain a thin cell membrane, Gram-positive microorganisms possess thicker cell walls consisting of peptidoglycan layers. However, Gram-negative bacteria have a lipopolysaccharide- (LPS-) based thick outer layer that covers their thin peptidoglycan wall that is missing in Gram-positive bacteria [12]. This thick outer layer has a diameter of about 10 nm. Due to the lack of an outer layer,

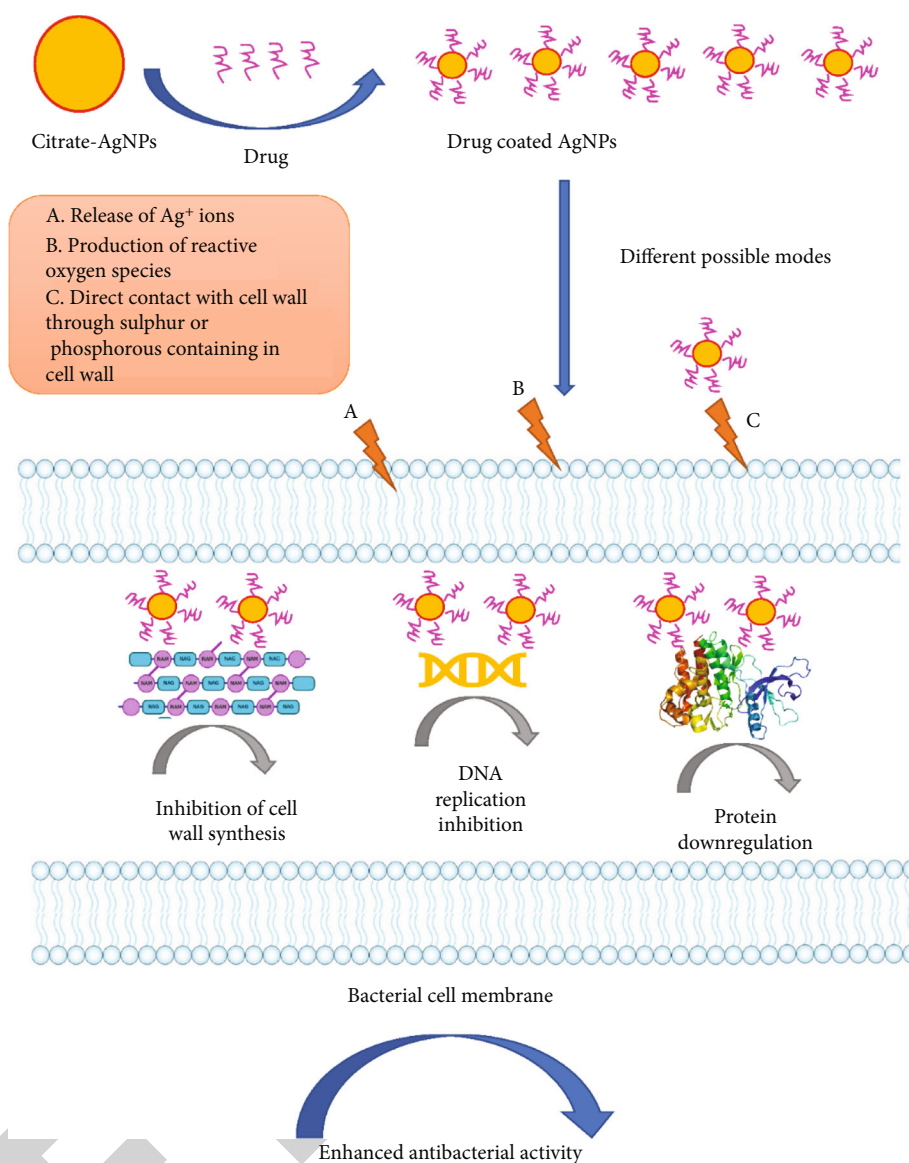


FIGURE 6: Proposed interaction between vancomycin-coated silver nanoparticle and bacterial cell walls.

Gram-negative bacteria are highly susceptible to AgNP-drug complexes although having a thicker peptidoglycan layer compared to Gram-positive bacteria [13].

**2.6. Proposed Interaction between Vancomycin-Coated Silver Nanoparticle (Van@AgNPs) and Bacterial Cell Walls (Figure 6).** Vancomycin's bactericidal action is dependent on the suppression of peptidoglycan-based bacterial cell wall production [14, 15]. However, this technique is no longer effective as some vancomycin-resistant bacteria (such as VRSA) have emerged. When combined with AgNPs, vancomycin has a synergistic antibacterial activity towards both experimental strains. As was before established, vancomycin forms the Van@AgNP complex via hydrogen bonding to AgNPs through citrate.

The stages in the process that result in a synergistic antimicrobial property might be used to describe the reaction mechanisms. These are the steps: vancomycin and AgNP

surface interaction.  $Ag^+$  ions or AgNPs are released by a complex that is bounded with the bacteria [16]. AgNPs become poisonous when they bind to the phosphorous in DNA and the sulfur in proteins. It impairs a number of bacterial processes, including DNA replication along with protein synthesis; they ultimately result in bacterial or cell death. The main interactional mechanism is this [17, 18]. Additionally, oxidative stress that affords another pathway for cellular disruption can be commenced from the production of reacting oxygen substance on the surface of AgNPs [19, 20]. Nevertheless, the specific process through which silver nanoparticles fight microorganisms is still unknown. The electrostatic interaction among nanoparticles and the bacterial cell wall was also shown in earlier investigations [21].

A number of variables, such as particle size, shape, aggregation, and capping agent, affect the rate at which silver ions are released. In comparison to bigger particles, the tiny silver nanospheres discharge ions more quickly. The

surface's complexation has an impact on the ion release rate as well. Contrary to more readily displaced stabilizing compounds like citrate, firmly bound thiol-containing capping agents often reduce release rates [22]. As a result, the ion release rate is significantly influenced by the citrate coating on the silver surface. The histogram in Figure 3 depicts the improvement of antibacterial potency towards *S. aureus* and *E. coli*. Such findings taken together show that Van@citrate-AgNPs gather inside the bacterial membrane as well as cytoplasm, proving Van@citrate-AgNPs are successfully supplied to the bacterium where silver ions, vancomycin, or a combination of the two, that would be the main process, can communicate among the cell membrane to restrict bacterial development. In conclusion, Van@citrate-AgNP bioconjugate compounds function as an efficient antagonist of both Gram-positive and Gram-negative bacteria.

### 3. Conclusion

The chemical reduction approach was used to generate vancomycin-coated AgNPs in the existence of the ionic capping material trisodium citrate that intern serves like a connector and stability enhancer for the drug molecules. Van@citrate-AgNPs had improved significant ability towards both *S. aureus* (Gram-positive) and *E. coli* (Gram-negative), according to an *in vitro* antibacterial assay. The findings suggest that examined microorganisms are effectively inhibited by citrate-AgNPs. Depending upon the outcomes, we are able to say that citrate-AgNPs are effective transported systems for the medication vancomycin and that, with minimal adjustments, they may be employed for controlled administration to bacterial cells. In the end, it is concluded that the Van@citrate-AgNP is more potent than the single entity vancomycin towards both *S. aureus* and *E. coli*.

### Data Availability

All data used to support the findings of this study are included within the article.

### Conflicts of Interest

The authors declare that they have no conflict of interest.

### References

- [1] M. M. Elsebaie, H. T. Nour el-Din, N. S. Abutaleb et al., "Exploring the structure-activity relationships of diphenylurea as an antibacterial scaffold active against methicillin- and vancomycin-resistant *Staphylococcus aureus*," *European Journal of Medicinal Chemistry*, vol. 234, article 114204, 2022.
- [2] S. Mittal and A. Roy, "Fungus and plant-mediated synthesis of metallic nanoparticles and their application in degradation of dyes," in *Photocatalytic Degradation of Dyes*, pp. 287–308, Elsevier, 2021.
- [3] A. Roy, A. Sharma, S. Yadav, L. T. Jule, and R. Krishnaraj, "Nanomaterials for remediation of environmental pollutants," *Bioinorganic Chemistry and Applications*, vol. 2021, Article ID 1764647, 16 pages, 2021.
- [4] A. Roy, V. Singh, S. Sharma et al., "Antibacterial and dye degradation activity of green synthesized iron nanoparticles," *Journal of Nanomaterials*, vol. 2022, Article ID 3636481, 6 pages, 2022.
- [5] M. U. Shinde, M. Patwekar, F. Patwekar et al., "Nanomaterials: a potential hope for life sciences from bench to bedside," *Journal of Nanomaterials*, vol. 2022, Article ID 5968131, 13 pages, 2022.
- [6] A. Oloffs, C. Grosse-Siestrup, S. Bisson, M. Rinck, R. Rudolph, and U. Gross, "Biocompatibility of silver-coated polyurethane catheters and silvercoated Dacron® material," *Biomaterials*, vol. 15, no. 10, pp. 753–758, 1994.
- [7] F. I. Patwekar, M. F. Patwekar, A. Muhammad, H. Sanjeev, and A. A. Mohsin, "Activity guided separation of phytoconstituents from the flowers of *Ichnocarpus frutescens* L. and evaluation for antioxidant property," *Research Journal of Pharmaceutical, Biological and Chemical Sciences*, vol. 1, no. 4, pp. 318–323, 2010.
- [8] L. M. Dalla Costa, P. E. Reynolds, H. A. Souza, D. C. Souza, M. F. Palepou, and N. Woodford, "Characterization of a divergent *vanD*-type resistance element from the first glycopeptide-resistant strain of *Enterococcus faecium* isolated in Brazil," *Antimicrobial Agents and Chemotherapy*, vol. 44, no. 12, pp. 3444–3446, 2000.
- [9] F. I. Patwekar, S. Heroor, M. F. Patwekar, and M. Asif, "Evaluation of antimicrobial activity of *Tephrosia procumbens* Buch-Ham," *Research Journal of Pharmacognosy and Phytochemistry*, vol. 2, no. 3, pp. 238–240, 2010.
- [10] D. Xia, T. An, G. Li, W. Wang, H. Zhao, and P. K. Wong, "Synergistic photocatalytic inactivation mechanisms of bacteria by graphene sheets grafted plasmonic AgAgX (X= Cl, Br, I) composite photocatalyst under visible light irradiation," *Water Research*, vol. 99, pp. 149–161, 2016.
- [11] W. K. Jo, S. Kumar, M. A. Isaacs, A. F. Lee, and S. Karthikeyan, "Cobalt promoted TiO<sub>2</sub>/GO for the photocatalytic degradation of oxytetracycline and Congo red," *Applied Catalysis B: Environmental*, vol. 201, pp. 159–168, 2017.
- [12] A. Patil, N. Munot, M. Patwekar et al., "Encapsulation of lactic acid bacteria by lyophilisation with its effects on viability and adhesion properties," *Evidence-based Complementary and Alternative Medicine*, vol. 2022, Article ID 4651194, 9 pages, 2022.
- [13] N. Mujaddidi, S. Nisa, S. Al Ayoubi et al., "Pharmacological properties of biogenically synthesized silver nanoparticles using endophyte *Bacillus cereus* extract of *Berberis lyceum* against oxidative stress and pathogenic multidrug-resistant bacteria," *Saudi Journal of Biological Sciences*, vol. 28, no. 11, pp. 6432–6440, 2021.
- [14] F. Islam, S. Shohag, M. J. Uddin et al., "Exploring the journey of zinc oxide nanoparticles (ZnO-NPs) toward biomedical applications," *Materials*, vol. 15, no. 6, p. 2160, 2022.
- [15] C. Walsh, "Deconstructing vancomycin," *Science*, vol. 284, no. 5413, pp. 442–443, 1999.
- [16] M. Patwekar, F. Patwekar, A. Mezni et al., "Assessment of antioxidative and alpha-amylase potential of polyherbal extract," *Evidence-based Complementary and Alternative Medicine*, vol. 2022, Article ID 7153526, 10 pages, 2022.
- [17] Q. L. Feng, J. Wu, G. Q. Chen, F. Z. Cui, T. N. Kim, and J. O. Kim, "A mechanistic study of the antibacterial effect of silver ions on *Escherichia coli* and *Staphylococcus aureus*," *Journal of Biomedical Materials Research*, vol. 52, no. 4, pp. 662–668, 2000.

## *Retraction*

# **Retracted: Central Composite Designed Fast Dissolving Tablets for Improved Solubility of the Loaded Drug Ondansetron Hydrochloride**

### **BioMed Research International**

Received 8 January 2024; Accepted 8 January 2024; Published 9 January 2024

Copyright © 2024 BioMed Research International. This is an open access article distributed under the Creative Commons Attribution License, which permits unrestricted use, distribution, and reproduction in any medium, provided the original work is properly cited.

This article has been retracted by Hindawi following an investigation undertaken by the publisher [1]. This investigation has uncovered evidence of one or more of the following indicators of systematic manipulation of the publication process:

- (1) Discrepancies in scope
- (2) Discrepancies in the description of the research reported
- (3) Discrepancies between the availability of data and the research described
- (4) Inappropriate citations
- (5) Incoherent, meaningless and/or irrelevant content included in the article
- (6) Manipulated or compromised peer review

The presence of these indicators undermines our confidence in the integrity of the article's content and we cannot, therefore, vouch for its reliability. Please note that this notice is intended solely to alert readers that the content of this article is unreliable. We have not investigated whether authors were aware of or involved in the systematic manipulation of the publication process.

Wiley and Hindawi regrets that the usual quality checks did not identify these issues before publication and have since put additional measures in place to safeguard research integrity.

We wish to credit our own Research Integrity and Research Publishing teams and anonymous and named external researchers and research integrity experts for contributing to this investigation.






The corresponding author, as the representative of all authors, has been given the opportunity to register their agreement or disagreement to this retraction. We have kept a record of any response received.

### **References**

- [1] C. Thalluri, R. Amin, J. R. Mandhadi et al., "Central Composite Designed Fast Dissolving Tablets for Improved Solubility of the Loaded Drug Ondansetron Hydrochloride," *BioMed Research International*, vol. 2022, Article ID 2467574, 13 pages, 2022.

## Research Article

# Central Composite Designed Fast Dissolving Tablets for Improved Solubility of the Loaded Drug Ondansetron Hydrochloride

Chandrashekar Thalluri,<sup>1</sup> Ruhul Amin ,<sup>1</sup> Jithendar Reddy Mandhadi,<sup>1</sup> Amel Gacem,<sup>2</sup> Talha Bin Emran ,<sup>3,4</sup> Biplab Kumar Dey,<sup>1</sup> Arpita Roy ,<sup>5</sup> Mohammed S. Alqahtani ,<sup>6,7,8</sup> Moamen S. Refat,<sup>9</sup> Sher Zaman Safi,<sup>10,11</sup> and Amnah Mohammed Alsuhaibani <sup>12</sup>

<sup>1</sup>Faculty of Pharmaceutical Science, Assam Down Town University, Panikhaiti, Guwahati, Assam 781026, India

<sup>2</sup>Department of Physics, Faculty of Sciences, University 20 Août 1955, Skikda, Algeria

<sup>3</sup>Department of Pharmacy, BGC Trust University Bangladesh, Chittagong 4381, Bangladesh

<sup>4</sup>Department of Pharmacy, Faculty of Allied Health Sciences, Daffodil International University, Dhaka 1207, Bangladesh

<sup>5</sup>Department of Biotechnology, School of Engineering & Technology, Sharda University, Greater Noida 201310, India

<sup>6</sup>Radiological Sciences Department, College of Applied Medical Sciences, King Khalid University, Abha 61421, Saudi Arabia

<sup>7</sup>Bioimaging Unit, Space Research Centre, Michael Atiyah Building, University of Leicester, Leicester LE1 7RH, UK

<sup>8</sup>Research Center for Advanced Materials Science (RCAMS), King Khalid University, Postcode: 9004, Zip code: 61413, Abha, Saudi Arabia

<sup>9</sup>Department of Chemistry, College of Science, Taif University, P.O. Box 11099, Taif 21944, Saudi Arabia

<sup>10</sup>Faculty of Medicine, Bioscience and Nursing, MAHSA University, Jenjarom, 42610 Selangor, Malaysia

<sup>11</sup>IRCBM, COMSATS University Islamabad, Lahore Campus, Lahore, Pakistan

<sup>12</sup>Department of Physical Sport Science, College of Education, Princess Nourah bint Abdulrahman University, P.O. Box 84428, Riyadh 11671, Saudi Arabia

Correspondence should be addressed to Ruhul Amin; [ruhulglp18@gmail.com](mailto:ruhulglp18@gmail.com), Talha Bin Emran; [talhabmb4@gmail.com](mailto:talhabmb4@gmail.com), and Arpita Roy; [arpita.roy@sharda.ac.in](mailto:arpita.roy@sharda.ac.in)

Received 19 July 2022; Revised 31 July 2022; Accepted 1 August 2022; Published 21 August 2022

Academic Editor: Senthil Rethinam

Copyright © 2022 Chandrashekar Thalluri et al. This is an open access article distributed under the Creative Commons Attribution License, which permits unrestricted use, distribution, and reproduction in any medium, provided the original work is properly cited.

Ondansetron tablets that are directly compressed using croscopovidone and croscarmellose as a synthetic super disintegrant are the subject of this investigation. A central composite, response surface, randomly quadratic, nonblock (version 13.0.9.0)  $3^2$  factorial design is used to optimize the formulation (two-factor three-level). To make things even more complicated, nine different formulation batches (designated as F1–F9) were created. There were three levels of croscopovidone and croscarmellose (+1, 0, -1). In addition to that, pre- and postcompressional parameters were evaluated, and all evaluated parameters were found to be within acceptable range. Among all postcompressional parameter dispersion and disintegration time, *in vitro* drug release experiments (to quantify the amount of medication released from the tablet) and their percentage prediction error were shown to have a significant influence on three dependent variables. Various pre- and postcompression characteristics of each active component were tested *in vitro*. Bulk density, tap density, angle of repose, Carr's index, and the Hausner ratio were all included in this analysis, as were many others. This tablet's hardness and friability were also assessed along with its dimension and weight variations. Additional stability studies may be conducted using the best batch of the product. For this study, we utilised the Design-Expert software to select the formulation F6, which had dispersion times of  $17.67 \pm 0.03$  seconds, disintegration times of  $120.12 \pm 0.55$  seconds, and percentage drug release measurements of  $99.25 \pm 0.36$  within 30 minutes. Predicted values and experimental data had a strong correlation. Fast dissolving pills of ondansetron hydrochloride may be created by compressing the tablets directly.

## 1. Introduction

Super disintegrates are a novel class of agents created in recent years. Excipients such as “Super disintegrates” assist break apart compacted mass when used in a liquid environment. This is critical for products that need quick release [1]. These novel compounds have better disintegration efficiency and mechanical strength at lower concentrations. Super disintegrants are the basis for developing rapid dissolving pills (RDPs). Super disintegrants are important in dissolving and disintegrating pills. Choosing the right super disintegrant concentration is critical for fast disintegration and high dissolution rates [2]. The combination of swelling and water absorption by the formulation causes super disintegration. The swelling of super disintegrants increases the wetted surface of the carrier, boosting wettability and dispensability of the system [3–5]. The ideal super disintegrant concentration is determined by the disintegrant’s critical concentration. When the super disintegrant concentration is below a certain level, the disintegration time of the tablet decreases, but when the concentration is higher, the disintegration time remains constant or even increases [6, 7]. Croscarmellose sodium (Vivasol, AcDiSol) is a starch-free cross-linked cellulose that expands 4-8 folds in 10 seconds via both swelling and wicking mechanisms. It also swells in two dimensions and is best adapted for direct compression or granulation. In contrast to croscarmellose sodium, crospovidone acts through capillary action. Get a water-insoluble, spongy tablet. It gives empirical models (linear and quadratic) that characterize the influence of processing factors on the response investigated. The experimental design technique reduced the number of trials, identified factor interactions, identified the ideal response within the experimental zone, and empirically modelled the data [8]. The experiments used a two-factor, three-level central composite design. This architecture explores quadratic response surfaces and allows for polynomial model building. Central composite design can estimate second and third order effects, discover interfactor interactions, and find response optimums [9].

In addition to treating nausea and vomiting caused by cancer treatment, ondansetron hydrochloride has been shown to have anxiolytic and neuroleptic characteristics. It is highly powerful, deliquescent and metabolized rapidly in the liver [10]. Because patients with nausea and vomiting cannot take oral anti emetics, 5-HT<sub>3</sub> receptor antagonists like ondansetron hydrochloride were first created as injectable. This is because it is simpler to administer oral antiemetic medicines than intravenous. Noninjectable ondansetron hydrochloride fast-dissolving tablets are a superior choice for cancer patients suffering from nausea, vomiting, and swallowing difficulties. For oral or buccal absorption, it may increase bioavailability. In tablet format, ondansetron hydrochloride is a low-dose drug, therefore, diluent action is more pronounced [11]. For the optimization of a new quick dissolving tablet formulation, ondansetron hydrochloride was chosen as a medication candidate.

TABLE 1: Variables in 3<sup>2</sup> full factorial design.

Formulation code	X <sub>1</sub>	X <sub>2</sub>
F1	0	0
F2	+1	0
F3	-1	-1
F4	+1	-1
F5	0	-1
F6	+1	+1
F7	-1	0
F8	-1	+1
F9	0	+1

## 2. Materials and Methods

Gifts from Torrent Pharma in Ahmedabad, India, and the Wockhardt Research Centre in Aurangabad, India, included ondansetron hydrochloride, the crospovidone and croscarmellose sodium formulations, respectively. Mannitol directly compressible was made possible by the kind donations of Indian lactose spray dried from Strides Arco Labs in Bangalore, Glenmark Ltd. in Nashik, and Alkem Labs Pvt Ltd. in Mumbai (Pearlitol SD 200). Analytical reagent quality was found in all of the other substances.

**2.1. Experimental Design.** There is an embedded factorial or fractional factorial design in the core composite design, which is supplemented with a collection of star points to enable for curvature estimate. Each face of the factorial space has a star point in the face-centered central composite design [12]. The regression analysis of the statistically relevant variables was used to create the second-order regression models [13, 14]. Regression models are of the following type:

$$Y = B_0 + B_1 X_1 + B_2 X_2 + B_{12} X_1 X_2 + B_{11} X_{12} + B_{22} X_{22}. \quad (1)$$

Each factor-level combination of X<sub>1</sub> and X<sub>2</sub> is analyzed; B<sub>0</sub> is an intercept; B<sub>1</sub> – B<sub>22</sub> are regression coefficients. Y is the constructive response associated with each factor-level combination. Predicting dispersion time (Y<sub>1</sub>), disintegration time (Y<sub>2</sub>), and percentage drug release (Y<sub>3</sub>) from fast dissolving tablets was made possible via the application of polynomial equations derived from this optimization approach. The validity of the response surface models was further evaluated by comparing predicted values for Y<sub>1</sub>, Y<sub>2</sub>, and Y<sub>3</sub> with experimental data.

**2.2. UV Absorption Spectroscopy.** Using UV spectroscopy, it was determined that the drug concentration had been discovered. For the stock solution, the ondansetron hydrochloride was dissolved in a pH 6.8 phosphate buffer. A volumetric flask of 100 mL was used to transfer 100 mg of medicine. Using pH 6.8 phosphate buffer, the volume of stock solution (B) was brought up to the mark by diluting one mL of stock solution A with 100 mL of the buffer. For this experiment, aliquots of stock solution (B) (pH 6.8 phosphate buffer) were serially diluted from 2 to 20 microgram of



TABLE 2: Composition of 3<sup>2</sup> factorial design formulations of ondansetron hydrochloride fast dissolving tablets.

Name of ingredients in mg	F1	F2	F3	F4	F5	F6	F7	F8	F9
Ondansetron hydrochloride	10	10	10	10	10	10	10	10	10
Crospovidone (%w/w)	0	7.5	2.5	7.5	5	7.5	2.5	2.5	0
Croscarmellose (%w/w)	0	5	2.5	2.5	2.5	7.5	5	7.5	7.5
Spray dried lactose	150	150	150	150	150	150	150	150	150
Mannitol	q.s.	q.s.	q.s.	q.s.	q.s.	q.s.	q.s.	q.s.	q.s.
Magnesium stearate	7.5	7.5	7.5	7.5	7.5	7.5	7.5	7.5	7.5
Talc	7.5	7.5	7.5	7.5	7.5	7.5	7.5	7.5	7.5

drug per millilitre (mcg/mL). The absorbance of the final solutions was measured at 248 nm using a Systronics AU-2701 spectrophotometer in Mumbai, India [15].

**2.3. Fourier Transform Infrared Spectroscopy (FTIR).** The FTIR spectra of the pure drug and the drug combination with super disintegrants were both reported. FTIR spectroscopy was used to evaluate the materials using the KBr pellet technique [7]. An equal amount of dry potassium bromide and 10 milligrams of the formulation are then blended together. Pestle and mortar are used to grind the mixture to a fine powder. A hydraulic press compresses the mixture into pellets. The findings were obvious when the transparent pellets were scanned using a frequency range of 4000–400 cm<sup>-1</sup> [16].

**2.4. Preparation of Ondansetron Hydrochloride Fast Dissolving Tablets by Direct Compression.** By using the direct compression approach, it was possible to create ondansetron pills that dissolve quickly. Step by step, each component was combined, then sieved (number 100), and mixed with the medicine in a plastic bag for 15 minutes. At the end of this powder combination, talc and magnesium stearate were added and stirred for another 5 minutes. A single punch tablet machine was used to compress the active mixes into 200 milligram tablets. Preliminary batch findings were used to create 3<sup>2</sup> factorial designs with two independent variables, X<sub>1</sub> and X<sub>2</sub>, where X<sub>1</sub> represents the quantity of crospovidone, and X<sub>2</sub> represents the amount of croscarmellose in the final formulation. For each component, three levels (-1, 0, and +1) were chosen to represent low, centre, and high values [17]. There were at least nine batches of fast-dissolving tablet formulations evaluated before and after compression. Tables 1 and 2 show the arrangement and content of 3<sup>2</sup> factorial designs for the ondansetron fast dissolving tablet formulation [18].

Where +1 is the high value, -1 is the low value, and 0 is the centre value for the factors X<sub>1</sub> and X<sub>2</sub>. X<sub>1</sub> is the amount of crospovidone, X<sub>2</sub> is the amount of croscarmellose.

**2.5. Precompression Parameters.** Analysis of the precompression properties of each batch was carried out in accordance with established protocols, such as angle of repose, bulk density, tapped density, the Carr's consolidation index, and the Hausner's ratio [19].

## 2.6. Evaluation Parameters

**2.6.1. Weight Variation Test.** Each of the 20 pills was weighed separately using a computerized weighted scale (Ohaus, USA). Calculate the average weight of 20 pills and compare the individual tablet weights (Table 3) [20, 21].

**2.6.2. Thickness.** Placing the tablet between two arms of the vernier calliper (Indian calliper industries, Ambala, India), three pills from each batch were tested for thickness [20].

**2.6.3. Hardness.** Tablet tensile strength (kg/cm<sup>2</sup>) is the force required to compress a tablet. The Monsanto Hardness Tester was used here (Perfit). A random selection of three tablets from each batch was made [22].

**2.6.4. Friability Test.** Friability was assessed using a Roche friabilator. Twenty pills from each formulation were weighed and spun for four minutes at a speed of 25 resolution per minute. Removed any excess powder and then counted. The formula for determining how much weight one has lost is

$$\% \text{Friability} = W_1 - W_2 \times \frac{100}{W_1}. \quad (2)$$

W<sub>1</sub> is the pretest weight, and W<sub>2</sub> is the posttest weight.

**2.6.5. Dispersion Time.** Five 10 cm diameter tissue sheets were put in a petri plate (10 cm diameter). 10 mL eosin-water soluble dye was put to petri plate. On the tissue paper was carefully put a tablet. Wetting time is the time it takes for water to reach the tablet's top surface [22].

**2.7. In Vitro Disintegration Test.** For this test, the USP disintegration device was employed. Tested in 900 mL water at 37°C with six pills per formulation, the study was tripled [22].

**2.8. In Vitro Drug Release Studies.** The dissolving device USP II was used for this. At 37°C and 50 rpm, 900 mL pH 6.8 phosphate buffers were used for *in vitro* dissolving experiments. Five-minute aliquots were taken and analyzed at 248 nm on an Indian Systronics AU-2701 in Mumbai, India, at intervals of 5, 10, 15, 20, 25, and 30 minutes each. This was followed by a gradual release of medicines. There were three blindfolds in the test [23].

TABLE 3: Evaluation of postcompressional parameters of factorial design formulations of ondansetron fast dissolving tablets.

Parameters	F1	F2	F3	F4	F5	F6	F7	F8	F9
Hardness (kg/cm <sup>2</sup> )	3.41 ± 0.03	3.25 ± 0.14	3.34 ± 0.02	3.42 ± 0.40	3.37 ± 0.41	3.27 ± 0.19	3.38 ± 0.02	3.31 ± 0.04	3.34 ± 0.09
Friability (%)	0.54 ± 0.04	0.54 ± 0.02	0.560 ± 0.02	0.52 ± 0.09	0.58 ± 0.08	0.54 ± 0.02	0.57 ± 0.05	0.56 ± 0.01	0.60 ± 0.04
Weight variation test (mg)	201.12 ± 0.17	200.15 ± 0.19	201.24 ± 0.32	198.15 ± 0.74	200.14 ± 0.23	200.21 ± 0.25	200.01 ± 0.17	200.25 ± 0.18	202.38 ± 0.19
Dispersion time (seconds)	25.49 ± 0.02	19.83 ± 0.01	37.13 ± 0.03	22.24 ± 0.05	28.50 ± 0.04	17.67 ± 0.03	33.48 ± 0.01	27.74 ± 0.04	21.59 ± 0.02
Disintegration time (seconds)	132.13 ± 0.15	123.14 ± 0.17	147.25 ± 0.24	130.25 ± 0.28	142.21 ± 0.09	120.12 ± 0.55	145.12 ± 0.12	135.42 ± 0.29	125.14 ± 0.28
Percentage drug release (%)	93.87 ± 0.12	97.13 ± 0.23	90.25 ± 0.41	94.78 ± 0.31	93.14 ± 0.25	99.25 ± 0.36	91.18 ± 0.39	92.78 ± 0.15	95.12 ± 0.14

Data are represented as mean ± SD (n = 3).

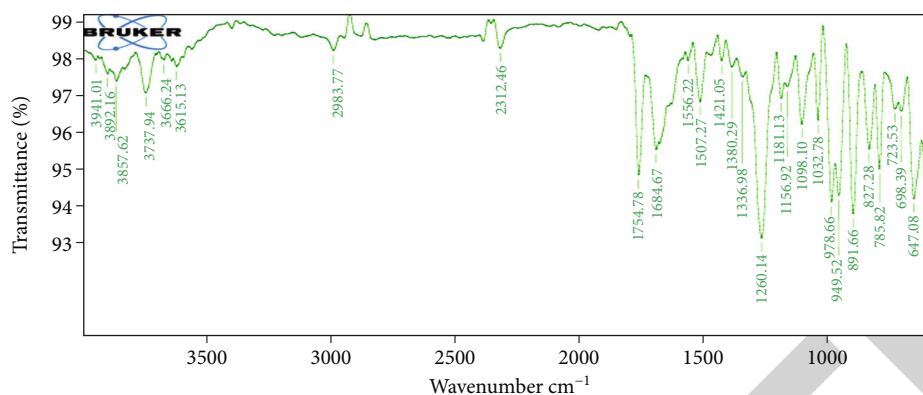


FIGURE 1: FTIR spectra of pure drug (ondansetron hydrochloride).

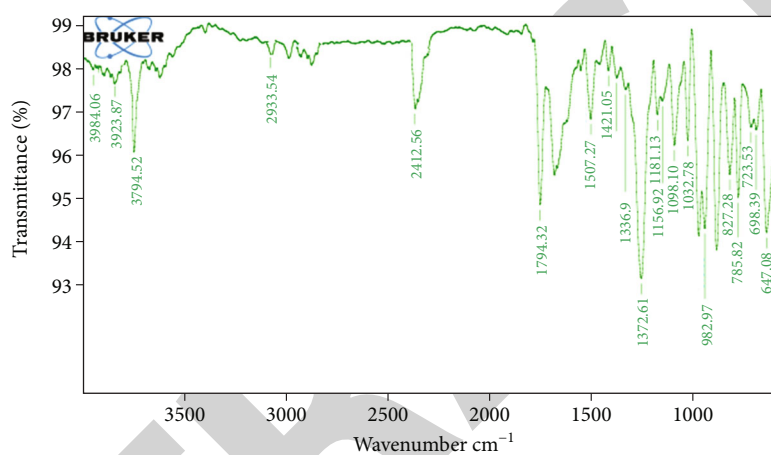


FIGURE 2: FTIR spectra of optimized formulation F6 ondansetron hydrochloride fast dissolving tablets.

**2.9. Accelerated Stability Studies.** For three months, the stability of selected tablet batches was investigated in a stability chamber at 40°C and 75% RH (Remi Instruments, India). To determine the stability of a tablet formulation, the physical characteristics of the tablet were measured at various temperatures and times. It was determined that *in vitro* dissolving time and dispersion time were evaluated after 15 days, one month, two months, and three months.

### 3. Results and Discussion

**3.1. FTIR Spectroscopy.** Figures 1 and 2 show IR spectra of pure drug (ondansetron hydrochloride) and optimized formulation F6 drug with super disintegrates (crospovidone and croscarmellose). Ondansetron hydrochloride has large IR absorption peaks at 3941.01 and 3892.17 perhaps owing to OH hydrogen bonding. Carbonyl group vibrations at 1754.8 and 1684.67 may be responsible for peak 2983.77, including 1754.78. Ring stretching may be seen in 1556.22, 1508.11, and 1507.27, and the existence of all drug peaks in the IR spectrum of the drug polymer combination shows no drug-carrier interaction.

**3.2. Precompression Parameters.** Table 4 shows the precompression results of final active blends (F1–F9). Bulk and

tapped densities varied from  $0.571 \pm 0.01$  to  $0.584 \pm 0.02$  and  $0.610 \pm 0.02$  to  $0.627 \pm 0.060$ , respectively. Carr's index ( $12.14 \pm 0.18$  to  $17.12 \pm 0.21$ ) and Hausner's ratio ( $1.14 \pm 0.13$  to  $1.24 \pm 0.17$ ) data also revealed favorable flow qualities.

**3.3. Postcompression Parameters.** Table 3 shows the outcomes of postcompression investigations. All nine formulations were similar in size and hardness, ranging from  $3.25 \pm 0.14$  to  $3.41 \pm 0.03$ . The low friability (1%) suggested good abrasion resistance. They passed the weight fluctuation test. All formulations had disintegration times under three minutes. The formulation that comprises F1, F3, and F6 formulations showed  $37.13 \pm 0.03$  to  $17.67 \pm 0.03$  and  $147.25 \pm 0.24$  to  $120.12 \pm 0.55$ . However, the disintegration qualities are not preferred when the quantity of both super disintegrants is arbitrarily changed from high to low. The dispersion time for F4 and F8 formulations ranged from  $130.25 \pm 0.28$  to  $135.42 \pm 0.29$ . Following the aforesaid observation, combining both disintegrates (7.5 percent of the total weight of tablet) has demonstrated a substantial effect and retards the optimal dispersion and disintegration time. The formulation of F6 revealed decrease dispersion and disintegration time of  $17.67 \pm 0.03$  and  $120.12 \pm 0.55$ ,

TABLE 4: Evaluation of precompression parameters of factorial design formulations of ondansetron hydrochloride fast dissolving tablets.

Parameters	F1	F2	F3	F4	F5	F6	F7	F8	F9
Bulk density (g/mL)	0.582 ± 0.01	0.584 ± 0.02	0.576 ± 0.01	0.572 ± 0.04	0.573 ± 0.02	0.571 ± 0.01	0.572 ± 0.01	0.574 ± 0.01	0.573 ± 0.02
Tapped density (g/mL)	0.614 ± 0.01	0.612 ± 0.02	0.610 ± 0.02	0.621 ± 0.08	0.618 ± 0.01	0.614 ± 0.02	0.622 ± 0.04	0.627 ± 0.06	0.615 ± 0.03
Angle of repose	21.14 ± 0.13	25.24 ± 0.31	22.34 ± 0.21	23.17 ± 0.21	22.21 ± 0.06	25.30 ± 0.51	24.72 ± 0.21	25.17 ± 0.08	25.48 ± 0.52
Carr's index	17.12 ± 0.21	12.27 ± 0.17	15.17 ± 0.11	13.54 ± 0.25	12.14 ± 0.18	15.02 ± 0.19	15.22 ± 0.21	14.12 ± 0.41	15.90 ± 0.25
Hausner ratio	1.22 ± 0.11	1.14 ± 0.13	1.24 ± 0.17	1.17 ± 0.21	1.15 ± 0.24	1.18 ± 0.22	1.19 ± 0.27	1.16 ± 0.15	1.14 ± 0.14

Data are represented as mean ± SD ( $n = 3$ ).

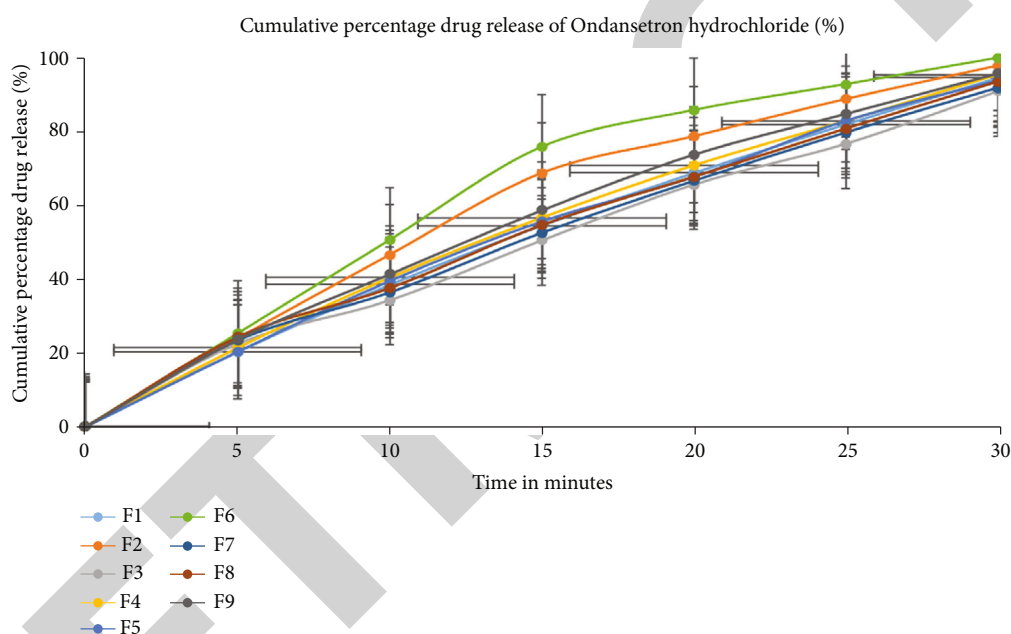


FIGURE 3: Cumulative percentage drug release of ondansetron hydrochloride fast dissolving tablets.

respectively. So, the optimal doses of both super disintegrants were added to improve the dissolving properties of formulation F6 ( $99.25 \pm 0.03$ ). Based on disintegration and dissolving statistics, this formulation seems promising.

**3.4. In Vitro Drug Release Studies.** Figure 3 shows the *in vitro* drug release of each final formulation batch (F1–F9). In all batches, more than 80% of the medication was released within 30 minutes. Increased super disintegrant concentration increases drug release considerably, as in the F6 formulation. More F1–F3–F6 batches were soluble due to myriad disintegration mechanism established by the combination of both super disintegrants than F7–F9. The most critical stage is caused by the swelling impact of additional water penetration. When disintegration comes into touch with an appropriate medium, it swells. Thus, the adhesion force between the tablet's ingredients is overcome, resulting in

the tablet disintegrating. The dissolving results indicated that the F6 formulation was the most promising batch, because the amount of drug release was found to be  $99.25 \pm 0.03$  in 30 minutes.

### 3.5. Factorial Design

**3.5.1. In Vitro Disintegration Time.** Crospovidone and croscarmellose concentrations were shown to affect disintegration time using a response surface plot (DT). According to the above findings, the disintegration times obtained were  $147.25 \pm 0.24$  to  $120.12 \pm 0.55$  seconds, with the polynomial equation producing a negative effect on disintegration time as concentrations of super disintegrates increased. This meant that as concentrations of super disintegrates increase, the disintegration time decreased. F4 and F8 were also found to have disintegration times of  $130.25 \pm 0.28$  and  $135.42 \pm 0.29$  seconds, respectively, based on the high-to-low-level

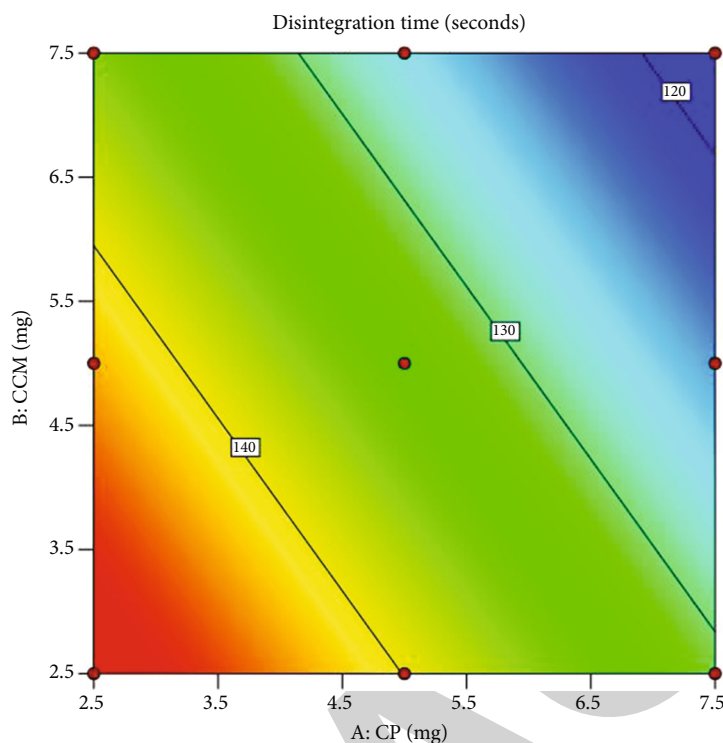


FIGURE 4: 2D contour plot graph for disintegration time with crospovidone and croscarmellose.

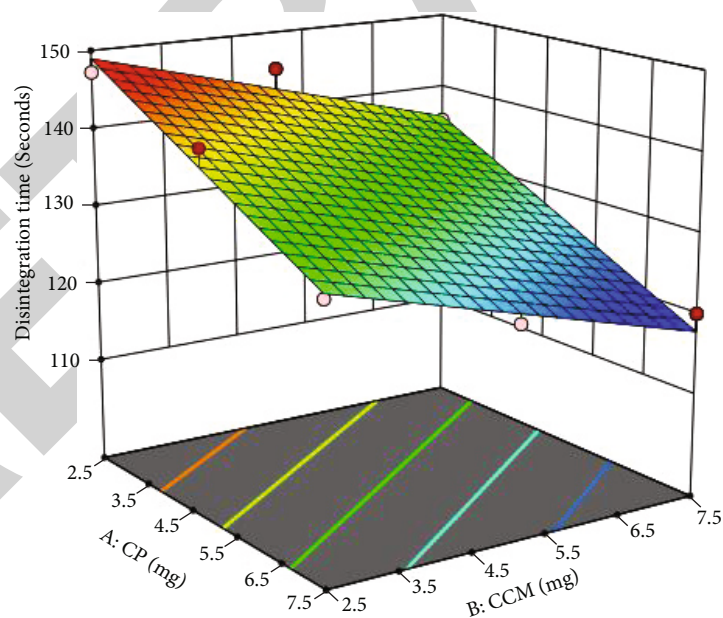


FIGURE 5: 3D RSM plot graph for disintegration time with crospovidone and croscarmellose.

or low-to-high-level disintegration levels. The capillary action of crospovidone super disintegrate has a more negative impact than that of croscarmellose, based on this finding. A random variation in disintegration time was seen because the concentrations of disintegrants could be varied from low to high levels, and the disintegration time

was reduced from  $142.21 \pm 0.09$  to  $123.14 \pm 0.17$  seconds in this study.

Here is a model equation that can explain the disintegration time of a parameter.

$$\text{Disintegration time} = +133.42 - 9.05 X_1 - 6.51 X_2. \quad (3)$$

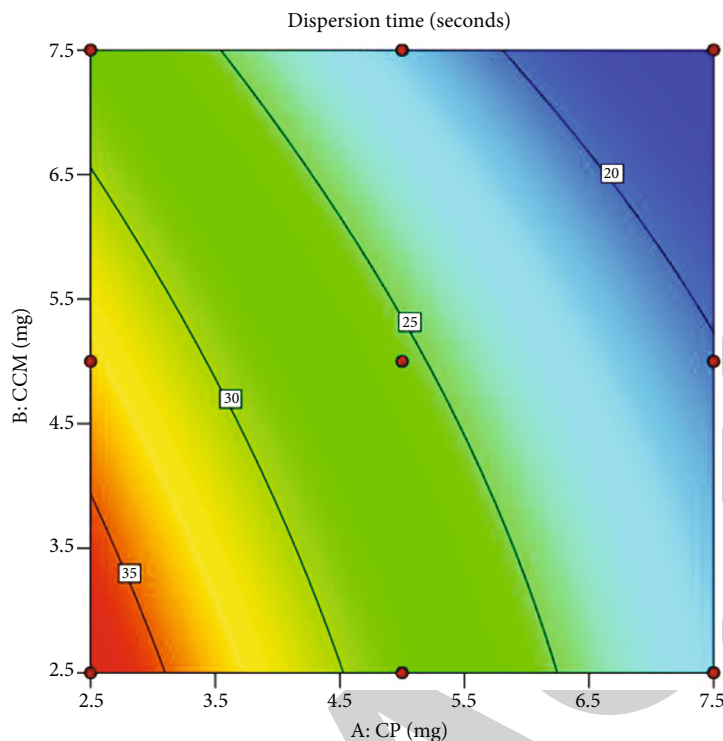


FIGURE 6: 2D contour plot graph for dispersion time with crospovidone and croscarmellose.

Coefficient values in the polynomial equation were discovered to be negative in proportion to the decay continuance of each super disintegrant as a result of increasing super disintegrant concentrations. The results are shown in Figures 4 and 5, respectively.

**3.5.2. Dispersion Time.** Crospovidone and croscarmellose were shown to affect dispersion time via the use of a response surface plot [24, 25]. Based on these findings, it can be concluded that the dispersion times obtained for crospovidone and croscarmellose are in the range of  $37.13 \pm 0.03$  to  $17.67 \pm 0.03$  seconds, with the polynomial equation producing a negative effect on dispersion time. This means that as concentrations of super disintegrates rise, so does the time required for their decomposition to take place.

As an additional measure, the dispersion time response was tested using two formulations: F4 which had high levels of crospovidone while having low levels of croscarmellose, and F8 which contained low levels while having a high level of crospovidone. After calculating the polynomial equation for both formulations F4 and F8, we found that the dispersion time was  $22.24 \pm 0.05$  seconds for F4 and  $27.74 \pm 0.04$  seconds for F8 when the concentration of each disintegrates or independent variable changed significantly. If you have ever had to break a pill in half because of a lack of super disintegrant, you will know what I am talking about.

Although the dispersion time of formulations including F2, F5, F7, and F9 was arbitrarily adjusted due to the concentrations of disintegrates being able to be modified from low to high, the disintegration time eventually decreased to

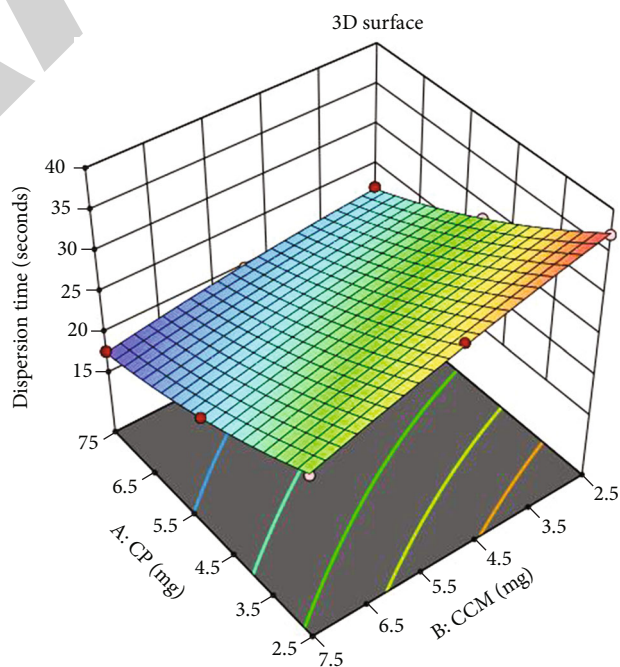


FIGURE 7: 3D RSM plot graph for dispersion time with crospovidone and croscarmellose.

be  $33.48 \pm 0.01$  to  $19.83 \pm 0.01$  seconds. Using the following model equation, dispersion time may be explained.

$$\begin{aligned} \text{Dispersion time} = & +25.50 - 6.44 \times X_1 - 3.48 \times X_2 + 1.21 \\ & \times X_1 \times X_2 + 1.15 X_1^2 - 0.4550 \times X_2^2. \end{aligned} \quad (4)$$

TABLE 5: Response parameters of various formulations.

Formulation code	Concentration of CP (X1)	Concentration of CCM (X2)	Dispersion time in seconds	Disintegration time in second	Percentage drug release (%)
F1	5	5	25.49 ± 0.02	132.13 ± 0.15	93.87 ± 0.12
F2	7.5	5	19.83 ± 0.01	123.14 ± 0.17	97.13 ± 0.23
F3	2.5	2.5	37.13 ± 0.03	147.25 ± 0.24	90.25 ± 0.41
F4	7.5	2.5	22.24 ± 0.05	130.25 ± 0.28	94.78 ± 0.31
F5	5	2.5	28.50 ± 0.04	142.21 ± 0.09	93.14 ± 0.25
F6	7.5	7.5	17.67 ± 0.03	120.12 ± 0.55	99.25 ± 0.36
F7	2.5	5	33.48 ± 0.01	145.12 ± 0.12	91.18 ± 0.39
F8	2.5	7.5	27.74 ± 0.04	135.42 ± 0.29	92.78 ± 0.15
F9	5	7.5	21.59 ± 0.02	125.14 ± 0.28	95.12 ± 0.14

Data are represented as mean ± SD (n = 3).

TABLE 6: Summary of results of regression analysis and ANOVA for measured response.

Parameters	Response	B <sub>0</sub>	B <sub>1</sub>	B <sub>2</sub>	B <sub>12</sub>	B <sub>11</sub>	B <sub>22</sub>	Model lack of fit
Dispersion time in seconds	Coefficients	25.49	-6.43	-3.47	1.20	1.15	-0.45	Insignificant
	P value	—	0.0001	0.0002	0.0086	0.0249	0.1982	
	Regression	DF = 5	MS = 65.99	SS = 329.94	F = 432.20	R <sup>2</sup> = 0.9986	—	
Disintegration time seconds	Coefficients	133.42	-9.05	-6.51	—	—	—	Insignificant
	P value	—	<0.0001	0.0003	—	—	—	
	Regression	DF = 2	MS = 372.47	SS = 744.94	F = 81.80	R <sup>2</sup> = 0.9646	—	
Percentage drug release	Coefficients	94.17	2.82	1.50	—	—	—	Insignificant
	P value	—	<0.0001	0.0006	—	—	—	
	Regression	DF = 2	MS = 30.66	SS = 61.32	F = 96.41	R <sup>2</sup> = 0.9698	—	

The coefficient values of the polynomial equation were found to have a negative effect on wetting time when the concentrations of both disintegrates were at their highest, and a positive coefficient effect was found when the concentrations of the super disintegrate fluctuated randomly between the highest and lowest levels [26, 27]. Figures 6 and 7 depict the findings.

**3.6. Percentage Drug Release.** The dispersion time was shown to be affected by the quantity of crospovidone and croscarmellose in the solution [28]. The percentage drug release (percent) was found to range from 90.25 ± 0.41 to 99.25 ± 0.36 within 30 minutes, and the polynomial equation producing the positive effect on percentage drug release indicates that, as the concentration of super disintegrates increase, the percentage drug release increases [27, 29].

For this reason, the formulations F4 and F8, which contain low levels of crospovidone but high concentrations of croscarmellose, respectively, were created to guarantee that the interaction between two independent variables may affect drug release percentages in a positive manner. According to the polynomial equation, the

change in concentration of either disintegrates or the independent variable displayed on the dependent response variable, i.e., the percentage drug release, was determined to be 94.78 ± 0.31 and 92.78 ± 0.15 within 30 minutes for formulations F4 and F8, respectively. A random variation in disintegration time was observed because the concentrations of disintegrates could be changed from low to high level, and thus, the percentage drug release was found to be between 91.18 ± 0.39 and 97.13 ± 0.23 within 30 minutes, despite the fact that the formulations contained F2, F5, and F7 as well. Figure 3 depicts the findings: as a result, the model equation for percentage medication release may be summarized as follows:

$$\begin{aligned} \text{Percentage drug release (30 minutes)} = & +94.17 + 2.82 X_1 \\ & + 1.50 X_2. \end{aligned} \tag{5}$$

Regression and ANOVA summaries, as well as a three-dimensional RSM plot for drug release percentage, are provided in Tables 5 and 6, respectively. Dispersion

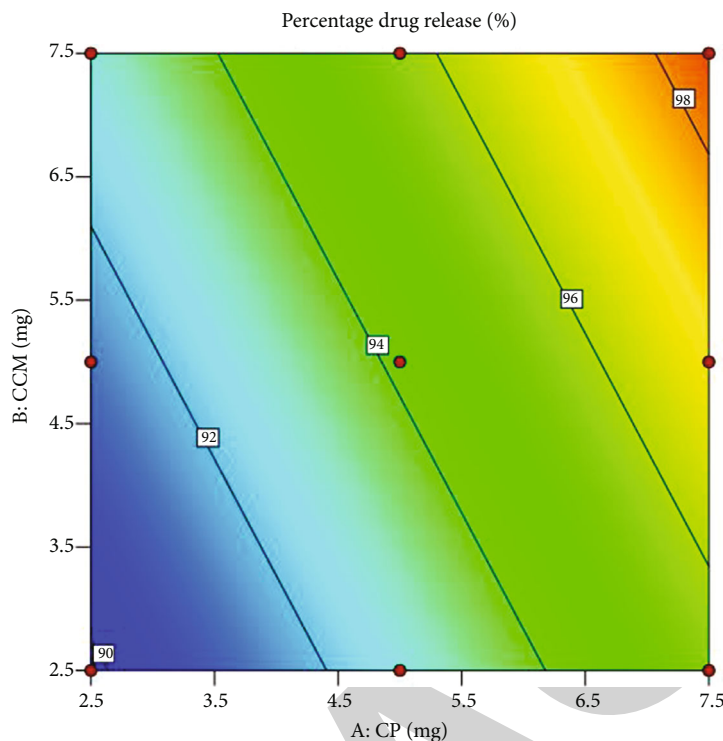


FIGURE 8: Contour plot graph for percentage drug release with crospovidone and croscarmellose.

time, disintegration time, and *in vitro* drug release are all shown in Figures 8 and 9 by 2D and 3D RSM plots.

**3.7. Numerical Optimization.** Figure 10 demonstrates the numerical optimization process used to produce a new formulation with desired answers. Crospovidone and croscarmellose concentration combinations with a desire of 0.9705 met the highest criteria of an optimal formulation during the study. Various dependent variables were tested with the improved formulation. Data was gathered and analyzed to see whether the observed results matched those expected (regression values such as adjusted  $R^2$  and predicted  $R^2$  values). Results are shown in Tables 6 and 7 along with percent prediction errors for actual and projected responses.

**3.8. Accelerated Stability Studies.** For 90 days, stability investigations were conducted under accelerated stability conditions (40°C/75 percent RH) using an optimal batch F6 according to ICH recommendations. Formulation F6 (physical-chemical characteristics and release profile) showed no notable modifications, as reported in Table 8. There is a high degree of stability in the formulation even when subjected to extreme stress. As shown in Figure 3, the *in vitro* drug release curves for the F6 tablet after three months of stability testing are parallel to those of the initial F6 batch (prior to stability). This shows there has been no change in the drug release behavior of the F6 tablet after three months of stability testing. In addition to that, optimized formulation F6

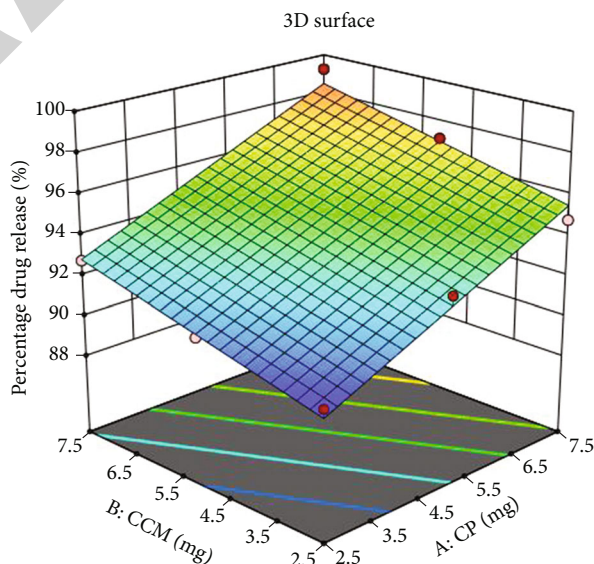


FIGURE 9: 3D RSM plot graph for percentage drug release with crospovidone and croscarmellose.

ondansetron hydrochloride was compared to that of marketed formulation (Zofran ODT), and the results were noticed and concluded that their significant changes were recorded by comparing the percentage drug release within 30 minutes.



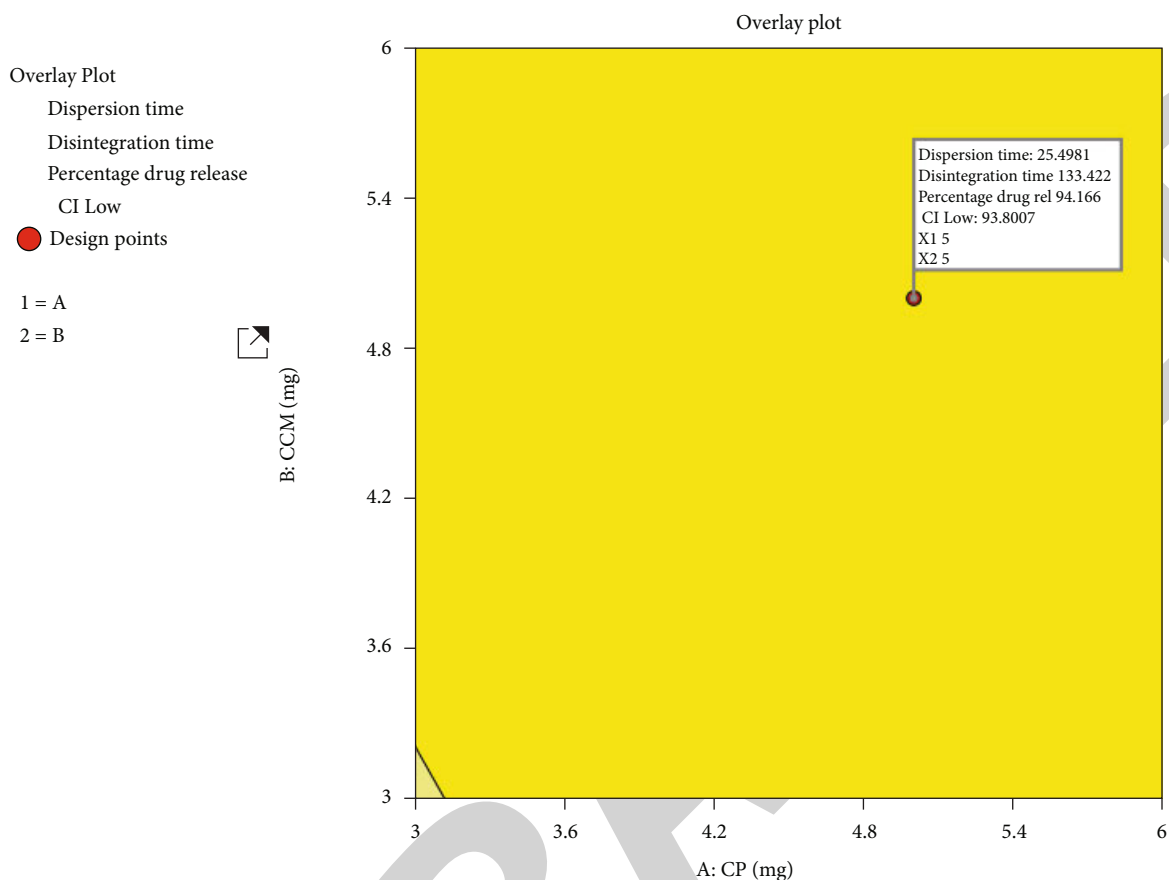


FIGURE 10: Overlay plot graph of ondansetron fast dissolving tablets.

TABLE 7: Comparison of regression values ( $R^2$ ) with the prediction error.

Response parameters	Constraints set	$R^2$ values	Adjusted $R^2$ values	Predicted $R^2$ values	% prediction error	Suggested model	$P$ values
Dispersion time	Minimize	0.9986	0.9963	0.9831	0.518	Quadratic model	0.0465
Disintegration time	Minimize	0.9646	0.9528	0.9186	2.554	Linear model	<0.0001
<i>In vitro</i> drug release	Maximize	0.9698	0.9598	0.9167	0.675	Linear model	<0.0001

TABLE 8: Stability studies of optimized batch F6 at accelerated condition.

Time	Tablet thickness	Tablet diameter	Hardness (kg/cm <sup>2</sup> )	Friability (%)	Dispersion time (seconds)	Disintegration time (seconds)	Percentage drug release (%)
15 days	3.36 ± 0.04	8.02 ± 0.01	3.27 ± 0.19	0.54 ± 0.02	17.67 ± 0.03	120.12 ± 0.55	99.25 ± 0.36
30 days	3.38 ± 0.04	8.04 ± 0.01	3.20 ± 0.21	0.52 ± 0.01	19.14 ± 0.07	123.21 ± 0.36	98.34 ± 0.17
60 days	3.41 ± 0.03	8.11 ± 0.03	3.24 ± 0.14	0.53 ± 0.01	18.35 ± 0.04	125.31 ± 0.18	97.35 ± 0.28
90 days	3.43 ± 0.04	8.13 ± 0.05	3.21 ± 0.16	0.53 ± 0.04	17.54 ± 0.04	124.12 ± 0.39	96.28 ± 0.41

Data are represented as mean ± SD ( $n = 3$ ).

#### 4. Conclusion

Ondansetron hydrochloride fast-dissolving tablets were developed and improved utilizing a central composite, response surface, randomized, quadratic, nonblock (13.0.9.0 version)  $3^2$  factorial design. On the basis of early research, two independent variables, crospovidone and croscarmellose, were chosen. There were three levels of each of these independent variables. Dispersion time, disintegration properties, and drug release are all significantly affected by the abovementioned combination of super disintegrants, such as crospovidone and croscarmellose, at the same proportion (7.5% with formulation F6). Due to water penetration, the tablet's adhesiveness is overcome, causing the tablet to dissolve and break apart. Fast dissolving tablets' maximum release of medication was made possible by the combination of tablet porosity and disintegrate wicking characteristics. Optimum formulas were selected via feasibility and grid searches using Design-Expert software to optimize and construct response surface plots and contour plots. Multivariate regression analysis yielded statistically meaningful polynomial mathematical models for a variety of response variables. The Design-Expert programmed picked formulation F6 because it had a dispersion time of  $17.67 \pm 0.03$  seconds, a disintegration time of  $120.12 \pm 0.55$  seconds, and an *in vitro* drug release of  $99.25 \pm 0.36$  percent within 30 minutes.

#### Data Availability

The data used to support the findings of this study are included within the article.

#### Conflicts of Interest

The authors declare no conflicts of interest.

#### Acknowledgments

The authors express their appreciation to The Research Center for Advanced Materials Science (RCAMS) at King Khalid University, Saudi Arabia, for funding this work under the grant number RCAMS/KKU/018-20; and Taif University Researchers Supporting Project number (TURSP-2020/01), Taif University, Taif, Saudi Arabia.

#### References

- [1] H. Seager, "Drug-delivery products and the Zydis fast-dissolving dosage form," *Journal of Pharmacy and Pharmacology*, vol. 50, no. 4, pp. 375–382, 1998.
- [2] T. Makino, M. Yamada, and J. I. Kikuta, "Fast Dissolving Tablet and Its Production," U.S. Patent 5,720,974, 1998.
- [3] S. Bharawaj, V. Jain, S. Sharma, R. C. Jat, and S. Jain, "Orally disintegrating tablets: a review," *Drug Invention Today*, vol. 2, 2010.
- [4] G. Bolhuis, K. Zuurman, and G. Te Wierik, "Improvement of dissolution of poorly soluble drugs by solid deposition on a super disintegrant. II. The choice of super disintegrants and effect of granulation," *European Journal of Pharmaceutical Sciences*, vol. 5, no. 2, pp. 63–69, 1997.
- [5] D. Masih and R. Gupta, "Mouth dissolving tablets—a review," *Pharmaceutical and Biosciences Journal*, vol. 1, pp. 18–24, 2013.
- [6] H. Heinemann and W. Rothe, "Preparation of porous tablets," U.S. Patent 3,885,026, 1975.
- [7] M. Mohana and S. Vijayalakshmi, "Development and characterization of solid dispersion-based orodispersible tablets of cilnidipine," *Beni-Suef University Journal of Basic and Applied Sciences*, vol. 11, no. 1, pp. 1–12, 2022.
- [8] R. S. Upasani and A. K. Banga, "Response surface methodology to investigate the iontophoretic delivery of tacrine hydrochloride," *Pharmaceutical Research*, vol. 21, no. 12, pp. 2293–2299, 2004.
- [9] Y.-J. You, Y. Kim, G.-Y. Song, and B.-Z. Ahn, "(E)-6-(1-alkyloxyiminoalkyl)-5,8-dimethoxy-1,4-naphthoquinones: synthesis, cytotoxic activity and antitumor activity," *Bioorganic & Medicinal Chemistry Letters*, vol. 10, no. 20, pp. 2301–2303, 2000.
- [10] S. Clarke, N. Austin, J. Bloomer et al., "Metabolism and disposition of  $^{14}\text{C}$ -granisetron in rat, dog and man after intravenous and oral dosing," *Xenobiotica*, vol. 24, no. 11, pp. 1119–1131, 1994.
- [11] M. K. Dudhat and A. Dhingani, "A design research on formulation and characterization of gastro-retentive tablet to target ulcer and control emesis," *International Journal of Pharmaceutical and Bio Medical Science*, vol. 2, pp. 81–91, 2022.
- [12] S. L. M. Ribeiro Filho, C. T. Garcia, M. V. Donadon, F. Scarpa, and T. H. Panzera, "The impact behaviour of hybrid fibre-particle composites based on a full factorial design," *Communications*, vol. 31, article 103459, 2022.
- [13] S. Shirsand, S. Suresh, V. Kusumdevi, and P. Swamy, "Formulation design and optimization of fast dissolving clonazepam tablets by sublimation method," *Indian Journal of Pharmaceutical Sciences*, vol. 73, no. 5, p. 491, 2011.
- [14] S. Sharma, S. Bharadwaj, and G. Gupta, "Fast dissolving tablets of promethazine theoclate by using natural superdisintegrants," *Research Journal of Pharmacy and Technology*, vol. 1, pp. 218–224, 2008.
- [15] M. Koland, V. Sandeep, and N. Charyulu, "Fast dissolving sublingual films of ondansetron hydrochloride: effect of additives on *in vitro* drug release and mucosal permeation," *Journal of Young Pharmacists*, vol. 2, no. 3, pp. 216–222, 2010.
- [16] A. Roy, A. Sharma, S. Yadav, L. T. Jule, and R. Krishnaraj, "Nanomaterials for remediation of environmental pollutants," *Bioinorganic Chemistry and Applications*, vol. 2021, 2021.
- [17] N. Bhadkwade, S. Rawat, and U. Galgatte, "Formulation and evaluation of oral disintegrating tablets of lornoxicam by  $3^2$  factorial design," *Journal of Applied Pharmaceutical Science*, vol. 3, pp. S42–S52, 2013.
- [18] L. Kaur, R. Bala, N. Kanojia, M. Nagpal, and G. A. Dhingra, "Formulation development and optimization of fast dissolving tablets of aceclofenac using natural superdisintegrant," *International Scholarly Research Notices*, vol. 2014, Article ID 242504, 10 pages, 2014.
- [19] Y. Bi, H. Sunada, Y. Yonezawa, K. Danjo, A. Otsuka, and K. Iida, "Preparation and evaluation of a compressed tablet rapidly disintegrating in the oral cavity," *Chemical and Pharmaceutical Bulletin*, vol. 44, no. 11, pp. 2121–2127, 1996.
- [20] Y. Bi, H. Sunada, Y. Yonezawa, and K. Danjo, "Evaluation of rapidly disintegrating tablets prepared by a direct compression method," *Drug Development and Industrial Pharmacy*, vol. 25, no. 5, pp. 571–581, 1999.